Università di Genova

Dottorato di Ricerca in Ingegneria dei Modelli delle Macchine e dei Sistemi per l'Energia, l'Ambiente e i Trasporti

Curriculum Ingegneria delle Macchine e dei Sistemi per l'Energia, l'Ambiente e la Propulsione

XXXIV Ciclo

Aeroelastic study of the effect of the leakage flow in shrouded low-speed fans

Mehrdad Moradi

Supervisors: Prof. Edward Canepa, Prof. Andrea Cattanei

and Prof. Luigi Carassale

A thesis submitted to the University of Genoa for the degree of Doctor of Philosophy

December 2022

Abstract

A large-amplitude axial vibration of a rotor fan with shrouded blades has been experimentally observed. Various mechanical measurements have been performed to characterize this vibration. To this aim, a new test stand has been designed. The analysis of the Campbell diagram shows that the vibration is related to a backward-whirl vibrational mode of the rotor which is always present, with different amplitudes depending on the operating conditions and configuration. Modifications of the shroud roughness and insertion of small obstacles in the gap region have independently shown that leakage flow fluctuations constitute the excitation of the large-amplitude vibration. This indicates that the phenomenon is likely an aeroelastic flutter, as it is also suggested by the observed intermittency and aerodynamic stiffening. A complete series of aerodynamic measurements have been carried out, employing complementary techniques (PIV and LDA), to supply general information on the flow as well as deepen the unsteady flow involved in the flutter phenomenon. The PIV measurements have shown a recirculating flow downstream of the fan due to the presence of the obstruction disk which results in a backflow entering the gap between the rotating ring and the stationary shroud (the leakage flow). Large-scale eddies have been found at the edge and inside of this recirculating flow by investigating the PIV snapshots and have been proved by POD analysis. The LDA measurements close to the gap region have confirmed that the leakage flow enters from the gap downstream of the fan and mixes with the rotor inflow upstream of the fan when it leaves the gap.

Using a new double phase ensemble average technique, the periodic part of the LDA signals related to the vibration has been investigated; it allows studying the effect of the precession motion of the rotor on the flow. Analyzing the flow using this method shows that the flutter also affects the relative flow angle at the rotor inlet, and consequently the angle of attack at the blade tips, which finally causes the aeroelastic phenomenon. Moreover, it has been found that the maxima and minima in the velocity field are located at angular positions different from the ones at which the gap outlet area is maximum and minimum, but a certain delay exists.

Dedicated to all women and men who are fighting for freedom and knowledge.

Especially Iranian Women.

Acknowledgments

This doctoral thesis is the result of my work at the DIME department of the University of Genoa, from November 2018 to December 2022. I would like to express my deepest gratitude to my supervisor Prof. Andrea Cattanei for making it possible to do my doctoral studies at the University of Genoa. Without his continuous academic and mental support, this work would not have been possible. He has been a constant source of brilliant ideas and motivation and I am grateful for his invaluable tutorials on turbomachinery and aeroacoustics. I am extremely grateful to my supervisor Prof. Luigi Carassale who also provided first-class academic and technical support at every stage of my PhD. His ingenuity in the field of rotor dynamics and vibrations has been the solution to my problems many times. Also, I could not have undertaken this journey without the great support of Prof. Edward Canepa. He is a generous man who taught me a lot about experimental measurements and he has always been very kind and understanding during my PhD. Thanks for offering help to me whenever I need it and for all conversations and guidance about life.

I would also like to thank my parents, family, and friends for their support in various forms; and little Anya with her lovely drawings. My final and special thanks are directed to my little brother, Mehran, a beautiful mind.

Cogito, ergo sum.

Genoa, December 2022

Contents

List of Tables

List of Figures

Nomenclature and Acronyms

BB	broadband noise
BPF	$= z_R \Omega/2\pi$, blade passing frequency
BW	backward
c	blade chord
DP	design point
f	frequency
$F_{int}(f)$	interference function of the rotor
f_r	rotation frequency
f_v	vibration frequency
FEM	finite element method
FRF	frequency-response function
FT	Fourier transform
FW	forward
HI	harmonic index
i	imaginary unit
k	kinetic energy
IRF	impulse-response function
LDA	laser doppler anemometry
LDV	laser doppler velocimetry
LTI	linear time-invariant
m	blade index
Ma	mach number
n	harmonic order
PDF	probability density function
PIV	particle image velocimetry
POD	proper orthogonal decomposition
PSD	power spectral density
Q	volumetric flow rate
r_{hub}	rotor hub radius
r_{tip}	rotor tip radius
Re	Reynolds number
R_ϑ	blading non-uniformity parameter
SF	$= \Omega/2\pi$, shaft frequency
St	$= 2\pi f/\Omega$, Strouhal number
std	standard deviation
S_{pp}	one-sided auto power spectral density of p
TN	tonal noise
Tu	turbulence intensity
u_{tip}	the peripheral speed of the blade
v	flow velocity
VFD	variable frequency drive
x_1	axial displacement of the ring
z	blade number
z_R	total rotor blade number
Δp	pressure rise
ϑ	blade position in the circumferential direction (relative to the first blade)
τ	blade time delay

Φ	flow coefficient, $\frac{Q}{u_{tip}\,\pi\,r_{tip}{}^2}$
Ψ	pressure rise coefficient, $\frac{\Delta p}{0.5\,\rho_0\,u_{tip}{}^2}$
ω_r	rotational speed
Ω	rotational speed (expressed in rad/s)
ω_v	vibration speed

Superscripts

$\sim$	related to the ensemble average (periodic component)
$-$	related to the time average
$'$	related to non-periodic instantaneous fluctuation

Subscripts

a	axial
bl	related to the blade
r	radial
rot	related to the rotor
tonal	related to tonal components
θ	tangential

1. INTRODUCTION AND BACKGROUND

In automobile engine cooling systems, radiators work only if air flows through them, which is why a low-speed electric fan is vital to provide suitable airflow under different operating conditions: e.g. when the vehicle is idle, driving at low speed, and under high loading as uphill driving.

Choosing the appropriate fan will depend on many factors including the available space, the driving method, mechanical and aerodynamic efficiency, as well as its mechanical strength, noise levels, and ultimately its cost. Depending on where they are placed, cooling fans can either push or pull air through radiators, and in addition to their layout and positioning, these large-scale products have peculiar shapes. For instance, there are important differences between radially stacked (i.e. straight) and leaned/swept (i.e. curved) fan blades. The former have usually better aerodynamic performance and fewer structural problems than the latter but are noisier. This is why, nowadays, curved blades are almost universally adopted despite the resulting complications. Other characteristics of low-speed fans, such as low-solidity blading, large gaps between stationary and rotating parts, and small hub-to-tip diameters ratio, can produce high mechanical flexibility and flow distortions, which may result in phenomena that are unusual for more widely examined turbomachines such as axial compressors and even industrial fans.

In some types of cooling fans, centrifugal force and aerodynamic load cause the blades to deform, which is often limited by a ring connecting the blade tips [1]. This rotating ring, which rotates in a stationary shroud with a gap in between, in addition to strengthening the rotor, further increases the fan's volumetric efficiency since it limits the recirculating airflow at the blade tip; however, it may increase the radiated noise and may result in unusual phenomena, e.g., it creates a peculiar flutter-like vibration as in the present case.

In this research, a cooling fan of this type with unequally spaced 7 blades and a 456-mm-external-diameter external ring is studied. This rotor is installed on and guided by a stationary shroud that in production units supports the radiator. In addition, a disk has been placed downstream of the rotor to simulate the aerodynamic obstruction caused by the thermal engine.

The problem starts when the fan approaches the design speed; at this point, simultaneously with the rotation of the fan, a high-amplitude axial oscillation is observed, which, in the outer ring, may reach more than ± 5 mm.

Investigating the cause of these vibrations can be complicated because of interactions between the inertial, elastic, and aerodynamic forces occurring while the rotor is exposed to the fluid flow which

turns this flutter-like oscillation into an aeroelastic problem. Two aspects are investigated in this research, which are expected to cause this aeroelastic phenomenon. The first one is related to the fan outflow (downstream), which hits the obstruction disk and quickly becomes centrifugal. This flow is associated with a recirculating flow that enters the gap as a backflow. The second subject is related to the axial displacement of the rotor ring inside the stationary shroud due to the periodic vibration; this causes a periodic modification in the gap geometry (gap size), namely, in the opening and closing of the gap outlet upstream of the fan. As a result, a periodic perturbation of the fan inflow likely results in a periodic aerodynamic force, which in turn drives the vibration in a typical aeroelastic loop.

There has been a lot of research on the tip-leakage flow of axial flow fans in recent years, e.g. see Refs. [2-8]. Blade tip noise in low-speed shrouded fans has also been investigated by Moreau and Kindler, e.g. see Refs. [9-11]. In addition, many articles have been published in the field of aeroelasticity, especially in turbomachines, e.g. see Refs. [12-13], but none of those are related to shrouded fans and those studies are different from the investigated subject in this research. Hence, to the best knowledge of the author, this flutter-like problem has never been reported before in the literature for the shrouded fans.

This research aims to identify and describe systematically this flutter-like phenomenon, experimentally studying both the vibration and the flow upstream and downstream of the fan. Then, an attempt will be made to study the interaction of aerodynamic forces on the elastic structure and also the flow behavior in the area close to the gap to find an answer to the reason for this flutter-like oscillation.

Investigating this phenomenon in this study may also help to better understand aeroelastic phenomena related to the leakage flow in more important turbomachines such as axial compressors and turbines.

Since we are dealing with an aeroelastic problem, the flutter-like vibration is studied from two aspects: structural and aerodynamic points of view. For this purpose, several experiments have been conducted on these two aspects, with the final aim of investigating the interaction of these two. Due to both the lack of information about the nature of this phenomenon and the practical difficulties related to aerodynamic measurements in such a complicated geometry, a kind of trial-and-error approach has been followed. To perform all these experiments, a new test stand has been designed which is suitable for simultaneous mechanical and aerodynamic measurements on fans.

This research is outlined in the following way:

In Chapter One, the context of the study is introduced. The research objectives and questions are identified, and the value of such research is argued. No related bibliography has been reviewed because, to the knowledge of the author, such a problem has never been reported in the literature.

In Chapter Two, the experimental setup and measurement techniques are reviewed including the test stand specifications and the measurement devices and methods that will be used for structural and aerodynamic measurements.

In Chapter Three, the theoretical background of data processing techniques is presented. In addition, a new double ensemble average technique is introduced.

In Chapter Four, the general characteristics of the fan are reported. Results of both an experimental and a FEM modal analysis are investigated. A comprehensive mechanical investigation is performed using different measurement devices and methods. Then, the dynamic and aeroelastic behavior of the fan is discussed. Finally, theoretical background for the structural and aerodynamic forces is developed.

In Chapter Five, in order to study the flow characteristics relevant to the vibration, the result of a wide range of aerodynamic investigations are reported and analyzed, which have been performed by means of PIV and LDA measurements.

In Chapter Six, finally, conclusions are drawn and an outlook is given.

2. EXPERIMENTAL SETUP AND MEASUREMENT TECHNIQUES

2.1. Test stand

2.1.1. General information

The new test stand has been designed and manufactured to provide reliable and reproducible tests. For this purpose, this test stand has been designed based on ISO standard 5801 and made of 3-mm-thick iron plate, is almost 4-m long (2.2 m without the auxiliary centrifugal fan) and has a 1.7-m diameter, Fig 2.1; This stand consists of 5 sections (tubes). Two flanges are welded to the front and back of each section so that the sections can be connected to each other. At the front and back of the test stand, two round flat plates, which are reinforced by several ribs, are connected to the first and final sections. The front plate has a test panel installation area of $1 \times 1\ m$ and the back plate has an external appendage to let the flow enter and exit and connect the chamber to the auxiliary fan. The front section has 3 windows at the sides and top for optical tests. For installing measuring instruments access to the inside of the chamber is possible through these windows. 4 holes and wall pressure tappings have been embedded equally angular spaced in the front section at the same axial location to measure the average static pressure at the wall. In addition, 3 holes have been considered for insertion of the Pitot-static tube at the different axial positions of the front section. The 3 middle sections are for flow straightening. First, two layers of nets and behind those a layer of honeycomb to prevent the growth of swirl in a normally axial flow and to reduce turbulence in the settling chamber. A window is designed at the back section of the enclosure to provide easier access for the installation and maintenance of the flow control system. The flow control system is a conical valve

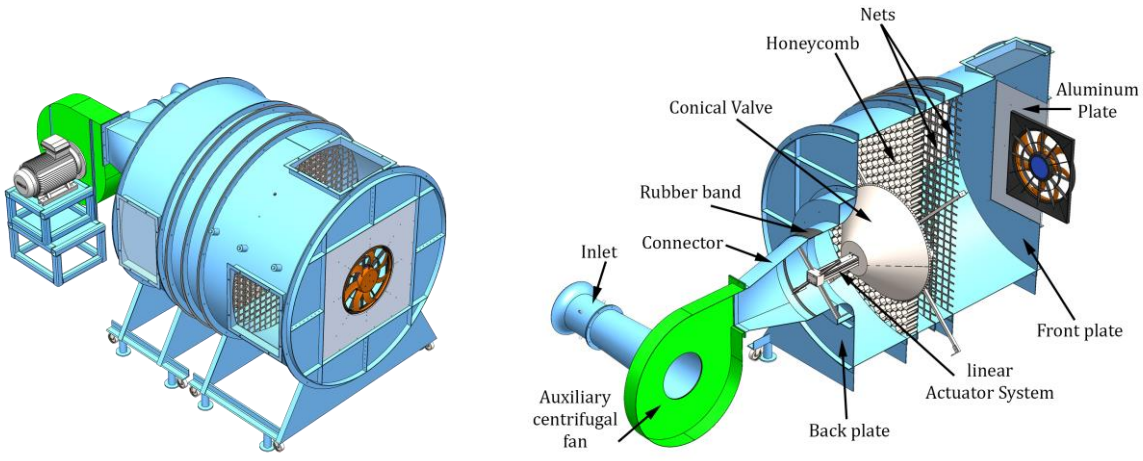

Figure 2.1. Test stand with auxiliary centrifugal fan (The mesh size is not the actual size for nets and honeycomb).

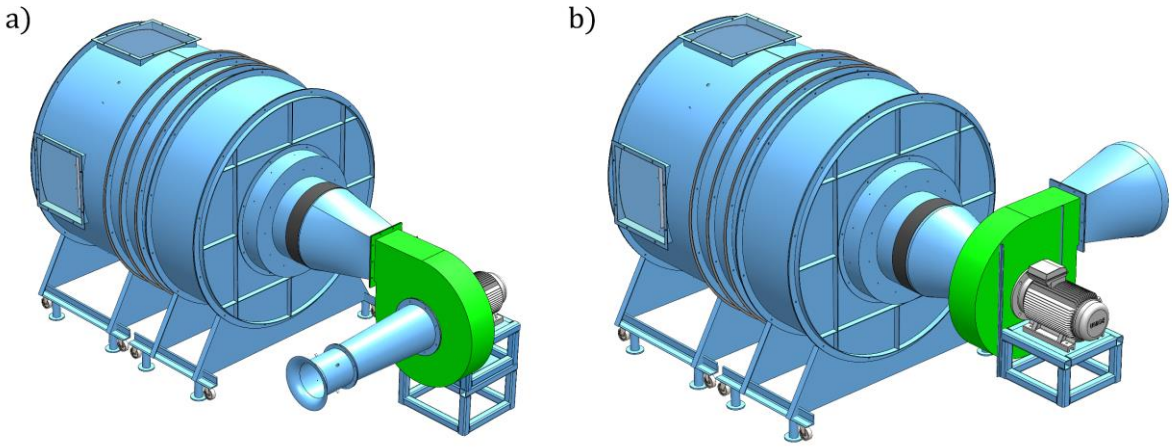

Figure 2.2. Two configurations of test stand. a) pushing air. b) sucking air.

controlled by a linear electrical actuator and it can provide the volumetric flow rate in the ranges of 0 to 3 m^3/s. This system has been mounted and fixed to the walls of the back section of the test stand and the external connector of the back plate using two cross beams. For ease of carrying, there are separate bases under the front and back sections of the system, allowing the system to be separated into two parts. These bases are equipped with rubber pads for fixing and separate wheels for mobility.

For mounting the fan to the front plate, a replaceable 1×1 m and 10 mm thick aluminum test plate has been designed which also allows the installation of measuring devices.

This test stand may be operated in two different configurations. Namely, the basic configuration is of the "pushing" kind, Fig 2.2a, i.e. air is pushed from the settling chamber into the fan, but the flow direction may be reversed, i.e. air may be pushed into the settling chamber by the fan, "sucking" kind Fig 2.2b.

The auxiliary fan is a centrifugal fan that can provide a maximum of 3 m^3/s volumetric flow rate and 10790 N/m^2 total pressure. By turning the fan and using two different connectors which are designed for this purpose this fan can be used in both configurations of sucking and pushing the air. For the determination of flow rate at the inlet, two sets of bell-mouth inlets have been designed to cover all the needed flow rate ranges, Fig 2.3. Besides, a safety cage has been provided to cover the test area at the front of the test stand.

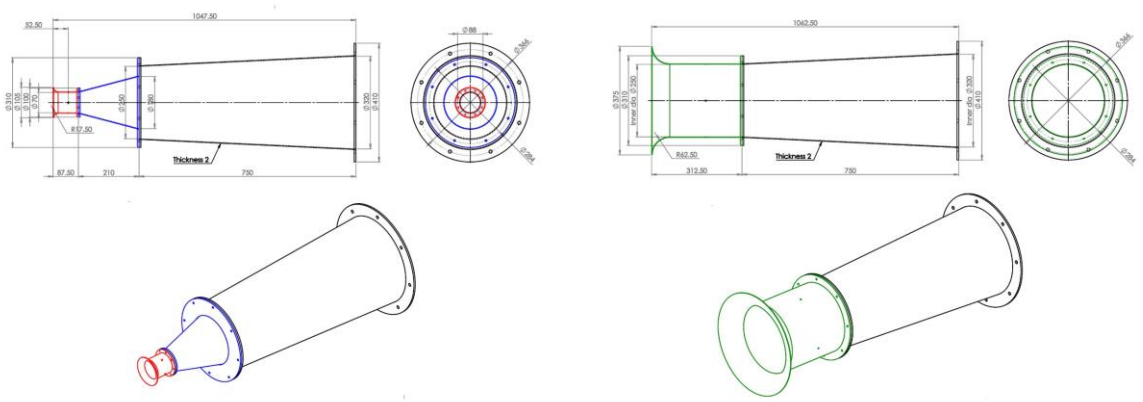

Figure 2.3. Geometry of inlets.

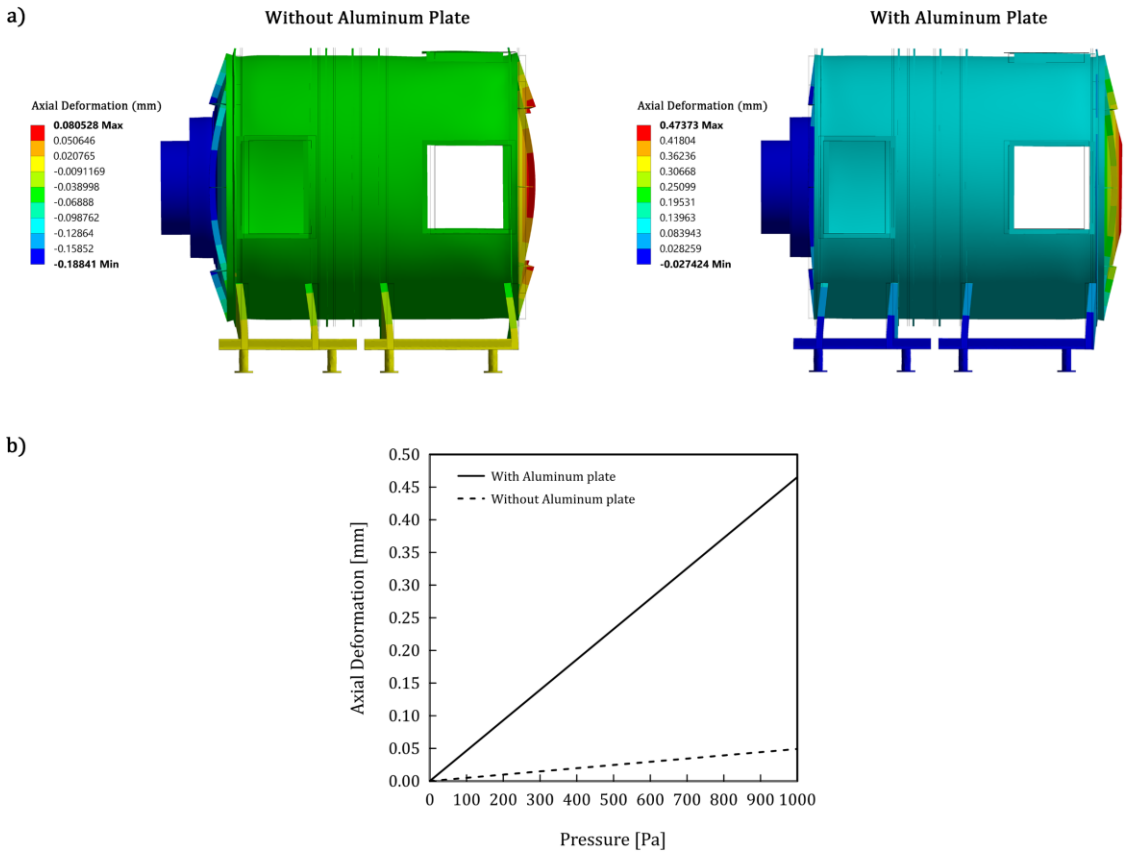

Figure 2.4. a) Axial deformation up to maximum pressure (1000 Pa) inside the test stand. b) Axial deformation at the center of the front plate due to the pressure increase.

2.1.2. Structural analysis

For proper design of the test-plenum and in order to have suitable mechanical characteristics of the whole assembly, stress, and buckling FEM analyses have been done; a modal analysis has also been

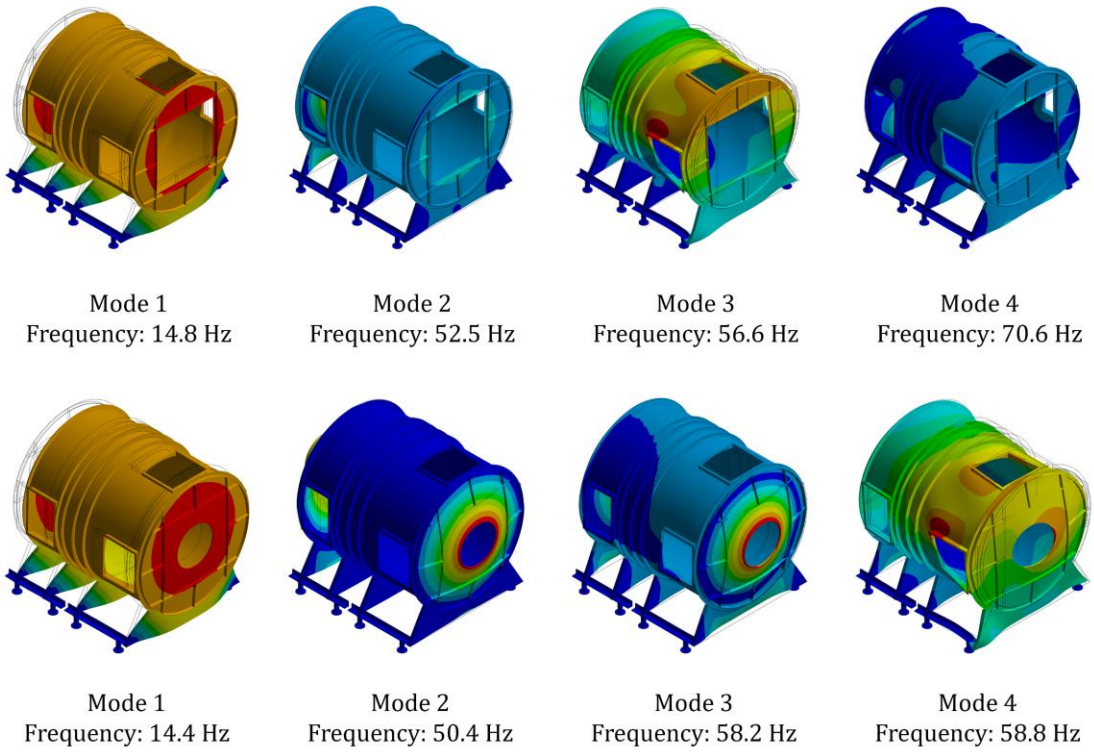

Figure 2.5. First 4 mode shapes and frequencies of the test stand, top row: without aluminum panel, bottom row: with aluminum panel.

performed in order to check that the modal frequencies of the test-stand are larger than the expected vibration frequency of the investigated fan. These analyses have been carried out on the test stand geometry with and without the aluminum plate to also consider the effect of this plate.

2.1.2.1. Stress and deformation analysis

The stress and deformation FEM analysis have been done to determine where the maximum deformation takes place and to be sure the maximum stress is less than the yield stress of the structure. One of the important points to monitor the deformation is the center of the front plate where the cooling fan is going to be mounted. An increasing pressure ramp at the range of 0 to 1000 Pa has been applied inside the chamber and as the axial deformation is the most important part of total deformation, the axial deformation of the test stand at maximum pressure (1000 Pa) has been reported in Fig 2.4a for both cases with and without the aluminum plate. In the case with the aluminum plate, it can be seen that the maximum stress and deformation take place at the center of the front plate where the stress and deformation are 10 MPa and 0.47 mm respectively. While the maximum stress and deformation in the case without the aluminum plate are in the back plate of the

test stand which are 5.89 MPa and 0.19 mm respectively. This analysis shows the maximum stress due to the pressure rise in the test stand is far below the yield stress of the structure's material, both steel and aluminum.

Another aspect is by measuring the maximum deformation in the center of the aluminum test plate where the fan is mounted at the maximum investigated pressure range for the studied fan which is almost 500 Pa it can be seen that the axial deformation is almost 0.2 mm which is negligible, Fig 2.4b.

2.1.2.2. Buckling analysis

The failure mode known as buckling is defined by the abrupt failure of a structural part under high compressive loads, where the actual compressive stresses at failure are lower than the ultimate compressive stresses the material can take. Elastic buckling of shell structures, such as cylindrical shells subjected to external pressure and loaded in axial compression, is extremely sensitive to defects and can be disastrous. Linear buckling analysis prevents any structural buckling failure related to pressure rise inside the test stand. To do this, the test stand has been considered with and without the aluminum plate at the maximum external pressure, 1000 Pa, when the air is sucked into the chamber. By performing the linear buckling analysis, the first critical mode with mounting the aluminum plate on the test stand happens at 149 times applied maximum external pressure, 149000 Pa. This result shows that buckling failure happens much higher than the ultimate compressive stresses. This first critical mode for the case without the aluminum plate is 420 times.

2.1.2.3. Modal analysis

In this study, the dynamic behavior of the fan is supposed to be investigated and it is important to know the dynamic characteristics of the test stand as well. One method for evaluating the dynamic behavior of mechanical parts and structures is modal analysis. The natural properties of a structure, such as its natural frequency and mode shapes, can also be explained using this technique. Performing a FEM modal analysis for the test stand both with and without the aluminum plate cases gives natural frequency and mode shapes. Figure 2.5 shows the first 4 mode shapes and frequencies of the test stand for both with and without aluminum plate cases. The first natural frequency in the case with the aluminum plate is 14.4 Hz and the next modes are happening at frequencies higher than 50 Hz which is higher than the design rotational speed.

The test stand has been constructed and completed in May 2020. After installation and setup in the DIME laboratory, a set of measurement devices have been installed for mechanical and fluid dynamic measurements (upstream and downstream). The test stand has been designed in order to allow

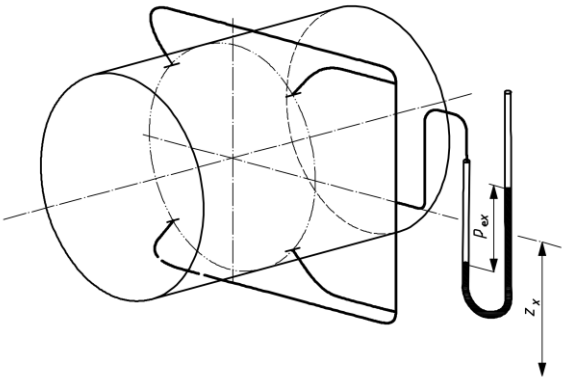

Figure 2.6. Four interconnected wall tappings for pressure measurements [14].

maximum flexibility: it may be used as a wind tunnel and also to test low-speed axial compressor models.

2.2. Measurement of operating parameters

2.2.1. Pressure measurements

It is essential to ensure that static pressure measurements on the fan's inlet and outlet are taken relative to atmospheric pressure or the pressure present in a common test enclosure. When the flow is reasonably uniform, free of swirl and separation, four interconnected wall tappings can be used, Fig 2.6. In accordance with ISO 5801 [14], fan pressure is defined as the difference between stagnation pressures at the fan outlet and inlet. In the case of standard air with duct velocities less than 40 m/s and Mach numbers less than 0.122, the stagnation pressure is virtually equal to the total pressure.

2.2.2. Rotational speed

Various types of tachometers can be used to measure rotational speed. Accuracy is important since fan performance is sensitive to even small variations in speed and thereafter this change of speed matters because the flow rate varies directly as the speed, pressure as the square of the speed, and absorbed power as the cube of the speed. For the desired experiments two sets of optical sensors have been mounted on the wooden panel with reflective elements as a target on the rotor.

2.2.3. Particle Image Velocimetry

Particle Image Velocimetry (PIV) is a flow field measurement technique that provides instantaneous, cross-sectional measurements of flow velocity vectors. Normally, two velocity components are measured. However, a stereoscopic approach is able to record three velocity components, which

results in instantaneous 3D velocity vectors for the entire area. This method can cover the velocity range from zero to supersonic and does not require intrusive approaches to measure the velocities of micron-sized particles passing through the flow [15].

The operation process of a PIV system is briefly shown in Fig 2.7. PIV measures the particle movement between two pulses of light to obtain velocity vectors of the particle-seeded flow on the sub-sections of the targeted area. A light sheet (laser sheet) illuminates the flow in the target area. Digital cameras are able to capture separate image frames when the target area at each light pulse is captured by the camera lens. Following the recording of two light pulses, the images are divided into small subsections, known as interrogation areas (IA). The pixels in I_1 and I_2 of each interrogation area are then correlated with each other. A signal peak is produced by the correlation, which identifies ΔX, the common particle displacement:

$$\bar{V} = \frac{\Delta \bar{X}}{t} \tag{2.1}$$

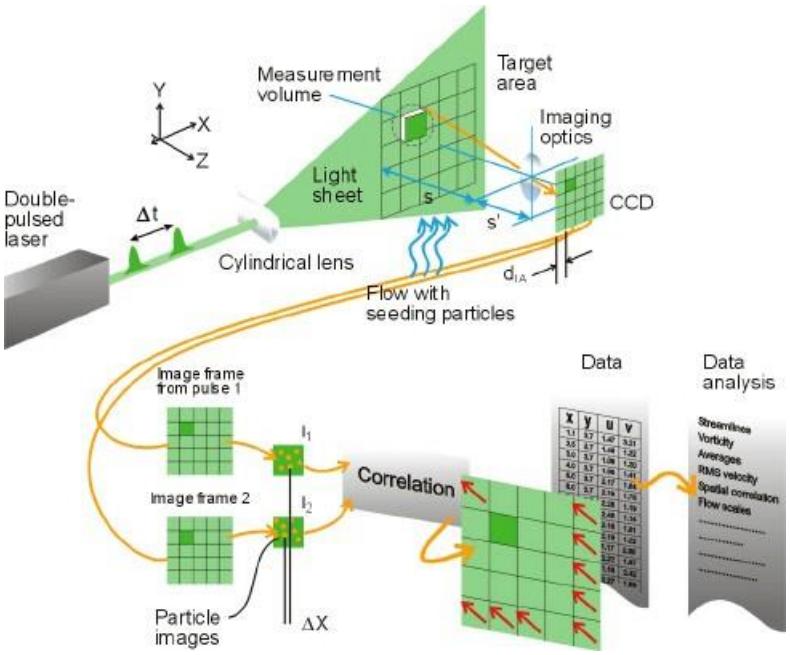

Figure 2.7. The operation process of a PIV system [15].

In order to obtain a velocity vector map over the entire target area, the cross-correlation for each interrogation area needs to be repeated over the two image frames captured by the camera. The flow structure can be clearly identified by recording both light pulses in the same image frame to trace the particles' motions. Seeding particles in air flows are generally oil droplets with a range of 1 μm to 5 μm.

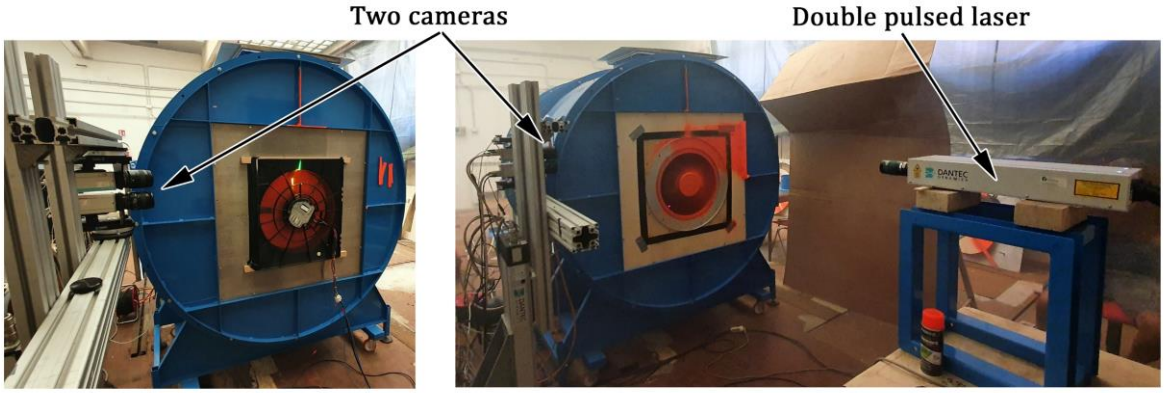

Figure 2.8. The PIV system.

As shown in Fig 2.8 the PIV system that has been used for instantaneous imaging in the University of Genoa laboratory includes: A double-cavity Nd:Yag pulsed laser (pulses of energy 400 mJ at a wavelength of 532 nm, with pulse duration of 8 ns and maximum repetition rate of 10 Hz), and the two laser beams are merged to make a 2mm thick light sheet; Two Dantec High Sense Mk II digital cameras with a 1344 × 1024 CCD matrix to record the light scattered by the seeding particles; Although the frame rate can be changed, the maximum value in double frame mode is 6 Hz; A fog generator that can generate particles in a range of diameter between 0.5 - 2 μm.

2.2.4. Laser Doppler Anemometry

For more than three decades, the Laser Doppler Anemometer, or LDA, has been a widely accepted tool for fluid dynamic research in gases and liquids and it is a well-known method for determining flow velocity. Because of its non-intrusive principle and directional sensitivity, it is well suited for applications including reversing flow and rotating machinery in situations where physical sensors are difficult or impossible to use. In addition to being non-intrusive, the method has several advantages, including high spatial and temporal resolution, no calibration required, and the ability to measure in reverse flow conditions [16].

The basic configuration of an LDA is depicted in Fig 2.9 and can be described as follows: A laser-generated continuous wave; Transmitting optics that include a beam splitter to split the continuous

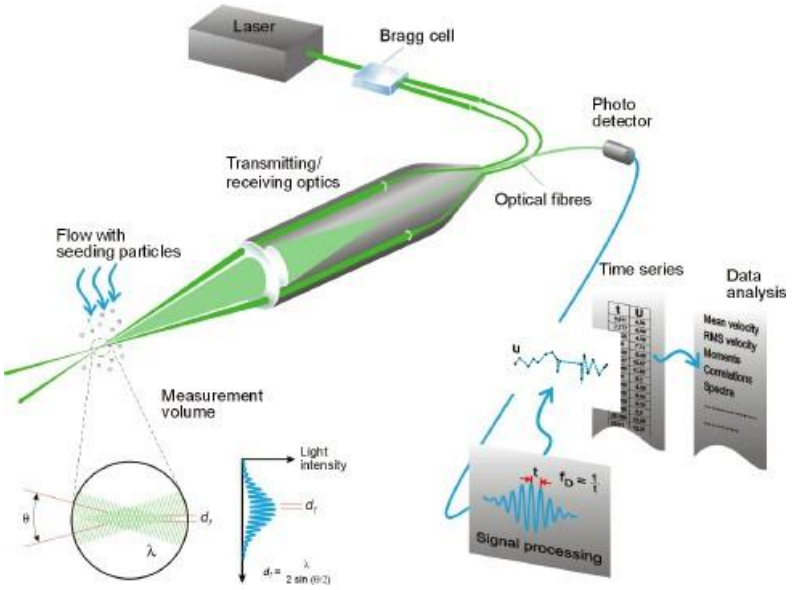

Figure 2.9. The basic configuration of an LDA system [16].

wave and a focusing lens; Receiving optics to collect and concentrate the return beam, containing a focusing lens, an interference filter, and a photodetector; Finally, to process the return beam a signal conditioner and a signal processor.

As a beam splitter, a Bragg cell is commonly used. It consists of a glass crystal with an attached piezo crystal that vibrates and produces acoustic waves that act as an optical grid. The Bragg cell produces two equal-intensity beams with frequencies f_0 and f_{shift}. These are focused into optical fibers, which are then sent to a probe. The parallel exit beams from the fibers are concentrated by a lens in the probe, causing them to intersect in the probe volume.

Typically, the probe volume has only a few millimeters long. Interference between the laser beams causes the light intensity to be modulated. Fringes are the result of this, which are parallel planes of high light intensity. The wavelength of the laser light, λ, as well as the angle between the beams, θ, determine the fringe distance d_f:

$$d_f = \frac{\lambda}{2\sin(\theta/2)} \tag{2.2}$$

The light scattered by each particle passage is proportional to the local light intensity. Light scattered by very small "seeding" particles conveyed in the fluid as they travel through the probe volume provides information on flow velocity. In the probe volume, the scattered light has a Doppler shift with a Doppler frequency f_D, which is perpendicular to the bisector of the two laser beams and

proportional to the velocity component. To gather the particles' information a receiver lens collects the scattered light and focuses it on a photodetector. An interference filter placed before the photodetector allows only the required wavelength to pass the photodetector. This eliminates noise from ambient light as well as other wavelengths. By using a photodetector, light intensity fluctuations can be converted into an electrical signal called the Doppler burst that due to the intensity profile of the laser beams has a sinusoidal waveform with a Gaussian envelope. In the signal processor, the Doppler bursts are filtered and amplified, which calculates f_D for each particle, usually using frequency analysis for instance a robust Fast Fourier Transform algorithm. Given that velocity equals distance divided by time, the velocity expression is as follows:

$$V = d_f \times f_D \tag{2.3}$$

Where the fringe spacing d_f represents the distance that the particle traveled and the Doppler frequency f_D delivers information about the time, $t = 1/f_D$.

Two more beams in a plane perpendicular to the first beams can be added to the optics to measure two velocity components. In this configuration, all the beams intersect in a common volume, and different wavelengths are used to separate the measured components.

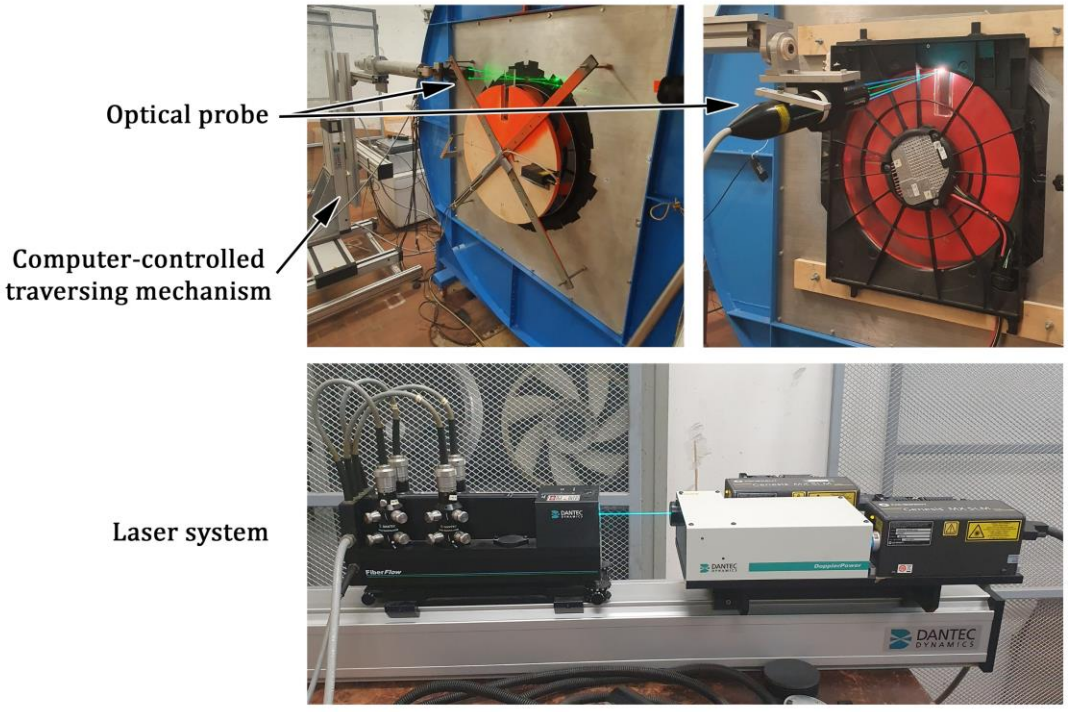

Figure 2.10. The LDA system.

In most cases, the flow must be seeded. The particles should ideally be small enough to follow the flow while still being large enough to scatter enough light to get a decent signal-to-noise ratio at the photodetector output.

Many challenges with the application of this technique, such as determination of the sign of the flow direction, and three-component measurements, are not addressed here.

The LDA system that has been used for doing tests in the laboratory of the University of Genoa is a two-color, four-beams laser LDA system (Dantec Fiber Flow) with a backward-scatter configuration, Fig 2.10. The light sources are two 200 mW diode-pumped solid-state lasers that emit two pairs of green and blue beams, allowing for simultaneous measurement of two velocity components. The probe volume has a 1.4 mm length with a 0.09 mm cylinder diameter. A fog generator seeded the flow with particles with a diameter of 0.5e2 mm. The control system of the optical probe is a three-axis computer-controlled traversing mechanism. The minimum linear translation step for this system is 1 mm. Also, a Burst Spectrum Analyzer (Dantec BSA P70 processor) module is used to process the photomultiplier signals.

3. DATA PROCESSING TECHNIQUES

3.1. Spectral analysis

This section provides some theoretical background on the traditional spectral analysis based on the Fourier transform and introduces the wavelet transform as a generalization or extension of the usual Fourier framework.

3.1.1. Fourier transform

This section provides the background on the Fourier transform. This information is available in most of the textbooks on signal properties, transform defining concepts and properties that will be employed in the subsequent sections. Some reasons for its fundamental importance and its limitations are discussed as well.

3.1.1.1. Definition

Given a function y(t), depending on the time t, its Fourier Transform (FT) is defined as:

$$\hat{y}(\omega) = \int_{-\infty}^{\infty} y(t)\, e^{-i\,\omega t}\, d\ t = \mathcal{F}_{\omega}[y] \tag{3.1}$$

where the symbol $\mathcal{F}_{\omega}[\bullet]$ can be reviewed as a linear operator (a functional) providing a complex number for any value of the parameter $\omega \in \mathbb{R}$. On the other hand, the integral of Eq. (3.1) represents the correlation of $y(t)$ with $e^{i\,\omega t}$, thus the FT may be interpreted as a measure of the similarity between the given function and the harmonic functions. Since the parameter ω multiplies the time in the argument of the harmonic function, it takes the meaning of circular frequency. However, it is just the case to note that, in general, t may be any ordering parameter and ω takes a consequent meaning (e.g. if t is a spatial coordinate, ω is the wave number).

Eq. (3.1) can be inverted retrieving $y(t)$ from its FT as

$$y(t) = \frac{1}{2\pi}\int_{-\infty}^{\infty} \hat{y}(\omega)\, e^{i\,\omega t}\, d\ t = \mathcal{F}_{t}^{-1}[\hat{y}] \tag{3.2}$$

The FT pair exists for any absolutely integrable function, i.e. $y \in L^1(\mathbb{R})$, but its domain can be extended to the set of the square-integrable functions $L^2(\mathbb{R})$ through a limit operation, with the advantage of enabling the use of the Hilbert space framework. In this way, the FT can be reviewed as an inner product or, geometrically, as an orthogonal projection

$$\mathcal{F}_\omega[y] = \langle y, e^{i\,\omega t} \rangle \tag{3.3}$$

where the symbol ⟨•,•⟩ represents the inner product defined as

$$\langle y, z \rangle = \int_{-\infty}^{\infty} y(t) z^*(t)\, d\ t \tag{3.4}$$

in which * represents the complex conjugate. The norm induced by the inner product (3.4) is

$$\|y\|^2 = \int_{-\infty}^{\infty} |y(t)|^2\, d\ t \tag{3.5}$$

3.1.1.2. Relevant properties

The substitution of Eq. (3.2) (to represent both y and z through their FTs) into Eq. (3.4) provides the relationship:

$$\begin{aligned}
&\langle y, z \rangle = \int_{-\infty}^{\infty} y(t) z^*(t)\, d\ t = \\
&= \int_{-\infty}^{\infty} \frac{1}{2\pi} \int_{-\infty}^{\infty} \hat{y}(\omega)\, e^{i\,\omega t}\, d\ \omega \frac{1}{2\pi} \int_{-\infty}^{\infty} \hat{z}^*(\omega')\, e^{-i\,\omega' t}\, d\ \omega'\, d\ t = \\
&= \frac{1}{4\pi^2} \int_{-\infty}^{\infty} \int_{-\infty}^{\infty} \hat{y}(\omega) \hat{z}^*(\omega') \int_{-\infty}^{\infty} e^{i(\omega - \omega')t}\, d\ t\, d\ \omega\, d\ \omega' = \\
&= \frac{1}{2\pi} \int_{-\infty}^{\infty} \hat{y}(\omega) \hat{z}^*(\omega)\, d\ \omega = \frac{1}{2\pi} \langle \hat{y}, \hat{z} \rangle
\end{aligned} \tag{3.6}$$

where it has been used the orthogonality of the harmonic functions, i.e., $\langle e^{i\,\omega_1 t}, e^{i\,\omega_2 t} \rangle = 2\pi\delta(\omega_1 - \omega_2)$, δ being the Dirac function. Eq. (3.6) is referred to as the Parseval theorem and states the invariance of the inner product with respect to the FT (but the factor 2π). Eq. (3.6) can be obviously particularized for y = z resulting

$$\|y\|^2 = \int_{-\infty}^{\infty} |y(t)|^2\, d\ t = \frac{1}{2\pi} \int_{-\infty}^{\infty} |\hat{y}(\omega)|^2\, d\ \omega = \frac{1}{2\pi} \|\hat{y}\|^2 \tag{3.7}$$

This property can be interpreted as a conservation of energy across the passage between the time domain and frequency domain.

Table 3.1 shows some fundamental properties of the FT.

	$f(t)$		$\hat{f}(\omega)$
Translation	$f(t+t_0)$	→	$\widehat{e^{i\omega t_0}f}(\omega)$
Modulation	$e^{i\omega_0 t}f(t)$	→	$\hat{f}(\omega-\omega_0)$
Dilation	$f\left(\frac{t}{s}\right)$	→	$\lvert s\rvert\hat{f}(s\omega)$
Derivation	$f^{(p)}(t)$	→	$(i\omega)^p\hat{f}(\omega)$

Table 3.1. Some fundamental properties of the FT.

3.1.1.3. Fourier transform and Linear Time Invariant systems

If $x(t)$ and $y(t)$ are, respectively, the input and the output of a linear time-invariant (LTI) system $\mathcal{L}$, i.e., $y = \mathcal{L}[x]$, then their relationship is explicitly given by the convolution integral:

$$y(t) = \int_{-\infty}^{\infty} h(t-\tau)x(\tau)\,d\ t \tag{3.8}$$

where h is the Impulse-Response Function (IRF) of $\mathcal{L}$. Using Eq. (3.8) it is easy to show that if x is a harmonic function, then y is a harmonic with the same frequency, i.e.:

$$x(t) = e^{i\omega t} \quad \rightarrow \quad \mathrm{y(t)} = \hat{h}(\omega)e^{i\omega t} \tag{3.9}$$

where $\hat{h}$ is the Frequency-Response Function (FRF) of $\mathcal{L}$. Eq. (3.9) states that the harmonic functions are the eigenfunctions of LTI systems and the FRF represents the set of their eigenvalues (which is called spectrum). The use of this property in conjunction with Eq. (3.1) provides the frequency-domain counterpart of Eq. (3.8)

$$\hat{y}(\omega) = \hat{h}(\omega)\hat{x}(\omega) \tag{3.10}$$

It is worth noting that the FT $\hat{y}(\omega)$ is defined by an integral involving the whole support of $y(t)$ and, for this reason, it is referred to as a global representation. This property makes the FT relatively simple to use but may result in serious limitations. To explain this concept, let us consider the signal $f(t) = sin\,\omega\,t$, with $\omega = 3\ rad/s$ for $t < 0$ and $\omega = 9\ rad/s$ for $t \geq 0$ (Fig. 3.1a). Its FT (Fig. 3.1b) contains two peaks located at the frequencies corresponding to the two portions of the signal. However, two serious drawbacks appear.

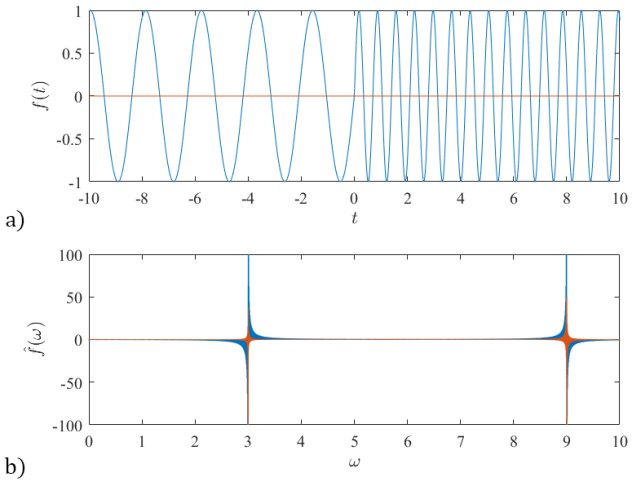

Figure 3.1. a) A sinusoidal signal containing two distinct frequencies, b) FT of the signal.

First, by observing the FT it is not possible to tell if $f(t)$ is the sum of two narrow-band components (e.g., modulated harmonics) or a single harmonic that changes its frequency at some time (like it actually is).

Second, besides the two peaks at 3 and 9 rad/s, the FT is non-zero in relatively large neighborhoods of these frequency values. These contributions are necessary to cancel the harmonic at 3 rad/s for $t > 0$ and the harmonic at 9 rad/s for $t < 0$, making the representation highly inefficient.

3.1.2. Demodulation and instantaneous frequency

The poor efficiency of the Fourier transform in the representation of the signal shown in Figure 3.1 is determined by the time variation of the frequency. The definition of an instantaneous frequency, possibly changing with time, is somehow problematic since the frequency is defined as a property of the harmonic functions (number of cycles in the unit time) and therefore is necessarily a constant. On the other hand, it is obvious that signals with variable frequency do exist, therefore the instantaneous frequency needs a proper definition.

The instantaneous frequency of a signal may be defined in a different way, but the definition related to analytic signals is probably the most adopted in the data processing community.

A function $f_a(t)$ is said analytic if its FT $\hat{f}_a(\omega)$ is zero for any negative frequency. According to this definition, an analytic signal is necessarily complex-valued, but it is entirely defined on the basis of its real part. Indeed, the real part $f(t)$ of $f_a(t)$ is given by the obvious relationship

$$f(t) = real\big(f_a(t)\big) = \frac{1}{2}\big(f_a(t) + f_a^*(t)\big) \tag{3.11}$$

which can be translated in terms of FT as

$$\hat{f}(\omega) = \frac{1}{2}\Big(\hat{f}_a(\omega) + \hat{f}_a^*(-\omega)\Big) \tag{3.12}$$

Taking into account that fa is an analytic signal (its FT is zero for negative frequency), Eq. (3.12) can be rewritten as

$$\begin{aligned} \hat{f}_a(\omega) &= \begin{cases} 2\hat{f}(\omega) \text{if } \omega \geq 0 \\ 0 \text{if } \omega < 0 \end{cases} \\ &= \hat{f}(\omega) + sign(\omega)\,\hat{f}(\omega) \\ &= \hat{f}(\omega) + i[-isign(\omega)]\,\hat{f}(\omega) \end{aligned} \tag{3.13}$$

The last of Eq. (3.13) demonstrates that the FT of fa can be calculated from the FT of f. This relationship can be converted in the time domain as

$$f_a(t) = f(t) + i\,\mathcal{H}[f(t)] \tag{3.14}$$

where the operator $\mathcal{H}[\bullet]$ is called Hilbert transform and is defined through the convolution integral

$$\mathcal{H}[f] = \frac{1}{\pi}\int_{-\infty}^{\infty} \frac{f(\tau)}{t-\tau} d\ \tau \tag{3.15}$$

By comparing Eq. (3.14) and Eq. (3.15), it can be deduced that the FRF of the Hilbert transform is -i for any positive frequency and i for negative frequency. This implies that the Hilbert transform is an ideal filter that shifts the phase of the input signal by 90 deg.

On the bases of this interpretation, given any real signal f, an analytic signal can be computed by adding an imaginary component equal to the shifted version of f computed through the Hilbert transform.

Analytic signals have a fundamental importance in demodulation, i.e., the estimation of the instantaneous amplitude and phase of signals of the type:

$$f(t) = A(t)\cos\phi\,(t) \tag{3.16}$$

for which the instantaneous frequency is defined as the time derivative of the phase

$$\omega(t) = \frac{d\,\phi\,(t)}{d\;t} \tag{3.17}$$

Assuming that amplitude and frequency change slowly with time, the Hilbert transform of f results

$$\mathcal{H}[A(t)\,cos\,\phi\,(t)] \simeq A(t)\,sin\,\phi\,(t) \tag{3.18}$$

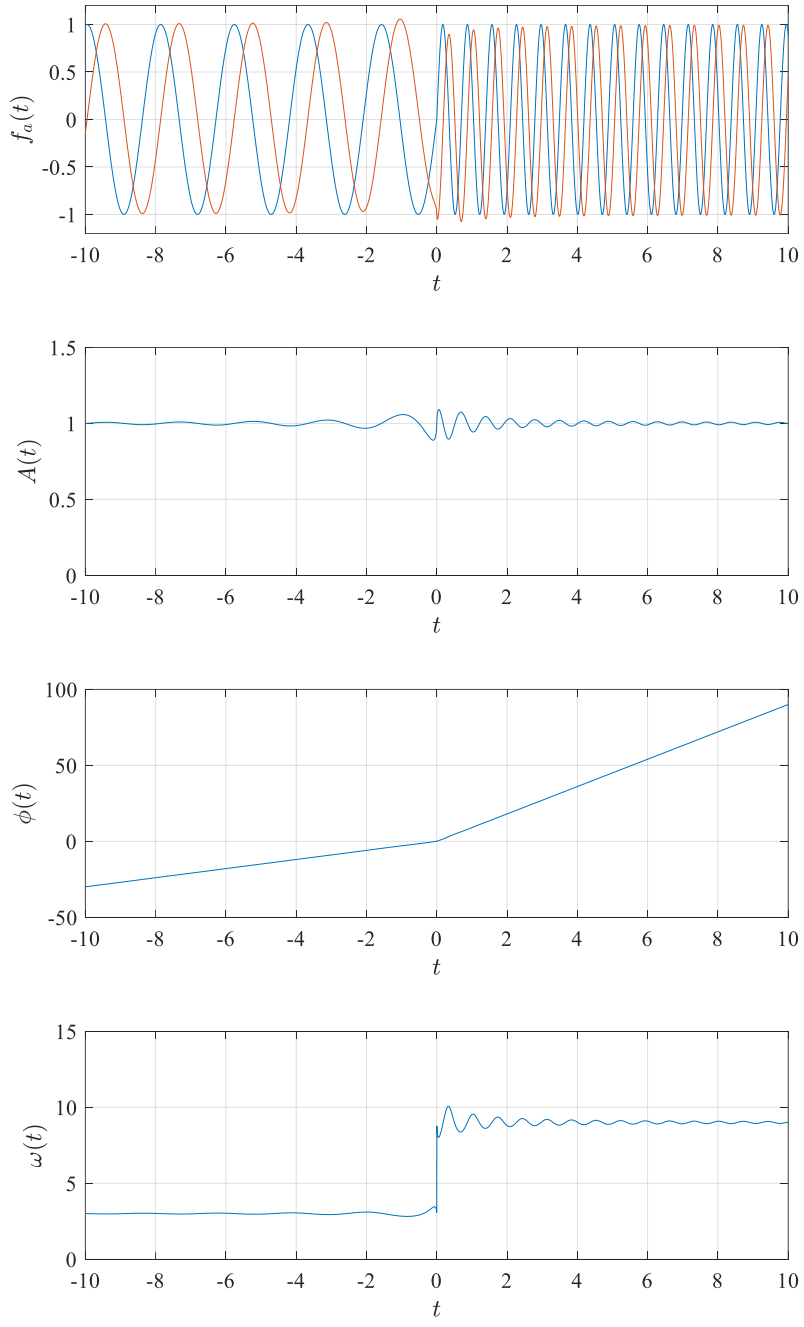

Figure 3.2. Analytic signal and demodulation of the signal reported in Figure 3.1 as well as the instantaneous amplitude, phase, and frequency.

Accordingly, Eq. (3.14) reads

$$f_a(t) = A(t)\cos\phi(t) + i\,A(t)\sin\phi(t) = A(t)e^{i\,\phi(t)} \tag{3.19}$$

From Eq. (3.19) it is clear that the instantaneous amplitude and phase of $f(t)$ can be estimated as

$$A(t) = |f_a(t)| \qquad \phi(t) = \angle f_a(t) \tag{3.20}$$

Figure 3.2 shows the analytic signal obtained from the signal reported in Figure 3.1, as well as the instantaneous amplitude, phase, and frequency. It can be observed that the amplitude and frequency are estimated correctly with the exception of some distortion occurring about $t = 0$.

Eq. (3.20) and Eq. (3.17) strictly hold only for amplitude-phase modulated signals and cannot be used directly to process a generic signal possibly including multiple harmonic components. Indeed, the demodulation procedure described above is regularly applied after a preprocessing aimed at separating the spectral component of interest. The simplest approach is band-pass filtering.

3.1.3. Time-frequency localization

The major drawback of the FT is its inability of detecting (and represent efficiently) time variations of the signal properties. This limitation is intimately related to the use of the harmonics as basis functions, which extends from -∞ to +∞ keeping the same characteristics. On the contrary, to identify the local properties of a signal, it is necessary to correlate it with functions that are well localized in time. This can be done by generalizing the FT by a transformation that retains the form of Eq. (3.1), i.e.

$$\mathcal{T}_\gamma^{\phi}[f] = \int_{-\infty}^{\infty} f(t)\phi_\gamma^*(t)\,d\ t = \langle f, \phi_\gamma \rangle \tag{3.21}$$

where $\phi_\gamma \in L^2(\mathbb{C})$ are a set of basis functions depending on one or more parameters collectively identified with the symbol γ. The operator $\mathcal{T}_\gamma^{\phi}$ is called time-frequency transformation, while the basis functions ϕ_γ are called time-frequency atoms. The FT is clearly a particular case of time-frequency transformation for which $\phi_\gamma(t) = e^{i\gamma t}$ and $\gamma = \omega$.

To proceed further with this idea, it is necessary to specify more clearly what time localization means and how to measure it. Accordingly, we can identify the central time of ϕ_γ and measure its time spread by the relationships

$$u = \int_{-\infty}^{\infty} t\left|\phi_\gamma(t)\right|^2 d\ t$$
$$\sigma_t^2 = \int_{-\infty}^{\infty} (t-u)^2\left|\phi_\gamma(t)\right|^2 d\ t \tag{3.22}$$

which have a clear analogy with the definition of mean value and variance in probability theory, with the difference that the function ϕ_γ is squared as it is normalized in L^2 instead of in L^1 likewise for the probability density function. Relying on this definition, we may desire to have a set of functions ϕ_γ having a time-spread small compared to the time scale of the signal variations and that can be located in time to explore the evolution of the signal.

On the other hand, the time-frequency transformation defined by Eq. (3.21) can be expressed in the frequency domain using the Parseval theorem Eq. (3.6), yielding

$$\mathcal{T}_\gamma^{\phi}[f] = \frac{1}{2\pi}\int_{-\infty}^{\infty} \hat{f}(\omega)\hat{\phi}_\gamma^*(\omega)\, d\ \omega = \frac{1}{2\pi}\langle \hat{f}, \hat{\phi}_\gamma \rangle \tag{3.23}$$

from which it is clear that $\mathcal{T}_\gamma^{\phi}$, besides measuring the correlation of f with ϕ_γ, also measure the correlation of $\hat{f}$ with $\hat{\phi}_\gamma$. On this bases, we can conclude that if we wish to distinguish the contribution of different harmonics possibly present in the signal, we need to select a function ϕ_γ whose FT is well localized in frequency. In analogy to Eq. (3.22), the central frequency and the frequency spread of ϕ_γ is defined as

$$\xi = \int_{-\infty}^{\infty} \omega\left|\hat{\phi}_\gamma(\omega)\right|^2 d\ \omega$$
$$\sigma_\omega^2 = \int_{-\infty}^{\infty} (\omega-\xi)^2\left|\hat{\phi}_\gamma(\omega)\right|^2 d\ \omega \tag{3.24}$$

It is easy to deduce that for the particular case of the FT $\sigma_t = \infty$ and $\sigma_\omega = 0$. This result confirms that the basis functions of the FT are perfectly localized in frequency but are fully spread in time. As a consequence, using the FT it is theoretically possible to separate harmonic components that are infinitely close to each other but it is impossible to distinguish events happening at different times.

In principle, it would be desirable to define a set of time-frequency atoms that are well localized both in time and frequency. Unfortunately, this result is not achievable due to the third of the properties of the FT reported in Table 3.1, which states if a function is dilated in time, then its FT contracts in frequency (and vice versa). The impossibility of reducing arbitrarily the time and the frequency spread at the same time is formally expressed by the Heisenberg uncertainty principle, which sets the condition:

$$\sigma_t \sigma_\omega \leq \frac{1}{2} \tag{3.25}$$

3.1.4. Continuous wavelet transform

Given a function $f(t) \in L^2$, its wavelet transform is obtained by correlating f with the time-frequency atoms $\psi_{u,s}$ called wavelets, parametrized by their central time u and their scale s.

$$\begin{aligned} W_{u,s}[f] &= \langle f, \psi_{u,s} \rangle = \int_{-\infty}^{\infty} f(t) \psi_{u,s}^*(t) dt \\ &= \frac{1}{2\pi} \langle \hat{f}, \hat{\psi}_{u,s} \rangle = \frac{1}{2\pi} \int_{-\infty}^{\infty} \hat{f}(\omega) \hat{\psi}_{u,s}^*(\omega) d\omega \end{aligned} \tag{3.26}$$

The wavelet atoms are derived from a prototype function called the mother wavelet through a translation and dilation process. For any u and s in $\mathbb{R}$, they are defined as

$$\psi_{u,s}(t) = \frac{1}{\sqrt{s}} \psi\left(\frac{t-u}{s}\right) \tag{3.27}$$

where the factor $s^{-0.5}$ has the function of keeping the L^2 norm of the wavelet constant after dilation. The translation and dilation of the mother wavelet induce a contraction and modulation of its FT (properties 1 and 3 of Table 3.1):

$$\hat{\psi}_{u,s}(\omega) = \sqrt{s} \hat{\psi}(s\omega)\, exp(-i\omega u) \tag{3.28}$$

Without any loss of generality, we assume that the mother wavelet has a unit norm, thus

$$\begin{aligned} \|\psi_{u,s}\|^2 &= \int_{-\infty}^{\infty} |\psi_{u,s}(t)|^2 dt = 1 \\ \|\hat{\psi}_{u,s}\|^2 &= \int_{-\infty}^{\infty} |\hat{\psi}_{u,s}(\omega)|^2 dt = 2\pi \end{aligned} \tag{3.29}$$

To analyze the time evolution of the frequency components of the signal it is necessary to use an analytic wavelet to separate amplitude and phase information. The Fourier transform of an analytic wavelet vanishes for $\omega < 0$. Besides, it can be proved that the wavelet transform can be inverted, i.e., f can be reconstructed from $W_{u,s}[f]$ if the so-called compatibility condition is fulfilled:

$$C_\psi = \int_0^{+\infty} \frac{\left|\hat{\psi}(\omega)\right|^2}{\omega} d\omega < +\infty \tag{3.30}$$

In this work, we select a wavelet constructed by the frequency modulation of a Gaussian function. Wavelets of this kind are referred to as Gabor or Morlet wavelets. Such a wavelet and its Fourier transform have the form:

$$\psi(t) = \sqrt[4]{\frac{2\sigma_\omega^2}{\pi}} exp(i\,\omega_c\,t)\, exp(-\sigma_\omega^2 t^2) \tag{3.31}$$

$$\hat{\psi}(\omega) = \sqrt[4]{\frac{2\pi}{\sigma_\omega^2}} exp\left(-\frac{(\omega-\omega_c)^2}{4\sigma_\omega^2}\right) \tag{3.32}$$

where ω_c and σ_ω are two parameters having the meaning of central (circular) frequency and frequency spread, respectively.

When the mother wavelet is translated and dilated through Eq. (3.27) and Eq. (3.28), the wavelet $\psi_{u,s}$ and its Fourier transform $\hat{\psi}_{u,s}$ remain centered, respectively, on the time u and the central frequency $\eta = \omega_c/s$, indeed:

$$\int_{-\infty}^{\infty} t\left|\psi_{u,s}(t)\right|^2 dt = u \tag{3.33}$$

$$\xi = \frac{1}{2\pi}\int_{-\infty}^{\infty} \omega\left|\hat{\psi}_{u,s}(\omega)\right|^2 d\omega = \frac{\omega_c}{s} \tag{3.34}$$

On the other hand, the spread of the wavelet about its time location u and of its Fourier transform around the central frequency ξ can be evaluated (using an L^2 measure) as

$$\sigma_{t,s}^2 = \int_{-\infty}^{\infty} (t-u)^2\left|\psi_{u,s}(t)\right|^2 dt = \frac{s^2}{4\sigma_\omega^2} \tag{3.35}$$

$$\sigma_{\omega,s}^2 = \frac{1}{2\pi}\int_{-\infty}^{\infty} (\omega-\xi)^2\left|\hat{\psi}_{u,s}(\omega)\right|^2 d\omega = \frac{\sigma_\omega^2}{s^2} \tag{3.36}$$

and depend on the scale s. In particular, the ratio between the scale s and the wavelet parameter ω_c determines both the time spread $\sigma_{t,s}$ of $\psi_{u,s}$ and the frequency spread $\sigma_{\omega,s}$ of $\hat{\psi}_{u,s}$, but, if the time spread increases, then the frequency spread decreases of the same fraction keeping the product $\sigma_{t,s}\sigma_{\omega,s}$ constant. It can be demonstrated that the product $\sigma_{t,s}\sigma_{\omega,s}$ cannot be lower than $1/2$, independently of the wavelet type chosen, according to the time-frequency Heisenberg uncertainty theorem. The practical consequence of this principle is that the wavelet transform $W_{u,s}[f]$ represents the (complex) amplitude of $f(t)$ in a neighborhood of the time $t = u$ and frequency $\xi = \omega_c/s$, having a characteristic size $\sigma_{t,s}$ and $\sigma_{\omega,s}$. The finite size of this neighborhood implies that the wavelet transform operates a local averaging in the time-frequency plane.

In practice, when we analyze a signal, we are interested in locating a wavelet atom at a specific time u and at a given central frequency ξ. To obtain this result, we can choose arbitrarily the central frequency ωc of the mother wavelet and then determine the scale $s = \omega_c/\xi$ through Eq. (3.34). In this case, the time and frequency spread are

$$\sigma_{t,s} = \frac{1}{2}\frac{\omega_c}{\sigma_\omega}\frac{1}{\xi}; \qquad \sigma_{\omega,s} = \frac{\sigma_\omega}{\omega_c}\xi \tag{3.37}$$

showing that the time and frequency localization characteristics of the wavelet depend on the ratio σ_ω/ω_c, which can be regarded as the frequency spread non-dimensionalized by the central frequency.

3.1.5. Spectral representation of stationary random processes

When a signal is an interpreter as a random process, its representation involves statistical quantities. If these statistics are invariant for shifts of the temporal reference, a random process is called stationary. It should be mentioned that the realizations of a stationary random process are functions that, in principle, never vanish and therefore cannot be in L^2. For this reason, the realizations of a stationary random process do not possess a Fourier transform.

Let $x(t)$ be a realization of a random process (that for simplicity is assumed as zero-mean) and $x_T(t)$ a function obtained by windowing $x(t)$ in $t \in (-T/2, T/2)$.

$$x_T(t) = \begin{cases} x(t) & \text{for } t \in \left(-\frac{T}{2}, \frac{T}{2}\right) \\ 0 & \text{otherwise} \end{cases} \tag{3.38}$$

Assuming that $x_T \in L^1(-T/2, T/2)$, its Fourier transform is:

$$\hat{x}_T(\omega) = \int_{-\infty}^{\infty} x_T(t)\, e^{-i\,\omega t} dt = \int_{-T/2}^{T/2} x(t)\, e^{-i\,\omega t} dt \tag{3.39}$$

and exists for any finite value of T, while $x_T(t)$ can be reconstructed by the formula:

$$x_T(t) = \frac{1}{2\pi} \int_{-\infty}^{\infty} \mathrm{e}^{i\,\omega t} \hat{x}_T(\omega) d\omega \tag{3.40}$$

The energy of the function $x_T(t)$ is defined as

$$Enrg[x_T(t)] = \int_{-\infty}^{\infty} x_T^2(t)\, dt = \int_{-T/2}^{T/2} x^2(t)\, dt \tag{3.41}$$

Since $x_T(t)$ is a realization of a random process, the energy can be interpreted as a random variable. The limit for $T \to \infty$ of the energy diverges when $x(t)$ is a realization of a stationary process. The power of the function $x_T(t)$ is defined as:

$$Pwr[x_T(t)] = \frac{1}{T} \int_{-\infty}^{\infty} x_T^2(t)\, dt = \frac{1}{T} \int_{-T/2}^{T/2} x^2(t)\, dt \tag{3.42}$$

It can be observed that the limit of power for $T \to \infty$ coincides with the temporal mean square of $x(t)$:

$$\overline{x^2} = \lim_{T\to\infty} Pwr[x_T(t)] = \lim_{T\to\infty} \frac{1}{T} \int_{-\infty}^{\infty} x_T^2(t)\, dt \tag{3.43}$$

The variance of the process $x(t)$ corresponds to the expected value of the temporal mean square ($x(t)$ is assumed as zero mean), thus it yields

$$\sigma_x^2 = E\left[\overline{x^2}\right] = E\left[\lim_{T\to\infty} \frac{1}{T} \int_{-\infty}^{\infty} x_T^2(t)\, dt\right] \tag{3.44}$$

where, the integral of the process $x_T(t)$ can be interpreted as a random variable whose realizations are obtained by integrating the realizations of $x_T(t)$. The integral in Eq. (3.43) can be rewritten using the Parseval theorem:

$$\int_{-\infty}^{\infty} x_T^2(t)\, dt = \frac{1}{2\pi} \int_{-\infty}^{\infty} |\hat{x}_T(\omega)|^2\, d\omega \tag{3.45}$$

Eq. (3.45) is valid for any realization of $x_T(t)$, thus can be applied to rewrite Eq. (3.44) in the form:

$$\sigma_x^2 = \int_{-\infty}^{\infty} S_{xx}(\omega) d\omega \tag{3.46}$$

where

$$S_{xx}(\omega) = \frac{1}{2\pi} \lim_{T\to\infty} \frac{1}{T} E[|\hat{x}_T(\omega)|^2] \tag{3.47}$$

in which $\hat{x}_T(\omega)$ is interpreted as the random process (as a function of frequency) whose realizations are the Fourier transform of the realizations of x_T; the function $S_{xx}(\omega)$ is called Power Spectral Density (PSD). From Eq. (3.47) it is possible to deduce that the PSD is real-valued and non-negative. Eq. (3.47) can be used for estimation purpose.

3.2. Phase locked ensemble average

In the study of turbomachinery, the ensemble average technique is commonly used to reconstruct the flow in a rotor employing a stationary probe; information about the time structure of the signal in the rotating frame is lost. Samples related to different time instants are acquired at a fixed tangential position in the absolute frame. As for the present PIV measurements, this technique can be used to rebuild a periodic signal starting from a highly under-sampled one. Considering the relative frame of reference anchored to the rotor, the corresponding tangential position varies linearly with time due to rotation; this implies a relationship between the periodic part of the flow in the absolute frame and its tangential distribution in the rotating one. As a matter of fact, a velocity sample acquired at a certain time may also be assigned to a certain angular position of the rotor. The employ of optical measurement techniques, such as the LDV or PIV, drives further difficulty, as samples are not acquired evenly spaced in time (LDV) or the sampling rate is nearly one order of magnitude lower than the rotational speed (PIV), i.e. the samples are not evenly spaced in the tangential direction in the relative frame. Hence, a suitable ensemble averaging technique has been applied: A tachometer signal which shows the angular position of the rotor at each rotation can be considered here as a reference phase signal, and the instantaneous velocity samples are sorted into I phase bins each representing a particular phase of the rotor revolution, i.e. a window in the rotating frame whose width equals $360/I\ deg$. This approach is depicted in Fig. 3.3 where a generic signal with a periodic part is considered; the tachometer reference signal is reported in the bottom part. The samples acquired at the same phase Φ, are assigned to the same bin i representing a finite discretization of the cycle τ.

Moreover, the triple decomposition scheme proposed by Hussain and Reynolds [17] has been employed:

$$v(t) = v'(t) + (\tilde{v}(t) - \bar{v}) + \bar{v} \tag{3.48}$$

Or in a more compact formulation:

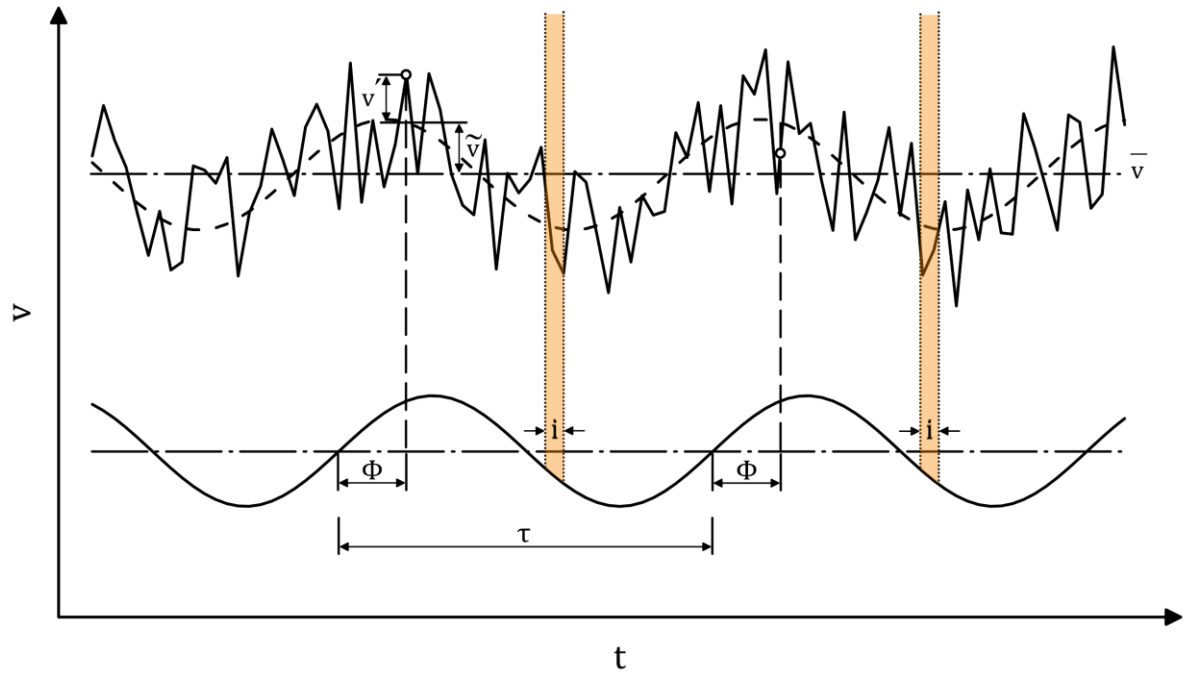

Figure 3.3. Ensemble phase averages of a random signal, top, using a reference signal, bottom.

$$v(t) = v'(t) + \tilde{v}(t) \tag{3.49}$$

Such a decomposition is suitable for the study of unsteady flows constituted by a periodic component $\tilde{v}(t)$ and by a zero-average fluctuating component $v'(t)$ (turbulent and/or coherent) not correlated with the rotor position. $\tilde{v}(t)$ may be further decomposed in a time-mean component $\bar{v}$ and in a zero-average, periodic one $(\tilde{v}(t) - \bar{v})$.

The acquisition provides a time sequence of instantaneous samples $v_h = v(t_h), \;\; h = 1,2, \dots, H$ which is rearranged based on the tacho signal: each sample is assigned to a window (bin i) within a rotor revolution (cycle τ). Let the indexes k and i be assigned to a revolution and to a window respectively; as the acquisition of LDV signals or PIV frames happens at random instants, the $i-th$ window contains $k = 1,2, \dots, K_i$ samples v_{ik}. $\tilde{v}_i$ is obtained by ensemble averaging the samples related to that window:

$$\tilde{v}_i = \frac{1}{K_i} \sum_{k=1}^{K_i} v_{ik}\,, \;\; i = 1,2, \dots, I \tag{3.50}$$

The time-averaged velocity component $\bar{v}$ is given by:

$$\bar{v} \equiv \overline{\tilde{v}} = \frac{1}{I}\sum_{i=1}^{I} \tilde{v}_i \tag{3.51}$$

and the instantaneous non-periodic component is given by $v'_{ik} = v_{ik} - \tilde{v}_i$. v'_{ik} is commonly referred to as "turbulent" component, but this definition is questionable since it presupposes that v'_{ik} is related to turbulence, while unsteady parts not correlated with the rotor position but spatially coherent are often present, too. A proper definition is unresolved (by the measurement technique) unsteadiness.

The number of bins I must be chosen in the way that the number of samples per bin should be statistically significant and this aspect may be decided in the data post-processing phase by evaluating the statistical uncertainty.

Then, a phase-averaged standard deviation (i.e. variance estimate) of v' may be computed:

$$\widetilde{v_i'^2} = \frac{1}{K_i}\sum_{k=1}^{K_i} {v'_{ik}}^2, \quad i = 1,2,\dots,I \tag{3.52}$$

as well as a time-averaged one:

$$\overline{\widetilde{v'^2}} = \frac{1}{I}\sum_{i=1}^{I} \widetilde{v_i'^2}, \quad i = 1,2,\dots,I \tag{3.53}$$

Summing the time-averaged variance estimates of the three components of the velocity vector allows computing time-averaged kinetic energy associated with the unresolved unsteadiness:

$$\bar{\tilde{k}} = \frac{1}{2}\left(\overline{\widetilde{v_x'^2}} + \overline{\widetilde{v_y'^2}} + \overline{\widetilde{v_z'^2}}\right) \tag{3.54}$$

which contains the turbulent kinetic energy and also the kinetic energy related to large coherent structures not periodic or at a period different from the considered one. $\bar{\tilde{k}}$ may be typically made non-dimensional, here by the peripheral speed of the blade (u_{tip}), in the way to extract the so-called turbulence intensity representative of the importance of the unresolved unsteadiness:

$$\overline{\widetilde{Tu}} = \frac{\sqrt{\bar{\tilde{k}}}}{u_{tip}} \tag{3.55}$$

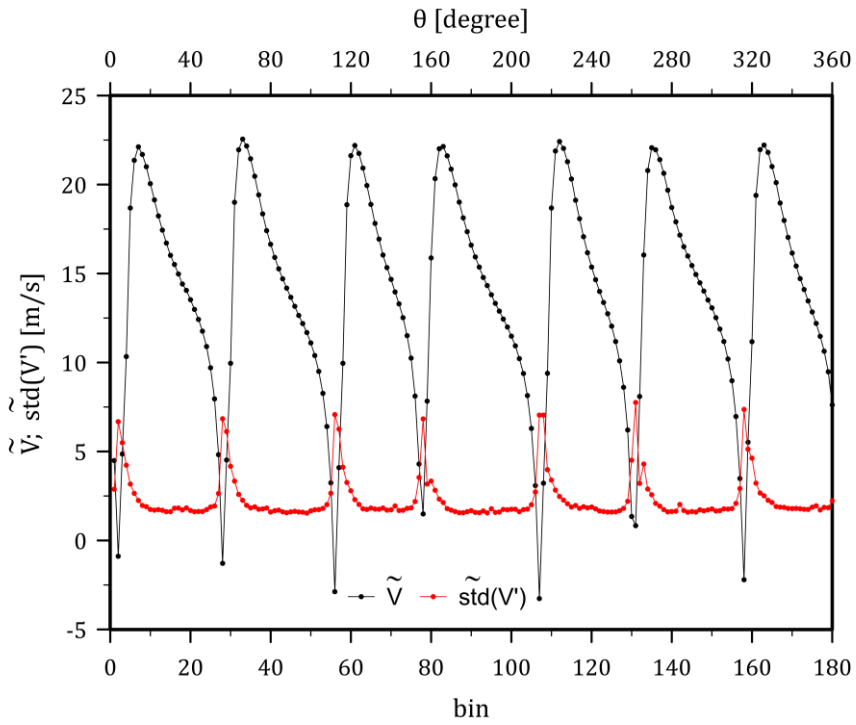

Figure 3.4. Example of ensemble averaged meridional velocity downstream of the fan.

For instance, the ensemble average of the meridional velocity measured downstream of the adopted fan is reported in Fig. 3.4, where both $\tilde{v}$ and $\widetilde{v'^2}$ (indicated as $\widetilde{std}(v')$) are depicted as a function of the phase bins as well as θ (angular position). In this case, 180 bins (2 degrees for each bin) are employed, such a scale could be replaced by the non-dimensional revolution period ranging from 0 to 1. The blade wakes can be clearly identified by the dips present in the velocity trend as well as by the maxima present in the unresolved unsteadiness standard deviation.

3.3. Double phase locked ensemble average

As previously mentioned, the present work deals with the study of a fluttering fan where the flutter motion may be considered similar to a precession of the fan-motor assembly. Such a flutter motion is characterized by a specific frequency and hence it may be considered a periodic motion of the fan axis. Thus, taking into account, for instance, a velocity measurement carried out in front of the fan, close to the blade tip region, it is reasonable to state that the velocity signal should be characterized by two simultaneous periodic components, one related to the blade passing period (or the fan rotational period being the fan blades unevenly spaced) and the other related to the flutter phenomenon.

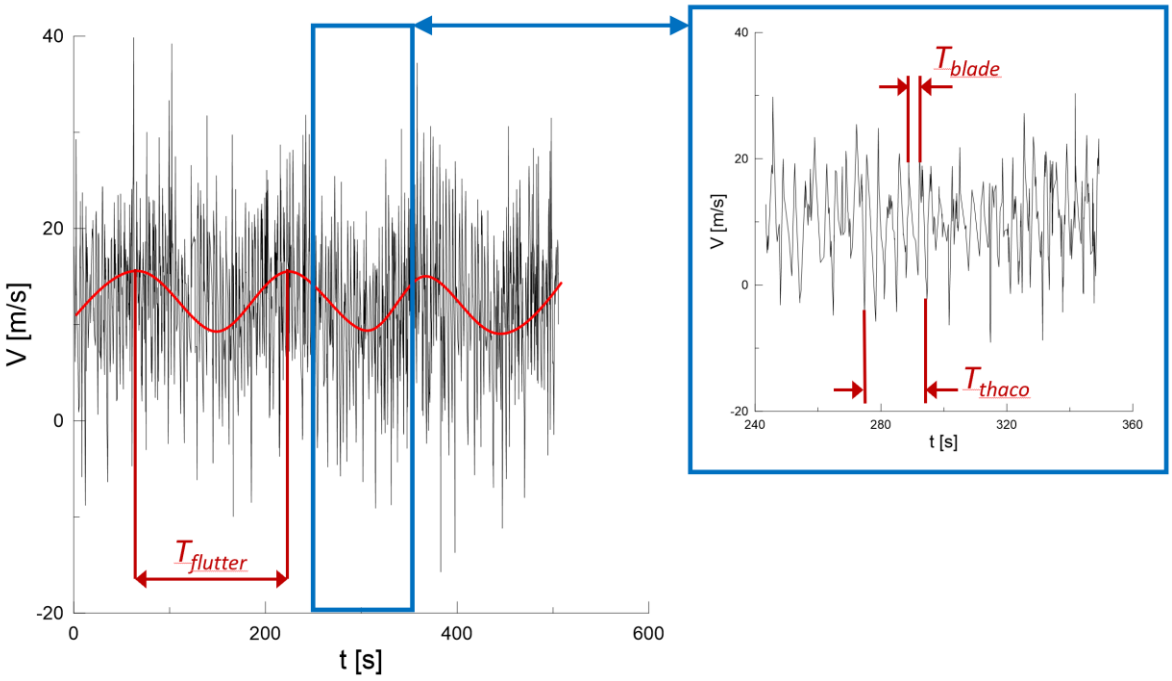

Figure 3.5. Example of measured velocity in the proximity of the blade tip.

In Fig. 3.5 the meridional velocity measured in a generic point located close to the blade tip region is reported as a function of the sampling time. The red line (hand-sketched) in the left time trace represents a hypothetical periodic contribution due to the flutter oscillation, while in the right part of the figure, the enlarged time scale allows identifying the revolution period and the blade passing one.

Hence, a single velocity sample may be assigned simultaneously to two bins: one related to the flutter period, and the other to the revolution one (indicated as Tacho-period). In other words, the sample is considered assigned to a very specific angular position of the rotor and of the flutter oscillation. Considering I and J the number of bins used to discretize the tacho-period and the flutter one (indicated as Vibro-period) respectively, then the periodic velocity may be defined as:

$$\tilde{v}_{ij} = \frac{1}{K_{ij}} \sum_{k=1}^{K_{ij}} v_{ijk}\,, \quad i = 1,2,\dots,I,\ j = 1,2,\dots,\mathrm{J} \tag{3.56}$$

where K_{ij} represents the overall number of samples corresponding to the ij bin.

As a result, $\tilde{v}_{ij}$ depends on the variables and may not be represented as a standard x-y curve, but as a contour plot where the two axes refer to the Tacho-bin and Vibro-bin respectively, while the velocity

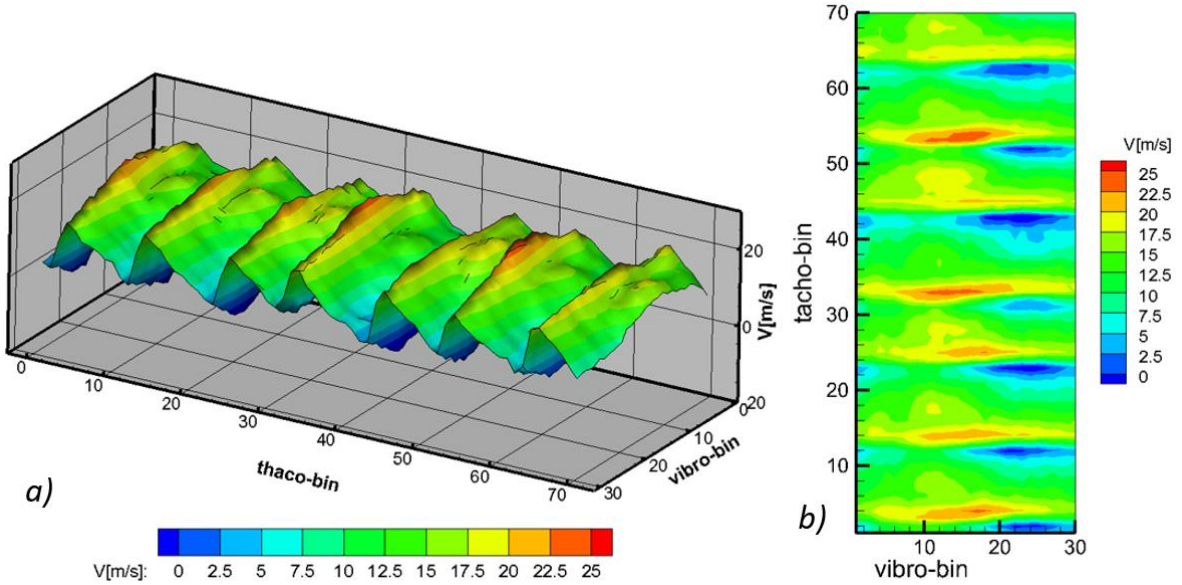

Figure 3.6. Example of representation of the double phase ensembled averaged meridional velocity.

magnitude is indicated by the color scale. Similarly, a 3D surface may also be employed having the same x and y axes, but the velocity magnitude is reported on the z one.

This technique, which to the best of the author's knowledge, is original and has never been developed before it; may be referred to as double phase ensemble average.

In Fig. 3.6 an example of this post-processing method is applied to the meridional velocity that has been measured previously. In this case, 70 Tacho-bins and 30 Vibro-bins (2100 bins in total) have been adopted. In the contour plot in Fig. 3.6b, a vertical cut at a fixed Vibro-bin describes the flow behavior in the measuring point as if the flutter oscillation could be frozen while the fan could keep on rotating. Conversely, a horizontal one at a fixed Tacho-bin describes the flow as if the fan could be stopped in a fixed angular position while the flutter oscillation is evolving. Even if the description of the flow field is not deputed to this chapter, it could be interesting to highlight some aspects: in Fig. 3.6 the flutter oscillation seems to have a modulating effect on typical velocity trend (see for instance Fig. 3.4) and this effect is particularly clear taking in account the oscillations which are present in the maxima and minima values. As a matter of fact, since the flutter precession motion is inducing an axial oscillation of the fan, particularly of the shroud and of the tip of the blade, the trailing edge of the blade is moving axially in front of the measuring point, which is at a fixed position in the absolute frame of reference. Such a geometry modification must be taken into account when discussing the effects of the combined effect of flutter and fan rotation.

According to Eq. 3.51, the time-averaged velocity component $\bar{v}$ may be computed as:

$$\bar{v} \equiv \overline{\tilde{v}} = \frac{1}{I}\frac{1}{J}\sum_{i=1}^{I}\sum_{j=1}^{J}\tilde{v}_{ij} \tag{3.57}$$

Then, a phase-averaged standard deviation of v' may be computed:

$$\widetilde{v'^2_{ij}} = \frac{1}{K_{ij}}\sum_{k=1}^{K_{ij}} {v'_{ijk}}^2, \quad i = 1,2,\dots,I, \; j = 1,2,\dots,\mathrm{J} \tag{3.58}$$

as well as a time-averaged one:

$$\overline{\widetilde{v'^2}} = \frac{1}{I}\frac{1}{J}\sum_{i=1}^{I}\sum_{j=1}^{J}\widetilde{v'^2_{ij}}, \quad i = 1,2,\dots,I, \; j = 1,2,\dots,\mathrm{J} \tag{3.59}$$

Another interesting feature of the double phase ensemble average technique may be obtained by analyzing Fig. 3.7 where the contour plot of the meridional velocity of Fig. 3.6 has been modified by changing the axes which now represents the non-dimensional time of each period. Assume that the rotational speed of the fan is 40 Hz, while the flutter frequency is 8 Hz. With this hypothesis,

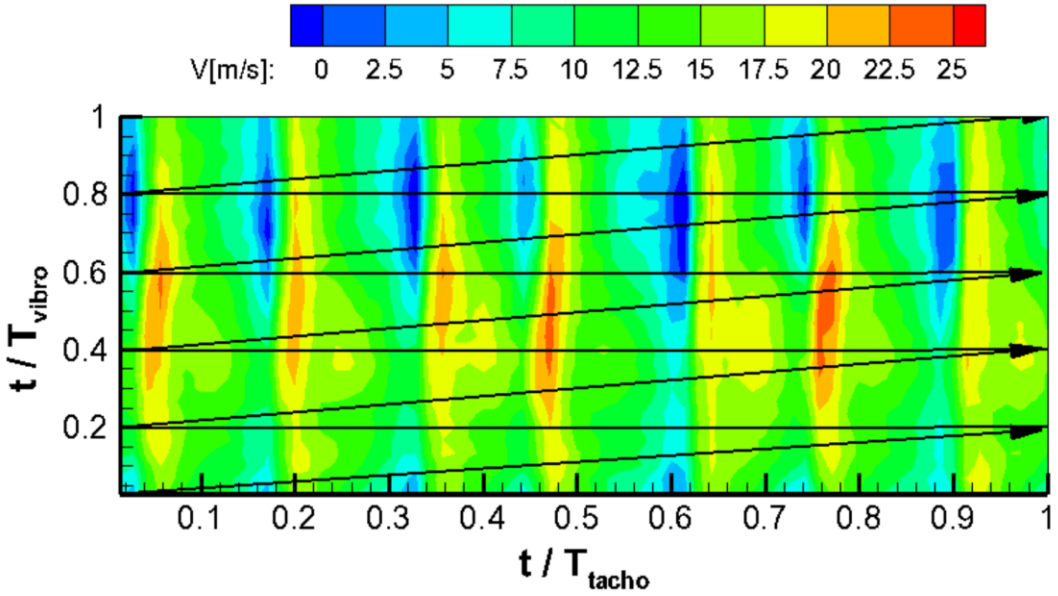

Figure 3.7. Contour plot of the double phase ensemble averaged meridional velocity with superposed the hypothetical time line (case $T_{vibro} = 5T_{tacho}$).

$T_{vibro}/T_{tacho} \in \mathbb{N}$, which is unrealistic but simplifies the explanation of this method, 5 full fan revolutions are required to complete an oscillation period of the flutter precession. Hence, choosing a starting point in the ij domain, i.e. choosing an initial value for t/T_{tacho} and t/T_{vibro}, then if the time is let to pass the next point should stay along an inclined line whose slope is $8/40$. If the (0,0) initial point is chosen as in Fig. 3.7, as time passes the ensemble-averaged velocity values, which should be seen by the probe, lay on the black inclined line and after a full fan revolution, the 20% of the Vibro-period has passed. In the second revolution of the fan, the starting point is going to be (0,0.2), leading to the saw-tooth trend which is visible in Fig. 3.7. It is important to underline that any ij point in the domain could be considered as the starting one, thus fixing the initial mutual position between the rotor, in terms of angular position, and the flutter precession one.

Considering a realistic case when $T_{vibro}/T_{tacho} \notin \mathbb{N}$; in this case, the fan rotational frequency is nearly 43 Hz, while the flutter one is 7.5, hence 5.67 fan revolutions are required to cover the precession period. If the meridional velocity is interpolated along the saw-tooth line representing the time evolution in Fig. 3.7, then it is possible to obtain the velocity distribution along an entire flutter period. The result is depicted in Fig. 3.8, where the ensemble-averaged meridional velocity time trace lasts for an entire flutter period.

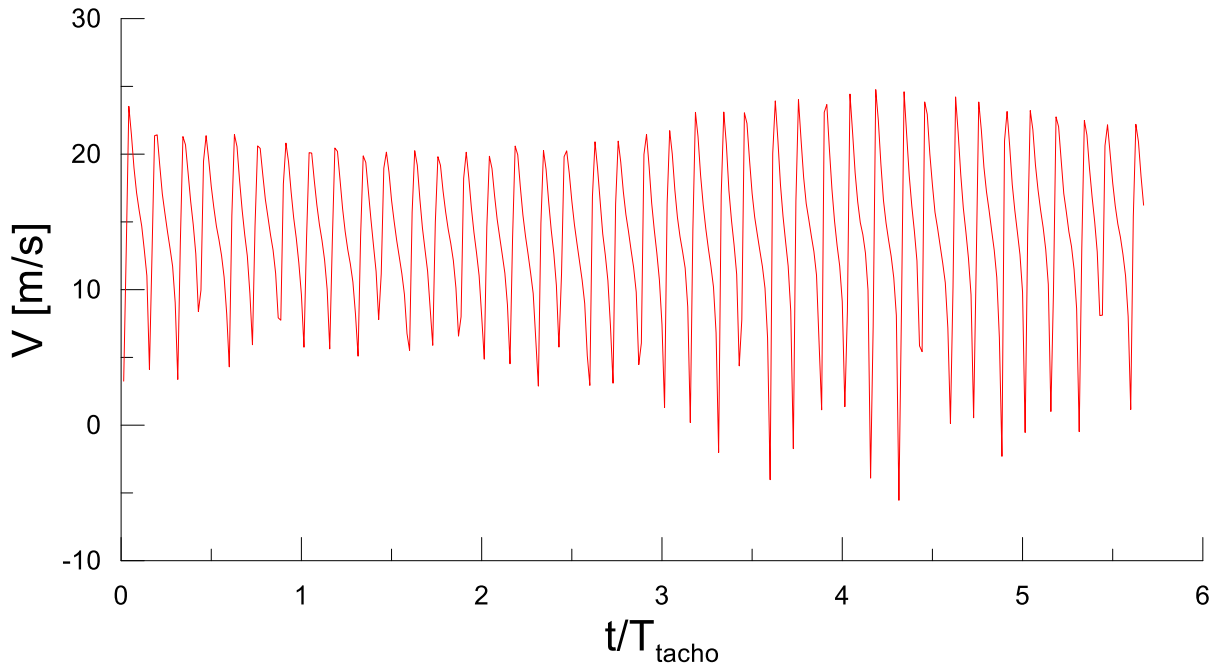

Figure 3.8. Time trace of the double phase ensemble averaged meridional velocity for an entire flutter period.

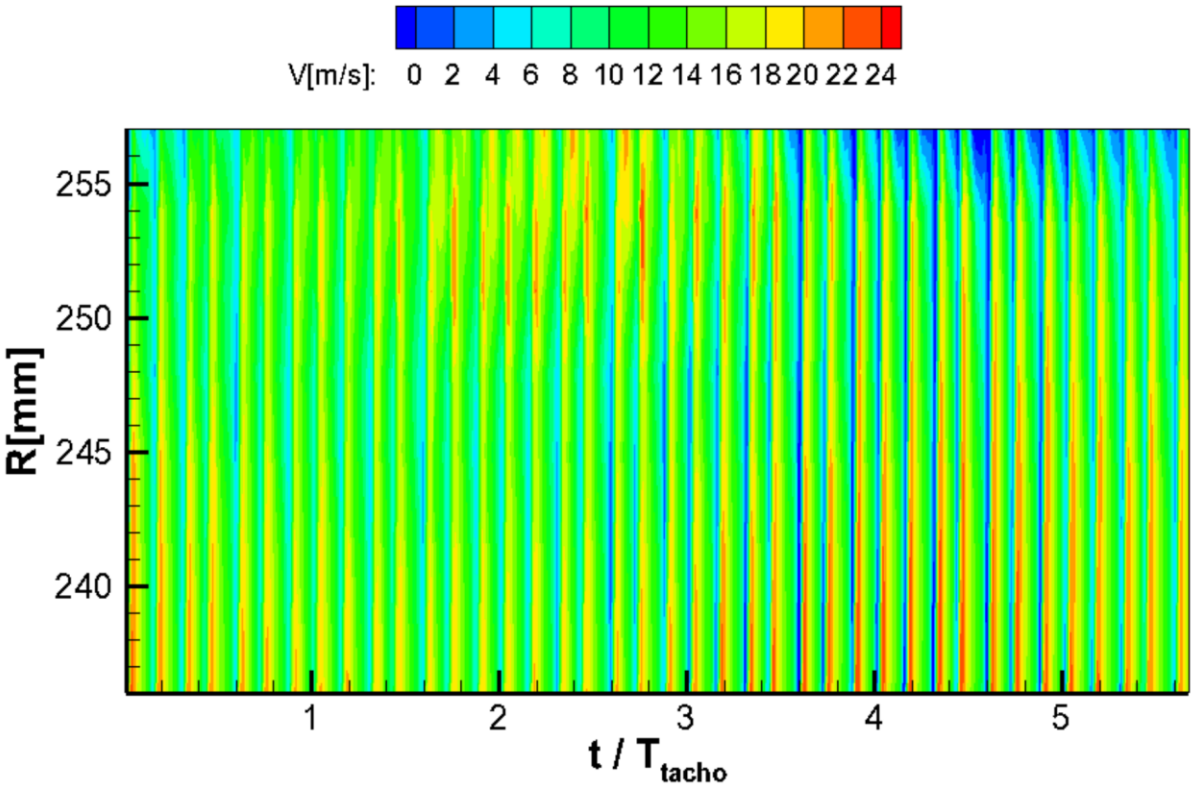

Figure 3.9. Contour plot of the time trace of the double phase ensemble averaged meridional velocity for a radial traverse.

Finally, if this procedure is repeated for all the points constituting a radial traverse, it is possible to generate a contour plot representing the time evolution of double phase ensemble averaged meridional velocity for all the points, see Fig. 3.9. In this way, the simultaneous effects of the wakes and the flutter can be monitored.

4. MECHANICAL INVESTIGATIONS

In this chapter, the dynamic and aeroelastic behavior of the fan is studied to characterize the high amplitude and low-frequency vibration. First, the general features of the fan including fan geometry and specifications, gap geometry, and characteristic curve of the fan are reported; then, the planarity of the ring is investigated since it may affect the vibrometers; after that, the dynamic behavior of the fan is analyzed using experimental and numerical (FEM) modal testing and the Campbell diagram obtained by FEM is discussed in detail. In the following, various vibrometric measurements are presented for the recognition and characterization of the aeroelastic flutter; the dependency of the flutter on the operating conditions is studied and the experimental Campbell diagram is obtained and compared to the FEM one; then, the origin of this aeroelastic flutter is discussed. Finally, different theoretical models for the dynamic and aeroelastic behavior of the fan are developed and presented.

4.1. General characteristics of the fan

In this section, the geometrical properties and the general characteristic of the fan will be presented. Figure 4.1 shows the studied cooling system, which includes a rotor and casing. The casing has an internal diameter of 520 mm, which is supported by the rods and rings to keep the electric motor fixed in the center and it will be mounted to the car body together with the radiator (Heat exchanger). In addition, an obstruction disk of 520-mm-diameter has been placed 80 mm downstream of the rotor to simulate the obstruction caused by the thermal engine. The rotor and casing are made of

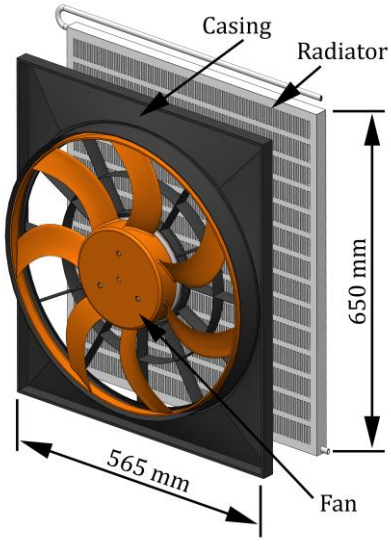

Figure 4.1. The cooling system.

The number of blades:	Seven unequally spaced
Blade tip diameter:	514 mm
Hub diameter:	192 mm
Blade chord:	60 ÷ 65 mm
Material:	PA6GF30 plastic
Design rotational speed:	2650 rev/min
Design flow rate:	1.3 m^3/s
Design flow coefficient:	0.088
Design pressure rise:	325 Pa
Design pressure rise coefficient:	0.108

Table 4.1. Fan specifications

PA6GF30 plastic; the rotor consists of seven unequally spaced blades that are connected by a 3-mm-thick rotating ring (the rotating shroud). The deformation of the blades due to centrifugal force and aerodynamic load is usually limited by including such a ring connecting the blade tips [1]. This ring strengthens the rotor and also increases the volumetric efficiency of the fan, but results in peculiar phenomena: First, the flow recirculating in the gap between the rotating ring and the casing is reingested by the fan. This phenomenon yields blade thrust fluctuations, whose typically studied consequence is a strong, sub-harmonic noise; different explanations may be found for this flow, e.g. see [2-8]. Second, the ring has a high moment of inertia and is connected to the hub through blades that are relatively flexible and low-damped. From the mechanical point of view, this constitutes a rotating system prone to potentially large-amplitude vibration at low frequency. This represents a major modification since the stiffening is not sufficient to compensate for the moment of inertia of the ring, which is quite larger than the one of the usual unshrouded blades and introduces an important gyroscopic effect.

Some of the features of the fan are listed as follows as well as Table 4.1: The blade chord c ranges between 60 - 65 mm, the rotor tip radius is $r_{tip} = 257$ mm, and the hub-to-tip diameter ratio is $r_{hub}/r_{tip} = 0.374$. Based on operating rotational speed, $f_r = 44$ Hz, the blade tip speed $u_{tip} = 71.2\,\mathrm{m/s}$ and the related Reynolds and Mach numbers are $Re_c = u_{tip}c_{tip}/\nu = 3.08 \times 10^5$ and $Ma_{tip} = u_{tip}/a_0 = 0.21$ respectively. At the design point (DP), the volumetric flow rate is $Q =$

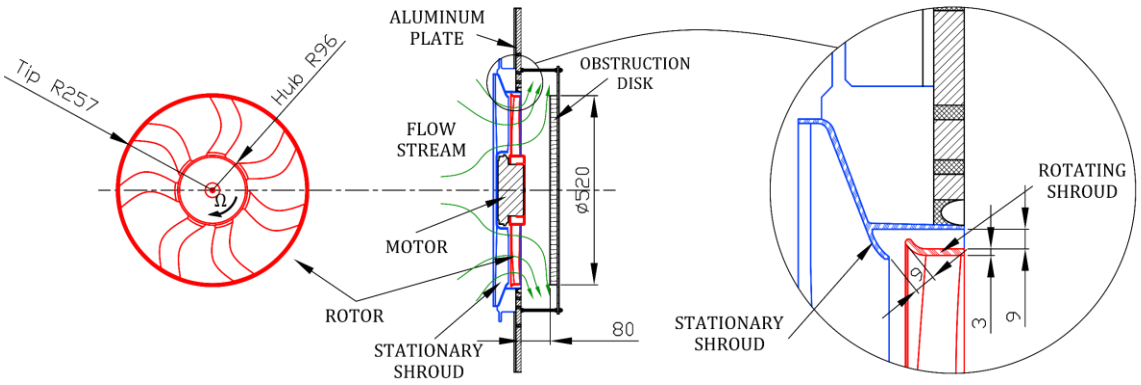

Figure 4.2. The tested fan with details of the gap geometry.

1.30 m3/s, the flow coefficient is $\varphi_{DP} = \frac{Q}{u_{tip}\,\pi\,{r_{tip}}^2} = 0.088$, the fan pressure rise is $\Delta p = 325$ Pa (outlet static pressure minus inlet total one), and the pressure rise coefficient is $\psi_{DP} = \frac{\Delta p}{0.5\,\rho_0\,{u_{tip}}^2} = 0.108$.

The assembly of the studied fan mounted on the test rig and the details of the gap geometry between the stationary shroud and rotating ring have been presented in Fig 4.2; it can be seen that there is a big gap between these two rings, 9 mm.

The characteristic curve of the fan is also shown in Fig 4.3.

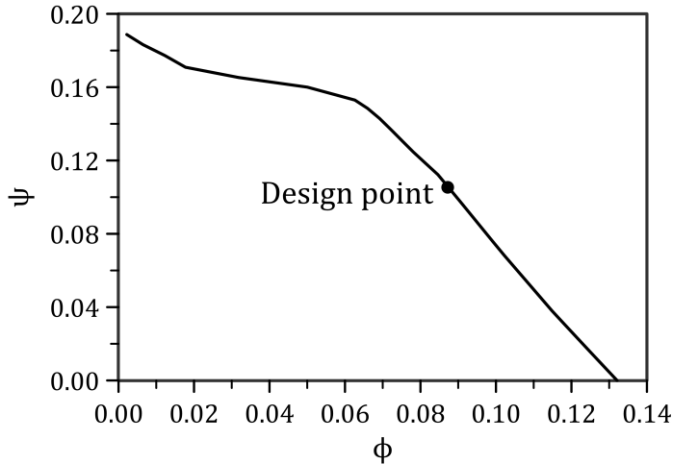

Figure 4.3. Characteristic curves of the fan.

4.2. Planarity of the ring

Low-speed fans are large-scale, low-cost products made of plastic material. The molding process and large tolerances lead to a final unperfect shape for the rotors. In the following chapters, measurements will be made on the hub and rotor's external ring to measure the hub and ring displacements and vibrations. To do so first it must be determined how are the shape of the ring and hub and how much planar those are.

To measure the planarity of the ring a combination of a laser vibrometer, pointing to the ring and measuring the axial displacement, and an optical tachometer as a reference signal, which measures the time interval between each fan revolution, are used. In order to measure the planarity of the ring without the effect of vibration, data collection has been done at the lowest rotational speed of the fan (rigid motion). Using the ensemble average technique, the axial displacement data of the vibrometer signal has been averaged in phase, based on the fan revolution cycle. By doing so the average axial location of the fan's ring is calculated for each angular position. The same procedure is applied for the hub and all the results are reported in Fig.4.4. In this figure the measurement locations on the rotor geometry are shown as black and magenta circles for the ring and the hub, respectively. The related plot shows the axial displacement at the hub is small and varies between $\pm 0.2\ mm$ while this axial nonplanarity is larger in the ring which varies between $\pm 1\ mm$.

Also, the blades passing effect are recognizable as 7 peaks in this plot, which are marked with the number of each blade at the top. The presence of the effect of the blades is perhaps due to the manufacturing process as well.

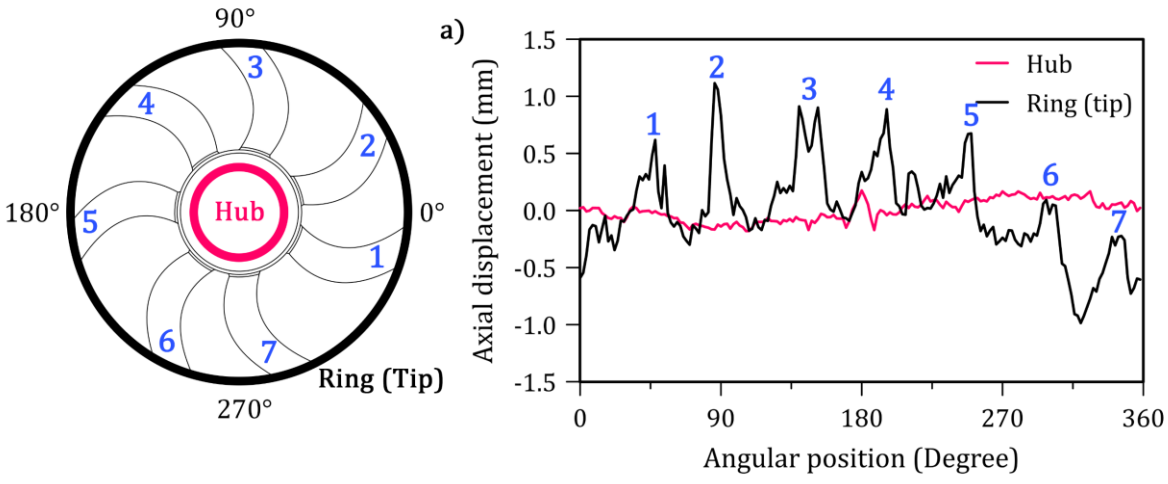

Figure 4.4. Planarity of the ring.

4.3. Dynamic behavior (Modal characteristics)

As mentioned earlier in the introduction chapter, a high amplitude oscillation appears at the design point of the fan and the neighboring operating points. In the following of this chapter, using experimental measurements the characteristics of these vibrations will be discussed in detail. However before that, in this section, it is useful to perform a comprehensive realistic FEM modal analysis of the whole assembly. Such an analysis helps understand the dynamic behavior of the fan under different circumstances, e.g., when the fan is idle or at different rotational speeds. The general way of this modal analysis performs during a speed ramp from where the fan is idle to the design rotational speed. In this way, numerical Campbell plots of the fan will be obtained.

The whole assembly of the fan is complicated and includes a rotor, casing, electric motor, bearings, shaft, etc; many parameters such as the standard material properties of the parts are necessary to perform the realistic FEM analysis of the whole assembly.

Before performing this analysis, the dynamic properties of the rotor and casing have been separately investigated using experimental and numerical modal analysis. Then the numerical model will be updated according to the experimental data.

Also, considering the mode shapes and their corresponding frequencies, the dynamic behavior of each component (here rotor and casing just be examined) can be investigated to maybe help find a connection between the natural frequency of the components and the high amplitude vibration of the fan at the design point.

In the next step of this section, by using the updated numerical model of the rotor and casing, applying the characteristics of the bearings, and finally replacing the electric motor geometry with a point mass, the dynamic behavior of the fan at different rotational speeds up to the design rotational speed will be studied. Also, later in this chapter, the Campbell diagram will be calculated experimentally and will be compared with the one obtained by numerical analysis in this section. It is not possible to obtain the mode shapes for the rotating fan (e.g. at the design point) using the experimental investigations and this indicates the importance and necessity of numerical modal analysis of the system and Campbell diagram.

Modal testing is a common method for assessing the vibrations of a structure by applying a known force and measuring the structure's response. It is possible to determine the structure's frequency response by measuring both the input and the response. The dynamic response of the structure can be estimated by calculating the frequency response at various points, either simultaneously or one at a time. The method of excitation will depend on the size and geometry of the test structure. Impact testing with a modal hammer and response accelerometer is one of the most commonly used techniques.

The impulse force that the impact hammer sends into the system is expected to excite a broad bandwidth. After data collection, the data are processed to identify the FRFs across the structure (modal frequencies and shapes). In most cases, mounting the accelerometer in a single spot and changing the impact location is simpler; this is known as a 'roving impact' modal test.

The experimental modal testing has been done in this way when the rotor is idle: Rotor and casing elastically suspended to simulate the free-free condition, see Fig. 4.5. A roving impact test has been used for both parts by using just one accelerometer on the hub location due to not adding extra weight to the system by increasing the number of accelerometers. Then using an impact hammer the impulse force has been sent to the system at different points circumferentially close to the blade tips for the rotor and various points circumferentially on the casing as well. After analyzing the FRFs of the systems, the modal frequencies and mode shapes have been calculated for both parts. At the same time, two FEM modal analyses based on preliminary information about the parts' material have been conducted. The experimental and FEM modal frequencies of both parts have been reported in Table

Figure 4.5. Casing elastically suspended to simulate the free-free condition for modal testing.

	Mode 1	Mode 2	Mode 3
Rotor Experimental	52.4	102.3	102.5
Rotor FEM	42.7	83.4	83.5
Casing Experimental	27	65.1	84
Casing FEM	22	53	68.3

Table 4.2. Experimental and FEM modal frequencies of Rotor and Casing in Hz.

4.2. By updating the material properties of both parts, the FEM modal frequencies become very close to the experimental values. The experimental and FEM modal frequencies and mode shapes for the first 3 modes of the rotor and casing are shown in Figures 4.6 and 4.7, respectively.

By looking at the mode shapes of the rotor, it can be seen that mode 1 is the first fundamental mode of a vibrating circular membrane, the (0,1)[1] mode, since there are no nodal diameters, but one circular node (the outer edge). The next two modes are the (1,1) pair modes with one nodal diameter and one circular node (the outer edge) that are almost in the same frequency and shifted 90 degrees compare to each other. The exact location of the nodal diameter depends on the homogeneity of the membrane and the initial conditions when the vibration starts. The frequency of these two modes must be 1.593 times the frequency of mode one in the membrane [18], but here in this geometry, the difference is nearly twice.

[1] In the following descriptions of the mode shapes of a circular membrane, the nomenclature for labelling the modes is (number of nodal diameters, number of nodal circles).

The casing geometry is a combination of several rings in a rectangular frame that in general can be considered as a rectangular membrane for modal analysis. Mode 1 is the $(2,2)^2$ mode that vibrates at 27 Hz with two antinodes and two nodal lines which is certainly not the first common fundamental

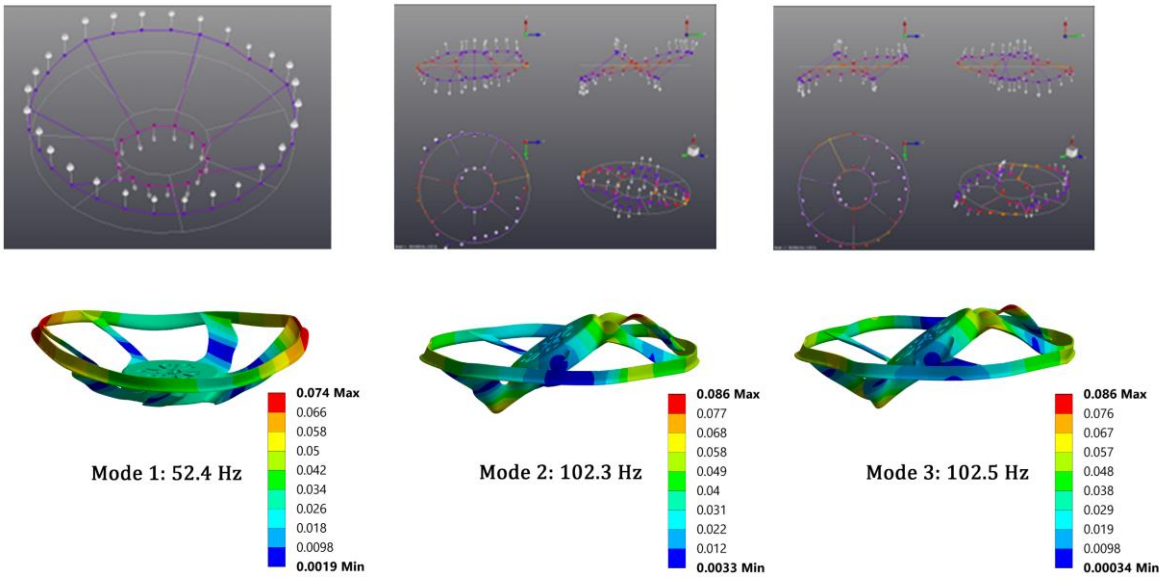

Figure 4.6. Mode shapes of the fan. Top: Experimental, Bottom: FEM (colorbar: deformation).

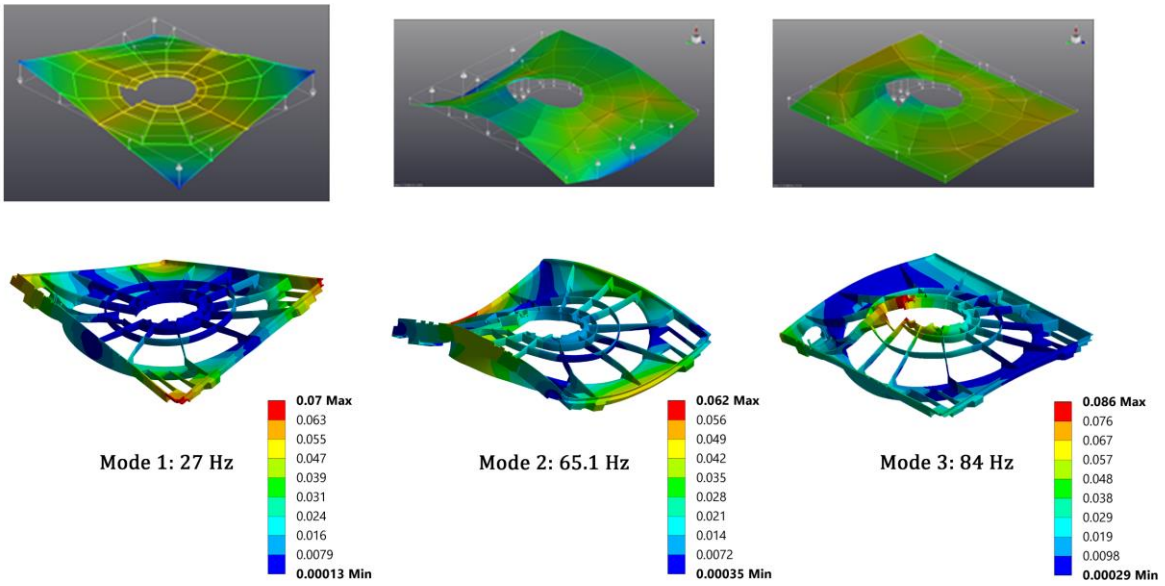

Figure 4.7. Mode shapes of the casing. Top: Experimental, Bottom: FEM (colorbar: deformation).

[2] In the following descriptions of the mode shapes of a rectangular membrane, the nomenclature for labelling the modes is (number of humps or antinodes, number of nodal lines).

mode of a rectangular membrane, the (1,1) mode, which appears in mode 3 with a higher frequency. Mode 2 looks like a saddle shape, and it is obtained by subtracting the two modes, $(1,3) - (3,1)$.

Using the updated FEM model, modal analysis can be performed for the entire fan assembly. In order to simplify the FEM model, the entire geometry of the electric motor has been replaced by a point mass. This point mass includes the main specifications of electric motor geometry such as mass, the center of mass, principal axes of inertia, and principal moments of inertia. In the Campbell diagram of Figure 4.8 obtained from the entire fan assembly FEM model, the variations in the modal frequencies with respect to the increase in rotational frequency up to mode 12 are calculated and illustrated. In this diagram, the red lines represent the harmonics of rotation frequency, f_r.

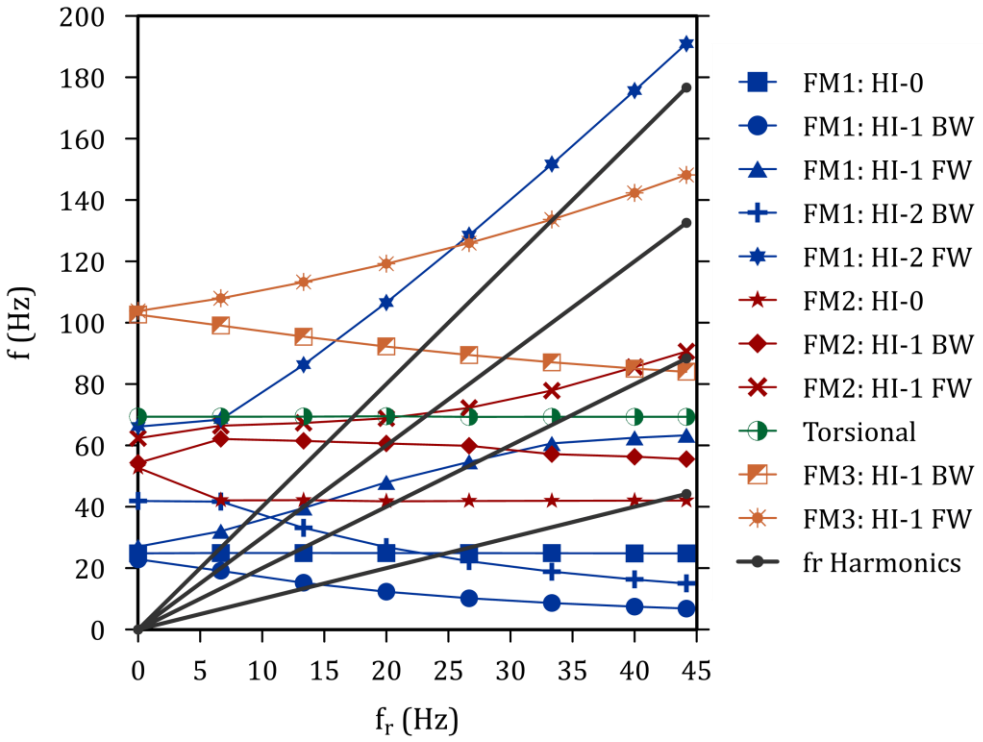

Figure 4.8. Campbell diagram obtained from the entire fan assembly FEM model.

Veering between pairs of coupled modes can be recognizable in the Campbell diagram. The phenomenon associated with the eigenvalue loci for a system with a changeable parameter is sometimes referred to as "mode veering": two branches come together, but instead of crossing, they veer away and separate. The veering is followed by mode coupling and fast eigenvector variations [19].

These 12 modes are divided into three family modes as follows:

- Family mode 1: hub and blade tips of the rotor are in the same phase (Those are displacing, deforming, and tilting in the same direction), also those are at the same phase of the casing, see Fig. 4.9.
- Family mode 2: hub and blade tips of the rotor are out of phase, while the hub of the rotor and casing are at the same phase, see Fig. 4.10.
- Family mode 3: hub and blade tips of the rotor are out of phase, also the hub of the rotor and casing are out of phase, also the blade tips and casing are at the same phase, see Fig. 4.11.

On the sides of the Campbell diagrams for these three family modes, the mode shapes corresponding to each modal frequency are depicted.

It should be noticed that the rotation and displacement of these modes overlap with the rotation caused by the rotor when the fan is operating.

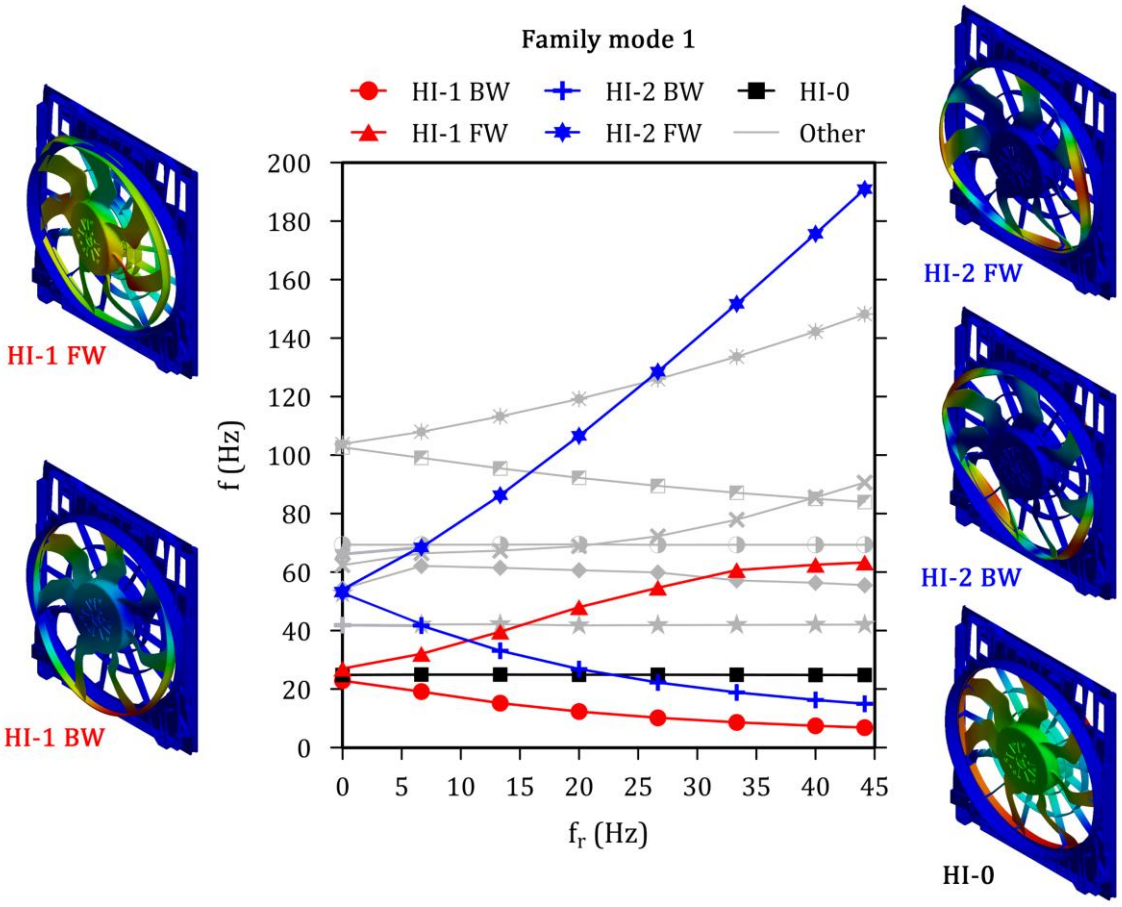

Figure 4.9. Family mode 1 Campbell diagram obtained from the FEM model (Includes modal frequencies and corresponding mode shapes).

In Figure 4.9 for family mode 1, three sets of modes are recognizable. At around 25 Hz when the fan is idle, there are two similar and coupled modes, the first set, with the same modal frequency and harmonic index 1 (HI-1, one nodal diameter), which have a 90-degree phase shift compared to each other. By increasing f_r these two modes couple and begin to whirl in two opposite directions and at different frequencies, two red lines. One of these coupled modes decreases in frequency when f_r increases and reaches $f = 7\ Hz$ at $f_r = 44\ Hz$; the direction of rotation of this one is the opposite of the direction of rotation of the fan and it is the first backward-whirling mode (BW) of the system (precession motion around the axial axis of the fan), see mode shape HI-1 BW at Figure 4.9. On the other hand, another branch of the first set of coupled modes rises to $f = 64\ Hz$ when f_r gets to $f_r = 44\ Hz$; this mode, which is labeled as mode HI-1 FW on the left side of Figure 4.9, is similar to the first Backward mode except that the direction of rotation of this mode is as same as the direction of rotation of the fan and it is the first forward-whirling mode (FW).

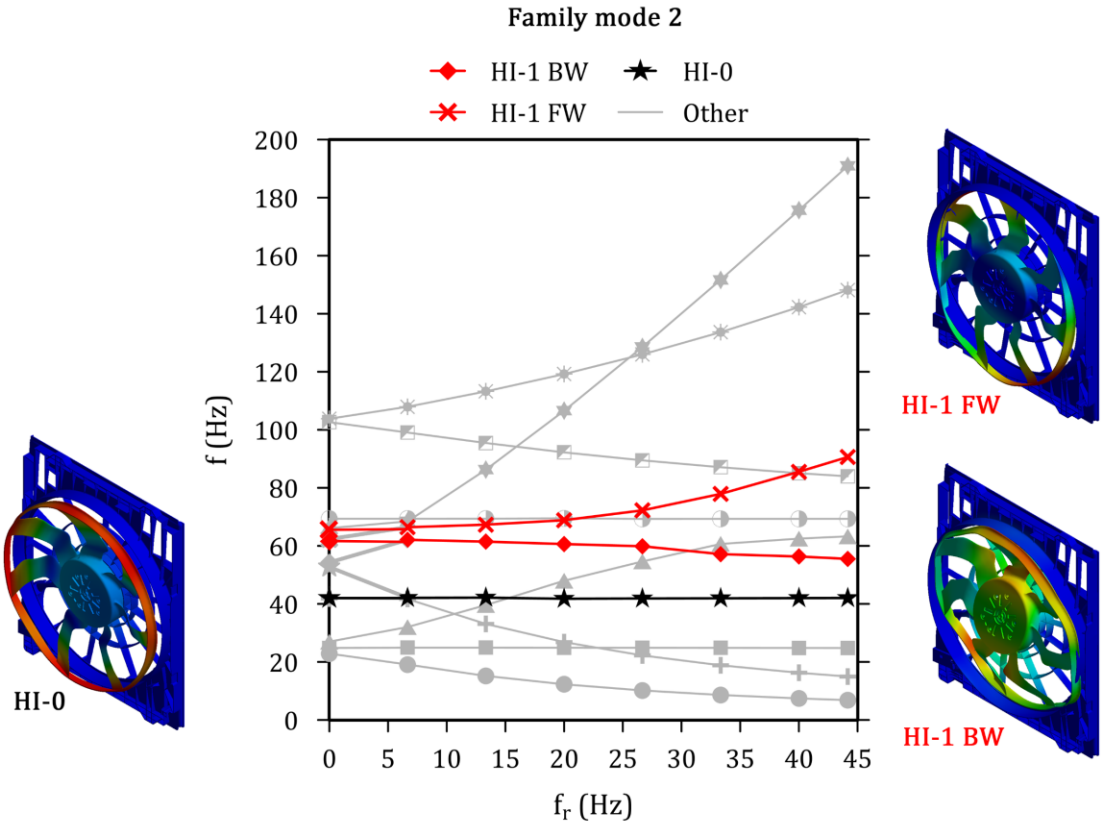

Figure 4.10. Family mode 2 Campbell diagram obtained from the FEM model (Includes modal frequencies and corresponding mode shapes).

Also, the second set of modes consists of another two coupled two nodal diameters modes, HI-2, at about $f = 54\,Hz$ when the fan is idle. These two modes are also similar in nature, just 90 degrees shifted in phase. Again, by increasing f_r up to 44 Hz, the second backward-whirling mode takes place at $f = 14\,Hz$, HI-2 BW. In like manner, the second forward-whirling mode branches from the aforementioned modes around $f = 54\,Hz$ and reaches $f = 190\,Hz$ when $f_r = 44\,Hz$; this mode, which is labeled as mode HI-2 FW, is also similar to the second Backward mode except that the opposite direction of rotation. The third set of modes is a non-rotation zero nodal diameter mode, HI-0, where the rotor and the casing axially displace at the same phase, Fig. 4.9.

The second family mode includes a non-rotation zero nodal diameter mode, HI-0, which takes place at about $f = 43\,Hz$. It can be seen that two HI-1 modes are coupled at about $f = 65\,Hz$ when the fan is idle then it separates into third backward and forward modes; the backward mode is decreasing and reaches $f = 55\,Hz$ when $f_r = 44\,Hz$; while the forward modes end up at $f = 92\,Hz$. The modal frequencies and mode shapes of this family mode have been presented in Fig. 4.10.

The third family mode is also a HI-1 coupled mode which starts approximately at $f = 104\,Hz$ when the fan is idle; when f_r increases, this coupled mode branches and creates the fourth backward and forward modes of the system; the backward mode decreases and ends up at around $f = 84\,Hz$, while the forward mode rises and reaches about $f = 147\,Hz$ when $f_r = 44\,Hz$. This family mode is reported in Fig. 4.11.

Finally, there is a distinct casing torsional mode that is not related to the other family modes. This mode is constant around $f = 70\,Hz$, see Fig. 4.11.

By evaluating and recognizing almost all the important frequency modes it can be concluded that the natural frequencies of the fan are almost similar to a rotary system on coupled anisotropic supports. In this study, the asymmetric casing which acts as a support for the electric motor and the rotor is not rigid and deforms and vibrates at its natural frequencies. This allows the system to have different family modes for rotor and casing in-phase and out-of-phase with each other.

The most important frequency modes are related to the family mode 1 as those happen in the frequencies lower than the f_r. The first backward-whirling mode can be the reason for the high amplitude and low-frequency vibration of the fan. In the next section using vibrometric measurements, this idea will be examined.

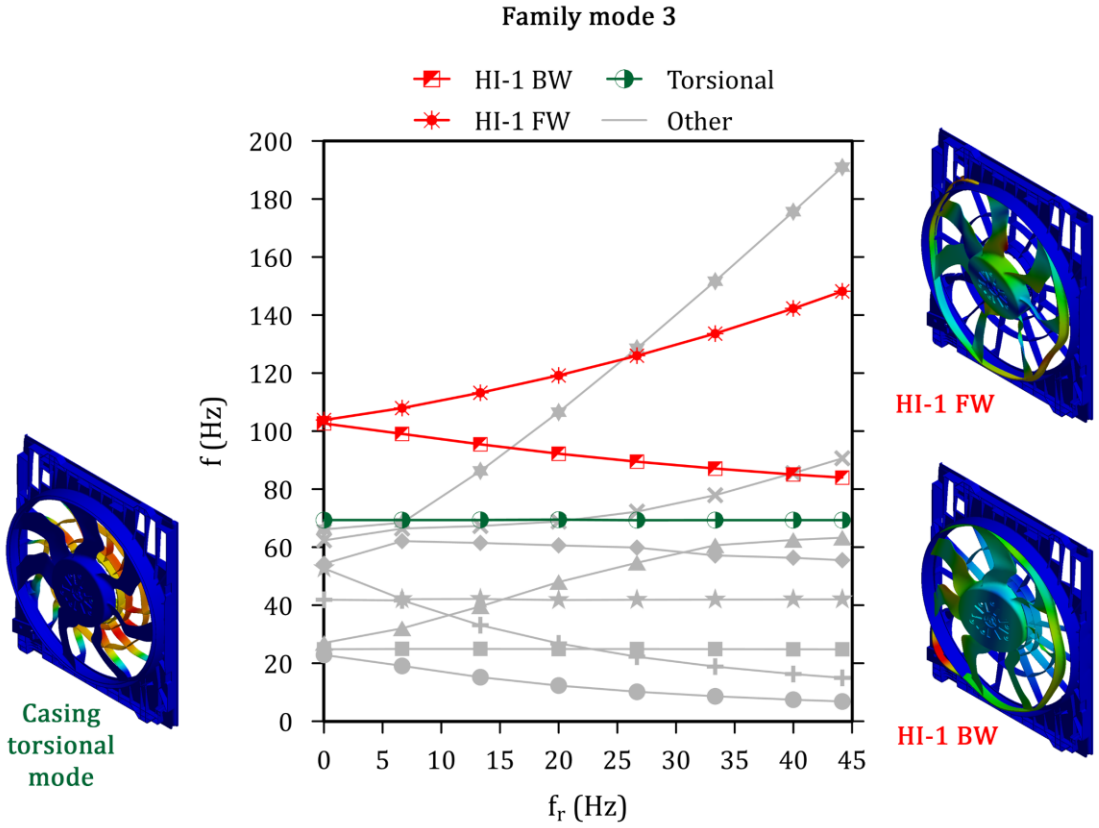

Figure 4.11. Family mode 3 Campbell diagram obtained from the FEM model (Includes modal frequencies and corresponding mode shapes).

4.4. Aeroelastic behavior

4.4.1. Recognition of flutter

As said, the present work stems from the observation of a large-amplitude, low-frequency vibration of the ring connecting the blades that, to the best knowledge of the author, has never been observed before. The vibration consists of a several-millimeters axial displacement x_1 of the ring. Based on vibrometric measurements, a vibration amplitude of 8 mm or even more has been found at design condition ($\varphi = 0.108$, $\psi = 0.088$) and $f_r = 44$ Hz; although the structural integrity of the fan is not affected, such large values are not compatible with the operation in an underhood compartment and may even be a frightening result.

In order to measure the magnitude of this axial displacement oscillation, two laser vibrometers (VIBRO 1 and VIBRO 2) 90 degrees shifted are located in front of the rotating ring where the maximum displacement is observed along the rotor radius. In addition, three accelerometers are

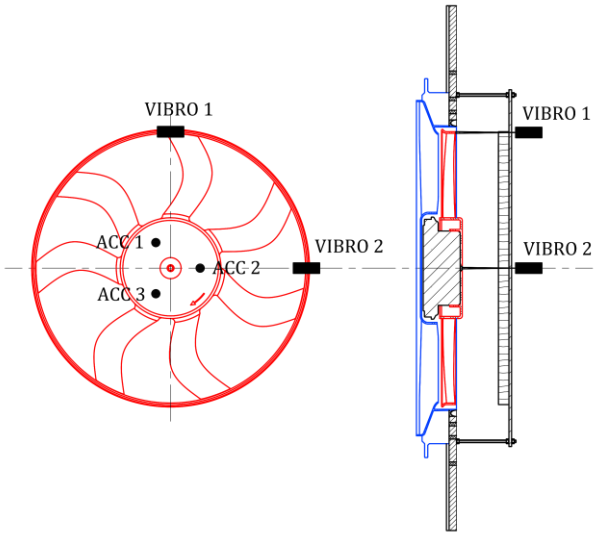

Figure 4.12. Location of vibrometers and accelerometers.

mounted on the hub with equal angular spacing able to measure the vibration at the hub and the axial displacement of the whole assembly. The locations of these probes are shown in Fig. 4.12.

Some preliminary tests have shown that the features of the vibration depend on both the rotational frequency f_r and the operating point, which is identified in the present work by the head coefficient ψ. Namely, the behavior may range from a very important, stationary vibration to no perceived vibration, but also lower amplitude and intermittent ones.

In the characteristic curves of Figure 4.13, all the investigated points are listed in this manner: The measurements have been done at different flow rates and pressure rises for 6 rotational speeds, f_r, which varies from 30 Hz to 44 Hz and these investigated points at different rotational speeds are labeled by the letters F to A; where F refers to the minimum investigated rotational speed and A to the maximum; Δp increases from point 1 at free discharge condition to point 13 at 560 Pa for each f_r.

In the following, these preliminary tests will be presented in two sets: The first set is measured by the vibrometer (VIBRO 1 at the ring) at the fixed rotational speed, $f_r = 44$, and increasing pressure rise for operating points A7 ($\psi = \psi_{DP} = 0.088$) with very large vibration (Flutter), A10 ($\psi = 0.138$) with an intermittent condition, and A12 ($\psi = 0.156$) with no perceived vibration (No-Flutter); the second set of the measurements is related to the design operating point at different rotational speeds (points from D7 to A7, $f_r = 37.4 \div 44$ Hz) that will be reviewed later in this section; the signals amplitude x_1 of these measured points are shown in the small windows in the characteristic curve of Figure 4.13; the duration of measurements is 240 s for each operating point.

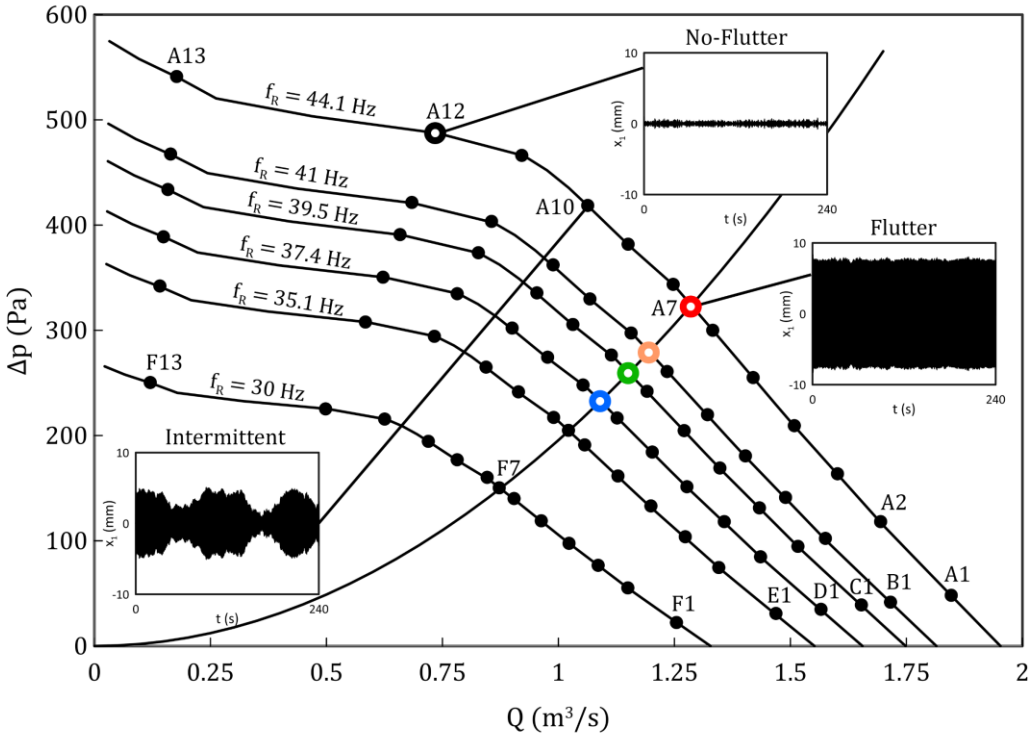

Figure 4.13. Measured points as black dots along the characteristic curve for different f_r, Q, and ΔP with time traces of x_1.

The PSD of two extreme cases, Flutter (A7, in red) and No-Flutter (A12, in black) are calculated, and the main features of the spectra are listed in the following. The most interesting part is the low-frequency one which includes f_r, i.e. below 55 Hz, see Fig. 4.14a; then, considering that the rotor has $Z_R = 7$ blades, the range that includes $7f_r = 308$ Hz, i.e. below $8f_r = 352$ Hz, provides useful information about the behavior at the neighboring frequencies, see Fig. 4.14c and Fig. 4.14d. Finally, the trend up to 10 kHz provides an overall picture of the involved phenomena, see Fig. 4.14b.

The vibration is related to the very prominent low-frequency peak ($f_v = 7.3$ Hz at point A7); such a peak is also present at point A12, but it is rather lower (more than three orders of magnitude, which means that the amplitude of the vibration is almost 40 times smaller) and the frequency is also slightly smaller.

In case A7, peaks at 2nd, 3rd, and 4th harmonics of f_v are present; no such peaks are present in case A12. In both cases, peaks are present at the harmonics of f_r with a small difference in frequency between the two cases. In both cases, four narrowband humps are present between (1) f_v and f_r, (2) f_r and $2f_r$, (3) $2f_r$ and $3f_r$, and (4) $4f_r$ and $5f_r$. They are higher in case A12. In case A7 only, side

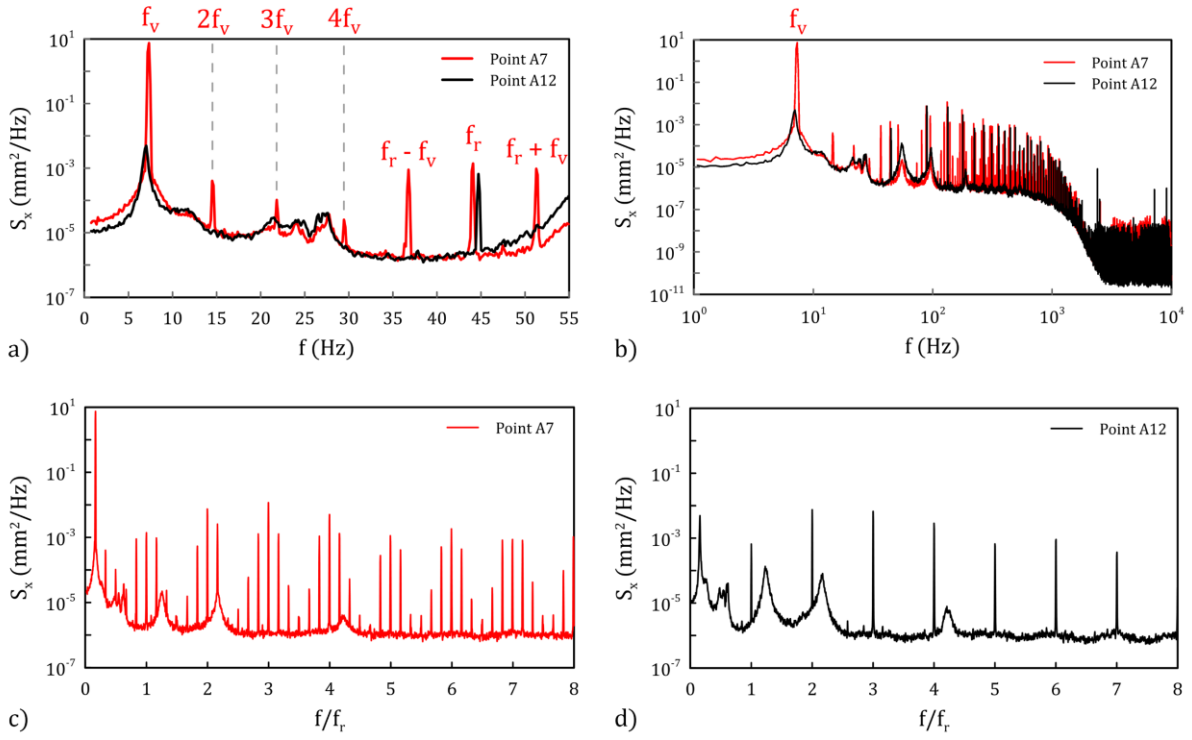

Figure 4.14. PSD of the axial displacements of the ring that are measured by the vibrometer for two operating points A7 and A12 at different frequency ranges.

peaks are present beside the ones at the f_r harmonics. Such peaks are shifted of $\pm f_v$ multiples, i.e. at $f_r \pm f_v$, $f_r \pm 2f_v$, and generally at $nf_r \pm kf_v$.

Fig. 4.14.b shows that the observed peaks at the f_r harmonics, with side peaks shifted of f_v multiples in case A7, extends beyond 2 kHz. The broadband part of the spectrum has a regular, slightly decreasing trend up to about 1 kHz; then, a steeper decrease takes place.

This short survey indicates that an explanation should also be provided for the peaks at the f_r harmonics with the side peaks system and for the narrowband humps; the f_r peaks are explained in this section and the side peaks system will be presented at the end of this chapter using a theoretical model.

The peaks at the f_r harmonics may be due to a residual static unbalance of the rotor, but as shown in section 4.2, such peaks surely receive an important contribution from the non-planarity of the ring due to the employed molding process: seven humps are present, see Fig. 4.4, that is perceived by the vibrometer as a one-per-revolution displacement. The side peaks at multiples of f_v observed in case A7 resemble the frequency modulation effect, as if a carrier wave at $f = f_r$ were modulated by a wave

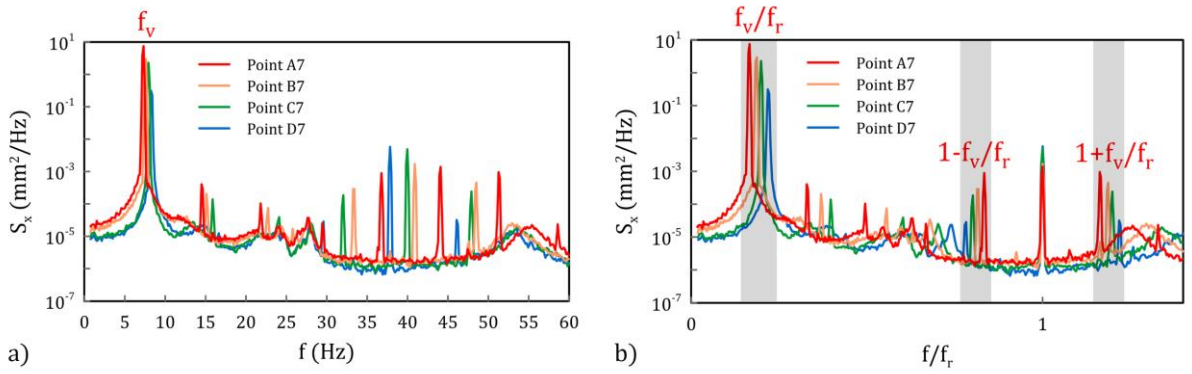

Figure 4.15. Effect of f_r changes at the PSD of the axial displacements of the ring.

at $f = f_v$. It will be experimentally shown that, in the presence of vibration, rotational speed oscillations take place with fundamental frequency f_v; then an analytic analysis will be provided that shows this is consistent with side peaks in the PSD of the rotational speed. As a result, such oscillations also affect the hump passing in front of the vibrometer, eventually yielding the modulation effect which is observed in the vibrometer signal. The relation between the side peaks' shift and f_v is apparent in Fig. 4.15, where the PSD of the second set of the measurements related to the design operating point at different rotational speeds are reported (points from D7 to A7, $f_r = 37.4 \div 44$ Hz, Fig. 4.13). In the two plots, the PSD is plotted either versus f or versus f/f_r; the first plot shows that if the peaks are disregarded, the trend of the spectra is generally independent of $f_r$while f_v decreases with f_r: $f_v = 8.24$ Hz at $f_r = 37.4$ Hz and $f_v = 7.3$ Hz at $f_r = 44$ Hz; this is consistent with a backward whirling mode of vibration of a rigid disk; the peak at $f = f_r$ may not be easily detected, due to the presence of the side peaks. On the contrary, when the PSD is plotted versus f/f_r, see Fig. 4.15b, all of the peaks at $f = f_r$ collapse at $f/f_r = 1$, while the side peaks shift to different values of f/f_r, i.e. to $f/f_r \cong \pm 0.78$ to $f/f_r \cong \pm 0.83$. Namely, the distance from the main peak decreases from about 0.22 for point D7 to about 0.17 for point A7; these values are consistent with the ones of f_v/f_r: $f_v/f_r = 7.3/44 = 0.166$ at point A7 and $f_v/f_r = 8.24/37.4 = 0.22$ at point D7.

It will also be shown in the following that the narrowband humps are related to a random, broadband excitation of rotor ring vibration, but for the order higher than the one related to the vibration at $f = f_v$.

The fact a low-frequency peak is always present suggests that the vibration is caused by a resonance; at certain operating conditions (e.g. point A12), it may be due to a broadband excitation similarly to the other narrowband humps, while at other operating conditions (e.g. point A7) a strong driving mechanism arises. The peaks at the 2nd, 3rd, and 4th f_v are clearly apparent, but their order of

magnitude is 5 to 6 times smaller, which means that the amplitude of the vibration is almost 100 to 500 times smaller; those could have a counterpart in other involved quantities, but such a large difference implies that they may be due to and may not be distinguished from nonlinear effects. The decrease in f_v from case A7 (7.3 Hz, strong vibration) to case A12 (7 Hz, no perceived vibration) is consistent with an aeroelastic nature of the phenomenon, as it may be ascribed to the aerodynamic stiffening effect.

4.4.2. Signals from different measuring devices

In these aforementioned investigations, the VIBRO1 signal has been used because the signals of other measuring devices (two vibrometers and three accelerometers, see Fig. 4.12) have similar characteristics. PSDs of one of the vibrometers and an accelerometer have been compared in Fig. 4.16 for two operating points B2 (No-Flutter) and B7 (Flutter). Characteristics such as low-frequency vibration peak, f_v, and rotational speed, f_r, are visible in all signals. As expected, due to the nature of the backward whirling motion of the rotor around the axial axis of the electric motor's shaft at f_v, the axial displacement at the tip of the blades where the vibrometer is located (rotating ring) is much greater, almost two orders of magnitude in the PSD, than the displacement at the hub where the accelerometer is mounted. This difference is shown in Fig. 4.17 for the Flutter case by filtering the two signals at $f_v \pm 0.5\ Hz$ frequency band; the vibration amplitude for the vibrometer is more than 10 times the accelerometer; the phase difference between these two measuring devices is due to the installation location.

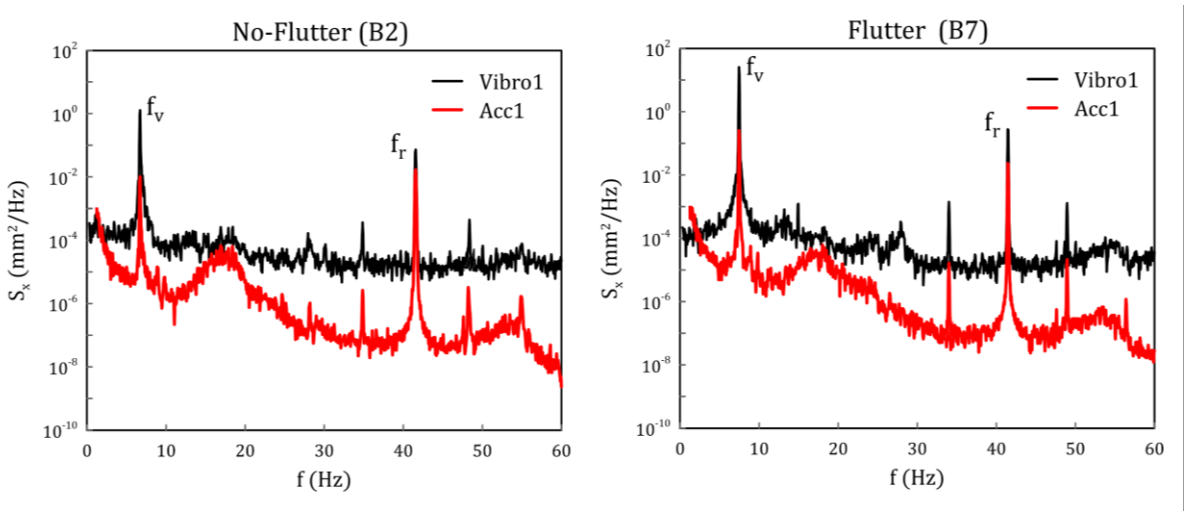

Figure 4.16. PSD comparison of vibrometer and accelerometer for two working points. a) No-Flutter (Point B2). b) Flutter (Point B7).

In Fig. 4.16, side peaks are present beside the ones at the f_r harmonics for both signals. Such peaks are shifted of $\pm f_v$ multiples. For the accelerometer signal, there is a narrowband hump in the range of 15 to 20 Hz in both Flutter and No-Flutter cases. Such a hump is not present for the vibrometer signal. Considering the slight differences between the measuring devices, it can be concluded that the reiteration of the analysis using other devices will produce similar results.

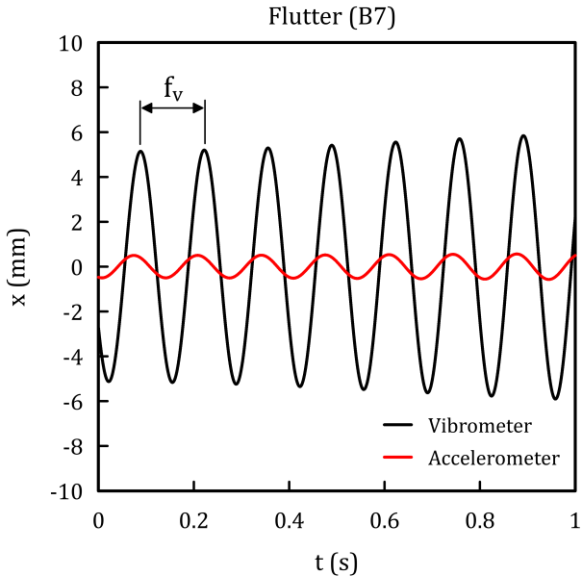

Figure 4.17. The vibration amplitude obtained by vibrometer and accelerometer at working point B7.

4.4.3. Dependency on the operating condition

The observation of the classic Campbell plots for stiff rotating disks, suggests that the observed low-frequency, subharmonic vibration could be related to a backward whirling one-nodal diameter mode. In order to confirm such an assumption, a number of tests, both experimental and numerical, have been done that include vibrometric measurements at different rotational speeds, and experimental and numerical modal analysis; the numerical modal analysis has been studied in section 4.3 while the experimental one will be present here. Then, the phase difference between the signal from vibrometers located at different angular positions has been employed to verify that the identified mode is in fact counter-rotating.

In order to build an experimental Campbell plot, the fan has been operated at different rotational speeds while keeping the plenum valve at a fixed opening, namely at design values of φ and ψ as f_r varied and the ring axial position has been measured by means of a vibrometer, see the signal plot in Fig. 4.18a where the gray signal is the acquired signal while the overlapped blue one is the filtered

signal (bandpass filter: $f_v \pm 2\ Hz$) which this filtered signal is supposed to be representative of the vibration. First, the fan has been excited by means of a compressed air jet impinging in the blade tip region and f_r has been slowly varied along a linear ramp from 11 Hz (minimum operational f_r) to 45 Hz (maximum operational f_r) in 135 s, then, for the next 15 s, the f_r has been kept constant at the maximum rotational speed.

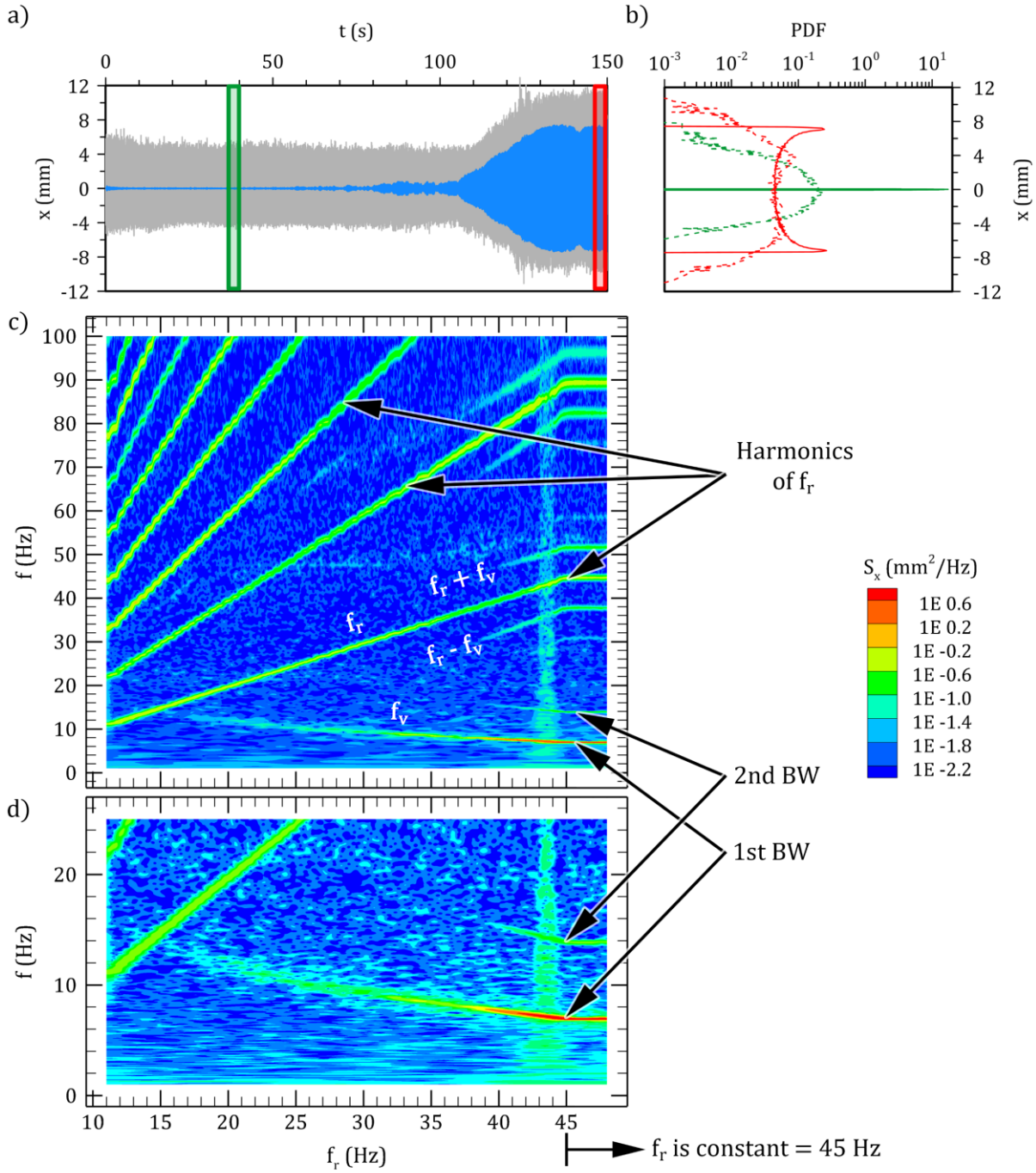

Figure 4.18. Experimental Campbell diagram of an f_r ramped signal.

The probability density function (PDF) of the acquired signal (dashed line) and the filtered signal (solid line) for two time periods, low (green) and high (red) amplitude is calculated, see Fig. 4.18b. In low amplitude fluctuations, the probability distribution appears as a distinct peak at the zero mean, on the contrary for high amplitude fluctuations, this probability distribution is bimodal, with peaks of nearly 8 mm, corresponding to a feature typical of reciprocating oscillating motion.

In Figs. 4.18c and 4.18d, the wavelet plot of the vibrometer signal is reported where f_r has been reported in the abscissas instead of t, due to proportionality between f_r and t during the linear speed ramp; as said, it should be kept in mind that this proportionality exists only up to the maximum rotational speed when the rotor's rotational frequency reaches 45 Hz; after 45 Hz the rotational velocity is constant. Straight lines at the 1st, 2nd, and 3rd harmonics of f_r are apparent with pairs of side crests at $f_r > 40$ Hz. These crests correspond to the side peaks in the PSD of Figs. 4.14 and 4.15 and appear when the vibration becomes evident. Furthermore, some crests may also be identified that are related to two narrowband humps out of the four observed in the PSD.

First of all, the vibration at $f = f_v = 7.3$ Hz is related to a crest at a frequency that decreases with f_v from about 16 Hz at $f_r = 11$ Hz to 7 Hz at $f_r = 45$ Hz; such a decreasing trend is typical of the first backward-whirling mode of a rotating disk. However, although it is rather stiff, the ring is not a disk and is connected to the hub by means of the blades, which are rather compliant. Therefore, before accepting that the kind of mode has been identified, a confirmation is necessary that it is one-nodal-diameter and counter-rotating. To identify the direction of rotation of backward whirling mode, the phase difference between the signal from two vibrometers located at almost 90 degrees angular positions has been computed. By calculating the phase at f_r and f_v for the signal from two vibrometers, it can be seen that the direction of rotation at f_v is in the opposite direction of f_r. The phases for vibrometers 1 and 2 at f_r are equal to 92° and 1° respectively yielding a phase difference of $+91^\circ$; while at f_v phases are equal to 125° and -146° for vibrometers 1 and 2 respectively yielding a phase difference of -89°. These phase differences are shown in Fig. 4.19.

So far, the nature of observed low-frequency, subharmonic vibration has been identified. In order to study the relationship between the excitation of this frequency mode and the parameters of f_r, Q (or φ), and ΔP (or ψ), comprehensive measurements have been done for the entire characteristic curve of the fan. Figure 4.13 shows the investigated points as black dots along the characteristic curve for different f_r, Q, and ΔP.

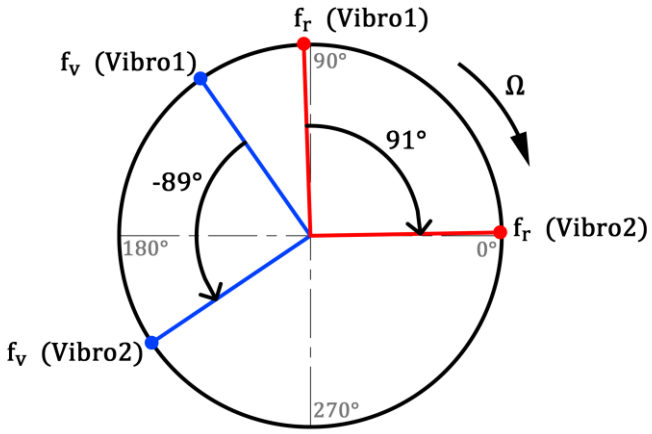

Figure 4.19. Direction of rotation of backward whirling mode.

The oscillating behavior for all the studied points is investigated by time averaging the amplitude of the oscillations related to the low-frequency vibration f_v, obtained by calculating the Hilbert envelope of the vibrometer signal at each point and is denoted by x_{f_v}. First, the amplitude of oscillations in logarithmic scale versus ψ is presented in Fig. 4.20a. Second, in a different illustration as a contour plot, Fig. 4.20b, x_{f_v} is plotted in logarithmic scale versus Q and ΔP. As ψ increases or decreases and approaches the design point $\psi_{DP} = 0.108$, the oscillation amplitude enhances sharply. Also, in the contour plot, which is divided into three zones of Flutter, No-Flutter, and Intermittent vibrational behavior, it can be clearly seen that by approaching point A7 (design point), either by increasing f_r or by opening and closing the inlet valve and changing Q and ΔP, the amplitude of oscillations increases significantly. For f_r less than 35 Hz as well as Q and ΔP outside the Flutter zone, the amplitude of oscillations is significantly reduced and its value is very close to zero. Also, the narrow area between the two zones of Flutter and No-Flutter indicates that the intermittent behavior is similar to the small window of point A10 in Fig 4.13.

Investigating experimentally the vibrational behavior of the fan during a rotational speed ramp which is presented by the Campbell diagram, shows that a low-frequency mode of the system causes high amplitude vibration; this decreasing frequency by increasing the rotational frequency of the rotor to the design point has the highest vibrational amplitude; the direction of rotation of this low-frequency mode is verified and it has been observed that it is a backward-whirling mode. Also, it has been found that the experimental results are compatible with the FEM model.

Finally, comprehensive measurements showed the relationship between the vibrational behavior of the fan and the parameters of f_r, Q (or φ), and ΔP (or ψ). By approaching the design point high

amplitude oscillations take place and it has been found that this vibrational behavior can be divided into three zones: Flutter, No-Flutter, and Intermittent behavior.

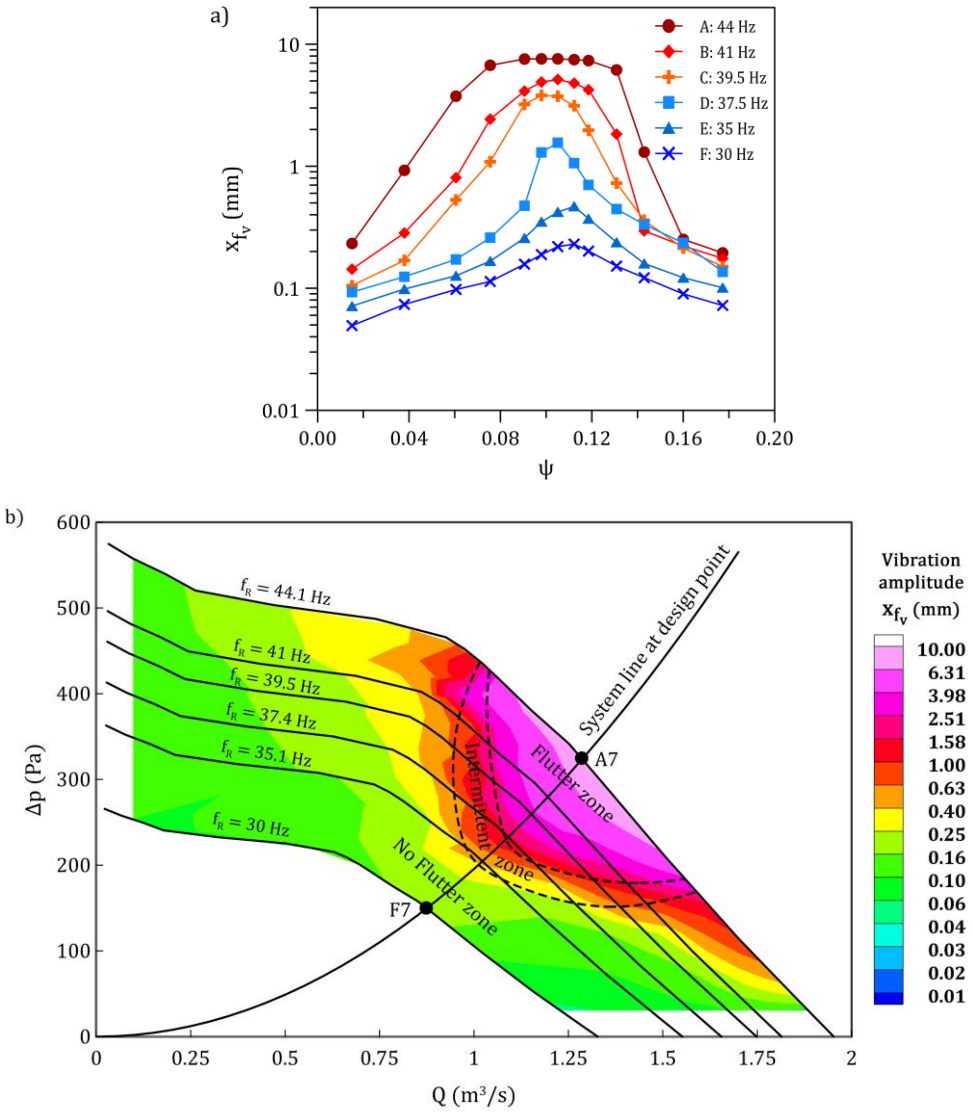

Figure 4.20. a) Vibration amplitude for the investigated points. b) Vibration amplitude for all the studied points presented in three zones of Flutter, No-Flutter, and Intermittent behavior.

4.4.4. The nature of the spectral peaks and the excitation mechanism

The first indication about the nature of the excitation mechanism comes from the intermittency observed at point A10, Fig. 4.13. The wavelet maps of three distinct cases of points A7, A10, and A12 represent Flutter, Intermittent, and No-Flutter conditions respectively as illustrated in Figure 4.21. It can be clearly seen that for point A10 at a certain time window, the amplitude of x_1 frequently decreases and increases. The amplitude of these oscillations in the maximum and

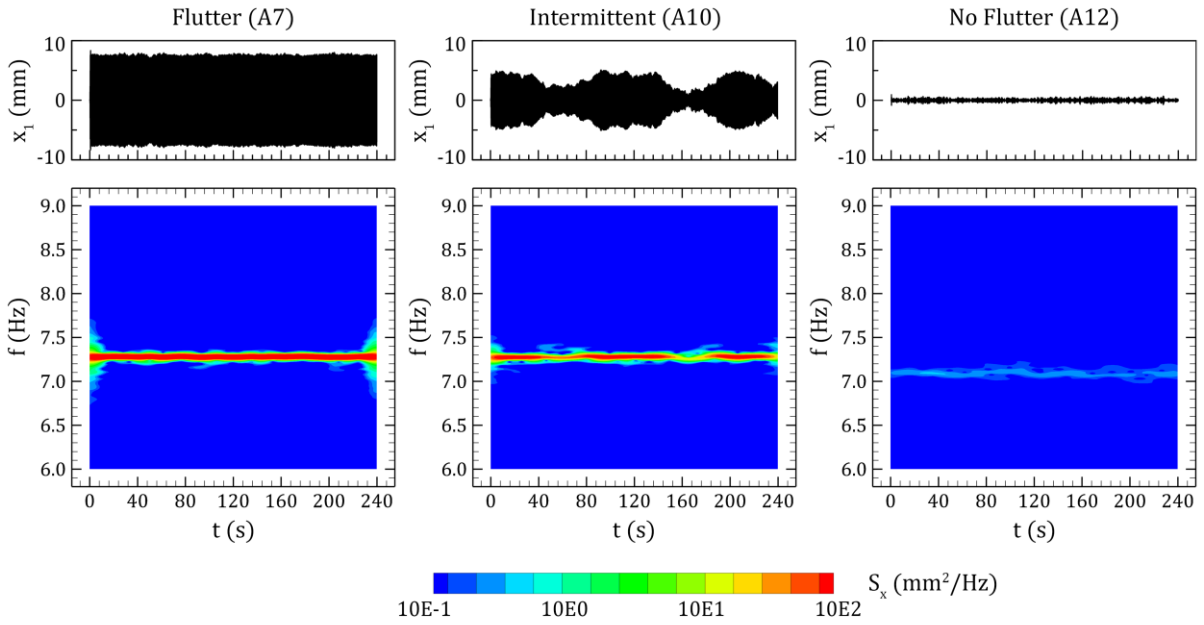

Figure 4.21. Wavelet plots and time traces for three sample cases A7, A10, and A12.

minimum parts of the signal is almost close to the case with high amplitude oscillations A7 and the case with very low amplitude oscillations A12, respectively. The corresponding wavelet maps clearly show this effect; considering that the these maps show the peak at f_v region between the frequency range of 6 to 9 Hz. In the Flutter case, the peak at f_v has the maximum amplitude, and its frequency along the measuring time window is almost constant. On the contrary, In the No-Flutter case, the PSD peak at f_v is barely visible and has the minimum amplitude, and its frequency decreases as it has been investigated by the PSD plots. All things considered and by exploring these two extreme points it can be seen that the vibrational behavior of the fan at f_v peak for the Intermittent case is a combination of these two, Flutter and No-Flutter cases. In the way that during the time the amplitude of the oscillation is high, the value of S_x is similar to the Flutter case, and in contrast, during the time the amplitude of the oscillation declines, the value of S_x and f_v are also decreasing analogous to the No-Flutter case. This slight f_v modification is visible in the A10 wavelet map.

The intermittent behavior at point A10 may provide information about the excitation mechanism but what causes this iterative behavior over time seems to be a relatively complex issue. Such an intermittent behavior is typical of aeroelastic phenomena and, namely, of flutter. Flutter is related to the existence of aerodynamic forces whose amplitude depends on the displacement and velocity of the rotor with respect to its rotating reference system. For their nature, these forces are called self-

excited or motion-induced forces. When the relationship between force and motion is linearized, the proportionality factor between displacement and force identifies the aerodynamic stiffness, while the proportionality factor between velocity and force is idealized as aerodynamic damping. In flutter, the aerodynamic stiffness has usually a minor role, producing a slight shift of the vibration frequency (the variation of f_v observed in the experiment is compatible with this phenomenon). On the other hand, the role of aerodynamic damping is dominant when its value is negative and large enough to cancel the mechanical damping. In this case, the negative total damping produces an increment of the vibration amplitude until some non-linearity lets the aeroelastic system saturate on a stable limit cycle. Random events, e.g. the ingestion of large-scale turbulence, may produce a temporary phase shift of the motion-induced forces and interrupt the aeroelastic feedback, resulting in an intermittent behavior.

The confirmation that the excitation is aeroelastic arrived fortuitously, by observing that positioning a thin bar downstream of the fan close to the gap, Fig. 4.22a, immediately suppresses the large-amplitude vibration, and removing the bar re-onsets the vibration rapidly [20]. Such behavior is documented in Fig. 4.22b by the measurements taken while the bar is present (point B7 in Fig. 4.13). When the bar is present the basic features of the vibration (time trace, amplitude, and frequency) are quite close to the ones related to the points at which the vibration is weak, see Fig. 4.23. The bar may suppress the vibration, even without any contact with the mounting panel. This indicates that the

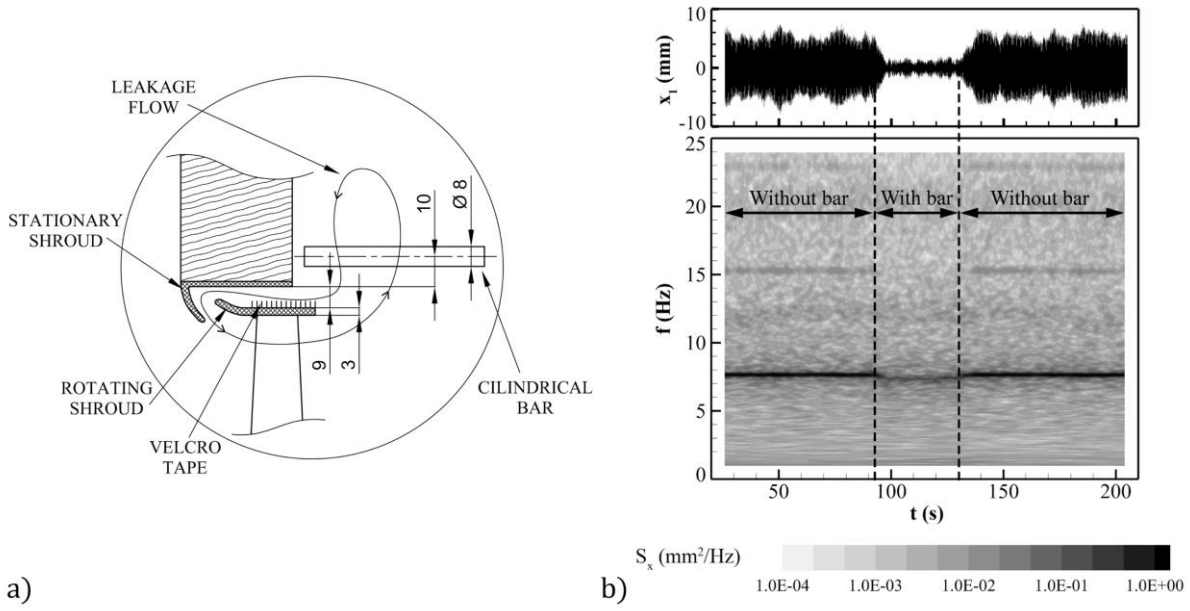

Figure 4.22. Placing a bar downstream of the fan adjacent to the gap. a) Details of the bar and gap geometry. b) Wavelet plot and time trace [20].

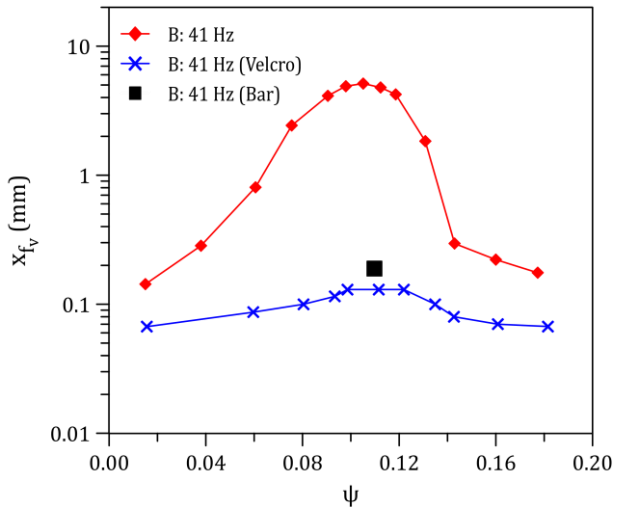

Figure 4.23. Vibration amplitude at $f_r = 41\ Hz$ for general case, with Velcro tape, and with bar.

excitation is not purely mechanical since the bar may act on the system only changing the flow field. The average axial gap size is independent of the presence of the bar, also according to the fact that the vibration amplitude does not change the operating point; this shows that the gap size does not univocally determine the characteristics of the vibration, e.g. x_{f_v} and f_v. However, aerodynamic disturbances are typically convective, i.e. they are transported streamwise by the mean flow. Upstream influence is possible but requires an obstacle located in the main flow at a short distance. In the present case, none of these conditions are apparently verified, as the bar is located in the downstream region, but outside the rotor outflow. Hence, the assumption that the bar acts on the leakage flow is reasonable due to the typical trend of the leakage flow streamlines, Fig. 4.22a. The vibration makes the gap non-axisymmetric as its size periodically varies at the frequency f_v, consistently with a counter-rotating mode shape, see Fig. 4.24. This produces a change in the gap flow, which, in turn, generates a variation of the aerodynamic load, resulting in aeroelastic feedback.

The hypothesis that the aeroelastic coupling occurs due to the leakage flow is further confirmed by tests carried out after increasing the roughness of the external surface of the rotor ring by means of a Velcro tape which has a negligible mass, Fig.4.22a. This yields a higher drag, which inhibits the possible counter-rotating flow in the gap. While this modification only slightly decreased the fan efficiency, the large-amplitude vibration observed at f_v completely disappeared. The corresponding x_{f_v} trends (Fig. 4.23) show a decrease larger than with the bar, thus confirming that the leakage flow is involved in the vibration.

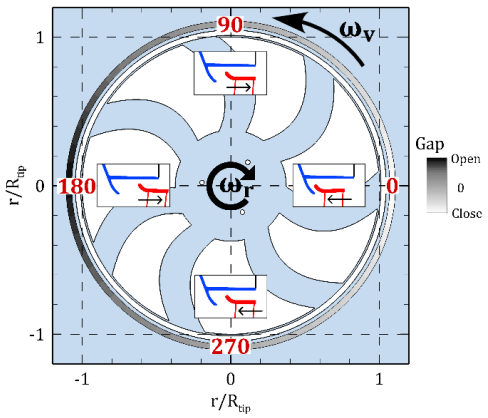

Figure 4.24. The direction of rotation of the rotor (ω_r) and whirling motion (ω_v), plus four schematic positions and a circular black and white contour strip illustrating the gap opening for one revolution of ω_v.

4.5. Theoretical models

The present section regards the frequency content of the aerodynamic excitation of a turbomachinery rotor constituted by $m = 1,2, \dots, z_R$ blades and is based on a kinematic model of both flow and rotor ring. An extension of the rotor interference theory employed in Aeroacoustics, e.g. see [21], and an application of the frequency modulation theory are reported.

First, it is assumed that deformations or vibrations are absent; hence, in the relative frame, the blades are stationary and are located at the circumferential positions $\vartheta_{rel,m} = \vartheta_m^0$ with $\vartheta_1^0 = 0$. Then the possibility of vibration and of rotational speed fluctuation is considered.

The evenly spaced rotor, for which

$$\vartheta_m^0 = (m-1)\frac{2\pi}{z_R} \tag{4.1}$$

is the most common one, but the present rotor has uneven blades, i.e. a generic distribution ϑ_m^0. The only constraint that the ϑ_m^0 distribution has to respect is that the rotor is statically balanced, which requires that $\sum_{m=1}^{z_R} \cos\vartheta_m^0 = 0$ and $\sum_{m=1}^{z_R} \sin\vartheta_m^0 = 0$; such a condition may be synthesized as

$$\sum_{m=1}^{z_R} \exp(i\vartheta_m^0) = 0 \tag{4.2}$$

Such a solution is often employed in fan rotors in order to reduce the tonal noise components at the blade passing frequency (BPF) and harmonics, at the cost of generating noise at the harmonics of the rotational frequency which are usually absent in evenly spaced rotors. As the harmonic content of the received noise is determined by the interference between acoustic waves generated by each blade, the key quantity that governs the phenomenon is called the rotor interference function and depends on both the harmonic order and the blades' angular positions.

4.5.1. The rotor interference function

In the following sections, it will be shown that the summation of the forces acting on the blades involves the quantity

$$F_{int}\left(n, \vartheta_1^0, \vartheta_2^0, \dots, \vartheta_{z_R}^0\right) = \sum_{m=1}^{z_R} \exp(in\vartheta_m^0) \tag{4.3}$$

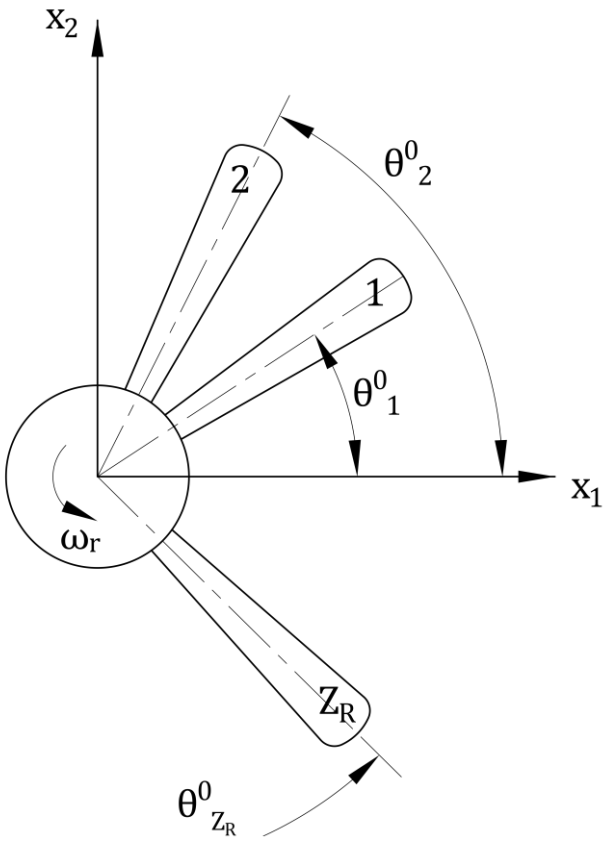

Figure 4.25. The rotor assembly.

that, in fan Aeroacoustics, is called the rotor interference function. The purpose of the present section is to show some interesting properties of F_{int}:

1) For any rotor

$$F_{int}\left(-n, \vartheta_1^0, \vartheta_2^0, \dots, \vartheta_{z_R}^0\right) = F_{int}\left(n, \vartheta_1^0, \vartheta_2^0, \dots, \vartheta_{z_R}^0\right)^* \tag{4.4}$$

where * denotes the complex conjugate value. Hence

$$\left|F_{int}\left(-n, \vartheta_1^0, \vartheta_2^0, \dots, \vartheta_{z_R}^0\right)\right| = \left|F_{int}\left(n, \vartheta_1^0, \vartheta_2^0, \dots, \vartheta_{z_R}^0\right)\right| \tag{4.5}$$

2) For any rotor

$$F_{int}\left(0, \vartheta_1^0, \vartheta_2^0, \dots, \vartheta_{z_R}^0\right) = z_R \tag{4.6}$$

If $n = 0$, $\exp(in\vartheta_m^0) = \exp(0) = 1$ for any value of ϑ_m^0. Hence

$$F_{int}\left(0, \vartheta_1^0, \vartheta_2^0, \dots, \vartheta_{z_R}^0\right) = \sum_m^{z_R} \exp(0) = \sum_m^{z_R} 1 = z_R \tag{4.7}$$

3) For any statically balanced rotor

$$F_{int}\left(1, \vartheta_1^0, \vartheta_2^0, \dots, \vartheta_{z_R}^0\right) = 0 \tag{4.8}$$

as $F_{int}\left(1, \vartheta_1^0, \vartheta_2^0, \dots, \vartheta_{z_R}^0\right) = \sum_m^{z_R} \exp(i\vartheta_m^0) = 0$ constitutes the static balancing condition. This means that no fluctuation may be present at $f = f_p$ (i.e. at $n = 1$), no matter whether a statically balanced rotor is evenly spaced or not.

4) For an evenly spaced rotor, i.e. $\vartheta_m^0 = (m-1)\frac{2\pi}{z_R}$, only fluctuations at z_R multiples are present (for a stationary disturbance, $f_p = -f_r$, and these are harmonics of the BPF), and the fluctuations at all of the other f_p harmonics are canceled. Namely

$$F_{int}\left(n, \vartheta_1^0, \vartheta_2^0, \dots, \vartheta_{z_R}^0\right) = \sum_{m=1}^{z_R} \exp(in\vartheta_m^0) = \sum_{m=1}^{z_R} \exp\left[in(m-1)\frac{2\pi}{z_R}\right] = \begin{cases} z_R & if \quad n = kz_R \\ 0 & if \quad n \neq kz_R \end{cases} \tag{4.9}$$

with any integer k. Namely, all of the harmonics of $z_R f_p$ are amplified by a factor of z_R (perfect constructive interference), while all of the remainders are completely canceled (perfect destructive interference). This may be demonstrated by posing $z = \exp\left(i\frac{2\pi n}{z_R}\right) = \cos\left(\frac{2\pi n}{z_R}\right) + i\sin\left(\frac{2\pi n}{z_R}\right)$:

$$F_{int}\left(n, \vartheta_1^0, \vartheta_2^0, \dots, \vartheta_{z_R}^0\right) = \sum_{m=1}^{z_R} \exp\left(in(m-1)\frac{2\pi}{z_R}\right) = \sum_{m=1}^{z_R} \exp\left(i\frac{2\pi n}{z_R}\right)^{m-1} = \sum_{m=1}^{z_R} z^{m-1} \\ = 1 + z + z^2 + \cdots + z^{z_R-1} \tag{4.10}$$

The two cases $n = kz_R$ and $n \neq kz_R$ with any integer k have to be considered:

- if $n = kz_R$, $z = \exp\left(i\frac{2\pi n}{z_R}\right) = \exp\left(i\frac{2\pi k z_R}{z_R}\right) = \exp(i2\pi k) = 1$ for any k. Then

$$F_{int}\left(n, \vartheta_1^0, \vartheta_2^0, \dots, \vartheta_{z_R}^0\right) = \sum_{m=1}^{z_R} \exp\left(in(m-1)\frac{2\pi}{z_R}\right) = \sum_{m=1}^{z_R} \exp\left(i\frac{2\pi k z_R}{z_R}\right)^{m-1} = \sum_{m=1}^{z_R} 1 = z_R \tag{4.11}$$

- if $n \neq kz_R$, the algebraic identity $\sum_{n=0}^{N} z^n = \frac{z^{N+1}-1}{z-1}$ has to be considered that yields

$$\sum_{m=1}^{z_R} z^{m-1} = \sum_{m'=1}^{z_R-1} z^{m'-1} = \frac{z^{z_R}-1}{z-1} = \frac{\exp\left(i\frac{2\pi n}{z_R}\right)^{z_R} - 1}{\exp\left(i\frac{2\pi n}{z_R}\right) - 1} = \frac{\exp\left(i2\pi n\frac{z_R}{z_R}\right) - 1}{\exp\left(i\frac{2\pi n}{z_R}\right) - 1} \tag{4.12}$$

in this case, $\exp(i2\pi n) = 1$ for any n, which indicates that the numerator is null, while the denominator cannot be null since $\frac{n}{z_R}$ is not an integer. Hence

$$F_{int}\left(n, \vartheta_1^0, \vartheta_2^0, \dots, \vartheta_{z_R}^0\right) = \sum_{m=1}^{z_R} \exp\left(in(m-1)\frac{2\pi}{z_R}\right) = \frac{\exp(i2\pi n) - 1}{\exp\left(i\frac{2\pi n}{z_R}\right) - 1} = 0 \tag{4.13}$$

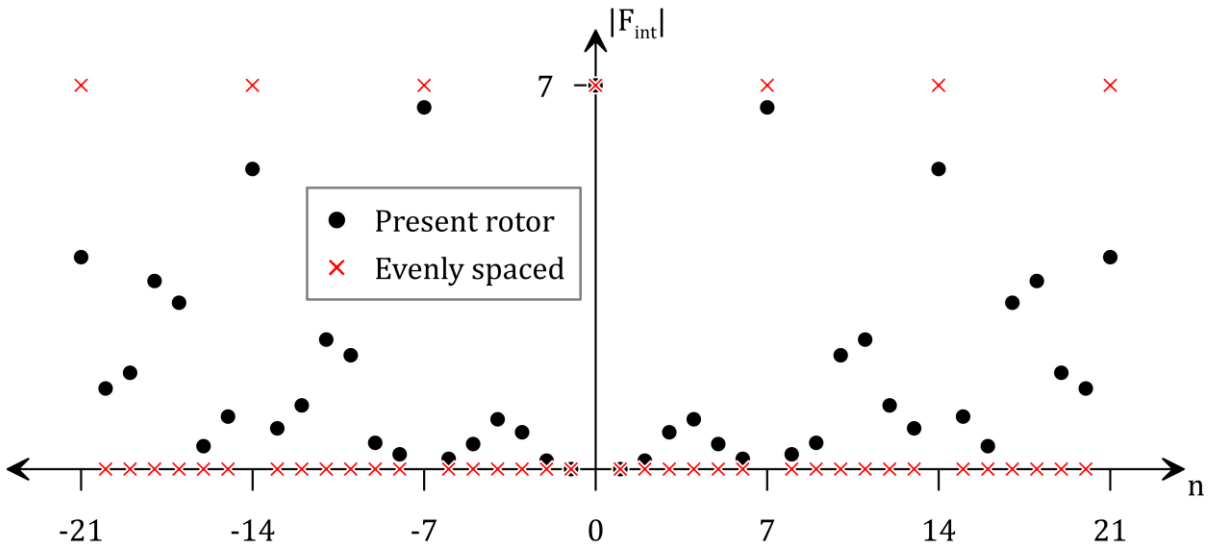

Figure 4.26. The rotor interference function.

Notice that, in the following, the blade spacing ϑ_m^0 is fixed. Hence, for the sake of space, when referring to $F_{int}\left(n, \vartheta_1^0, \vartheta_2^0, \dots, \vartheta_{z_R}^0\right)$, the angles $\vartheta_1^0, \vartheta_2^0, \dots, \vartheta_{z_R}^0$ will be omitted and it will be simply referred to as $F_{int}(n)$.

Summarizing, it has been shown that

- For any rotor, the constant part $(n = 0)$ of the blade force sum as there is no possibility of cancellation; hence, the force due to a blade simply multiplies by z_R;
- As the rotor is statically balanced, no fluctuation may be present at $f = f_p$ $(n = 1)$, no matter whether the rotor is evenly spaced or not;
- For an evenly spaced rotor, fluctuations at the harmonics of $z_R f_p$ are amplified of a factor z_R;
- For an evenly spaced rotor, no fluctuation may be present at the remainder of the f_p harmonics, while for unevenly spaced ones these may appear;

n	$(n+1)f_r + nf_v$	$\lvert F_{int}(n+1)\rvert$	$(n-1)f_r + nf_v$	$\lvert F_{int}(n-1)\rvert$
0	$1f_r = 44\ Hz$	$\lvert F_{int}(1)\rvert = 0$	$-1f_r = -44\ Hz$	$\lvert F_{int}(-1)\rvert = 0$
1	$2f_r + f_v = 95.5\ Hz$	$\lvert F_{int}(2)\rvert = 0.15$	$1f_v = 7.5\ Hz$	$\lvert F_{int}(0)\rvert = z_R = 7$
2	$3f_r + 2f_v = 147\ Hz$	$\lvert F_{int}(3)\rvert = 0.67$	$1f_r + 2f_v = 59\ Hz$	$\lvert F_{int}(1)\rvert = z_R = 0$
3	$4f_r + 3f_v = 198.5\ Hz$	$\lvert F_{int}(4)\rvert = 0.91$	$2f_r + 3f_v = 110.5\ Hz$	$\lvert F_{int}(2)\rvert = z_R = 0.15$

Table 4.3. The present rotor interference function for $n = 0,1,2, and\ 3$.

- However, if the spacing is only mildly uneven as in the present case, F_{int} is large at $z_R f_p$ and at it is lower harmonics, while it should be small at the intermediate ones.

4.5.2. Kinematic analysis of the rotor speed oscillation

The present analysis stems from the observation of the vibrometer signal PSD, see Fig. 4.14; namely, a peak at $f = f_r$ is present with and without flutter, i.e. no matter the peak at $f = f_v$ is present. But, with flutter, further peaks (in the following side peaks) appear at $f = f_r \pm f_v$. The peak at $f = f_r$ may be explained considering that the ring is not perfectly planar due to the molding process, see Fig. 4.4, which reports the shape of the ring in terms of axial position $x^0 = x^0(\vartheta_{rel})$, with ϑ_{rel} the angular position in the relative frame. As will be seen in the next section, the instantaneous absolute angular position ϑ_{abs} of a point of the ring identified by a ϑ_{rel} value is

$$\vartheta_{abs} = \vartheta_{rel} + 2\pi f_r t \tag{4.14}$$

hence, in the absence of vibration, the axial position $x^0_{ring}(t)$ of the ring at the location $\vartheta_{abs} = \vartheta_{vibro}$ where the vibrometer is located is given by

$$x^0_{ring}(t) = x^0(\vartheta_{vibro} - 2\pi f_r t) \tag{4.15}$$

having considered that $\vartheta_{rel} = \vartheta_{abs} - 2\pi f_r t$.

$x^0(\vartheta_{rel})$ may be expressed in terms of the Fourier series:

$$x^0(\vartheta_{rel}) = \sum_{n=-\infty}^{\infty} \tilde{x}^0_n \exp(in\vartheta_{rel}) \tag{4.16}$$

which, in the absolute frame, becomes

$$x^0_{ring}(t) = x^0(\vartheta_{abs}, t) = \sum_{n=-\infty}^{\infty} \tilde{x}^0_n \exp[in(\vartheta_{vibro} - 2\pi f_r t)] \tag{4.17}$$

This shows that, even in the absence of vibration, the rigid motion of a non-planar ring results in a periodic axial displacement with fundamental frequency f_r. The present section aims at showing that the side peaks are due to a fluctuation in the rotational speed combined with the rotor non-planarity.

It is assumed that the ring is stiff and of negligible radial size. As already said, a point on the ring is identified by its relative position ϑ_{rel} and the ring is not planar, i.e. the axial position of a point on it

is given by $x = x^0(\vartheta_{rel})$. It is assumed that the ring rotates at an average rotational speed $\omega_r = 2\pi f_r$ with superposed oscillations of the position given by $\vartheta_{ring}(t)$ that result in a rotational speed fluctuation $\dot{\vartheta}_{ring}(t)$. Then, the instantaneous absolute position ϑ_{abs} of the point identified by ϑ_{rel} is given by

$$\vartheta_{abs}(\vartheta_{rel}, t) = \vartheta_{rel} + \omega_r t + \vartheta_{ring}(t) \tag{4.18}$$

The rotational speed is measured by a stationary optical tachometer located at $\vartheta_{abs} = \vartheta_{tacho}$ that, ideally, emits a Dirac pulse $\delta(t - t_n)$ each time that a reflecting element is located at $\vartheta_{rel} = \vartheta_{refl}$ passes in front of the tachometer probe. This happens once per revolution, at the time $t = t_n$, $n = -\infty, \dots, -1,0,1, \dots, +\infty$; hence, a sequence

$$y(t) = \sum_{n=-\infty}^{+\infty} \delta(t - t_n) \tag{4.19}$$

is generated. If the rotational speed is constant, i.e. $\vartheta_{ring}(t) = 0$, the problem is trivial: the period of revolution is

$$T_r = \frac{1}{f_r} \tag{4.20}$$

and

$$t_n = nT_r \tag{4.21}$$

In case $\vartheta_{ring}(t) \neq 0$, one has to consider the instantaneous absolute position of the reflecting element:

$$\vartheta(t) = \vartheta_{abs}(\vartheta^0, t) = \vartheta_{refl} + \omega_r t + \vartheta_{ring}(t) \tag{4.22}$$

and a pulse is generated each time $t = t_n$ when $\vartheta(t) = \vartheta_{tacho} + 2\pi n$, that is

$$\vartheta_{tacho} = \vartheta_{refl} + \omega_r t + \vartheta_{ring}(t) - 2\pi n \tag{4.23}$$

For the sake of simplicity but without any loss of generality, one assumes that $\vartheta_{tacho}, \vartheta_{refl} = 0$. Then, t_n is the solution of the equation

$$\omega_r t_n + \vartheta_{ring}(t_n) - 2\pi n = 0 \tag{4.24}$$

It is also assumed that

$$\vartheta_{ring}(t) = \Theta \cos(2\pi f_\vartheta t + \phi) \tag{4.25}$$

with $\Theta \ll 2\pi$, under the assumption of small oscillations, and with f_ϑ being the frequency at which the rotor oscillates. Then, a transcendental equation in t_n yields

$$\omega_r t_n + \Theta \cos(2\pi f_\vartheta t_n + \phi) - 2\pi n = 0 \tag{4.26}$$

Then, one poses

$$t_n = nT_r + \Delta t_n \tag{4.27}$$

where, consistently with the small oscillation assumption, $\Delta t_n \ll T_r$ and $\Delta t_n \ll T_\vartheta = \frac{1}{f_\vartheta}$; this is a consequence of $\Theta \ll 2\pi$ and, overall, it means that the fluctuation in the period of revolution is small. Substituting in $\omega_r t_n$ and considering that $\omega_r T_r = 2\pi$, one obtains $\omega_r t_n = \omega_r(nT_r + \Delta t_n) = 2\pi n + \omega_r \Delta t_n = 2\pi n + 2\pi f_r \Delta t_n$. Then, the equation

$$2\pi n + 2\pi f_r \Delta t_n + \Theta \cos[2\pi f_\vartheta (nT_r + \Delta t_n) + \phi] - 2\pi n = 0 \tag{4.28}$$

yields whose solution is

$$\Delta t_n = -\frac{\Theta \cos[2\pi f_\vartheta (nT_r + \Delta t_n) + \phi]}{2\pi f_r} \tag{4.29}$$

but

$$\begin{aligned} &\cos[2\pi f_\vartheta (nT_r + \Delta t_n) + \phi] \\ &\qquad = \cos(2\pi f_\vartheta n T_r + \phi)\cos(2\pi f_\vartheta \Delta t_n) - \sin(2\pi f_\vartheta n T_r + \phi)\sin(2\pi f_\vartheta \Delta t_n) \end{aligned} \tag{4.30}$$

Having assumed that $\Delta t_n \ll T_r$ and $\Delta t_n \ll T_\vartheta$ allows writing

a) $$\cos[2\pi f_\vartheta (nT_r + \Delta t_n) + \phi] \cong \cos(2\pi f_\vartheta n T_r + \phi) - \sin(2\pi f_\vartheta n T_r + \phi) 2\pi f_\vartheta \Delta t_n \tag{4.31}$$

b) $$\cos[2\pi f_\vartheta (nT_r + \Delta t_n) + \phi] \cong \cos(2\pi f_\vartheta n T_r + \phi) \tag{4.32}$$

and hence

a) $\Delta t_n \cong -\frac{\cos(2\pi f_\vartheta n T_r+\phi)}{2\pi f_r}+\frac{f_\vartheta}{f_r}\sin(2\pi f_\vartheta n T_r+\phi)\Delta t_n$

$$\Delta t_n\left(1-\frac{f_\vartheta}{f_r}\sin(2\pi f_\vartheta n T_r+\phi)\right)\cong -\frac{\cos(2\pi f_\vartheta n T_r+\phi)}{2\pi f_r}$$

$$\Delta t_n \cong -\frac{1}{\left(1-\frac{f_\vartheta}{f_r}\sin(2\pi f_\vartheta n T_r+\phi)\right)}\frac{\cos(2\pi f_\vartheta n T_r+\phi)}{2\pi f_r} \tag{4.33}$$

b) $$\frac{f_\vartheta}{f_r}\ll 1\ \Delta t_n \cong -\frac{\Theta\cos(2\pi n f_\vartheta T_r+\phi)}{2\pi f_r} \tag{4.34}$$

Then (b)

$$t_n = nT_r+\Delta t_n =\cong nT_r-\frac{\Theta\cos(2\pi n f_\vartheta T_r+\phi)}{2\pi f_r}=T_r\left[n-\frac{\Theta\cos(2\pi n f_\vartheta T_r+\phi)}{2\pi}\right] \tag{4.35}$$

The Fourier transform of the signal $y(t)=\sum_{n=-\infty}^{+\infty}\delta(t-t_n)$ generated by the tachometer is

$$\tilde{y}(\omega)=\int_{-\infty}^{+\infty}\sum_{n=-\infty}^{+\infty}\delta(t-t_n)\exp(-i\omega t)\,dt=\sum_{n=-\infty}^{+\infty}\exp(-i\omega t_n)$$

$$=\sum_{n=-\infty}^{+\infty}\exp\left\{-i\omega T_r\left[n-\frac{\Theta\cos(2\pi n f_\vartheta T_r+\phi)}{2\pi}\right]\right\}$$

$$=\sum_{n=-\infty}^{+\infty}\exp(-i\omega n T_r)\exp\left\{i\omega T_r\left[\frac{\Theta\cos(2\pi n f_\vartheta T_r+\phi)}{2\pi}\right]\right\} \tag{4.36}$$

The Bessel series of $\exp(iB\cos(\beta))$ is

$$\exp[iB\cos(\beta)]=\sum_{k=-\infty}^{+\infty}i^k J_k(B)e^{ik\beta} \tag{4.37}$$

where $J_k(B)$ is the Bessel function of first kind and order k. Substituting $\exp\left\{i\omega T_r\left[\frac{\Theta\cos(2\pi n f_\vartheta T_r+\phi)}{2\pi}\right]\right\}$ to $\exp[iB\cos(\beta)]$, one obtains

$$\exp\left\{i\omega T_r\left[\frac{\Theta\cos(2\pi n f_\vartheta T_r+\phi)}{2\pi}\right]\right\}=\sum_{k=-\infty}^{+\infty}i^k J_k\left(\omega T_r\frac{\Theta}{2\pi}\right)\exp\big(ik(2\pi n f_\vartheta T_r+\phi)\big) \tag{4.38}$$

that yields

$$\tilde{y}(\omega) = \sum_{n=-\infty}^{+\infty}\left[\exp(-i\omega nT_r)\sum_{k=-\infty}^{+\infty} i^k J_k\left(\omega T_r\frac{\Theta}{2\pi}\right)\exp\big(ik(2\pi nf_\vartheta T_r+\phi)\big)\right]=$$

$$=\sum_{k=-\infty}^{+\infty}\left[i^k J_k\left(\omega T_r\frac{\Theta}{2\pi}\right)\sum_{n=-\infty}^{+\infty}\exp(-i\omega nT_r)\exp\big(ik(2\pi nf_\vartheta T_r+\phi)\big)\right]=$$

$$=\sum_{k=-\infty}^{+\infty}\left\{\left[i^k J_k\left(\omega T_r\frac{\Theta}{2\pi}\right)\exp(ik\phi)\right]\sum_{n=-\infty}^{+\infty}\exp[-i(\omega-k2\pi f_\vartheta)nT_r]\right\} \tag{4.39}$$

$\sum_{n=-\infty}^{+\infty}\exp[-i(\omega-k2\pi f_\vartheta)nT_r]$ may be further rearranged by means of the Poisson formula

$$\sum_{n=-\infty}^{+\infty}\exp(-i2\pi\alpha' nT_r)=\frac{1}{T_r}\sum_{n=-\infty}^{+\infty}\delta\left(\alpha'-\frac{n}{T_r}\right)=f_r\sum_{n=-\infty}^{+\infty}\delta(\alpha'-nf_r) \tag{4.40}$$

Where $2\pi\alpha'=(\omega-k2\pi f_\vartheta)$, i.e.

$$\sum_{n=-\infty}^{+\infty}\exp(-i\alpha nT_r)=\frac{1}{T_r}\sum_{n=-\infty}^{+\infty}\delta\left(\frac{\alpha}{2\pi}-\frac{n}{T_r}\right)=f_r\sum_{n=-\infty}^{+\infty}\delta\left(\frac{\alpha}{2\pi}-nf_r\right) \tag{4.41}$$

and posing $\omega-k2\pi f_\vartheta=\alpha$:

$$\begin{aligned}\sum_{n=-\infty}^{+\infty}\exp[-i(\omega-k2\pi f_\vartheta)nT_r] &= f_r\sum_{n=-\infty}^{+\infty}\delta\left(\frac{\omega-k2\pi f_\vartheta}{2\pi}-nf_r\right)\\ &= f_r\sum_{n=-\infty}^{+\infty}\delta\left(\frac{\omega}{2\pi}-(nf_r+kf_\vartheta)\right)\end{aligned} \tag{4.42}$$

Hence

$$\tilde{y}(\omega)=f_r\sum_{k=-\infty}^{+\infty}\left\{\left[J_k\left(\omega T_r\frac{\Theta}{2\pi}\right)\exp\left(ik\left(\phi+\frac{\pi}{2}\right)\right)\right]\sum_{n=-\infty}^{+\infty}\delta\left(\frac{\omega}{2\pi}-(nf_r+kf_\vartheta)\right)\right\} \tag{4.43}$$

This shows that

1) In case no rotational speed fluctuations take place ($\Theta=0$), the PSD of the tachometer signal contains peaks at the harmonics of f_r only (e.g. $\pm f_r$, $\pm 2f_r$,..., nf_r), and

2) in case of rotational speed fluctuations ($\Theta, f_\vartheta \neq 0$), beside peaks at the harmonics of f_r, side peaks appear at a frequency shifted of the harmonics of f_ϑ (e.g. $\pm f_r$, $\pm(f_r \pm f_\vartheta)$, $\pm(f_r \pm 2f_\vartheta)$, $\pm(2f_r \pm f_\vartheta)$, $\pm(2f_r \pm 2f_\vartheta)$,..., $nf_r + kf_\vartheta$). This is a typical effect of frequency modulation.

Proof:

1) In case no rotational speed fluctuations take place ($\Theta = 0$)

$$J_k\left(\omega T_r \frac{\Theta}{2\pi}\right) = J_k(0) = \begin{cases} 1 & k = 0 \\ 0 & k \neq 0 \end{cases} \tag{4.44}$$

hence, only the term with $k = 0$ is not null and the summation reduces to:

$$\begin{aligned} &\sum_{k=-\infty}^{+\infty} \left\{ \left[J_k\left(\omega T_r \frac{\Theta}{2\pi}\right) \exp\left(ik\left(\phi + \frac{\pi}{2}\right)\right)\right] \sum_{n=-\infty}^{+\infty} \delta\left(\frac{\omega}{2\pi} - (nf_r + kf_\vartheta)\right)\right\} \\ &\qquad = J_0(0)\exp(0) \sum_{n=-\infty}^{+\infty} \delta\left(\frac{\omega}{2\pi} - (nf_r + 0f_\vartheta)\right) = \sum_{n=-\infty}^{+\infty} \delta\left(\frac{\omega}{2\pi} - nf_r\right) \end{aligned} \tag{4.45}$$

which shows that only harmonics of f_r are present.

2) in case of rotational speed fluctuations ($\Theta, f_\vartheta \neq 0$), the Dirac pulse centered at $\omega = 2\pi(nf_r + kf_\vartheta)$ (i.e. at all of the harmonics of f_r and shifted of all of the harmonics of f_ϑ) is multiplied by, i.e. weighted by, the Bessel function $J_k\left(\omega T_r \frac{\Theta}{2\pi}\right)$ computed in

$$\omega T_r \frac{\Theta}{2\pi} = 2\pi(nf_r + kf_\vartheta)T_r \frac{\Theta}{2\pi} = (nf_r + kf_\vartheta)T_r\Theta = (n + kf_\vartheta T_r)\Theta = \left(n + k\frac{T_r}{T_\vartheta}\right)\Theta \tag{4.46}$$

In order to evaluate the effect of the Bessel function weighting, three properties are of interest: (1) $|J_k(x)| < 1$ for any x, (2) for any $x < 1.5$, $|J_k(x)|$ is strongly decreasing with k and (3) $J_k(x)$ has an oscillating trend with an envelope decreasing as $x^{-\frac{1}{2}}$.

In the present case, the oscillation is small, i.e. $\Theta \ll 1$, and $f_\vartheta = f_v$ with $f_v \cong \frac{1}{6} f_r$ ($f_r = 44\ Hz$ and $f_v = 7.5\ Hz$). Hence, $\frac{T_r}{T_\vartheta} = \frac{f_v}{f_r} \cong \frac{1}{6}$ and $\left(n + k\frac{T_r}{T_\vartheta}\right)\Theta \ll 1$ at low values of n and k. As a result, the side peaks' height is expected to decrease quickly.

The presence of side peaks with a frequency shift of f_v in the PSD of the tachometer signal constitutes the evidence of the rotational speed fluctuation at $\omega_v = 2\pi f_v$.

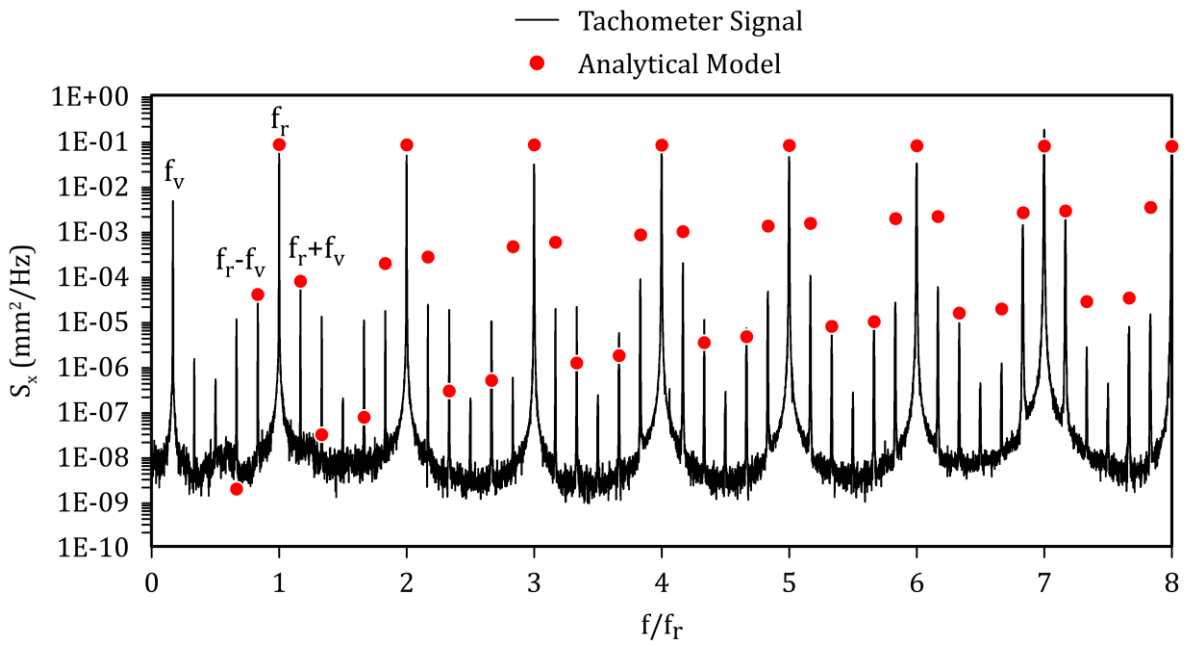

Figure 4.27. Analytic model for the side peaks compares to the experimental Tachometer signal (point A7 of Fig. 4.13).

A numerical model based on Eq. 4.43 has been calculated for the present model by considering $k = -2, \ldots, 2$, then the results are compared with the experimental tachometer signal (point A7 of Fig. 4.13) in Fig. 4.27.

Assuming that the ring is stiff and considering that $\vartheta_{abs}(\vartheta_{rel}, t) = \vartheta_{rel} + \omega_r t + \vartheta_{ring}(t)$, the instantaneous position of the point of the ring that is in front of the vibrometer, i.e. the vibrometer signal, is given by

$$x^0_{ring}(t) = x^0\left(\vartheta_{vibro} - 2\pi f_r t - \vartheta_{ring}(t)\right) \tag{4.47}$$

$x^0(\vartheta_{rel})$ may be expressed in terms of the Fourier series:

$$x^0(\vartheta_{rel}) = \sum_{n=-\infty}^{\infty} \tilde{x}^0_n \exp(in\vartheta_{rel}) = \sum_{n=-\infty}^{\infty} \tilde{x}^0_n \exp\left[in\left(\vartheta_{vibro} - 2\pi f_r t - \vartheta_{ring}(t)\right)\right] \tag{4.48}$$

Recalling that $\vartheta_{ring}(t) = \Theta\cos(2\pi f_v t + \phi)$ yields

$$x^0_{ring}(t) = \sum_{n=-\infty}^{\infty} \tilde{x}^0_n \exp\{in[\vartheta_{vibro} - 2\pi f_r t - \Theta\cos(2\pi f_v t + \phi)]\}$$
$$= \sum_{n=-\infty}^{\infty} \tilde{x}^0_n \exp\{in[\vartheta_{vibro} - 2\pi f_r t]\} \exp[in\Theta\cos(2\pi f_v t + \phi)] \quad (4.49)$$

Based on the Bessel series expansion, $\exp[in\Theta\cos(2\pi f_v t + \phi)]$ may be expressed as

$$\exp[in\cos(2\pi f_v t + \phi)] = \sum_{k=-\infty}^{+\infty} i^k J_k(n) e^{ik(2\pi f_v t + \phi)} \quad (4.50)$$

which justifies the presence of side peaks in the vibrometer signal generated by a non-planar ring that rotates at the rotational speed $2\pi f_r$ with a superposed precession motion at $f = f_v$.

4.5.3. Kinematic analysis of the flow field

As the rotor rotates at the average rotational speed $\omega_r = 2\pi f_r$, absolute and relative angular coordinates are related by

$$\vartheta_{abs} = \vartheta_{rel} + \omega_r t = \vartheta_{rel} + 2\pi f_r t \quad (4.51)$$

Then, the instantaneous position of the $m-th$ blade tip in the absolute frame is $\vartheta_{abs,m}(t) = \vartheta^0_m + \omega_r t + \vartheta_m(t)$ where $\vartheta_m(t)$ accounts for possible rotational speed fluctuations associated with the vibration. As the ring connecting the blade tips is very stiff, it is assumed that, for low-order modes such as the studied one, $\vartheta_m(t)$ is independent of the blade. Hence $\vartheta_m(t) = \vartheta_{ring}(t)$ and

$$\vartheta_{abs,m}(t) = \vartheta^0_m + \omega_r t + \vartheta_{ring}(t) \quad (4.52)$$

This also means that the instantaneous angular speed $\dot{\vartheta}_{abs,m}(t)$ of each blade is the same. It is also assumed that the blades are subjected to an external action, typically an aerodynamic thrust, that is the origin of the vibration. It is related to a perturbation $\mathbf{v}'(\vartheta_{abs}, t)$ of the absolute velocity $\mathbf{v}$ at the gap outlet/rotor inlet that, in the absolute frame, rotates at an angular speed $\omega_v = -2\pi f_v$ (a stationary disturbance, e.g. the wake from an upstream strut or a stator blade, would be characterized by $\omega_v = 0$). In turn, the periodic variation of the gap geometry results in a fluctuation $\mathbf{v}'$ synchronous with the vibration. The observed vibration is a one-nodal-diameter counter-rotating mode of frequency $f_v \cong 7.5$ Hz that results in an axial displacement $x(\vartheta_{abs}, t)$ of the ring given by

$$x(\vartheta_{abs}, t) = x(\vartheta_{abs} + 2\pi f_v t) = x^0 + \Delta x \cos(\vartheta_{abs} + 2\pi f_v t + \varphi_x) \tag{4.53}$$

with x^0 the average axial position that depends on the blade loading and centrifugal force (in the following, it is posed $x^0 = \tilde{x}_0^0$), but might be considered constant in the present analysis. In fact, the molding process yields a non-perfectly planar ring; hence

$$x^0 = x^0(\vartheta_{rel}) = \sum_{n=-\infty}^{\infty} \tilde{x}_n^0 \exp(in\vartheta_{rel}) \tag{4.54}$$

which, in the absolute frame, becomes

$$x^0(\vartheta_{abs}, t) = \sum_{n=-\infty}^{\infty} \tilde{x}_n^0 \exp\left[in\left(\vartheta_{abs} - 2\pi f_r t - \vartheta_{ring}(t)\right)\right] \tag{4.55}$$

as the instantaneous angular position of a point of the ring is given by $\vartheta_{abs} = \vartheta_{rel} + 2\pi f_r t + \vartheta_{ring}(t)$. Thus, the instantaneous position observed by a stationary sensor should be given by

$$x(\vartheta_{abs}, t) = x^0(\vartheta_{abs}, t) + \Delta x \cos(\vartheta_{abs} + 2\pi f_v t + \varphi_x) \tag{4.56}$$

that is

$$x(\vartheta_{abs}, t) = \sum_{n=-\infty}^{\infty} \tilde{x}_n^0 \exp\left[in\left(\vartheta_{abs} - 2\pi f_r t - \vartheta_{ring}(t)\right)\right] + \Delta x \cos(\vartheta_{abs} + 2\pi f_v t + \varphi_x) \tag{4.57}$$

For the moment, the non-planarity of the ring is neglected, i.e. $\tilde{x}_n^0 = 0$ for any $n \neq 0$ and $\tilde{x}_0^0$ depends on blade loading and centrifugal force only:

$$x(\vartheta_{abs}, t) = \tilde{x}_0^0 + \Delta x \cos(\vartheta_{abs} + 2\pi f_v t + \varphi_x) \tag{4.58}$$

However, it seems useful to disclose that rotational speed fluctuations due to the vibration may result in a modulation of $x(\vartheta_{abs}, t)$, i.e. in the appearance of a complicated and unexpected pattern of the PSD of $x(\vartheta_{abs}, t)$.

$\mathbf{v}'(\vartheta_{abs}, t)$ has to be consistent with the vibration and it could be assumed that $|\mathbf{v}'(\vartheta_{abs}, t)| \propto \cos(\vartheta_{abs} + 2\pi f_v t)$. However, the non-linearity of the relation between velocity and gap size suggests that the harmonics of $\vartheta_{abs} + 2\pi f_v t$ may be present in the $\mathbf{v}'$ expression although $x(\vartheta_{abs}, t)$ only contains the fundamental one.

$\mathbf{v}'$ is superposed to the time-averaged absolute velocity vector $\mathbf{v^0}(\vartheta_{abs})$ that is steady in the absolute frame:

$$\mathbf{v}(\vartheta_{abs}, t) = \mathbf{v^0}(\vartheta_{abs}) + \mathbf{v}'(\vartheta_{abs}, t) \tag{4.59}$$

although present, the dependence on r is neglected as it is not involved in the present analysis. The most general structure for $\mathbf{v^0}$ is given by

$$\mathbf{v^0}(\vartheta_{abs}) = \sum_{n=-\infty}^{\infty} \tilde{\mathbf{v}}_{\boldsymbol{n}}^{\mathbf{0}} \exp(in\vartheta_{abs}) \tag{4.60}$$

In order to be consistent with the observed mode of vibration, the most general structure for $\mathbf{v}'$ is given by a regressive wave (i.e. counter-rotating) propagating at the angular speed $-2\pi f_v$ in the absolute frame:

$$\mathbf{v}'(\vartheta_{abs}, t) = \mathbf{v}'(\vartheta_{abs} + 2\pi f_v t) = \sum_{n=-\infty}^{\infty} \tilde{\mathbf{v}}_{\boldsymbol{n}}' \exp[in(\vartheta_{abs} + 2\pi f_v t)] \tag{4.61}$$

with $\tilde{\mathbf{v}}_{\mathbf{0}}' = \mathbf{0}$.

Neglecting the blade velocity fluctuation $\vartheta_{ring}(t)$ and considering that $\vartheta_{abs} = \vartheta_{rel} + 2\pi f_r t$, the following structure results for $\mathbf{v^0}$ in the relative frame:

$$\mathbf{v^0}(\vartheta_{rel}, t) = \mathbf{v^0}(\vartheta_{rel} + 2\pi f_r t) = \sum_{n=-\infty}^{\infty} \tilde{\mathbf{v}}_{\boldsymbol{n}}^{\mathbf{0}} \exp[in(\vartheta_{rel} + 2\pi f_r t)] \tag{4.62}$$

the dependence on $\vartheta_{rel} + 2\pi f_r t$ shows that a disturbance that is steady in the absolute frame results in a regressive wave in the relative one, i.e. that it propagates at a negative angular speed $-2\pi f_r$. It may excite the rotor at all of the rotational frequency harmonics nf_r. Hence, as expected, steady disturbances may not excite subharmonic vibrations.

As for $\mathbf{v}'$, in the relative frame (i.e. substituting $\vartheta_{abs} = \vartheta_{rel} + 2\pi f_r t$) one obtains

$$\begin{aligned}\mathbf{v}'(\vartheta_{rel},t) &= \sum_{n=-\infty}^{\infty} \tilde{\mathbf{v}}'_{\boldsymbol{n}} \exp\{in[(\vartheta_{rel}+2\pi f_r t)+2\pi f_v t]\} \\ &= \sum_{n=-\infty}^{\infty} \tilde{\mathbf{v}}'_{\boldsymbol{n}} \exp\{in[\vartheta_{rel}+2\pi(f_r+f_v)t]\}\end{aligned} \tag{4.63}$$

which shows that, in the relative frame, a perturbation counter rotating at the angular speed $-2\pi f_p$ with $f_p = f_r + f_v$ is present:

$$\mathbf{v}'(\vartheta_{rel},t) = \sum_{n=-\infty}^{\infty} \tilde{\mathbf{v}}'_{\boldsymbol{n}} \exp\big[in\big(\vartheta_{rel}+2\pi f_p t\big)\big] \tag{4.64}$$

this indicates that, in the relative frame, the perturbation is co-rotating resulting in excitation at a frequency $f_p > f_v$; e.g., at the speed of 2640 rev/min that corresponds to $f_r = 44$ Hz, the frequency of the disturbance is $f_p \cong 51.5$ Hz. The combination of the two motions (rotation of both blades and flow structures) may result in a modulation of the excitation.

Based on such a model of the rotor inlet flow, a model has to be developed for the aerodynamic excitation of the blades. As the blade thrust is related to the relative velocity $\mathbf{w}$, the flow has to be observed from the relative system, i.e. the perturbation $\mathbf{w}'(\vartheta_{rel},t)$ has to be determined based on the fundamental kinematic relation

$$\mathbf{v} = \mathbf{w} + \mathbf{u} \tag{4.65}$$

where $\mathbf{u} = \mathbf{u^0} + \mathbf{u}'$ is the instantaneous blade velocity, $\mathbf{u^0}$ being the time average blade speed

$$\mathbf{u^0} = \mathbf{r} \times \boldsymbol{\omega}_{\boldsymbol{r}}^{\mathbf{0}} = u^0 \mathbf{e}_{\boldsymbol{\vartheta}} = \omega_r r_0 \mathbf{e}_{\boldsymbol{\vartheta}} = 2\pi f_r r_0 \mathbf{e}_{\boldsymbol{\vartheta}} \tag{4.66}$$

that yields the instantaneous mean relative velocity

$$\mathbf{w^0}(\vartheta_{rel},t) = \mathbf{v^0}(\vartheta_{rel},t) - \mathbf{u^0} = \sum_{n=-\infty}^{\infty} \tilde{\mathbf{v}}_{\boldsymbol{n}}^{\mathbf{0}} \exp[in(\vartheta_{rel}+2\pi f_r t)] - 2\pi f_r r_0 \mathbf{e}_{\boldsymbol{\vartheta}} \tag{4.67}$$

For the sake of simplicity, it has been assumed that the involved part of the blade is the blade tip region at a radius $r_0 \cong r_{tip}$, since the leakage flow is restricted to that zone.

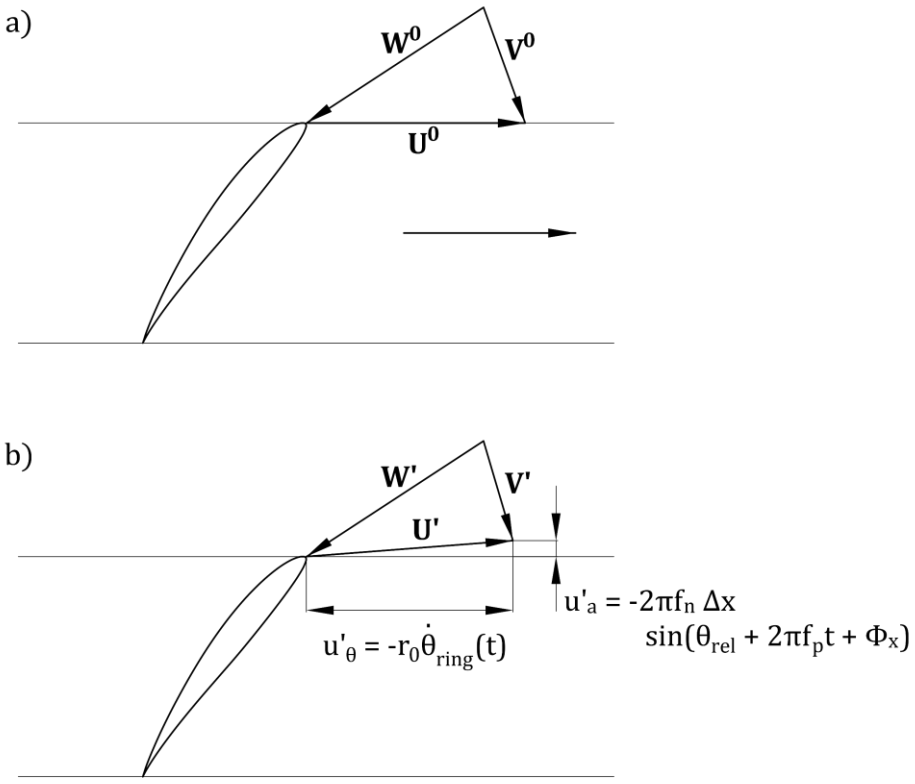

Figure 4.28. Velocity triangles. a) steady condition. b) vibration.

Opposite to $\mathbf{u^0}$, not only the fluctuating blade velocity $\mathbf{u}'$ has a tangential component, but it also has an axial one. For low order vibrations, the ring is very stiff, then it may be assumed that the tangential component of $\mathbf{u}'$ is independent of ϑ_{rel} and equals $r_0\dot{\vartheta}_{ring}(t)$. Being the positive direction for the rotor displacement opposite to the axial component v_a of the flow velocity, the ring vibration results in an axial component of the blade velocity $\mathbf{u}'$ given by $-\dot{x}(\vartheta_{abs}, t) = -[-2\pi f_v \Delta x \sin(\vartheta_{abs} + 2\pi f_v t + \varphi_x)]$. (Notice that with a 5-mm-amplitude of the vibration ($\Delta x = 5$ mm), the maximum axial velocity fluctuation is $2\pi f_v \Delta x = 2\pi \times 7.5 \times\ 5 \cdot 10^{-3} \cong 0.24$ m/s, i.e. about 2.5% of the mean axial velocity of the flow at the design operating point, an order of magnitude not negligible even under the small oscillation assumption.) Hence

$$\mathbf{u}'(\vartheta_{abs}, t) = 2\pi f_v \Delta x \sin(\vartheta_{abs} + 2\pi f_v t + \varphi_x)\mathbf{e}_{\boldsymbol{a}} + r_0\dot{\vartheta}_{ring}(t)\mathbf{e}_{\boldsymbol{\vartheta}} \tag{4.68}$$

And

$$\mathbf{u}'(\vartheta_{rel}, t) = 2\pi f_v \Delta x \sin[(\vartheta_{rel} + 2\pi f_r t) + 2\pi f_v t + \varphi_x]\mathbf{e}_{\boldsymbol{a}} + r_0\dot{\vartheta}_{ring}(t)\mathbf{e}_{\boldsymbol{\vartheta}} \tag{4.69}$$

i.e.

$$\mathbf{u}'(\vartheta_{rel},t) = 2\pi f_v \Delta x \sin\left(\vartheta_{rel} + 2\pi f_p t + \varphi_x\right)\mathbf{e}_{\boldsymbol{a}} + r_0\dot{\vartheta}_{ring}(t)\mathbf{e}_{\boldsymbol{\vartheta}} \tag{4.70}$$

Then, the instantaneous perturbation sensed by the rotor in the relative frame is given by

$$\mathbf{w}'(\vartheta_{rel},t) = \mathbf{v}'(\vartheta_{rel},t) - \mathbf{u}'(\vartheta_{rel},t) \tag{4.71}$$

i.e.

$$\begin{aligned}\mathbf{w}'(\vartheta_{rel},t) = &\sum_{n=-\infty}^{\infty} \tilde{\mathbf{v}}'_{\boldsymbol{n}} \exp\left[in\left(\vartheta_{rel} + 2\pi f_p t\right)\right] \\ &- 2\pi f_v \Delta x \sin\left(\vartheta_{rel} + 2\pi f_p t + \varphi_x\right)\mathbf{e}_{\boldsymbol{a}} - r_0\dot{\vartheta}_{ring}(t)\mathbf{e}_{\boldsymbol{\vartheta}}\end{aligned} \tag{4.72}$$

This indicates that the instantaneous blade thrust contains the harmonics of $f_p = f_r + f_v$ (it may be expected that the fundamental harmonic provides the major contribution, i.e. only $n = -1$ and 1 are relevant) and it may also be influenced by the rotor speed fluctuations, fluctuations $r_0\dot{\vartheta}_{ring}(t)$.

$\mathbf{v}'$ fluctuations at f_v in the absolute frame are a necessary consequence of the observed vibration and have also been observed experimentally; fluctuations at f_p in the relative frame are a kinematic consequence. The structure of $\dot{\vartheta}_{ring}(t)$ is unknown at the present level of discussion, but the presence of modulation (side peaks) in the PSD of the measured rotational speed indicates that fluctuations at f_v are present.

4.5.4. Dynamic analysis

Due to the angular distance between the blades, there is a time delay τ_m between the force $\mathbf{F}_m(t)$ acting on the $m-th$ blade and $\mathbf{F}_1(t) = \mathbf{F}(t)$, the force that acts on blade 1:

$$\mathbf{F}_m(t) = \mathbf{F}_1(t-\tau_m) = \mathbf{F}(t-\tau_m) \tag{4.73}$$

With

$$\tau_m = \frac{\vartheta_1^0 - \vartheta_m^0}{2\pi f_p} = -\frac{\vartheta_m^0}{2\pi f_p} \tag{4.74}$$

$\tau_m < 0$ as $\vartheta_1 = 0$ and $\vartheta_{z_R} > \vartheta_{z_R-1} > \cdots > \vartheta_2 > \vartheta_1$; $\tau_m < 0$ is also in agreement with the fact that blades with larger m encounter the disturbance earlier.

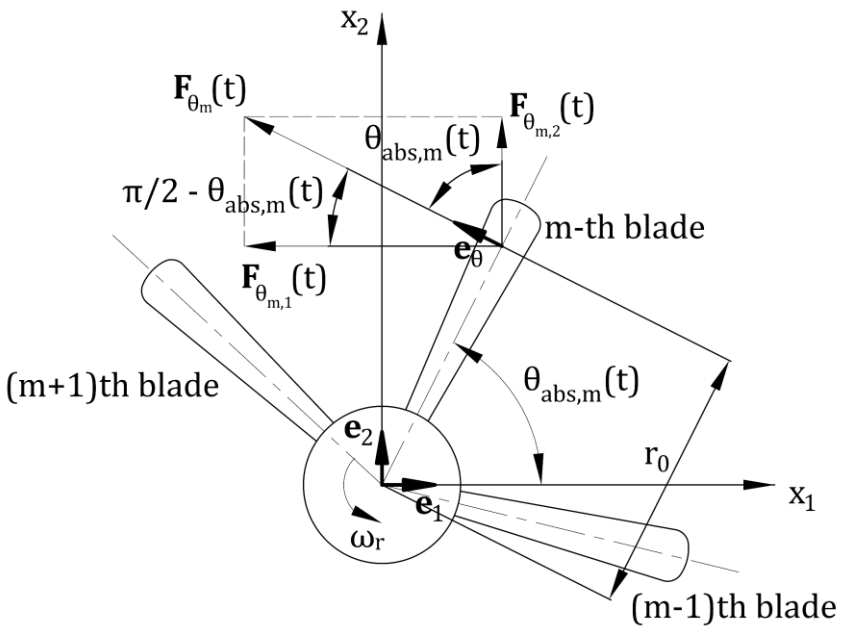

Figure 4.29. Blade forces.

The **F** components $F_a(t)$, axial, $F_\vartheta(t)$, tangential, and $F_r(t)$, radial, have the same frequency content as the relative velocity disturbance $\mathbf{w}'(\vartheta_{rel}, t)$. Neglecting for the moment the term $r_0\dot{\vartheta}_{ring}(t)$ that is unknown at the present level of the discussion, they may be expressed in terms of the Fourier series of unknown coefficients $\tilde{F}_{a_n}$ and $\tilde{F}_{\vartheta_n}$:

$$F_{\vartheta_1}(t) = F_\vartheta(t) = \sum_{n=-\infty}^{\infty} \tilde{F}_{\vartheta_n} \exp\left(i2\pi n f_p t\right) \tag{4.75}$$

For the $m-th$ blade, one obtains

$$F_{\vartheta_m}(t) = F_{\vartheta_1}(t-\tau_m) = F_\vartheta(t-\tau_m) = \sum_{n=-\infty}^{\infty} \tilde{F}_{\vartheta_n} \exp\left[i2\pi n f_p (t-\tau_m)\right] \tag{4.76}$$

Considering that $\tau_m = -\frac{\vartheta_m^0}{2\pi f_p}$ yields

$$F_{\vartheta_m}(t) = \sum_{n=-\infty}^{\infty} \tilde{F}_{\vartheta_n} \exp\left[i2\pi n f_p \left(t + \frac{\vartheta_m^0}{2\pi f_p}\right)\right] = \sum_{n=-\infty}^{\infty} \tilde{F}_{\vartheta_n} \exp\left(i2\pi n f_p t + in\vartheta_m^0\right) \tag{4.77}$$

And

$$F_{a_m}(t) = \sum_{n=-\infty}^{\infty} \tilde{F}_{a_n} \exp\left(i2\pi n f_p t + in\vartheta_m^0\right) \tag{4.78}$$

(An analogous expression yields for $F_r(t)$, which is usually negligible for axial rotors, and is thus not considered.) The further step consists in highlighting the main features of the excitations (forces acting on each blade and forces and related moments transmitted to the shaft and to the casing).

4.5.4.1. Resultant axial component of the blade force

The summation of the axial forces due to all of the blades yields a resultant force $F_a(t)$ that apparently has a fundamental frequency f_p. However, such a summation shows that, although the force acting on each blade is the same, some harmonics may be canceled (as the fundamental one) and other ones may be amplified (e.g. the blade passing frequency one) due to the time delay between forces acting on different blades.

$$\begin{aligned} F_a(t) = \sum_{m=1}^{z_R} F_{a_m}(t) &= \sum_{m=1}^{z_R} \left[\sum_{n=-\infty}^{\infty} \tilde{F}_{a_n} \exp\left(i2\pi n f_p t + in\vartheta_m^0\right) \right] \\ &= \sum_{n=-\infty}^{\infty} \left[\tilde{F}_{a_n} \exp\left(i2\pi n f_p t\right) \sum_{m=1}^{z_R} \exp\left(in\vartheta_m^0\right) \right] \end{aligned} \tag{4.79}$$

that is

$$F_a(t) = \sum_{n=-\infty}^{\infty} \left[\tilde{F}_{a_n} \exp\left(i2\pi n f_p t\right) F_{int}(n) \right] \tag{4.80}$$

The property that $F_{int}(1) = 0$ for statically balanced rotors, implies that no axial force fluctuation may be present at $f = f_p$ $(n = 1)$, no matter whether the rotor is evenly spaced or not. The property that $F_{int}(kz_R)$ is large for mildly unevenly spaced rotors shows that the axial force fluctuation should mainly excite the rotor and the casing at $z_R f_p$ and higher harmonics, which in the present case are rather large (as z_R=7, important vibration may be expected at 7×51.4 Hz ≅ 360 Hz and 14×51.4 Hz ≅ 720 Hz). On the contrary, the contribution at the lower f_p harmonics should be negligible, see the interference function plot.

4.5.4.2. Resultant torque due to the axial force

This component of the torque is a vector $\mathbf{M}_m(t)$ that lays in the rotational plane. For the sake of simplicity, it may be assumed that $F_{a_m}(t)$ is applied in the blade tip region at a radius $r_0 \cong r_{tip}$, since the leakage flow is restricted to that zone. The instantaneous point of application on the $m-th$ blade is given by the vector

$$\begin{aligned}\mathbf{r}_m(\mathrm{t}) &= r_0\left[\mathbf{e}_1 \cos\vartheta_{abs,m}(t) + \mathbf{e}_2 \sin\vartheta_{abs,m}(t)\right] \\ &= r_0[\mathbf{e}_1 \cos(\vartheta_m^0 + \omega_r t) + \mathbf{e}_2 \sin(\vartheta_m^0 + \omega_r t)]\end{aligned} \tag{4.81}$$

and the $m-th$ blade yields a torque

$$\mathbf{M}_m(t) = \mathbf{r}_m(\mathrm{t}) \times \mathbf{e}_3 F_{a_m}(t) \tag{4.82}$$

as the line of action of $F_{a_m}(t)$ is parallel to the rotational axis x_3. Hence

$$\begin{aligned}&\mathbf{M}_m(t) = r_0[\mathbf{e}_1 \cos(\vartheta_m^0 + \omega_r t) + \mathbf{e}_2 \sin(\vartheta_m^0 + \omega_r t)] \times \mathbf{e}_3 F_{a_m}(t) = \\ &= r_0[\mathbf{e}_1 \times \mathbf{e}_3 \cos(\vartheta_m^0 + 2\pi f_r t) + \mathbf{e}_2 \times \mathbf{e}_3 \sin(\vartheta_m^0 + 2\pi f_r t)]F_{a_m}(t) = \\ &= r_0[-\mathbf{e}_2 \cos(\vartheta_m^0 + 2\pi f_r t) + \mathbf{e}_1 \sin(\vartheta_m^0 + 2\pi f_r t)]F_{a_m}(t)\end{aligned} \tag{4.83}$$

Then the resultant torque is given by

$$\mathbf{M}(t) = \sum_{m=1}^{z_R} \mathbf{M}_m(t) =$$

$$= \sum_{m=1}^{z_R} r_0 F_{a_m}(t)[-\mathbf{e}_2 \cos(\vartheta_m^0 + 2\pi f_r t) + \mathbf{e}_1 \sin(\vartheta_m^0 + 2\pi f_r \omega_r t)] \tag{4.84}$$

It is necessary to analyze the terms $\sum_{m=1}^{z_R} F_{a_m}(t) \cos(\vartheta_m^0 + 2\pi f_r t)$ and $\sum_{m=1}^{z_R} F_{a_m}(t) \sin(\vartheta_m^0 + 2\pi f_r t)$:

$$\sum_{m=1}^{z_R} F_{a_m}(t) \cos(\vartheta_m^0 + 2\pi f_r t) = \sum_{m=1}^{z_R} \left[\sum_{n=-\infty}^{\infty} \tilde{F}_{a_n} \exp\left(i2\pi n f_p t + in\vartheta_m^0\right) \cos(\vartheta_m^0 + 2\pi f_r t) \right] =$$

$$= \sum_{m=1}^{z_R} \left[\sum_{n=-\infty}^{\infty} \tilde{F}_{a_n} \exp\left(i2\pi n f_p t\right) \exp(in\vartheta_m^0) \cos(\vartheta_m^0 + 2\pi f_r t) \right] =$$

$$= \sum_{n=-\infty}^{\infty} \tilde{F}_{a_n} \left[\sum_{m=1}^{z_R} \exp\left(i2\pi n f_p t\right) \exp(in\vartheta_m^0) \frac{\exp\left(i(\vartheta_m^0 + 2\pi f_r t)\right) + \exp\left(-i(\vartheta_m^0 + 2\pi f_r t)\right)}{2} \right] =$$

$$= \sum_{n=-\infty}^{\infty} \frac{\tilde{F}_{a_n}}{2} \left[\sum_{m=1}^{z_R} \exp\left(i2\pi n f_p t\right) \exp(in\vartheta_m^0) \exp\left(i(\vartheta_m^0 + 2\pi f_r t)\right) \right.$$

$$\left. + \exp\left(i2\pi n f_p t\right) \exp(in\vartheta_m^0) \exp\left(-i(\vartheta_m^0 + 2\pi f_r t)\right) \right] =$$

$$= \sum_{n=-\infty}^{\infty} \frac{\tilde{F}_{a_n}}{2} \left\{ \sum_{m=1}^{z_R} \exp\left[i2\pi\left(n f_p + f_r\right)t\right] \exp[i(n+1)\vartheta_m^0] + \exp\left[i2\pi\left(n f_p - f_r\right)t\right] \exp[i(n-1)\vartheta_m^0] \right\} =$$

$$= \sum_{n=-\infty}^{\infty} \frac{\tilde{F}_{a_n}}{2} \left\{ \exp\left[i2\pi\left(n f_p + f_r\right)t\right] \sum_{m=1}^{z_R} \exp[i(n+1)\vartheta_m^0] + \exp\left[i2\pi\left(n f_p - f_r\right)t\right] \sum_{m=1}^{z_R} \exp[i(n-1)\vartheta_m^0] \right\}$$

$$=$$

$$= \sum_{n=-\infty}^{\infty} \frac{\tilde{F}_{a_n}}{2} \left\{ \exp\left[i2\pi\left(n f_p + f_r\right)t\right] F_{int}(n+1) + \exp\left[i2\pi\left(n f_p - f_r\right)t\right] F_{int}(n-1) \right\}$$

$$\sum_{m=1}^{z_R} F_{a_m}(t) \sin(\vartheta_m^0 + 2\pi f_r t) = \sum_{m=1}^{z_R} \left[\sum_{n=-\infty}^{\infty} \tilde{F}_{a_n} \exp\left(i2\pi n f_p t + in\vartheta_m^0\right) \sin(\vartheta_m^0 + 2\pi f_r t) \right] =$$

$$= \sum_{m=1}^{z_R} \left[\sum_{n=-\infty}^{\infty} \tilde{F}_{a_n} \exp\left(i2\pi n f_p t\right) \exp(in\vartheta_m^0) \sin(\vartheta_m^0 + 2\pi f_r t) \right] =$$

$$= \sum_{n=-\infty}^{\infty} \tilde{F}_{a_n} \left[\sum_{m=1}^{z_R} \exp\left(i2\pi n f_p t\right) \exp(in\vartheta_m^0) \frac{\exp\left(i(\vartheta_m^0 + 2\pi f_r t)\right) - \exp\left(-i(\vartheta_m^0 + 2\pi f_r t)\right)}{2i} \right] =$$

$$= \sum_{n=-\infty}^{\infty} \frac{\tilde{F}_{a_n}}{2i} \left[\sum_{m=1}^{z_R} \exp\left(i2\pi n f_p t\right) \exp(in\vartheta_m^0) \exp\left(i(\vartheta_m^0 + 2\pi f_r t)\right) \right.$$

$$\left. - \exp\left(i2\pi n f_p t\right) \exp(in\vartheta_m^0) \exp\left(-i(\vartheta_m^0 + 2\pi f_r t)\right) \right] =$$

$$= \sum_{n=-\infty}^{\infty} \frac{\tilde{F}_{a_n}}{2i} \left\{ \sum_{m=1}^{z_R} \exp\left[i2\pi\left(n f_p + f_r\right)t\right] \exp[i(n+1)\vartheta_m^0] - \exp\left[i2\pi\left(n f_p - f_r\right)t\right] \exp[i(n-1)\vartheta_m^0] \right\} =$$

$$= \sum_{n=-\infty}^{\infty} \frac{\tilde{F}_{a_n}}{2i} \left\{ \exp\left[i2\pi\left(nf_p + f_r\right)t\right] \sum_{m=1}^{z_R} \exp[i(n+1)\vartheta_m^0] - \exp\left[i2\pi\left(nf_p - f_r\right)t\right] \sum_{m=1}^{z_R} \exp[i(n-1)\vartheta_m^0] \right\}$$

$$=$$

$$= \sum_{n=-\infty}^{\infty} \frac{\tilde{F}_{a_n}}{2i} \left\{ \exp\left[i2\pi\left(nf_p + f_r\right)t\right] F_{int}(n+1) - \exp\left[i2\pi\left(nf_p - f_r\right)t\right] F_{int}(n-1) \right\} \qquad (4.85)$$

The interesting feature of the obtained expressions is that the Fourier component $\tilde{F}_{a_n}$ at harmonic order n and oscillating at $f = nf_p$, results in excitation at frequencies shifted of $\pm f_r$, that is at $f = nf_p \pm f_r = (n \pm 1)f_r + nf_v$. Furthermore, the presence of the interference function $F_{int}(n \pm 1)$, shifted of ± 1, may have any consequence, e.g. leading to full cancellation (case $n = 0$, $F_{int}(\pm 1) = 0$) or to a strong amplification case $n = \pm 1$, $F_{int}(n \mp 1) = F_{int}(0) = z_R$. Limiting the analysis to the most important components, i.e. to $\tilde{F}_{a_0}$ and the pair $\tilde{F}_{a_{-1}}$ and $\tilde{F}_{a_1}$, it results that:

1. $\tilde{F}_{a_0}$, the steady axial force ($n = 0$), does not result in any torque in the rotational plane. This is a consequence of the fact that it is multiplied by $F_{int}(n \pm 1) = F_{int}(\pm 1)$ that is null as the rotor is statically balanced. In other terms, the system of (steady) forces results in a null torque on the rotor shaft.
2. $\tilde{F}_{a_1}$, the component at the fundamental frequency ($n = 1$), results in torques at $f = f_p + f_r = 2f_r + f_v$ (about 95.5 Hz) and at $f = f_p - f_r = f_v$ (about 7.5 Hz).

   From the plot of $F_{int}(n, \vartheta_m^0)$, one finds that the torque component at $f = 2f_r + f_v$ is small since it is multiplied by $F_{int}(n+1) = F_{int}(2)$, which is small as $|F_{int}(2)| \cong 0.15$; on the contrary, the component at $f = f_v$ is relevant because it is multiplied by $F_{int}(n-1) = F_{int}(0) = z_R$, which is the largest $F_{int}(n, \vartheta_m^0)$ value.

3. $\tilde{F}_{a_{-1}}$, the other component at the fundamental frequency ($n = -1$), has a dual behavior: it results in torques at $f = -f_p + f_r = -f_v$, and at $f = -f_p - f_r = -2f_r - f_v$.

   From the plot of $F_{int}(n)$, one finds that the torque component at $f = -2f_r - f_v$ is small since $|F_{int}(-2)| = |F_{int}(2)| \cong 0.15$ is small; on the contrary, the component at $f = -f_v$ is relevant because $F_{int}(0) = z_R$, which is the largest $F_{int}(n)$ value.

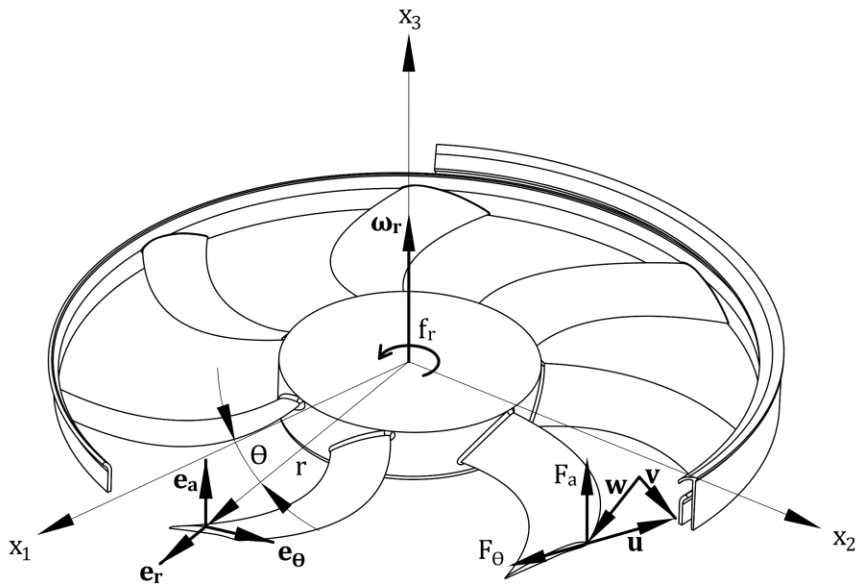

Figure 4.30. Sketch of the coordinate system and forces on the fan.

All this shows that the frequency shift causes a blade force oscillating at the frequency $f = f_p = f_r + f_v$ that excites the rotor at the frequency $f = f_p - f_r = f_v$ that is subharmonic. These forces act close to the blade tips and the blades are rather compliant; as a result, the moment is transmitted to the ring that vibrates.

$\mathbf{M}(t)$ requires further analysis in order to study the excitation at $f = f_v$. Grouping all of the terms, one obtains

$$\mathbf{M}(t) = \sum_{m=1}^{z_R} r_0 F_{a_m}(t)[-\mathbf{e}_2 \cos(\vartheta_m^0 + 2\pi f_r t) + \mathbf{e}_1 \sin(\vartheta_m^0 + \omega_r t)] =$$

$$= -\mathbf{e}_2 r_0 \sum_{n=-\infty}^{\infty} \frac{\tilde{F}_{a_n}}{2} \{\exp[i2\pi(nf_p + f_r)t]\, F_{int}(n+1) + \exp[i2\pi(nf_p - f_r)t]\, F_{int}(n-1)\} +$$

$$+\mathbf{e}_1 r_0 \sum_{n=-\infty}^{\infty} \frac{\tilde{F}_{a_n}}{2i} \{\exp[i2\pi(nf_p + f_r)t]\, F_{int}(n+1) - \exp[i2\pi(nf_p - f_r)t]\, F_{int}(n-1)\}$$

$$= r_0 \sum_{n=-\infty}^{\infty} \tilde{F}_{a_n} \left[-\frac{\exp\left[i2\pi\left(nf_p + f_r\right)t\right] F_{int}(n+1) + \exp\left[i2\pi\left(nf_p - f_r\right)t\right] F_{int}(n-1)}{2} \mathbf{e}_2 \right.$$
$$\left. + \frac{\exp\left[i2\pi\left(nf_p + f_r\right)t\right] F_{int}(n+1) - \exp\left[i2\pi\left(nf_p - f_r\right)t\right] F_{int}(n-1)}{2i} \mathbf{e}_1 \right] \tag{4.86}$$

The $\mathbf{M}(t)$ components resulting from $n = \pm 1$ ($f = f_p \pm f_r = f_v, 2f_r + f_v$) are

$$r_0 \tilde{F}_{a_1} \left[-\frac{\exp\left[i2\pi\left(f_p + f_r\right)t\right] F_{int}(2) + \exp\left[i2\pi\left(f_p - f_r\right)t\right] F_{int}(0)}{2} \mathbf{e}_2 \right.$$
$$\left. + \frac{\exp\left[i2\pi\left(f_p + f_r\right)t\right] F_{int}(2) - \exp\left[i2\pi\left(f_p - f_r\right)t\right] F_{int}(0)}{2i} \mathbf{e}_1 \right] +$$
$$r_0 \tilde{F}_{a_{-1}} \left[-\frac{\exp\left[i2\pi\left(-f_p + f_r\right)t\right] F_{int}(0) + \exp\left[i2\pi\left(-f_p - f_r\right)t\right] F_{int}(-2)}{2} \mathbf{e}_2 \right. \tag{4.87}$$
$$\left. + \frac{\exp\left[i2\pi\left(-f_p + f_r\right)t\right] F_{int}(0) - \exp\left[i2\pi\left(-f_p - f_r\right)t\right] F_{int}(2)}{2i} \mathbf{e}_1 \right]$$

The terms acting at $f = f_v$ may be obtained by eliminating the ones containing $F_{int}(\pm 2)$ and considering that $f_p - f_r = f_v$ and $F_{int}(0) = z_R$:

$$r_0 \tilde{F}_{a_1} \left[-\frac{\exp\left[i2\pi\left(f_p - f_r\right)t\right] F_{int}(0)}{2} \mathbf{e}_2 - \frac{\exp\left[i2\pi\left(f_p - f_r\right)t\right] F_{int}(0)}{2i} \mathbf{e}_1 \right] +$$

$$r_0 \tilde{F}_{a_{-1}} \left[-\frac{\exp\left[i2\pi\left(-f_p + f_r\right)t\right] F_{int}(0)}{2} \mathbf{e}_2 + \frac{\exp\left[i2\pi\left(-f_p + f_r\right)t\right] F_{int}(0)}{2i} \mathbf{e}_1 \right] =$$

$$= r_0 \tilde{F}_{a_1} \left[-\frac{\exp(i2\pi f_v t)\, F_{int}(0)}{2} \mathbf{e}_2 + \frac{-\exp(i2\pi f_v t)\, F_{int}(0)}{2i} \mathbf{e}_1 \right] +$$

$$r_0 \tilde{F}_{a_{-1}} \left[-\frac{\exp(-i2\pi f_v t)\, F_{int}(0)}{2} \mathbf{e}_2 + \frac{\exp(-i2\pi f_v t)\, F_{int}(0)}{2i} \mathbf{e}_1 \right] =$$

$$= z_R r_0 \left\{ \tilde{F}_{a_1} \left[-\frac{\exp(i2\pi f_v t)}{2} \mathbf{e}_2 - \frac{\exp(i2\pi f_v t)}{2i} \mathbf{e}_1 \right] + \tilde{F}_{a_{-1}} \left[-\frac{\exp(-i2\pi f_v t)}{2} \mathbf{e}_2 + \frac{\exp(-i2\pi f_v t)}{2i} \mathbf{e}_1 \right] \right\} =$$

$$= z_R r_0 \left\{ \left[-\frac{\exp(i2\pi f_v t)}{2i} \tilde{F}_{a_1} + \frac{\exp(-i2\pi f_v t)}{2i} \tilde{F}_{a_{-1}} \right] \mathbf{e}_1 - \left[\frac{\exp(i2\pi f_v t)}{2} \tilde{F}_{a_1} + \frac{\exp(-i2\pi f_v t)}{2} \tilde{F}_{a_{-1}} \right] \mathbf{e}_2 \right\} =$$

$$= -z_R r_0 \left\{ \left[\frac{\exp(i2\pi f_v t)}{2i} \tilde{F}_{a_1} - \frac{\exp(-i2\pi f_v t)}{2i} \tilde{F}_{a_{-1}} \right] \mathbf{e}_1 - \left[\frac{\exp(i2\pi f_v t)}{2} \tilde{F}_{a_1} + \frac{\exp(-i2\pi f_v t)}{2} \tilde{F}_{a_{-1}} \right] \mathbf{e}_2 \right\} =$$

as $\tilde{F}_{a_1} = |\tilde{F}_{a_1}| \exp(i\varphi_{a_1})$ and and $\tilde{F}_{a_{-1}} = \tilde{F}_{a_1}^* = |\tilde{F}_{a_1}| \exp(-i\varphi_{a_1})$

$$= -z_R r_0 \left\{ \left[\frac{\exp(i2\pi f_v t)}{2i} \tilde{F}_{a_1} - \frac{\exp(-i2\pi f_v t)}{2i} \tilde{F}_{a_{-1}} \right] \mathbf{e}_1 + \left[\frac{\exp(i2\pi f_v t)}{2} \tilde{F}_{a_1} + \frac{\exp(-i2\pi f_v t)}{2} \tilde{F}_{a_{-1}} \right] \mathbf{e}_2 \right\} =$$

$$= -z_R r_0 |\tilde{F}_{a_1}| \left\{ \left[\frac{\exp(i2\pi f_v t)}{2i} \exp(i\varphi_{a_1}) - \frac{\exp(-i2\pi f_v t)}{2i} \exp(-i\varphi_{a_1}) \right] \mathbf{e}_1 + \left[\frac{\exp(i2\pi f_v t)}{2} \exp(i\varphi_{a_1}) + \frac{\exp(-i2\pi f_v t)}{2} \exp(-i\varphi_{a_1}) \right] \mathbf{e}_2 \right\} =$$

$$= -z_R r_0 |\tilde{F}_{a_1}| \left\{ \left[\frac{\exp(i2\pi f_v t + i\varphi_{a_1})}{2i} - \frac{\exp(-i2\pi f_v t - i\varphi_{a_1})}{2i} \right] \mathbf{e}_1 + \left[\frac{\exp(i2\pi f_v t + i\varphi_{a_1})}{2} + \frac{\exp(-i2\pi f_v t - i\varphi_{a_1})}{2} \right] \mathbf{e}_2 \right\} =$$

$$= -z_R r_0 |\tilde{F}_{a_1}| [\sin(2\pi f_v t + \varphi_{a_1}) \mathbf{e}_1 + \cos(2\pi f_v t + \varphi_{a_1}) \mathbf{e}_2] =$$

$$= z_R r_0 |\tilde{F}_{a_1}| [-\sin(2\pi f_v t + \varphi_{a_1}) \mathbf{e}_1 - \cos(2\pi f_v t + \varphi_{a_1}) \mathbf{e}_2] =$$

$$\mathbf{M}_{f_v}(t) = z_R r_0 |\tilde{F}_{a_1}| \left\{ \cos\left[2\pi f_v t + \left(\varphi_{a_1} + \frac{\pi}{2} \right) \right] \mathbf{e}_1 - \sin\left[2\pi f_v t + \left(\varphi_{a_1} + \frac{\pi}{2} \right) \right] \mathbf{e}_2 \right\} \qquad (4.88)$$

as $-\sin(2\pi f_v t + \varphi_{a_1}) = \cos\left[2\pi f_v t + \left(\varphi_{a_1} + \frac{\pi}{2} \right) \right]$ and $\cos(2\pi f_v t + \varphi_{a_1}) = \sin\left[2\pi f_v t + \left(\varphi_{a_1} + \frac{\pi}{2} \right) \right]$

This shows that the torque $\mathbf{M}_{f_v}(t)$ has a constant amplitude that equals $z_R r_0 |\tilde{F}_{a_1}|$ and counter rotates at the angular speed $\omega_v = 2\pi f_v$ with a phase shift of $\frac{\pi}{2}$ with respect to the force $F_{af_v}(t) = |\tilde{F}_{a_1}| \cos(2\pi f_v t + \varphi_{a_1})$.

4.5.4.3. Resultant tangential force

In order to compute the resultant tangential force, the force $\mathbf{F}_{\vartheta_m}(t)$ acting on the $m-th$ blade has to be projected in the Cartesian directions. $\mathbf{F}_{\vartheta_m}(t)$ is given by

$$\mathbf{F}_{\vartheta_m}(t) = F_{\vartheta_m}(t) \mathbf{e}_{\boldsymbol{\vartheta}_m}(t) \qquad (4.89)$$

and yields the resultant force $\mathbf{F}_{\vartheta}(t)$ in the rotational plane:

$$\mathbf{F}_{\vartheta}(t) = \sum_{m=1}^{z_R} \mathbf{F}_{\vartheta_m} = \sum_{m=1}^{z_R} F_{\vartheta_m}(t)\mathbf{e}_{\boldsymbol{\vartheta}_m}(t) \tag{4.90}$$

where $\mathbf{e}_{\boldsymbol{\vartheta}_m}(t)$ is the versor of the ϑ direction at the point of application of the force on the $m-th$ blade. Since $\mathbf{e}_{\boldsymbol{\vartheta}_m}(t) = -\sin\left(\vartheta_{abs,m}(t)\right)\mathbf{e}_1 + \cos\left(\vartheta_{abs,m}(t)\right)\mathbf{e}_2$, the instantaneous components along the x_1 and x_2 axes are given by

$$F_{\vartheta_m,1}(t) = -F_{\vartheta_m}(t)\sin\left(\vartheta_{abs,m}(t)\right) \tag{4.91}$$

And

$$F_{\vartheta_m,2}(t) = F_{\vartheta_m}(t)\cos\left(\vartheta_{abs,m}(t)\right) \tag{4.92}$$

The Cartesian components of $\mathbf{F}_{\vartheta}(t)$ are

$$F_{\vartheta,1}(t) = -\sum_{m=1}^{z_R} F_{\vartheta_m}(t)\sin\left(\vartheta_{abs,m}(t)\right) = -\sum_{m=1}^{z_R}\left[\sum_{n=-\infty}^{\infty} \tilde{F}_{\vartheta_n}\exp\left(i2\pi n f_p t + in\vartheta_m^0\right)\sin\left(\vartheta_{abs,m}(t)\right)\right] =$$

$$= -\sum_{m=1}^{z_R}\left[\sum_{n=-\infty}^{\infty} \tilde{F}_{\vartheta_n}\exp\left(i2\pi n f_p t\right)\exp(in\vartheta_m^0)\sin(\vartheta_m^0 + 2\pi f_r t)\right] =$$

$$= -\sum_{n=-\infty}^{\infty} \tilde{F}_{\vartheta_n}\left[\sum_{m=1}^{z_R}\exp\left(i2\pi n f_p t\right)\exp(in\vartheta_m^0)\frac{\exp\left(i(\vartheta_m^0 + 2\pi f_r t)\right) - \exp\left(-i(\vartheta_m^0 + 2\pi f_r t)\right)}{2i}\right] =$$

$$= -\sum_{n=-\infty}^{\infty} \frac{\tilde{F}_{\vartheta_n}}{2i}\left[\sum_{m=1}^{z_R}\exp\left(i2\pi n f_p t\right)\exp(in\vartheta_m^0)\exp\left(i(\vartheta_m^0 + 2\pi f_r t)\right)\right.$$

$$\left. - \exp\left(i2\pi n f_p t\right)\exp(in\vartheta_m^0)\exp\left(-i(\vartheta_m^0 + 2\pi f_r t)\right)\right] =$$

$$= \sum_{n=-\infty}^{\infty} \frac{\tilde{F}_{\vartheta_n}}{2i}\left\{\sum_{m=1}^{z_R}\exp\left[i2\pi\left(n f_p + f_r\right)t\right]\exp[i(n+1)\vartheta_m^0] - \exp\left[i2\pi\left(n f_p - f_r\right)t\right]\exp[i(n-1)\vartheta_m^0]\right\} =$$

$$= \sum_{n=-\infty}^{\infty} \frac{\tilde{F}_{\vartheta_n}}{2i} \left\{ \exp\left[i2\pi\left(nf_p + f_r\right)t\right] \sum_{m=1}^{z_R} \exp[i(n+1)\vartheta_m^0] - \exp\left[i2\pi\left(nf_p - f_r\right)t\right] \sum_{m=1}^{z_R} \exp[i(n-1)\vartheta_m^0] \right\}$$

$$=$$

$$= \sum_{n=-\infty}^{\infty} \frac{\tilde{F}_{\vartheta_n}}{2i} \left\{ \exp\left[i2\pi\left(nf_p + f_r\right)t\right] F_{int}(n+1) - \exp\left[i2\pi\left(nf_p - f_r\right)t\right] F_{int}(n-1) \right\} \tag{4.93}$$

$$F_{\vartheta,2}(t) = \sum_{m=1}^{z_R} F_{\vartheta_m}(t) \cos\left(\vartheta_{abs,m}(t)\right) = -\sum_{m=1}^{z_R} \left[\sum_{n=-\infty}^{\infty} \tilde{F}_{\vartheta_n} \exp\left(i2\pi n f_p t + in\vartheta_m^0\right) \cos\left(\vartheta_{abs,m}(t)\right) \right] =$$

$$= \sum_{m=1}^{z_R} \left[\sum_{n=-\infty}^{\infty} \tilde{F}_{\vartheta_n} \exp\left(i2\pi n f_p t\right) \exp(in\vartheta_m^0) \cos(\vartheta_m^0 + 2\pi f_r t) \right] =$$

$$= \sum_{n=-\infty}^{\infty} \tilde{F}_{\vartheta_n} \left[\sum_{m=1}^{z_R} \exp\left(i2\pi n f_p t\right) \exp(in\vartheta_m^0) \frac{\exp\left(i(\vartheta_m^0 + \omega_r t)\right) + \exp\left(-i(\vartheta_m^0 + 2\pi f_r t)\right)}{2} \right] =$$

$$= \sum_{n=-\infty}^{\infty} \frac{\tilde{F}_{\vartheta_n}}{2} \left[\sum_{m=1}^{z_R} \exp\left(i2\pi n f_p t\right) \exp(in\vartheta_m^0) \exp\left(i(\vartheta_m^0 + 2\pi f_r t)\right) \right.$$

$$\left. + \exp\left(i2\pi n f_p t\right) \exp(in\vartheta_m^0) \exp\left(-i(\vartheta_m^0 + 2\pi f_r t)\right) \right] =$$

$$= \sum_{n=-\infty}^{\infty} \frac{\tilde{F}_{\vartheta_n}}{2} \left\{ \sum_{m=1}^{z_R} \exp\left[i2\pi\left(nf_p + f_r\right)t\right] \exp[i(n+1)\vartheta_m^0] + \exp\left[i2\pi\left(nf_p - f_r\right)t\right] \exp[i(n-1)\vartheta_m^0] \right\}$$

$$= \sum_{n=-\infty}^{\infty} \frac{\tilde{F}_{\vartheta_n}}{2} \left\{ \exp\left[i2\pi\left(nf_p + f_r\right)t\right] \sum_{m=1}^{z_R} \exp[i(n+1)\vartheta_m^0] + \exp\left[i2\pi\left(nf_p - f_r\right)t\right] \sum_{m=1}^{z_R} \exp[i(n-1)\vartheta_m^0] \right\}$$

$$=$$

$$= \sum_{n=-\infty}^{\infty} \frac{\tilde{F}_{\vartheta_n}}{2} \left\{ \exp\left[i2\pi\left(nf_p + f_r\right)t\right] F_{int}(n+1) + \exp\left[i2\pi\left(nf_p - f_r\right)t\right] F_{int}(n-1) \right\} \tag{4.94}$$

$F_{\vartheta,1}(t)$ and $F_{\vartheta,2}(t)$ lay in the rotational plane and apply a resultant force to the shaft, eventually yielding a torque on the motor supports and a deformation of the casing. Their expression is very similar to the one of the torque due to $F_a(t)$, namely, frequency shift and effect of the interference

function are the same. The analysis is not repeated here, but it is clear that $\mathbf{F}_\vartheta(t)$ has a resultant that excites the system at the frequency $f = f_v$ (for $n = -1, nf_p + f_r = -f_v$ and for $n = 1, nf_p - f_r = f_v$).

However, the line of action of such component of the tangential force is rather close to the supports: roughly speaking one half of the motor length, i.e. a lever arm of about 25 mm. The blade force fluctuations are due to the gap flow that is concentrated in the blade tip region ($r \cong 250$ mm); hence, the lever arm of the axial component is about ten times larger and it may be expected that the related torque is more important. Furthermore, due to the large blade stagger angle typical of axial fans, it is expected that $|F_a| > |F_\vartheta|$, which further indicates that the torque due to the axial component has a major effect.

4.5.4.4. Resultant axial torque

The summation of the axial torque components forces due to all of the blades yields a resultant torque $M_a(t)$ that apparently has a fundamental frequency f_p. However, such a summation shows that, although the force acting on each blade is the same, some harmonics may be canceled (as the fundamental one) and other ones may be amplified (e.g. the blade passing frequency one) due to the time delay between forces acting on different blades.

The torque due to the $m-th$ blade is given by

$$M_{a_m}(t) = r_0 F_{\vartheta_m}(t) \tag{4.95}$$

and the resultant axial torque is given by

$$\begin{aligned} M_a(t) = \sum_{m=1}^{z_R} M_{a_m}(t) = \sum_{m=1}^{z_R} r_0 F_{\vartheta_m}(t) = r_0 \sum_{m=1}^{z_R} \left[\sum_{n=-\infty}^{\infty} \tilde{F}_{\vartheta_n} \exp\left(i2\pi n f_p t + in\vartheta_m^0\right) \right] \\ = r_0 \sum_{n=-\infty}^{\infty} \left[\tilde{F}_{\vartheta_n} \exp\left(i2\pi n f_p t\right) \sum_{m=1}^{z_R} \exp(in\vartheta_m^0) \right] \end{aligned} \tag{4.96}$$

that is

$$M_a(t) = r_0 \sum_{n=-\infty}^{\infty} \left[\tilde{F}_{\vartheta_n} \exp\left(i2\pi n f_p t\right) F_{int}(n) \right] \tag{4.97}$$

This shows that $f_p = f_r + f_v$ is the resulting fundamental frequency of the axial component of the torque and that, based on this model of the force acting on the blade, no excitation at subharmonic

frequencies, namely f_v, may yield; hence, no aerodynamic cause for the observed rotational frequency fluctuation has been identified. The property that $F_{int}(1) = 0$ for statically balanced rotors implies that no axial force fluctuation may be present at $f = f_p$ $(n = 1)$, no matter whether the rotor is evenly spaced or not. The property that $F_{int}(kz_R)$ is large for mildly unevenly spaced rotors shows that the axial torque fluctuation should mainly excite the rotor and the shaft at $z_R f_p$ and higher harmonics, which in the present case are rather large (as z_R=7, important vibration may be expected at 7×51.4 Hz ≅ 360 Hz and 14×51.4 Hz ≅ 720 Hz). On the contrary the contribution at the lower f_p harmonics should be negligible, see the interference function plot. It may be concluded that the fluctuations in $\mathbf{F}_\vartheta$ cannot excite subharmonic oscillations in the axial torque and, hence, in the rotational speed. This term holds as long as the $F_{\vartheta_m}(t) = \sum_{n=-\infty}^{\infty} \tilde{F}_{\vartheta_n} \exp\left(i2\pi n f_p t + in\vartheta_m^0\right)$, i.e. its fundamental frequency is $f_p = f_r + f_v$.

5. AERODYNAMIC INVESTIGATIONS AND RESULTS

In the previous chapters, the elastic behavior of the fan has been studied experimentally, analytically, and numerically and the flutter aeroelastic phenomenon has been identified as a precession of the fan axis which generates high amplitude vibration at low frequencies, basically around 7 to 8 Hz with a peak to trough amplitude of the axial movement of the rotating shroud of almost 8 mm. A complete series of aerodynamic measurements have been carried out, employing complementary techniques, with the aim of supplying general information on the evolving flow as well as trying to deepen the unsteady phenomena which can set on the flutter phenomenon. As a matter of fact, since no information about similar phenomena has been found in the literature review, the employ of a certain measuring technique has been chosen to fill up a piece of knowledge about the flow characteristics and, if possible, to highlight some details of the aeroelastic phenomenon. Thus, it is possible to subdivide the results into the following points:

- Mean flow field (investigated by means of PIV and LDV measurements);
- Unsteady flow field (investigated by means of LDV measurements).

5.1. Mean flow field characteristics

5.1.1. PIV measurements

The flow field upstream and downstream of the fan has been surveyed in a vertical meridional plane using the 2D-PIV system previously described in chapter 2, see Fig. 2.8. The upstream investigated region is a rectangular area located at x = -25 mm from the tip of the fan ring with an axial and radial extension equal to $L_x = 114$ mm $\times L_r = 39$ mm, i.e. $r/r_{tip} = 0.91\text{-}1.07$ and $x/r_{tip} = 0.1\text{-}0.54$. The downstream one is a rectangular area located at x = 1.6 mm from the tip of the ring with the following axial and radial extensions: $L_x = 74$ mm $\times L_r = 199$ mm, i.e. $r/r_{tip} = 0.57\text{-}1.35$ and $x/r_{tip} = 0.006\text{-}0.29$, see Fig. 5.1.

The upstream investigation region has been covered by one camera, while for the downstream investigation region two cameras have been mounted radially shifted in order to expand the radial extension of the investigated area without diminishing the spatial resolution. A 25-mm overlapping region in the radial direction between the snapshots from the two cameras has been used in order to combine smoothly the resulting instantaneous vector fields. A suitable algorithm has been employed for this purpose. Because the corner of the upstream investigated region is overlapped by the geometry, a masked zone is introduced for future post-processing. Therefore, just the green zone contains information.

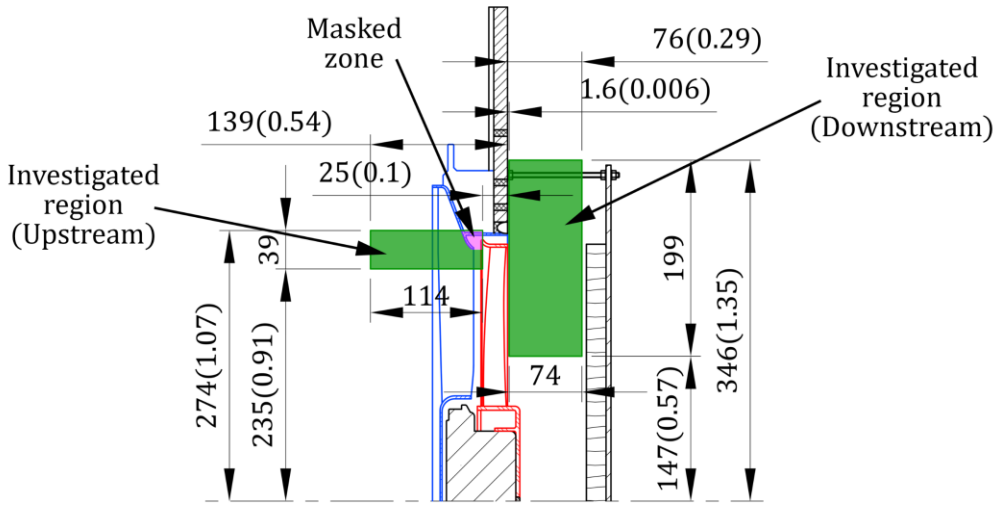

Figure 5.1. PIV investigation regions upstream and downstream of the fan.

Using an adaptive spatial cross-correlation function, the velocity fields (the axial and radial velocity components v_a and v_r) in the meridional plane have been acquired, providing instantaneous vector fields with 114×39 points for the upstream region as well as 74×199 points for the downstream region on a square grid of steps $\Delta x = \Delta r = 1.5$ mm. In the downstream case 800 instantaneous flowfields have been collected, which are sufficient for a mean flow survey, while in the upstream case the number has been increased to 1200 since some reflections from the casing and blades could reduce the statistical reliability of the ensemble.

The time-averaged velocity is obtained by averaging the instantaneous velocity components v_a and v_r:

$$\overline{v} = \frac{\frac{1}{I}\sum_{i=1}^{I} v(i)}{u_{tip}} \tag{5.1}$$

Where $i = 1, \dots, I$ is the index of each velocity sample during the time.

The time-averaged turbulence intensity can be expressed as $\overline{Tu}$ but contains all of the velocity fluctuations, i.e., periodic components related to the BPF and harmonics:

$$\overline{Tu} = \frac{\sqrt{\frac{\left(\overline{v_a'}\right)^2 + \left(\overline{v_r'}\right)^2}{2}}}{u_{tip}} \tag{5.2}$$

Where $\overline{v'}$ is the standard deviation of velocity:

$$\overline{v'} = std(v) = \sqrt{\frac{1}{(I-1)}\sum_{i=1}^{I}[v(i) - \overline{v}]^2} \tag{5.3}$$

All the aforementioned variables are normalized by u_{tip}. As the 2D-PIV system does not allow to measure v_θ, $\overline{Tu}$ only provides qualitative information about the flow unsteadiness.

Based on the PIV error studies of Grant [22] and Prasad et al. [23], the experimental uncertainty for the instantaneous velocity in the current study is approximated to be 3%. This estimate gives a rough evaluation of the whole examined domain and the selected operating points, see Canepa et al. [3]. The cross-plane velocity component v_θ is the main source of systematic bias in the present investigations and because $v_\theta$has not been measured, a proper estimation is difficult. This effect rises near the domain's boundaries thereafter it can result in a spatially varying uncertainty.

The statistical errors have been calculated using a 20% $\overline{Tu}$ value. For the time-averaged velocity components, v_a and v_r, the statistical uncertainty is 1.5% and 5% for $\overline{Tu}$.

The time-averaged axial velocity, v_a, and radial velocity, v_r, contours are reported in Figures 5.2 and 5.3 respectively. In all three working conditions, v_a and v_r have the maximum values when the flow leaves the fan close to the tip, i.e., in the range $r/r_{tip} = 0.8 - 1$ and $x/r_{tip} = 0 - 0.1$ for v_a and $r/r_{tip} = 1 - 1.3$ and $x/r_{tip} = 0.1 - 0.3$ for v_r. While v_a and v_r are positive almost all over the flow field, it is negative in some regions. Generally speaking, the presence of the downstream panel, which simulates the presence of the engine and is a common requirement for automotive cooling unit testing, constitutes a very strong boundary condition that is able to modify largely flow field at the

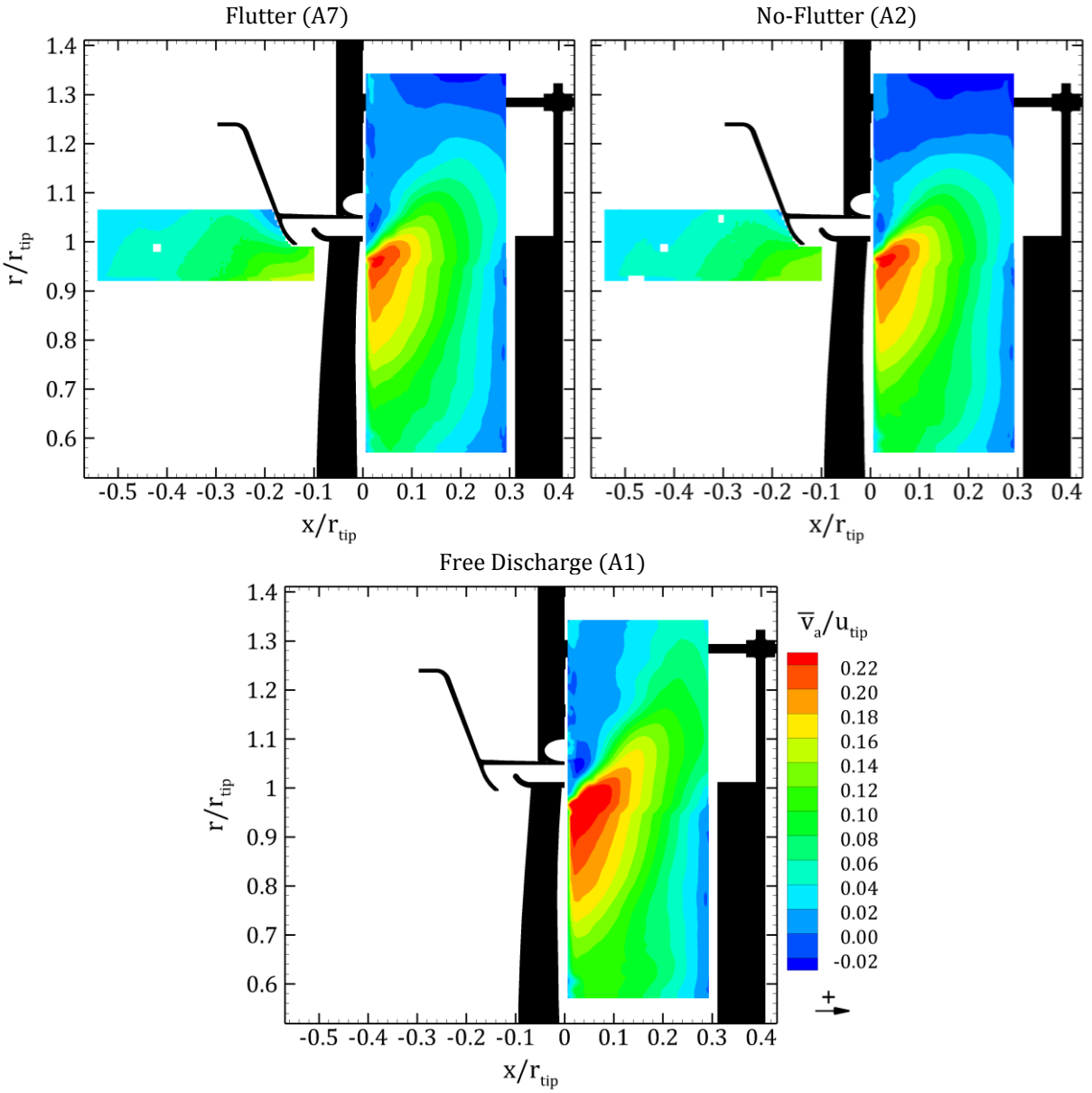

Figure 5.2. The time averaged axial velocity fields for three cases upstream and downstream of the fan.

rotor outlet even for largely different fan working points. In fact, it is well known that the flow downstream of an axial fan may assume a large radial velocity component, as a result of the tangential one since the flow is not confined. Such a behavior is typical of low mass flow rate and high-pressure rise working points. But a free discharge condition is expected to generate an axial jet-like flow pattern. Differently, in the present case, such a difference is not present and even in the free discharge condition, the flow is forced by the panel to become centrifugal at a very short axial distance from the fan outlet section. The contour plots of v_a and v_r confirm this effect and the difference between the

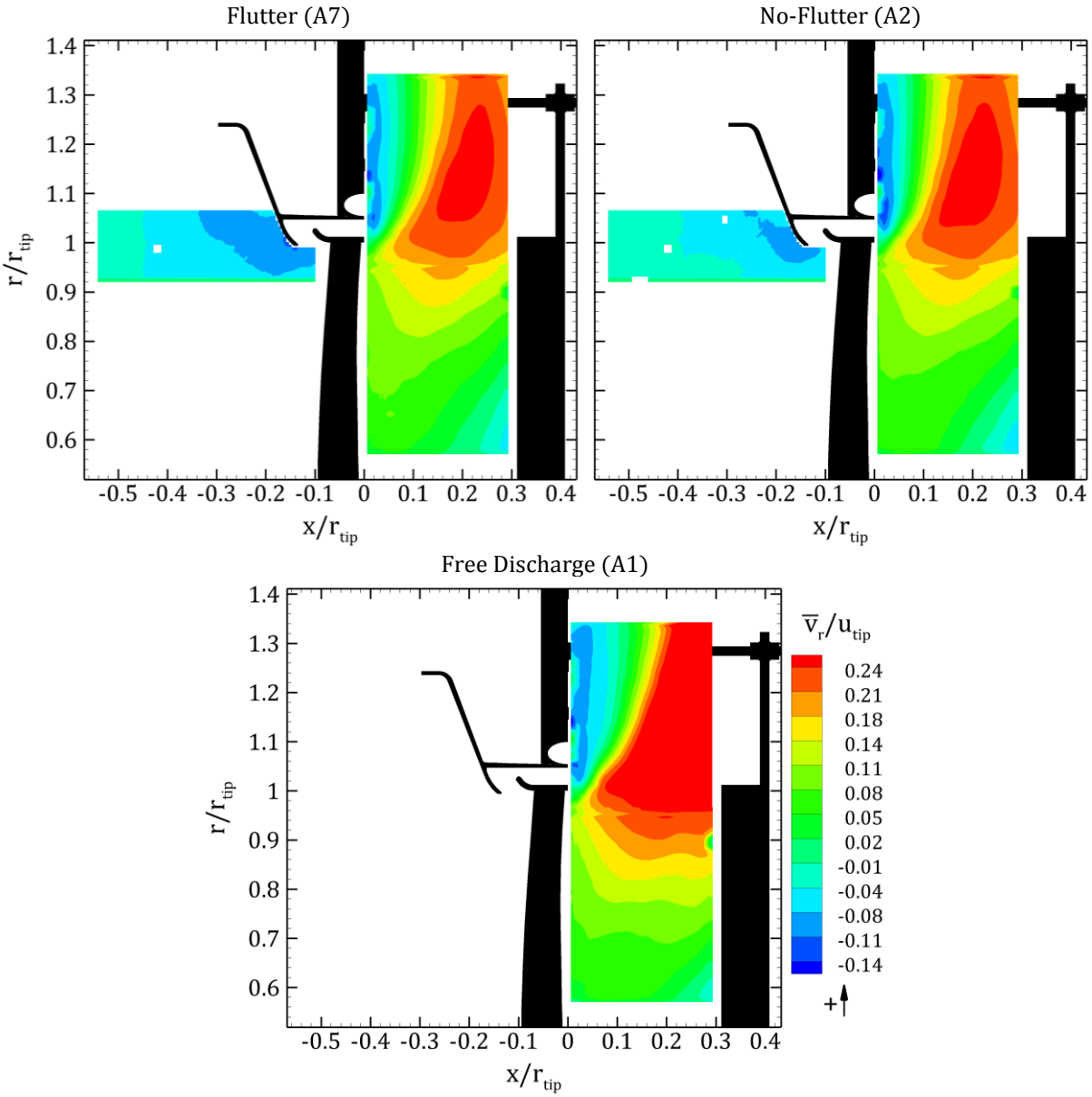

Figure 5.3. The time averaged radial velocity fields for three cases upstream and downstream of the fan.

three cases are very limited. In the free discharge condition v_a shows larger values than in the other two cases from the mid-blade region to the tip, and this is consistent with the larger flow rate. As a consequence, also the radial component becomes larger than the other cases close to the wooden panel. In all three cases, as the flow becomes radial, a separation bubble is generated in the zone which is close to the upstream panel, i.e. $x/r_{tip} = 0 - 0.05$ and $r/r_{tip} = 1 - 1.35$, where the flow is characterized by a centripetal motion, and probably a part is feeding the leakage flow passing through the gap.

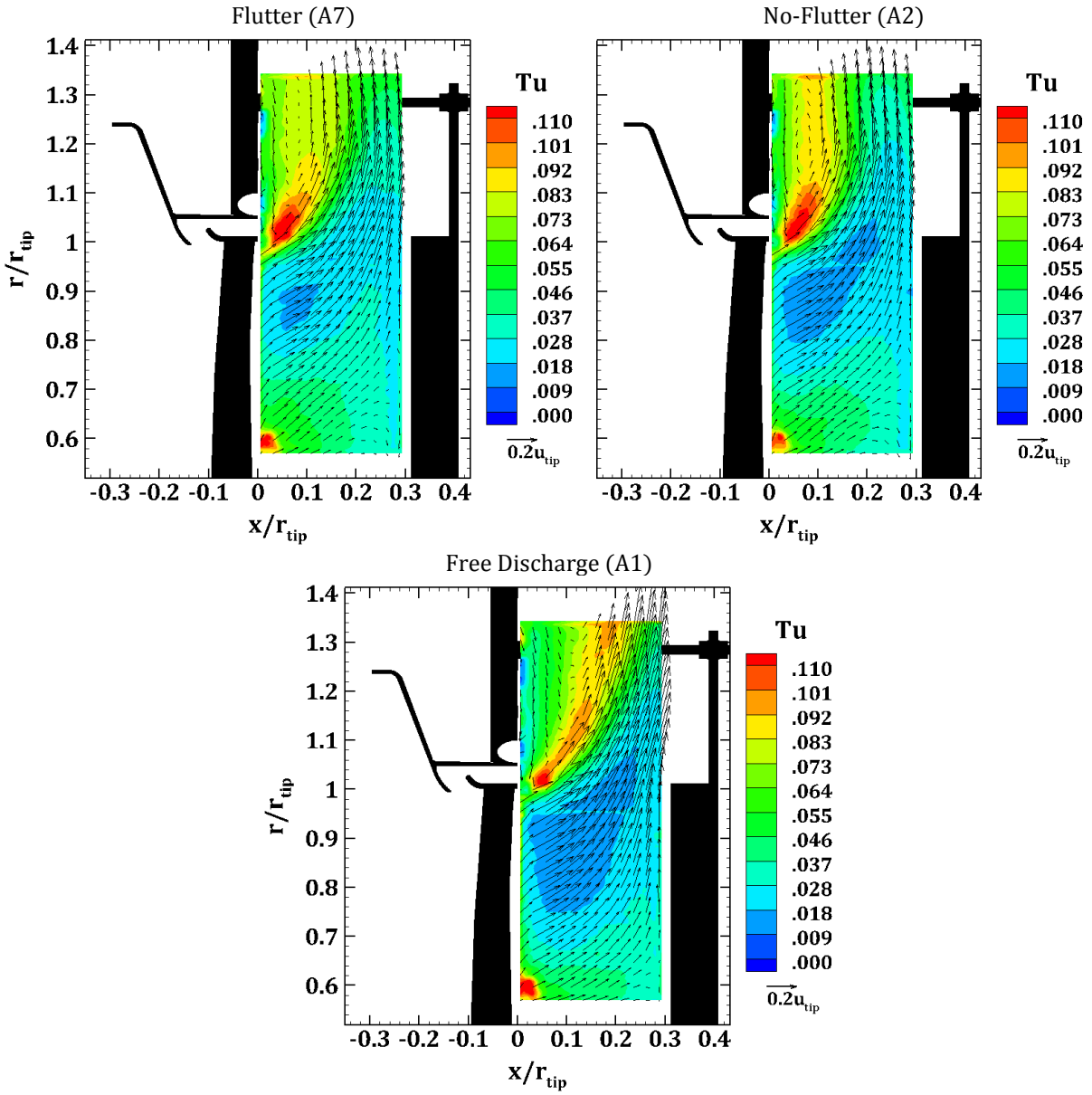

Figure 5.4. The time averaged turbulence for three cases upstream and downstream of the fan. The time averaged velocity vectors are superimposed on the contour plot.

The velocity vector plots, which are superposed to the turbulence contours and represented in Fig. 5.4, confirm this aspect. Moreover, the Tu distributions suggest that the largest unresolved unsteadiness is present in the shear layer between the fan jet and the recirculating flow which moves toward the gap. It is interesting to highlight that in the flutter condition the high turbulence spot, present slightly downstream on the blade tip, has the same magnitude as in the no-flutter condition, indicating thus that the shear layer is the major source of turbulence.

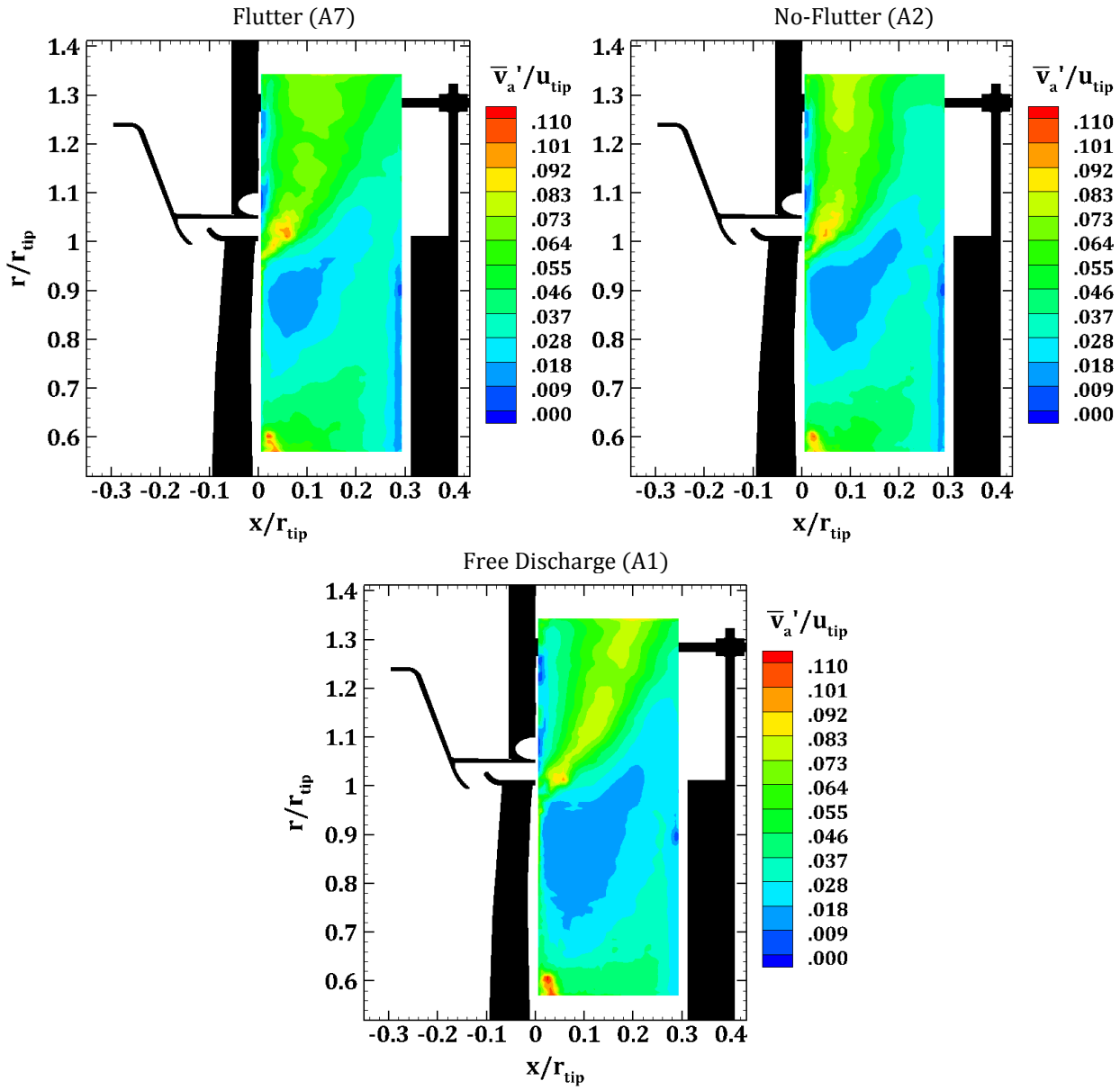

Figure 5.5. The time averaged standard deviation of axial velocity fields for three cases upstream and downstream of the fan.

Another interesting feature that can be seen in Fig. 5.4 is the high turbulence spot in the region $x/r_{tip} = 0 - 0.20$ and $r/r_{tip} = 0.6 - 0.65$ which is present in all the cases and probably indicates a large separation zone close to the fan hub.

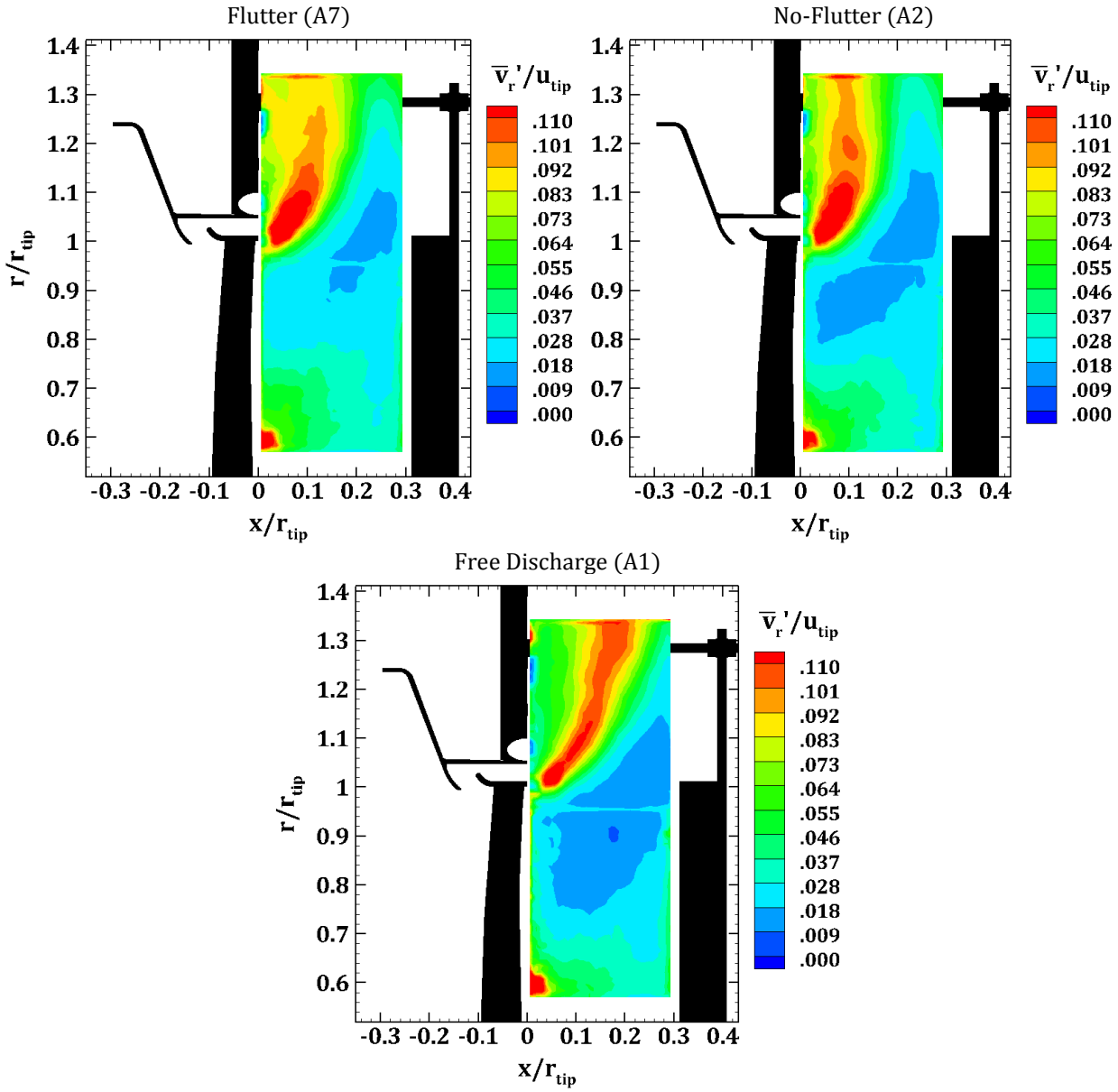

Figure 5.6. The time averaged standard deviation of radial velocity fields for three cases upstream and downstream of the fan.

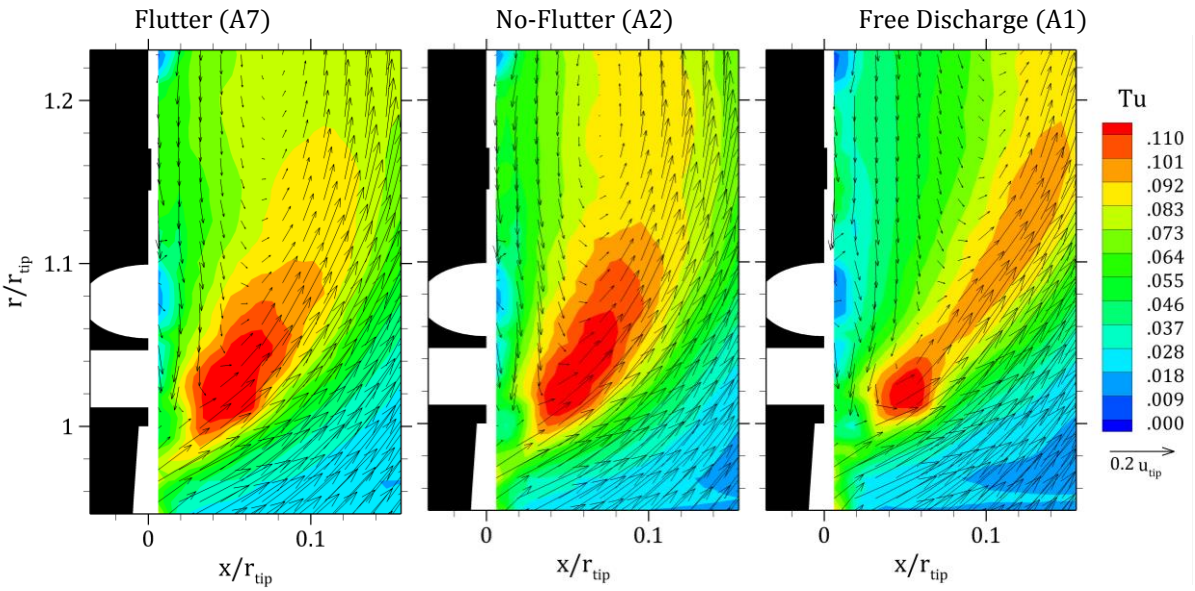

Figure 5.7. The time averaged turbulence for three cases upstream and downstream of the fan (enlarged zone close to the gap). The time averaged velocity vectors are superimposed to the contour plot.

For sake of completeness, the contours of the standard deviation of the axial component and the radial one have been represented in Figs 5.5 and 5.6.

If the zone close to the gap is enlarged the result is represented in Fig. 5.7, in this way it is possible to evaluate in a more detailed way the behavior of the shear layer zone between the jet and the recirculating flow. The strong resemblance between the flutter and no-flutter case is confirmed apart from a certain difference due to a greater elongation of the high turbulence zone at high radii for the no-flutter case. Such an aspect may be related to the enhanced mixing process which takes place in the flutter case due to the axial oscillating movement of the fan shroud and blades. In this way, the interface between the jet and the recirculating flow becomes, in mean terms, less steady and well-defined. In this set of PIV measurements, it has not been possible to study the flow very close to the gap inlet and blade tip, $x/r_{tip} = 0$, due to the reflected light of laser beams which are problematic for the images recorded by the cameras; in the next sections, this region very close to the gap inlet will be studied by means of LDA measurements and the return flow to the gap will be clearly visible in that region.

So far, comprehensive information on the time-mean flow behavior upstream and downstream of the fan has been obtained. In order to have more information on the unsteady characteristics, the instantaneous snapshots have been analyzed. Four selected snapshots, related to the flutter case, are illustrated in Fig. 5.8, by examining the velocity field frame by frame, hidden information about flow

behavior will be revealed. In all the instantaneous snapshots the flow is highly perturbated and large-scale vortices can be individuated. In Fig. 5.8a as the flow is leaving the tip of the blade is suddenly changing direction to radial, a vortex centered just above the gap is present and the flow keeps on being radial close to the panel in such a way that the separated centripetal flow is non-recognizable in the snapshot. In Fig 5.8b, c, and d at the interface between the jet and the recirculating flow, large-scale eddies (red color vectors) are present, as a matter of fact, the instantaneous interface is extremely curly in a way that could not be foreseen from the mean trends. Moreover, in Fig 5.8c and d the flow entering the gap is coming from two different regions (blue color vectors), the first source of the flow entering the gap is arriving directly from the blade tip region, while the second is from the

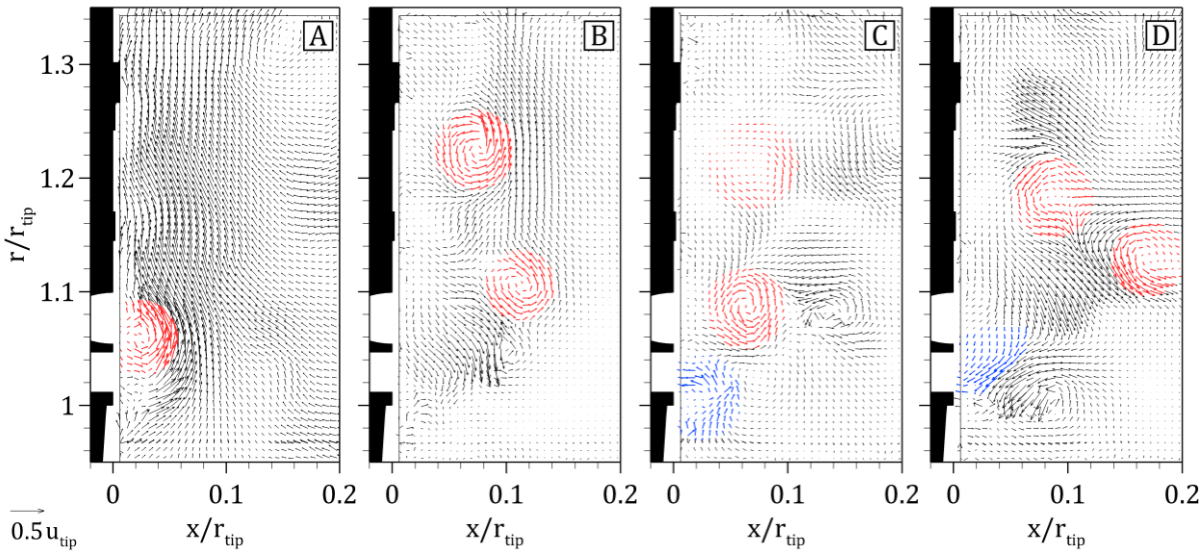

Figure 5.8. Downstream velocity vector snapshots for different cases.

separated region. The reverse flow entering the gap, which can be seen in all three studied cases (Flutter, No-Flutter, Free discharge), will be investigated in detail in later sections by LDA measurements in the region close to the gap.

The presence of the aforementioned large-scale turbulent structures suggested the need to statistically analyze the vector fields in order to eventually identify the ones which may have a deterministic presence. The proper orthogonal decomposition (POD) method has been used for this aim. In this method, repetitive patterns are ranked based on energy, which is the repeatability of that pattern in the flow. Here, by performing this technique on two distinct cases, Flutter and No-Flutter, separately for velocity components v_a and v_r, and also both velocity components, $v_a v_r$ (simultaneously), the dominant modes are obtained.

In Figure 5.9, the amount of energy of each mode as a percentage of the total energy of all modes has been presented. In this graph, the black line and symbols are related to the Flutter case and the red line and symbols are related to the No-Flutter case. The corresponding spatial modes are illustrated in Figures 5.10 to 5.12. Figures 5.10 and 5.11 show the spatial modes of velocity components v_a and v_r for the Flutter and No-Flutter cases, respectively; additionally, mean velocity streamlines have been added to these contour figures to clarify the direction of the velocity field leaving the fan and the location of the recirculating bubble. The contour plot of Figure 5.12 also refers to the spatial modes of both velocity components, $v_a v_r$, along with vectors of spatial components v_a and v_r related to that mode for Flutter and No-Flutter cases, respectively. The following equation is used to calculate the spatial mode of both velocity components, $v_a v_r$:

$$v_a v_r = \sqrt{{v_a}^2 + {v_r}^2} \tag{5.4}$$

Therefore, the contour of both components is always positive.

Before reviewing the modes, it is worth mentioning the type of modes is analogous to the variance. Because in this method, first the average of the data is deducted from them and the covariance matrix consisting of variance and covariance elements is formed on this basis; in the next step, the spatial and temporal modes are computed based on the covariance matrix and ranked according to the amount of energy. Therefore, these spatial modes can be compared with the previously mentioned time-averaged standard deviation and turbulence contours.

In the graph of Figure 5.9, by looking at the energy of the first 10 modes of the POD, the important point for most of these modes is that the energy of the velocity component v_r is greater than component v_a, and this is a fact for both cases under study, Flutter and No-Flutter. This indicates that, firstly, the velocity component v_r in the primary modes contains more energy, which means that the impact and pattern iteration of these modes are more than other low-energy modes compare to the component v_a. Secondly, the effect of this velocity component in the initial modes of combining both velocity components, $v_a v_r$, is greater than component v_a.

In both Flutter and No-Flutter cases, the amount of energy for the first two modes is higher than the next modes; the energy levels from mode 3 to the higher modes are gradually decreasing and are very close to each other. Considering the role of each velocity component separately, the energy of the velocity component v_r in mode 1 is almost 26% of the total energy, while this value is less than 16% for component v_a; this indicates that the impact of component v_r is more dominant in mode 1 of both velocity components, $v_a v_r$. This can be easily detected by comparing the spatial mode shape 1 for the components v_a, v_r, and $v_a v_r$ in Figures 5.10, 5.11, and 5.12, respectively. The dominance of the radial component decreases drastically by moving to the higher modes.

To some extent, the first and second modes can be related to the general big structure, recirculating bubble, of the leaving flow of the fan, which has been reported in the time-averaged velocity vector plots in Figures 5.4 and 5.7.

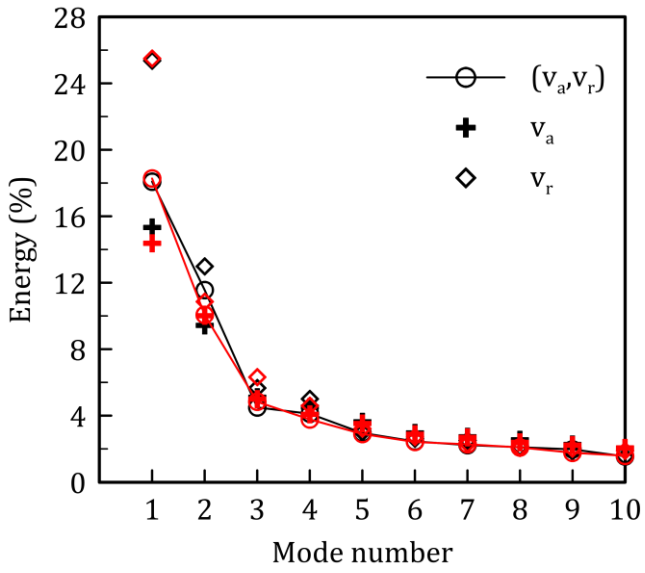

Figure 5.9. The relative energy of POD eigenvalues for the two velocity components v_a, v_r separately, and for both components $v_a v_r$ together. Black: Flutter, Red: No-Flutter.

By examining the spatial modes one by one and comparing them with the contours of time-averaged standard deviation, Figs. 5.5 and 5.6, time-averaged turbulence, Fig. 5.4, as well as velocity field snapshots, Fig. 5.8, a better understanding of the flow behavior especially after leaving the blade tip and the gap region can be obtained. For this purpose, some examples of these comparisons and connections are mentioned here: Due to the shape of higher spatial modes, these modes can be related to the small vortices which are developing and following the recirculating bubble. As the local maxima and minima in these modes in the area between $x/r_{tip} = 0 - 0.2$ and $r/r_{tip} = 1 - 1.3$ are very similar to the red vortices in the snapshots examined in Figure 5.8. However, due to the limitations of measuring devices and low data acquisition frequency (non-time resolved), it is not possible to truly study the modes related to vortices and the relationship between them, nevertheless, hypotheses such as other studies conducted by Canepa et al. [3] and Lengani et al. [24] can be expressed here. In these studies, modes with approximately the same energy that the maxima and minima between two spatial modes are shifted with a spatial wavelength can be considered as vortices in pair modes that convect with a specific frequency. Based on these hypotheses in the flutter case, due to the proximity of the energy of modes 3 and 4, these two modes can be considered pair modes. The maxima and minima of these two spatial modes represent vortices that move within the recirculating bubble from the tip of the blade to a higher radius and oscillate at an arbitrary frequency that cannot be measured here. The peaks of these pairs of spatial modes can be considered analogous to the red vortices in snapshot B of Figure 5.8. Taking into account the assumptions made, there is a possibility of the existence of a link between the oscillation frequency of the vortices of these two modes and the fan vibration frequency, f_v, which was investigated in the previous chapter. But the proof of this claim is beyond the scope of this study.

No-Flutter case has almost similar energy rank for each mode; also in this case spatial modes are similar to the Flutter case but with some minor differences. One of these differences is related to the center location of the recirculating bubble. In the spatial modes plots, it is clear that the dominant flow structures and vortices are following this bubble and recirculating around that. Hence, in the Flutter case compared to the No-Flutter case, as the bubble center is located in higher radii and it is axially a bit wider, therefore most of the flow structures are developing at the wider axial locations. These differences are easily recognizable by comparing all the first 5 spatial modes of Flutter and No-Flutter cases for both velocity components, see Figs. 5.10 and 5.11.

So far, the overall flow structure upstream and downstream of the fan has been investigated by PIV measurements. It has been found that the flow leaving the fan at the tips of the blades creates a recirculating bubble structure and it enters the gap as backflow from the higher radii close to the

aluminum panel. By investigating snapshots and using the POD method it has been also observed that inside this recirculating bubble structure, small vortex structures are formed and move from the tip of the blades to the higher radii. It is important to note that in these studies, the entering backflow to the gap was observed from two sides, one after leaving the tip of the blades and immediately rotating back into the gap, and the other one entering the gap from the higher radii carried by the recirculating bubble. In the following sections, in order to characterize the flow pattern and behavior upstream and downstream of the fan close to the gap region, a set of LDA radial traverse measurements will be done.

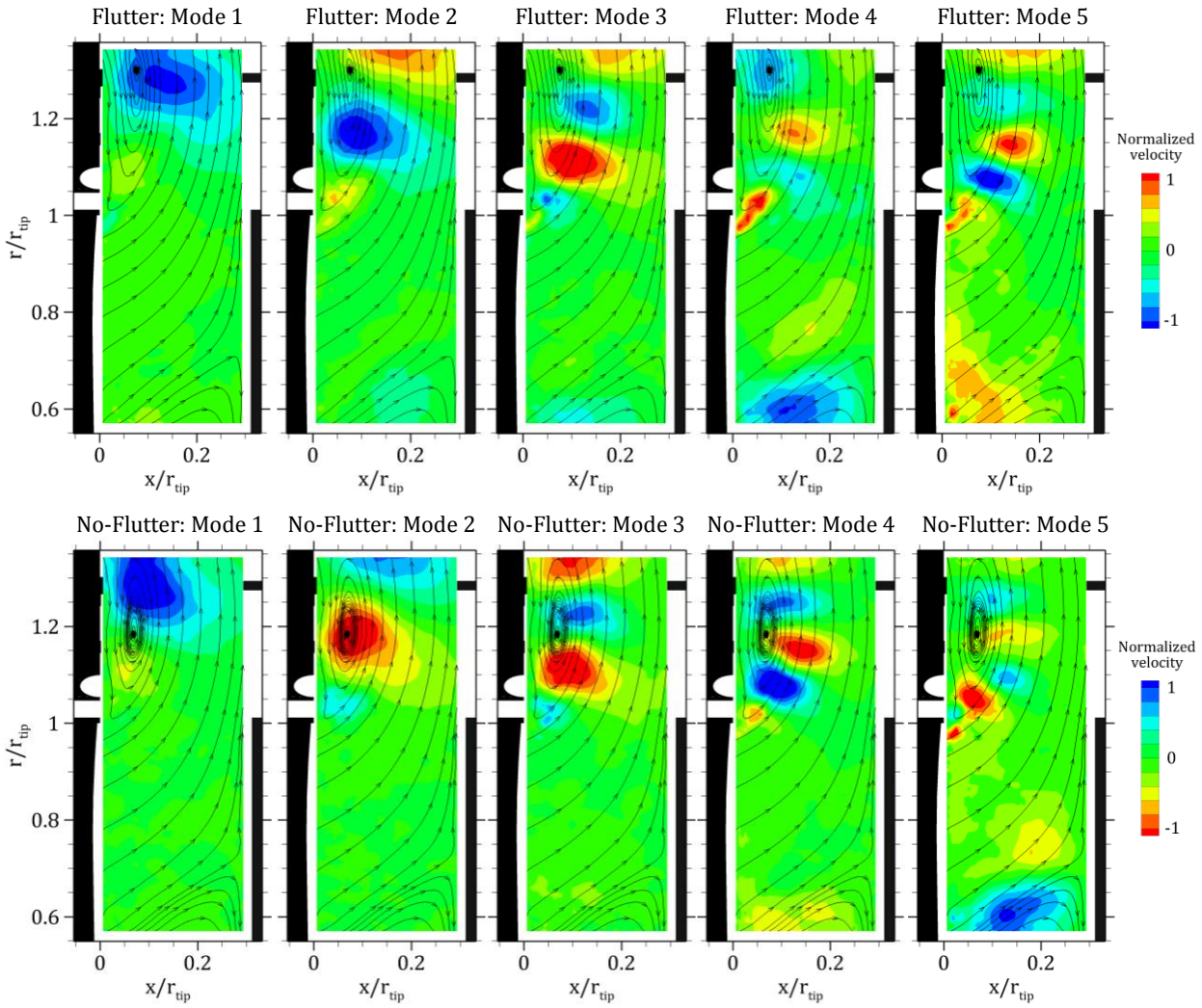

Figure 5.10. POD spatial Modes for velocity component v_a, Flutter and No-Flutter case downstream of the fan. Streamlines are for mean velocity.

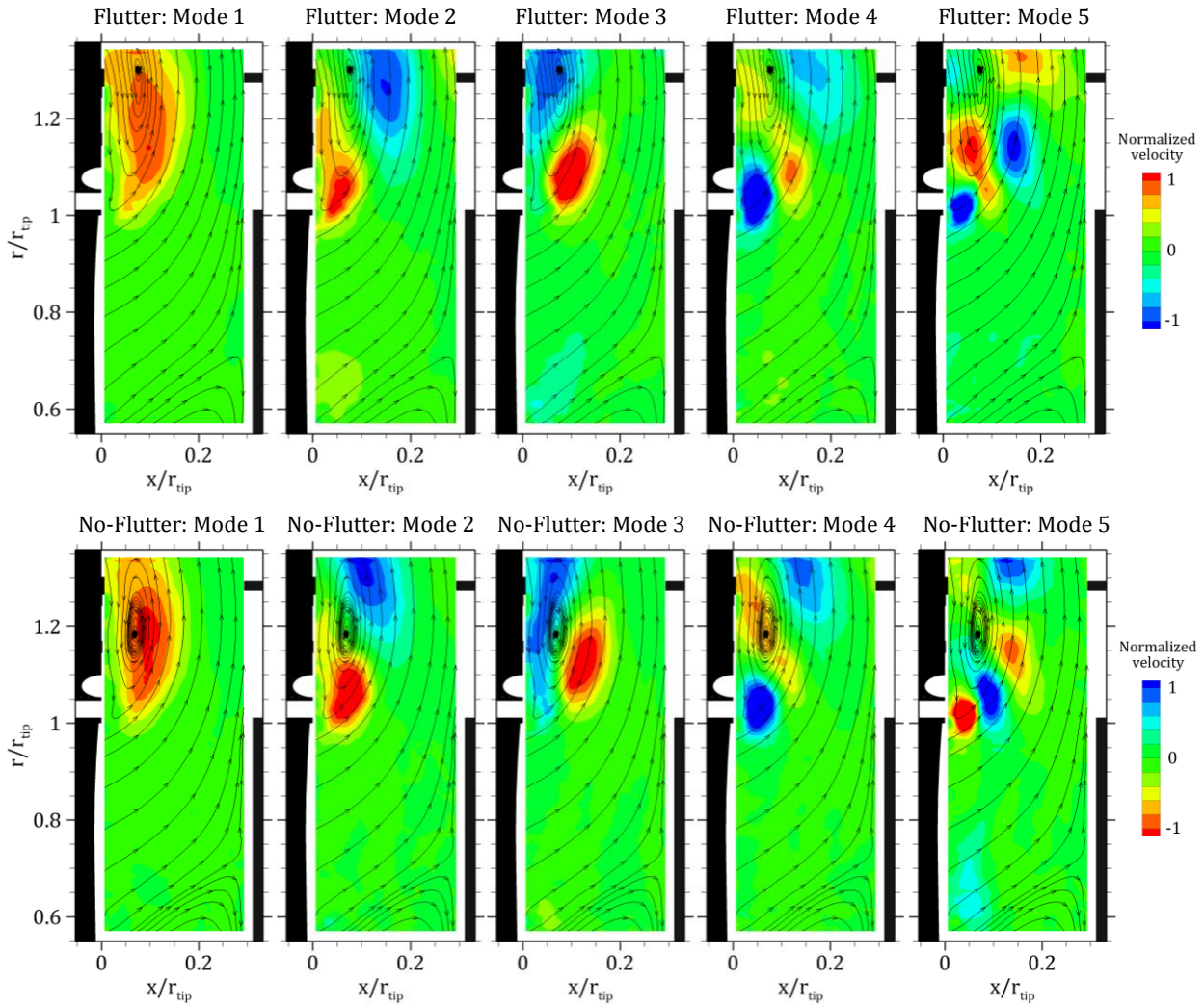

Figure 5.11. POD spatial Modes for velocity component v_r, Flutter and No-Flutter case downstream of the fan. Streamlines are for mean velocity.

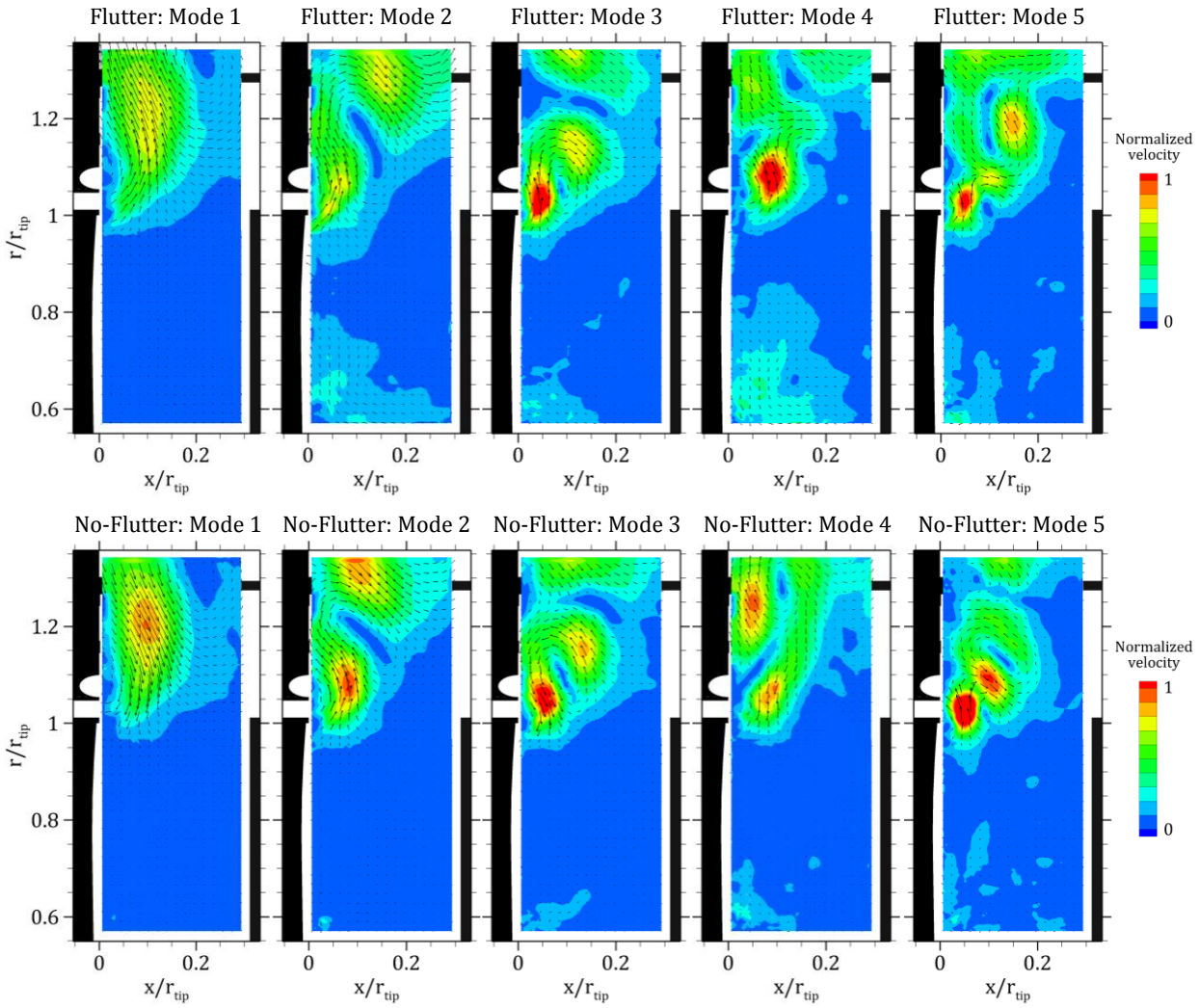

Figure 5.12. POD spatial Modes for velocity components $v_a v_r$, Flutter and No-Flutter case downstream of the fan. Streamlines are for.

5.1.2. LDV measurements

The LDV measurements have been operated in radial traverses placed upstream and downstream of the fan as well as the gap entrance, see Fig. 5.13. The upstream traverse starts radially from $r/r_{tip} = 0.8$ (point U1) and extends to the gap zone $r/r_{tip} = 1$ (point U12) with 5 mm radial steps with an exception point at U11 which is 3 mm below point U12 and 2 mm above point U11. The measuring points have been positioned in a way to be as closer as possible in the axial direction to the blade in order to survey the gap flow in an optimal way. The downstream one starts from $r/r_{tip} = 0.87$ (point D1) and finishes at $r/r_{tip} = 1.15$ (point D15) with 5 mm radial steps and it is axially located 5 mm downstream of the aluminum panel which has been the minimum distance that allowed measuring

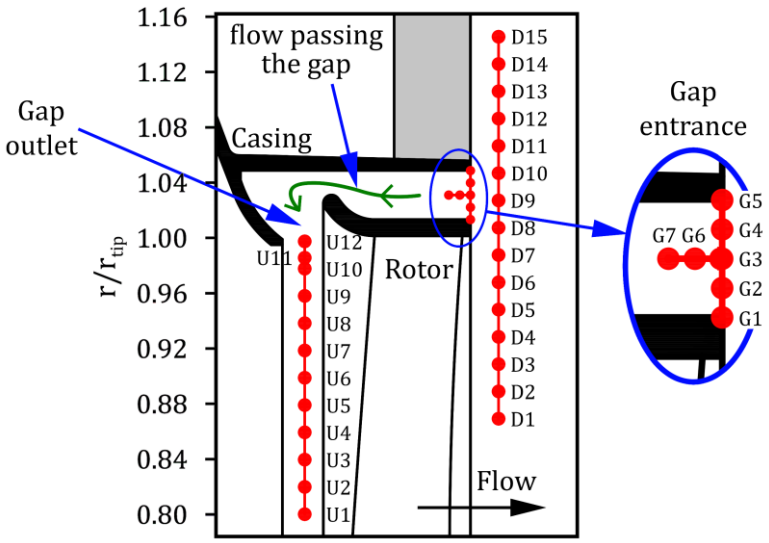

Figure 5.13. LDV measuring points: Upstream (U1-U12), Downstream (D1-D15), and Gap entrance (G1-G7).

in the shroud region in flutter condition. In addition, to complete this survey, 7 points have been measured at the gap entrance with 2 mm radial steps (points G1 to G5) also 2 points in the middle of the gap with 2 mm axial steps (points G6 and G7).

These mean trends have been obtained with the double phase average technique that is explained in chapter 3. Basically, the effects of blade passing perturbation and flutter vibration are identified and subtracted from the mean values.

The double phase average technique requires a very large amount of samples to yield a good statistical uncertainty, due to the highly increased number of bins compared to the standard ensemble average one. Besides, it has to be considered that the data rate, i.e. the number of samples

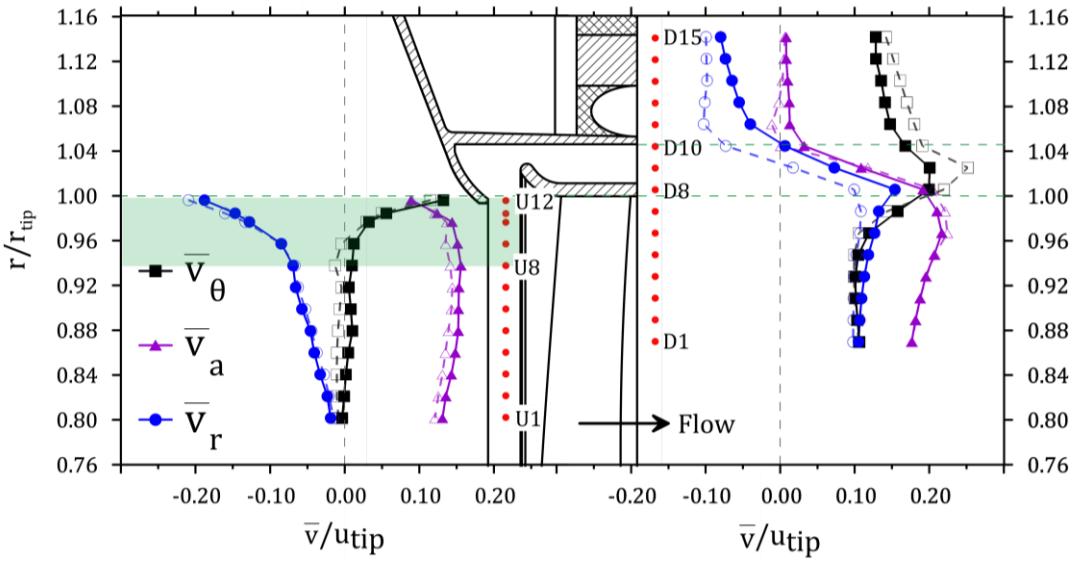

Figure 5.14. Mean velocity components upstream and downstream of the fan in flutter and no-flutter conditions (dashed lines refer to No-flutter case).

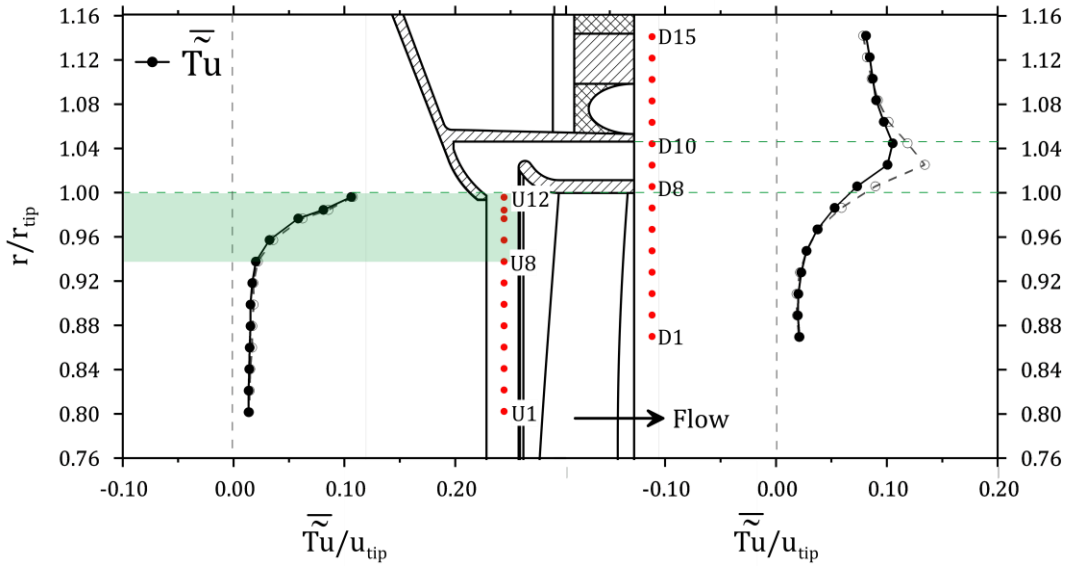

Figure 5.15. Mean turbulence intensity upstream and downstream of the fan in flutter and no-flutter conditions (No-flutter with dashed lines).

per second that are acquired, is highly variable between the point. Therefore, it has been decided to fix the acquisition duration to 360 s, in this way the total amount of collected data is variable per point, and generally, it varies between 800000 and 1500000.

The three velocity components' mean values, evaluated according to Eq. 3.51, and mean turbulence intensity, evaluated according to Eq. 3.55, are depicted in Figs. 5.14 and 5.15 respectively in both

traverses upstream and downstream of the fan for both Flutter (operating point A7 in Fig. 4.13) and No-Flutter (operating point E7 in Fig. 4.13) cases. In Figs. 5.14 and 5.15 the solid lines and filled symbols are indicating the Flutter case while the dashed lines and hollow symbols are referring to the No-Flutter case. The red dots are the measuring points. All the mean velocity components and turbulence intensity are normalized by U_{tip}.

Tangential velocity, $\bar{v}_\theta$, upstream of the fan is almost equal to zero from $r/r_{tip} = 0.8$ to $r/r_{tip} = 0.94$, while in the higher radii it increases rapidly to $\bar{v}_\theta/U_{tip} = 0.14$ when it reaches $r/r_{tip} = 1$, highlighted as a green zone in Figs. 5.14. Downstream of the fan for the flutter case, $\bar{v}_\theta$ is constant when it leaves the fan at the front of the blades, $r/r_{tip} = 0.86 \div 0.96$. When it reaches the blade tip increases to $\bar{v}_\theta/U_{tip} = 0.19$ and it lasts along the gap region and after that decreases to $\bar{v}_\theta/U_{tip} = 0.125$. These trends happen for turbulence intensity, $\widetilde{\overline{Tu}}$, as well as the tangential velocity, see Fig. 5.15. To some extent, tangential velocity and turbulence intensity upstream of the fan are tracers of the backflow entering the gap. An increase in tangential velocity as well as turbulence intensity in the higher radii ($r/r_{tip} = 0.94 \div 1$) close to the gap (highlighted green zone in Figs. 5.14) indicates a backflow that has entered the gap downstream of the fan exits at the outlet of the gap upstream of the fan and interacts with the main flow entering the fan. The gap entrance, the gap outlet, and the streamline passing through the gap are illustrated in Fig. 5.13. For the turbulence intensity, the value at the gap outlet, point U12, is almost equal to the gap entrance, e.g., point D9, which is $\widetilde{\overline{Tu}}/U_{tip} = 0.11$. For the tangential velocity, this difference is around 70% ($\bar{v}_\theta/U_{tip} = 0.14/0.19 = 70\%$). Considering that the measuring points downstream of the fan are axially 5 mm downstream of the aluminum panel and are not exactly at the gap entrance.

Radial velocity, $\bar{v}_r$, upstream of the fan is incrementally negative (pointing down) by moving to higher radii. It is almost zero at $r/r_{tip} = 0.8$ and it gradually decreases up to the lower boundary of the highlighted green zoon at $r/r_{tip} = 0.94$, then it sharply decreases to almost $\bar{v}_r/U_{tip} = -0.2$ at $r/r_{tip} = 1$. It indicates that also radial velocity is affected by the backflow jet leaving the gap outlet, which causes the main entering flow to be more centripetal at the higher radii. Axial velocity, $\bar{v}_a$, upstream of the fan is almost constant and positive below the highlighted green zone while when it mixes with the backflow from the gap outlet it decreases almost 40% form $\bar{v}_a/U_{tip} = 0.15$ to $\bar{v}_a/U_{tip} = 0.085$.

Downstream of the fan, $\bar{v}_r$ shows when the flow is either centrifugal or centripetal. Due to the presence of the wooden panel, when flow leaves the fan at the front of the rotor from $r/r_{tip} = 0.86$

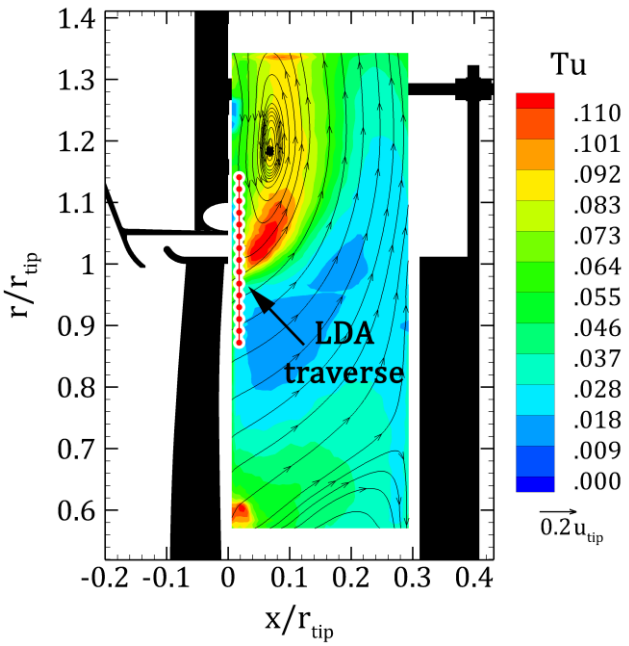

Figure 5.16. Velocity streamlines added to the turbulence contour measured by PIV downstream of the fan. Red dots indicating the measured LDV radial traverse.

up to the blade tip it is always positive with the value increasing from $\bar{v}_r/U_{tip} = 0.1$ to $\bar{v}_r/U_{tip} = 0.15$ for the flutter case. By moving to the higher radii first it decreases along the gap entrance and becomes zero at $r/r_{tip} = 1.045$ for the flutter case, then the sign changes and flow is centripetal along the aluminum panel, $r/r_{tip} = 1.045 \div 1.15$. The trend of axial velocity downstream of the fan is almost similar to the radial one except that it is always positive below the blade tip and by moving to the higher radii at the gap region it decreases and becomes zero along the aluminum panel.

These results are consistent with the PIV measurements downstream of the fan which for ease of understanding this consistency, velocity streamlines added to the turbulence contour are illustrated in Fig. 5.16 with red dots indicating the measured LDV radial traverse. By looking at the streamlines, measured LDV points located below the blade tip are at the path of leaving flow jet which immediately becomes centrifugal. At the higher radii along the aluminum panel, $r/r_{tip} = 1.045 \div 1.15$, measured LDV points located at the edge of recirculating bubble which is fully centripetal with almost zero axial velocity, and it is why the sign of radial velocity in the LDA trend becomes negative.

In this set of LDA measurements downstream of the fan it was expected to see negative axial velocity entering the gap but because the measured points are axially located 5 mm downstream of the aluminum panel, axial velocity along the gap region is positive. Due to this reason to measure flow

entering the gap a new set of LDA measurements has been operated exactly at the gap entrance as shown in Fig. 5.13 (points G1 to G5).

Gap entrance three velocity components' mean values and mean turbulence intensity traverse are depicted in Figs. 5.17 and 5.18 respectively for both Flutter and No-Flutter cases. Here also the solid lines and filled symbols are indicating the Flutter case while the dashed lines and hollow symbols are referring to the No-Flutter case. The red dots are the measuring points. All the mean velocity components and turbulence intensity are normalized by U_{tip}.

Tangential velocity and turbulence intensity along the gap entrance (points G1 to G5) are almost equal to the gap outlet value upstream of the fan. Tangential velocity decreases by moving to the higher radii from point G1 ($\bar{v}_\theta/U_{tip} = 0.2$) to G5 ($\bar{v}_\theta/U_{tip} = 0.15$) while at the gap outlet (point U12) it is equal to 0.14. Furthermore, turbulence intensity increases by moving to the higher radii from point G1 ($\overline{\widetilde{Tu}}/U_{tip} = 0.09$) to G5 ($\overline{\widetilde{Tu}}/U_{tip} = 0.12$) while at the gap outlet (point U12) it is equal to 0.11.

Radial and axial velocity were positive downstream of the fan along the gap region (points D8 to D10) at 5 mm axially far from the aluminum plate, while at the gap entrance radial velocity starts from almost zero at point G1 ($\bar{v}_r/U_{tip} = -0.02$) and reaches -0.16 at higher radii (point G5). Meanwhile, axial velocity also turns to the negative and varies between $\bar{v}_a/U_{tip} = -0.15 \div -0.1$. It means at the gap entrance backflow enters the gap which is not present in a few millimeters (Here 5 mm) axially far from the gap entrance. In other words, the backflow may enter the gap from the lower radii, from the blade's tip, or from the upper radii, the recirculating bubble flow close to the aluminum panel, which will be discussed in the next sections. But whatever the origin of the backflow is, it is observed that this backflow moves in a thin layer near the gap entrance and enters it.

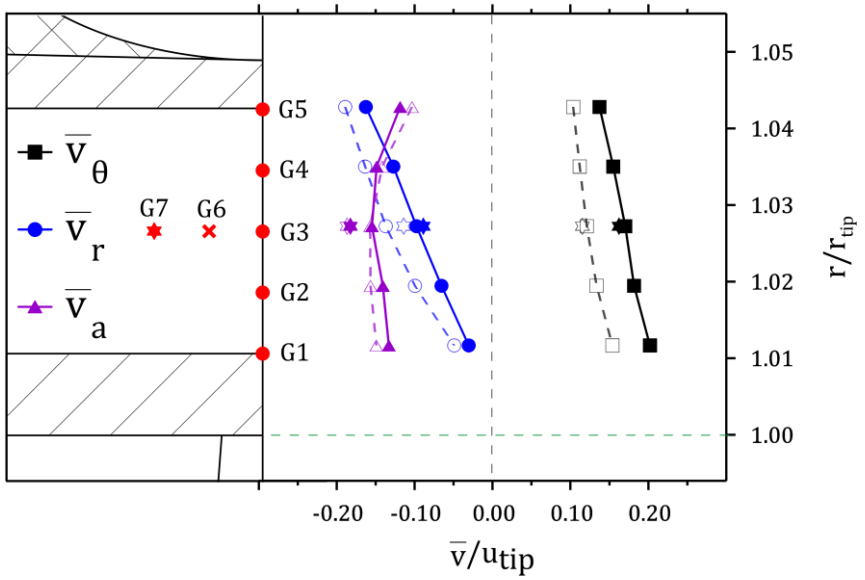

Figure 5.17. Mean velocity components downstream of the fan (Gap region) for flutter and no-flutter conditions (no-flutter with dashed lines).

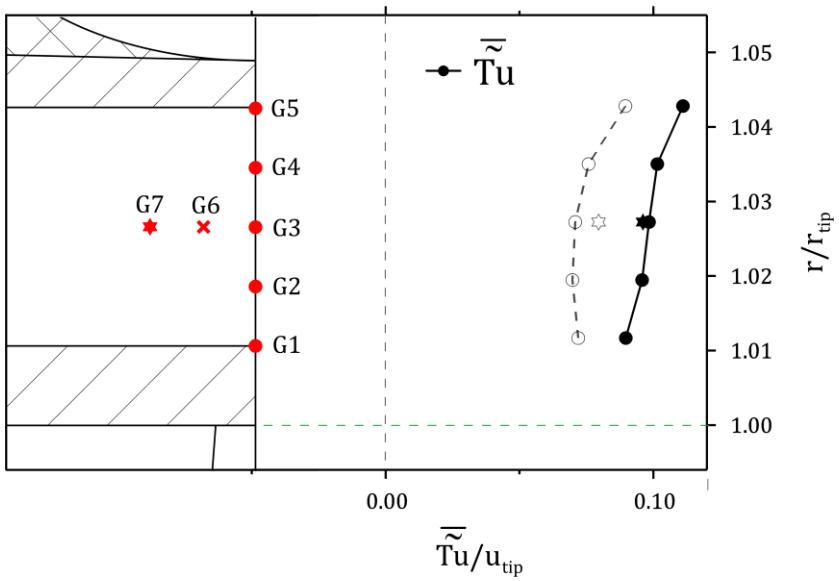

Figure 5.18. Mean turbulence intensity downstream of the fan (Gap region) for flutter and no-flutter conditions (no-flutter with dashed lines).

5.2. Double phase ensemble averaged periodic flow filed

In section 5.1, a complete survey has been done upstream and downstream of the fan and the mean flow field has been characterized close to the gap region. It has been found that a recirculating flow takes place downstream of the fan right after the flow leaves the fan from the blade tip to the higher radii then it enters the gap as a backflow, after passing through the gap at the gap outlet it mixes with the entering flow close to the blade tip upstream of the fan. The mean flow of LDA measurements was calculated by the double phase locked ensemble average technique. In this technique which is introduced in Chapter 3, the velocity signal is characterized by two simultaneous periodic components, one related to the blade passing period or the fan rotational period which is measured by a Tachometer and here it is called Tacho-periodicity, and another periodic component is related to the flutter phenomenon which is measured by a Vibrometer and here it is called Vibro-periodicity.

In order to better interpret the velocity contours upstream and downstream of the fan, the schematic of the fan is depicted in Fig 5.19a. In the figure the fan's direction of rotation (ω_r), precession motion (ω_v), and the axial position of the rotor within the stationary shroud is illustrated. This axial position, which is calculated with regard to the precession motion, is shown by a black and white contour stripe around the rotor.

As explained in previous chapters, precession motion tilts the rotor in the stationary shroud, in a way that for instance at 0° in the plot, the rotor's ring axially leans toward upstream of the fan and closes

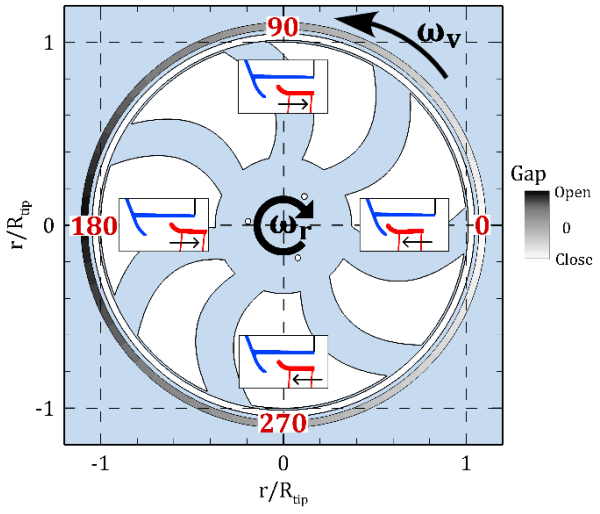

Figure 5.19. Direction of rotation of the rotor (ω_r) and whirling motion (ω_v), plus four schematic positions and a circular black and white contour strip illustrating the gap opening.

the outlet gap (the small schematic figure of 0° position) which for simplicity from now this position will be named closed-gap.

At the same time, in the opposite direction at 180°, the rotor's ring axially leans toward downstream of the fan and opens the gap outlet (the small schematic figure of 180° position) which for simplicity from now this position will be named open-gap.

However, at the angular positions of 90° and 270°, the axial position of the rotor's ring is in the neutral state without any movement (the small schematic figures of 90° and 270° position).

To have a better understanding of the following contour plots, this contour strip and the four schematic figures related to the rotor's precession motion and axial position of the rotational ring within the stationary shroud are combined with the contours of the phase average of all velocity components, turbulence intensity, and β angle based on Vibro-periodicity.

This section is divided into two subsections: the first subsection will be studied the LDA radial traverse measurements upstream (points U1 to U12) and downstream (points D1 to D15) of the fan; in the second subsection, the LDA radial traverse measurements at the gap entrance (points G1 to G5) will be discussed.

5.2.1. Double phase ensemble averaged periodic flow field upstream and downstream of the fan

1. Upstream of the fan (points U1 to U12), Tacho-periodicity:

The typical effect of the potential field of the blade is present in all the velocity components and turbulence intensity, see Figs. 5.19 and 5.21. Generally, at the upstream of the axial fans the absolute flow field must be only axial, while here due to the shape of the casing which is playing as a convergent duct, the flow has a negative radial component at the range of $r/r_{tip} = 0.8 \div 1$ carrying from the higher radii which is reported (mean velocity) in Fig. 5.14. Furthermore, at the gap outlet, backflow exits the gap and mixes with the axial main flow entering the fan in the range of $r/r_{tip} = 0.94 \div 1$; due to this reason at this range close to the blade tip, flow is not purely axial and it has tangential and additional radial components which are carried by the backflow through the gap to the main inflow upstream of the fan. Similar to mean velocity this effect is evident as a presence of a periodic pattern of high positive v_r and negative (centripetal) v_θ in the range of $r/r_{tip} = 0.94 \div 1$ in Figs. 5.19 and 5.21. The presence of non-zero tangential velocity surely needs evaluation of the angle of attack in this range. This evaluation can be done by analyzing the β angle (angle between relative

and blade linear velocities) which is presented in Fig. 5.22. The β angle is consistent with the flow periodicity and the effect of backflow mixes the main inflow which has been characterized already for velocity components.

Evaluating turbulence in Fig. 5.21 also shows a high turbulence zone at $r/r_{tip} = 0.94 \div 1$ which has been carried by the backflow through the gap and released from the gap outlet with a certain periodicity. Such a periodicity may be due to the pressure field of the blade which is reorienting or changing flow leaving the gap, or it is also possible this periodicity has been carried by the backflow.

Below this range, where the backflow affects the main inflow, at lower radii ($r/r_{tip} < 0.94$) the presence of the blade is inducing acceleration, deceleration, and the reorientation of the incoming flow according to the pressure field in the way to generate a periodic pattern in velocity components. The amplitude of periodicity is strictly related to the aerodynamic field of the blades, e.g., angle of attack, and also the axial distance from the blades. In this case, it is even more complicated to discuss this periodic distribution because the blade is not radially stacked; it means the axial distance of each measuring point to the blade's surface changes at different radii.

Comparing No-Flutter and Flutter cases it can be seen that apart from minor differences there is no apparent dissimilarity between these two cases.

2. Upstream of the fan (points U1 to D12), Vibro-periodicity:

Figures 5.23 and 5.24 show velocity components and turbulence intensity which has driven by the double phase ensemble average base on Vibro-periodicity. Unlike double phase ensemble average base on Tacho-periodicity, using the Vibro-periodicity makes it possible to lock the flow in the period of the vibration and see the effect of the precession motion of the rotor when the rotor is in the position of open- or closed-gap.

The most noticeable point among all the velocity components is the difference between Flutter and No-Flutter cases. In all the Flutter contour plots a kind of circumferential disuniformity related to the precession motion of the rotor is present while in the No-Flutter case, velocity components are axisymmetric and without any periodicity; it shows the presence of flutter completely changes the flow field. The effect of flutter can change the behavior of the blades, introducing an increase or decrease in turbulence production due to different angles of attack on the blade.

In all three velocity components for the Flutter case, there is a maximum velocity region that takes place at almost the angular range of $90^{\circ} \div 160^{\circ}$ and its center is at 120°; also a minimum velocity region with 180° shift to the maximum and its center is around 300°; it means when the rotor is

vibrating (fluttering) and whirling counterclockwise around its axis it tilts, and at 180° where it is at the open-gap position or in other words the rotor's ring is axially moved downstream of the fan, an increase for all the velocity components is present with a certain delay of almost 60° ($180^{\circ} - 120^{\circ}$). Also, it should be considered that when the rotor is at the open-gap position at 180° as the measuring point is a fixed point in space, data are measured axially closer to the rotor's ring than the neutral position of the rotor when the fan is not fluttering. On the contrary, at the closed-gap position at 0° data are measured axially farther from the rotor's ring than the neutral position of the rotor.

These changes in the velocity components are consistent with the change in β angle because this angle also has a maximum variation at the same angular position (around 120°), see Fig. 5.25

To make a comparison, contours of velocity components, turbulence, and β angle in angular positions of maximum and minimum for flutter and no flutter cases are sliced radially, Figs. 5.23, 5.24, and 5.25. Slice line 1 in black is representing the radial cut at maxima peaks, 120°, and slice line 2 in magenta is associated with the radial cut at minima peaks, 300°.

In Fig 5.26a and Fig 5.26b, which are showing Flutter and No-Flutter cases respectively, the black and magenta lines are representing the radial traverse of three velocity components at slice lines 1 and 2, respectively, and the dashed grey lines are associated with the mean profiles which were introduced previously in Fig 5.14 and Fig 5.15.

Focusing on the range $r/r_{tip} = 0.94 \div 1$ (green zone) where flow leaving the gap outlet mixes with flow entering the fan; in slice line 1 which is associated with the open-gap position, considering the gap outlet is increased and more open, flow in comparison to the mean profile is more axial and less radial, while, tangential velocity and turbulence are the same; on the other hand, in slice line 2 which is associated with the closed-gap position, due to a decrease in gap outlet area, the flow compared to the mean profile is more radial and less axial; here again, the tangential velocity and turbulence remain constant.

Knowing that the tangential velocity is not changing in any of the cases while axial, radial, and subsequently, meridional velocities are changing, it can be seen that the affected β angle by backflow in the green zone is changing accordingly. This change in β angle is evidence of a change in the angle of attack at the blade's tip.

For the No-Flutter case, since there is no axial displacement in the rotating ring also, no change in the gap outlet area, the whole velocity components, turbulence, and β are axisymmetric, hence all the radial traverse values in slice lines 1 and 2 are equal to the mean profile.

3. Downstream of the fan (points D1 to D15), Tacho-periodicity:

Considering measuring LDA traverse on the PIV mean velocity streamlines in Fig. 5.16, similar to the mean velocity for points D1 to D15 which has been discussed in section 5.1 here the flow field can be radially separated into three zones: Zone 1, from the lower radii to the blade tip ($r/r_{tip} = 0.86 \div 1$) where the flow leaves the fan and becomes centrifugal; Zone 2, the gap region ($r/r_{tip} = 1 \div 1.045$); Zone 3, from the point D10 to the higher radii ($r/r_{tip} = 1.045 \div 1.15$) where the flow is fully centripetal along the aluminum panel (almost zero axial velocity).

Looking in Figs. 5.27 and 5.28, in zone 1, the presence of the wake is easily recognizable at the trailing edge of the blades where the turbulence and tangential velocity are high; due to the shape of the blades highlighting the wake for radial and axial velocities are not so easy; however, both radial and axial components are positive, it means flow leaving the gap and it is centrifugal; high and low axial velocities take place in the position of the blades and the middle pitch of the blades, respectively.

It is worth mentioning that at the blade tip when the flow is passing along the inner surface of the rotating ring which has a speed $u_{tip} = 71.2\,\mathrm{m/s}$ for the flutter case, the tangential velocity rapidly increases due to the skin friction drag; it is present as a high amplitude red region from the mid chord of the blade to the leading edge; this effect is also can be recognizable in the turbulence plot in the same region.

In zone 2 or the gap region, the backflow enters the gap from the two sides (lower radii or blade tip and higher radii or along the aluminum panel) and passes along the outer surface of the rotating ring inside the gap. This backflow has a certain large tangential velocity and turbulence intensity due to different origins; one of the important origins can be carried from the blade tip to the gap which is recognizable as a high amplitude red region from the mid chord of the blade to the leading edge close to the inner and outer surface of the rotating ring; another important origin is due to the skin friction drag inside the gap between the backflow and the outer surface of the rotating ring; the minor origin maybe is due to the tangential velocity that is carried by the backflow entering from the higher radii (the edge of recirculating flow along the aluminum panel).

In zone 3, axial velocity is almost zero, radial velocity is centripetal, and tangential velocity is small because this zone is located at the edge of recirculating flow coming back from higher radii, see Figs. 5.27 and 5.28.

Similar to the upstream of the fan, by comparing No-Flutter and Flutter cases it can be seen that apart from minor differences there is no dissimilarity between these two cases. Also, for sake of completeness β angle is added here, Fig. 5.29.

4. Downstream of the fan (points D1 to D15), Vibro-periodicity:

It can be hypothesized that, if there is a kind of Vibro-periodicity that has been found upstream of the fan due to the precession motion of the rotor then this periodicity should be present downstream of the fan as well, even if it is not always granted.

Figures 5.30 and 5.31 are showing velocity components and turbulence intensity which has driven by the double phase average base on Vibro-periodicity.

Using the same determined radial zones, for the Flutter case at zone 1 in the range of $r/r_{tip} = 0.86 \div 0.94$ where the backflow is not effected the main inflow, there is a low tangential velocity region, $\tilde{V}_\theta/U_{tip} \cong 0.098$, spread around 0° angular position when the gap is close and the flow is less deflected by the fan, while on the other side, 180° angular position, when the gap is open the tangential velocity is slightly higher, $\tilde{V}_\theta/U_{tip} \cong 0.116$; at the higher radii up to the blade tip, $r/r_{tip} = 0.94 \div 1$, where the backflow mixes with the main inflow there is an augmentation of high tangential velocity attached to the inner surface of the rotating ring due to the skin friction drag at the angular range of $20^\circ \div 150^\circ$. Radial velocity is always positive in this zone and the maximum takes place around 120° angular position while the minimum is shifted 180° from the maxima; the position of these maximum and minimum are similar to the radial velocity upstream of the fan. The axial velocity is a bit peculiar because the maximum is located at the angular position of 180° where the gap is open and it extends with a small decrease to 0°, while the minimum is at the angular position of 90°. Furthermore, it is hard to talk about the turbulence intensity in this zone as it has different maxima and minima.

In zone 2 or the gap region, an augmentation of tangential velocity and turbulence intensity is present as confirmed by the mean profile in Fig 5.14. Tangential velocity in the gap region has two maxima and perhaps two origins, one is coming from the blade tip and is started from the angular position of 150° continuous to 220° and it is close to the lower radii of the gap; another one that is close to the upper radii of the gap and located in the angular range of $260^\circ \div 330^\circ$ has a different unknown origin (it may come from the higher radii by backflow). In the continuation of the radial velocity in zone 1, also in the gap region, the maximum velocity takes place around 120° angular position. Axial velocity

is always positive as it is axially 5 mm downstream of the fan. Similar to zone 1 again it is difficult to characterize the origin of the two high turbulence regions in this zone.

In zone 3 where the flow is centripetal and comes from the recirculating bubble, the tangential velocity is minimum at the angular range of $90^{\circ} \div 220^{\circ}$; to some extent, this is in contrast to zones 1 and 2 where the maxima are located in this angular range. Radial velocity is centripetal in this zone but it has the same angular position of maximum and minimum regions as inner radii where the flow is centrifugal. Axial velocity is almost zero in this zone but similar to the radial component it has the same angular position of minimum and maximum comper to the lower radii where the flow leaves the fan as a jet. It seems at angular positions where the flow is more axial it is less radial and vice versa. The turbulence distribution in this zone with two high angular spots is again very complex.

In the No-Flutter case, velocity components and turbulence intensity are axisymmetric and without any periodicity. Also, for sake of completeness β angle is added here, Fig. 5.32.

5.2.2. Double phase ensemble averaged periodic flow field at gap entrance

In the previous section by studying the mean flow field characteristic it has been found that by moving the measuring LDA points to the gap entrance the flow pattern behaves differently and in this location, more complete and accurate information about the backflow entering the gap has been obtained. Due to this reason, the double phase ensemble average analysis has been applied to the velocity components data collected by LDA measurements at the gap entrance. This kind of analysis again can provide a better view of the flow entering the gap.

1. The gap entrance (points G1 to G5), Tacho-periodicity:

By looking in Figs. 5.33 and 5.34, as expected and analogous to the mean velocity profiles the axial component in the Flutter case is always negative; at the blade presence as well as the higher radii (close to the stationary shroud) it has the maximum negative value and in the middle pitch of the blades it has the minimum negative; the presence of maxima and minima close to the stationary shroud shows that in this radius the flow is more affected by blade passing than the radii close to the rotating ring.

For the radial velocity in the Flutter case also the effect of blades passing is present; it is almost always negative, which means it is centripetal; the most interesting fact is that the maximum negative velocity is close to the stationary shroud while it is close to the zero and perhaps sometimes positive (centrifugal) at lower radii near to the ring. It proves that the flow enters the gap from two opposite

radial directions: higher radii along the aluminum panel and lower radii at the front of the blade tip leading edge.

Comparing No-Flutter and Flutter cases for axial and radial velocity components it can be seen that apart from minor differences there is no dissimilarity between these two cases.

It has been discussed previously for the tangential velocity at radial traverse of points D1 to D15 specifically close to the gap entrance (D7 to D11), the backflow has a certain large tangential velocity and turbulence intensity due to different origins. By moving axially to the gap entrance almost the same pattern happens. Here is also important tangential velocity in the Flutter case comes from the blade tip as it can be seen in Fig. 5.34, the high tangential zone is close to the ring. This effect is partially related to the skin friction drag inside the gap between the backflow and the outer surface of the rotating ring.

As for the turbulence intensity in the Flutter case, the high turbulence flow comes from the higher radii and it has the maximum value close to the stationary shroud. By approaching lower radii (close to the ring) the turbulence decreases to its minimum value where the tangential velocity is maximum. It means the flow entering the gap from the higher radii is already more turbulent than the flow coming from the blade tip.

In the No-Flutter case, tangential velocity and turbulence intensity decrease but those follow the same pattern as in the Flutter case. Also, for sake of completeness β angle is added here, Fig. 5.35.

2. The gap entrance (points G1 to G5), Vibro-periodicity:

Investigating entering backflow to the gap at the gap entrance by considering the vibration periodicity can provide interesting information related to the precession motion of the rotor and gap size, and this information can be compared with the flow leaving the gap at the gap outlet upstream of the fan; when comparing these two, it has to be considered that at the gap outlet just a point at the middle of gap outlet has been measured, point U12.

Similar to the velocity components at the gap outlet the most perceptible point among all the velocity components at the gap entrance is the difference between Flutter and No-Flutter cases. In all the Flutter contour plots a kind of periodicity related to the precession motion of the rotor is present while in the No-Flutter case, velocity components are almost axisymmetric and without any periodicity.

In all three velocity components, turbulence intensity, and β angle for the Flutter case, there is a maximum or minimum that takes place at almost the angular range of $70^{\circ} \div 130^{\circ}$ with a center in 100° which is almost 20° $(120^{\circ} - 100^{\circ})$ shifted as a center of velocities peaks compared to the flow leaving the gap outlet; these minima and maxima peaks happen with a certain delay $(180^{\circ} - 100^{\circ} = 80^{\circ})$ relative to the gap fully open condition at 180°, see Figs. 5.36, 5.37, and 5.38.

For the three velocity components when the rotor is vibrating (fluttering) and whirling counterclockwise around its axis, by monitoring the gap size the following points are noteworthy:

By moving from 0° where the gap is close and axially more upstream of the fan and before reaching the gap fully open condition (180°), the gap opens and at a certain angular position (100°) the axial distance of the ring relative to the stationary shroud is such a way that lets the backflow coming from the higher radii along the aluminum panel enter the gap axially with the maximum speed; it means that at this condition (angular position) the most flow suction to the gap happens. At the same time and same angular position, the radial velocity at the radii close to the ring is slightly centrifugal (positive) which means at this condition flow enters the gap directly from the blade tips.

Tangential velocity is also maximum at this condition specifically at the radii close to the ring due to the skin friction drag and also the flow that comes from the blade tips has more tangential velocity. Furthermore at this angular position from the higher radii flow carries the tangential velocity from the recirculating bubble but with a smaller value than the lower radii origin.

Turbulence intensity follows the same pattern; at the same angular position (100°) turbulence increases specifically at the higher radii where the flow that comes from the recirculating bubble is more turbulent.

The β angle is consistent with the velocity components and it has the maximum at the higher radii and the minimum close to the ring at the aforementioned angular position.

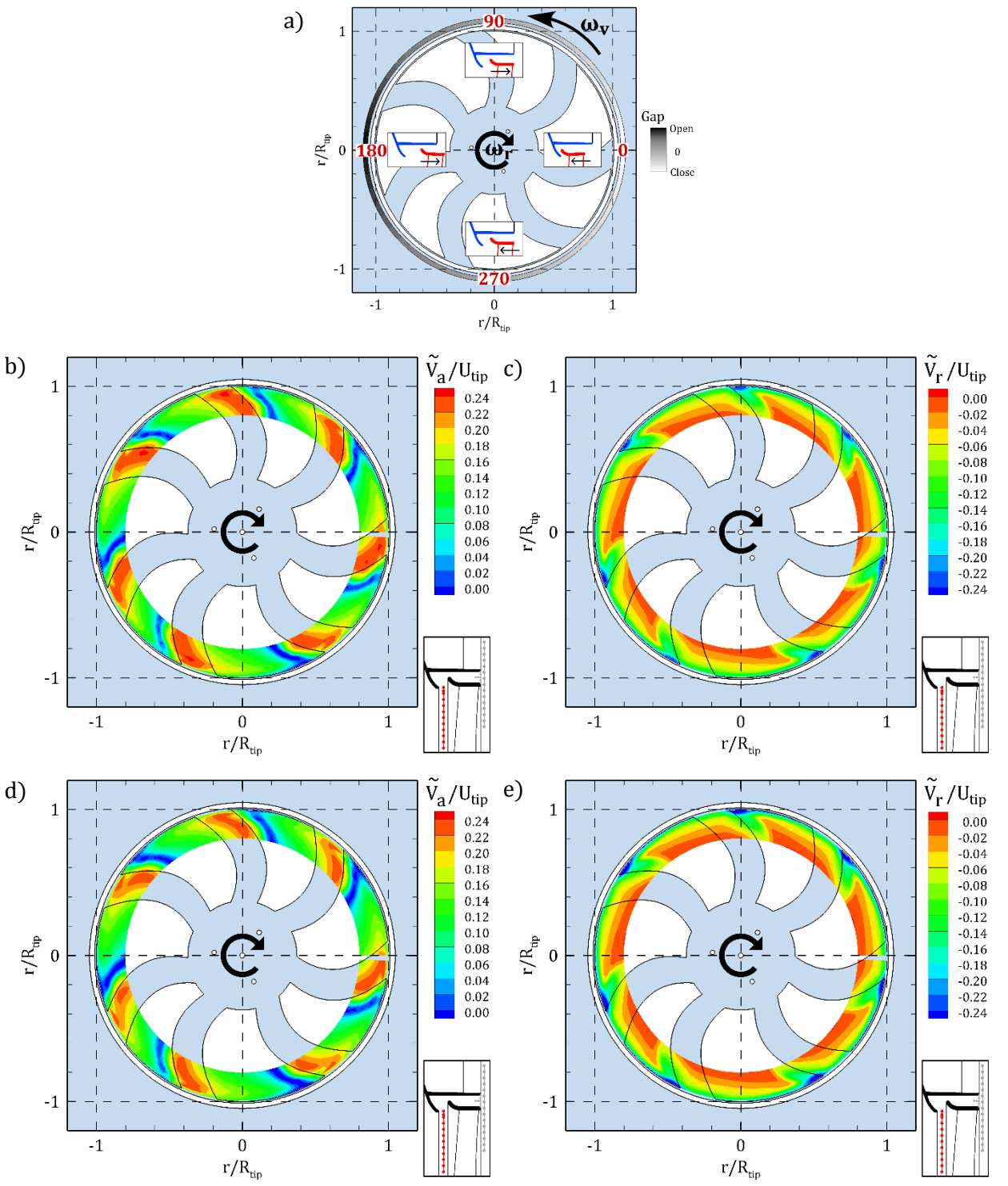

Fig. 5.20. Double phase average (Tacho periodicity) of LDV radial traverse measurements upstream of the fan. a) Direction of rotation of the rotor (ω_r) and whirling motion (ω_v), plus four schematic positions and a circular black and white contour strip illustrating the gap opening. b) Axial velocity (Flutter). c) Radial velocity (Flutter). d) Axial velocity (No-Flutter). e) Radial velocity (No-Flutter).

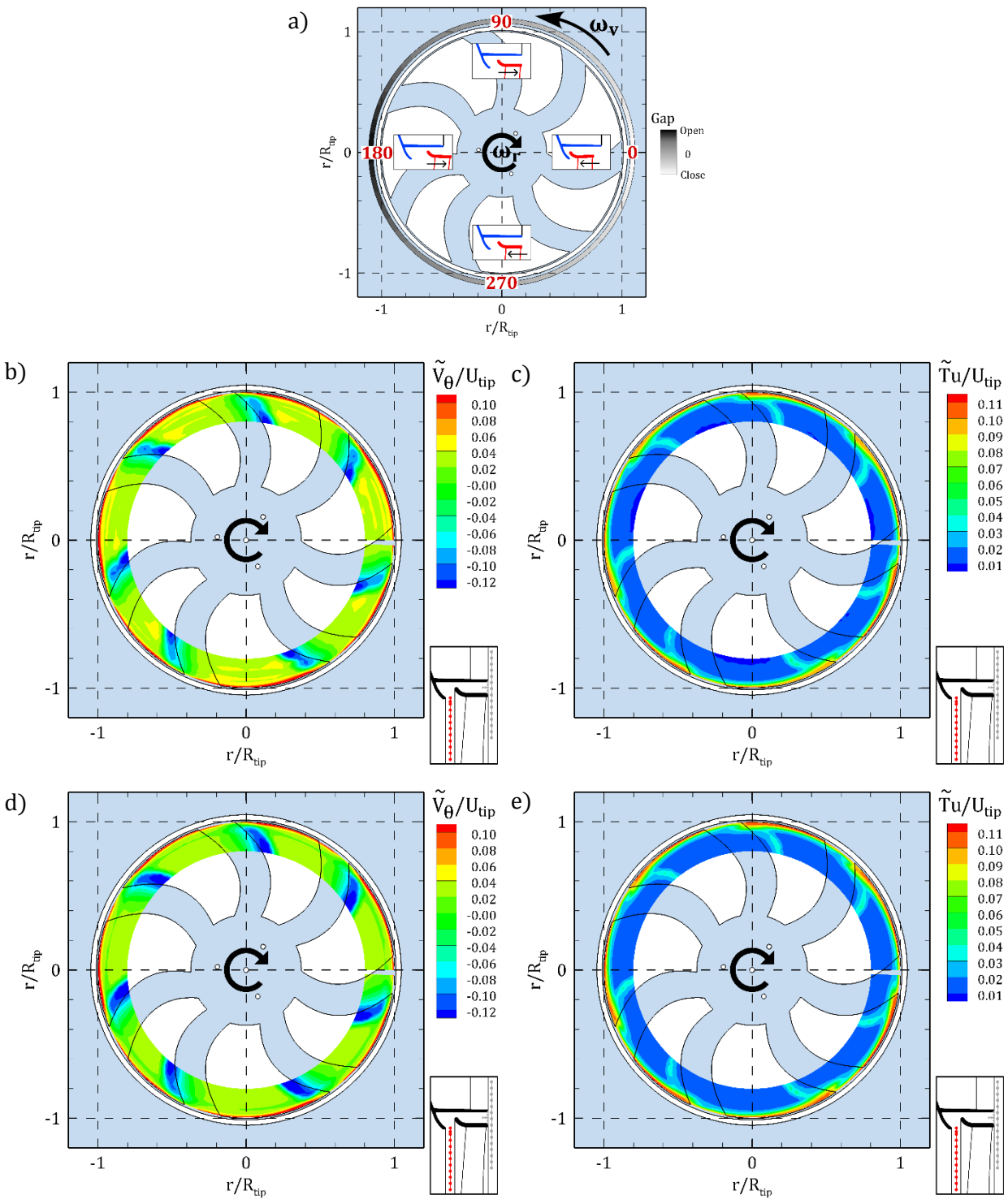

Fig. 5.21. Double phase average (Tacho periodicity) of LDV radial traverse measurements upstream of the fan. a) Direction of rotation of the rotor (ω_r) and whirling motion (ω_v), plus four schematic positions and a circular black and white contour strip illustrating the gap opening. b) Tangential velocity (Flutter). c) Turbulence intensity (Flutter). d) Tangential velocity (No-Flutter). e) Turbulence intensity (No-Flutter).

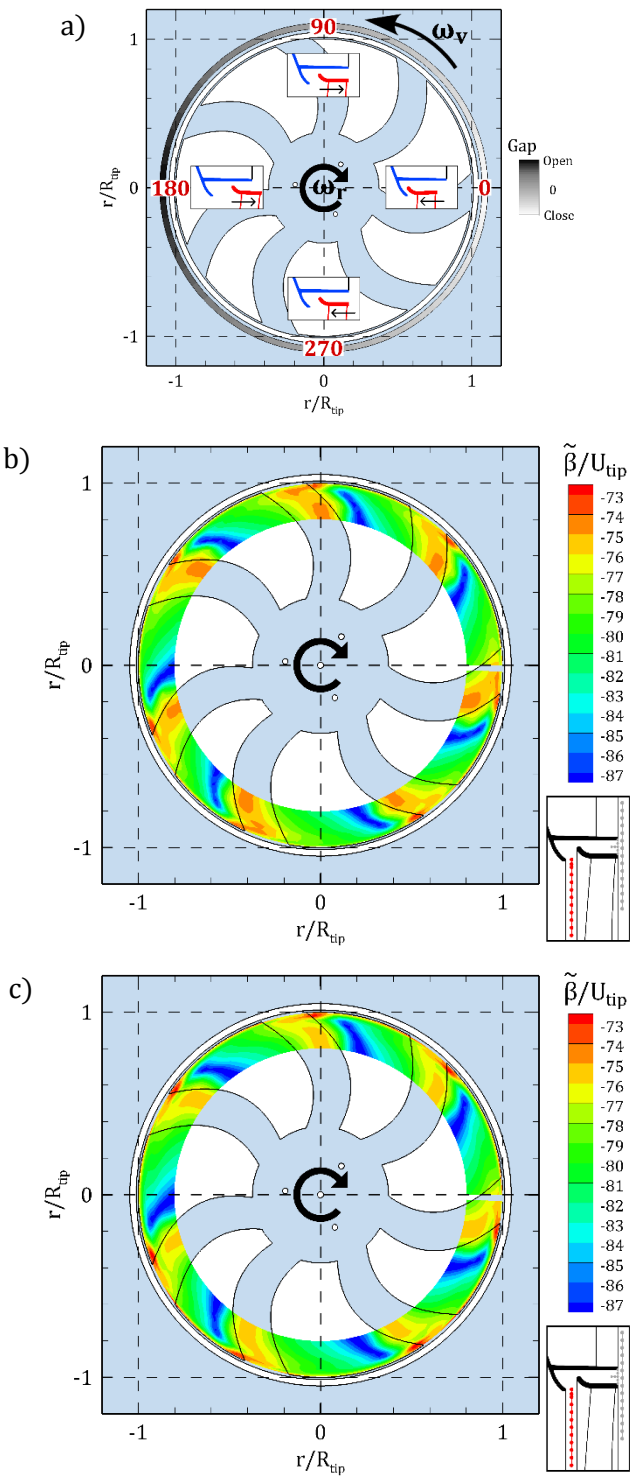

Fig. 5.22. Double phase average (Tacho periodicity) of LDV radial traverse measurements upstream of the fan. a) Direction of rotation of the rotor (ω_r) and whirling motion (ω_v), plus four schematic positions and a circular black and white contour strip illustrating the gap opening. b) β angle (Flutter). c) β angle (No-Flutter).

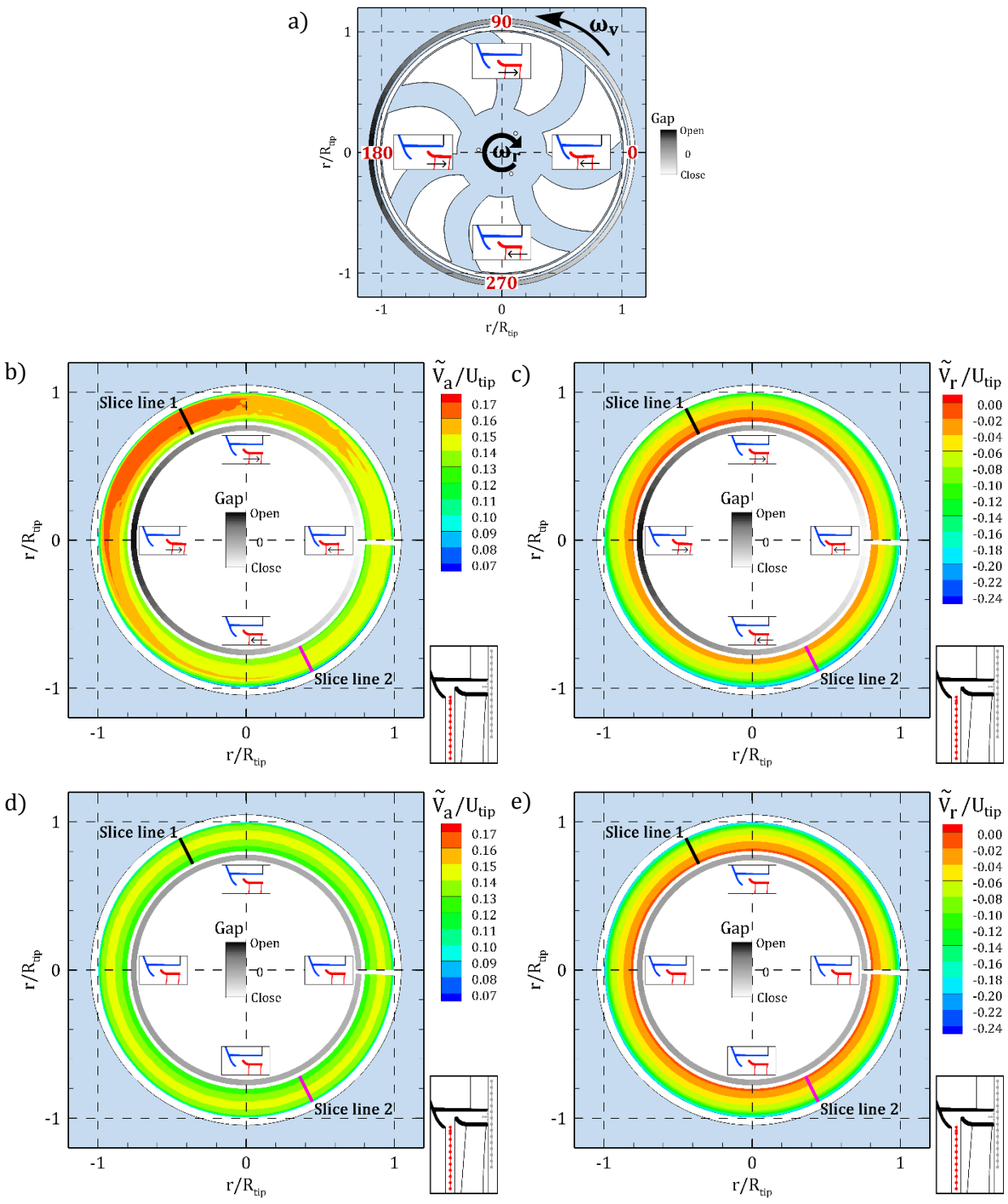

Fig. 5.23. Double phase average (Vibro periodicity) of LDV radial traverse measurements upstream of the fan. a) Direction of rotation of the rotor (ω_r) and whirling motion (ω_v), plus four schematic positions and a circular black and white contour strip illustrating the gap opening. b) Axial velocity (Flutter). c) Radial velocity (Flutter). d) Axial velocity (No-Flutter). e) Radial velocity (No-Flutter).

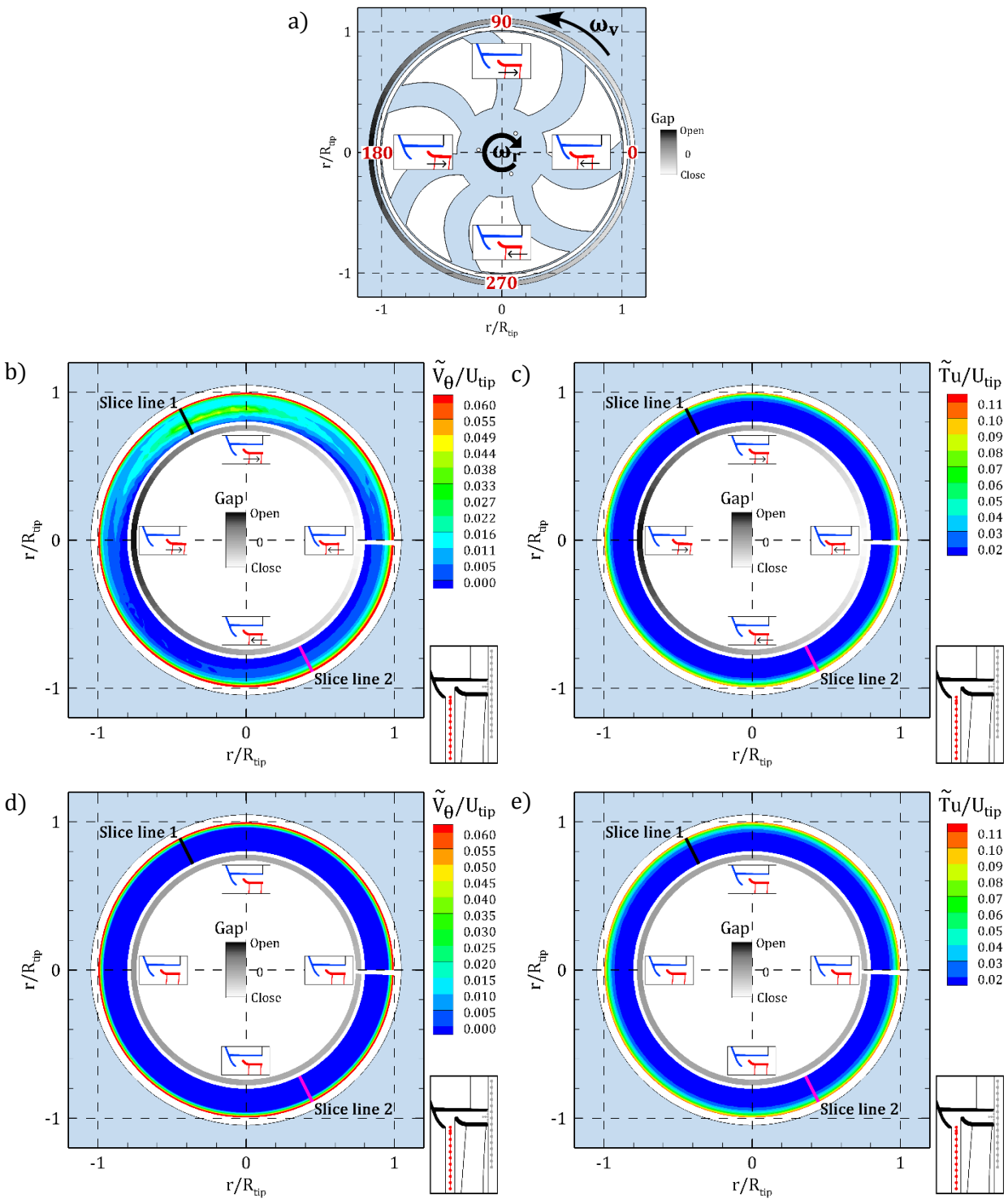

Fig. 5.24. Double phase average (Vibro periodicity) of LDV radial traverse measurements upstream of the fan. a) Direction of rotation of the rotor (ω_r) and whirling motion (ω_v), plus four schematic positions and a circular black and white contour strip illustrating the gap opening. b) Tangential velocity (Flutter). c) Turbulence intensity (Flutter). d) Tangential velocity (No-Flutter). e) Turbulence intensity (No-Flutter).

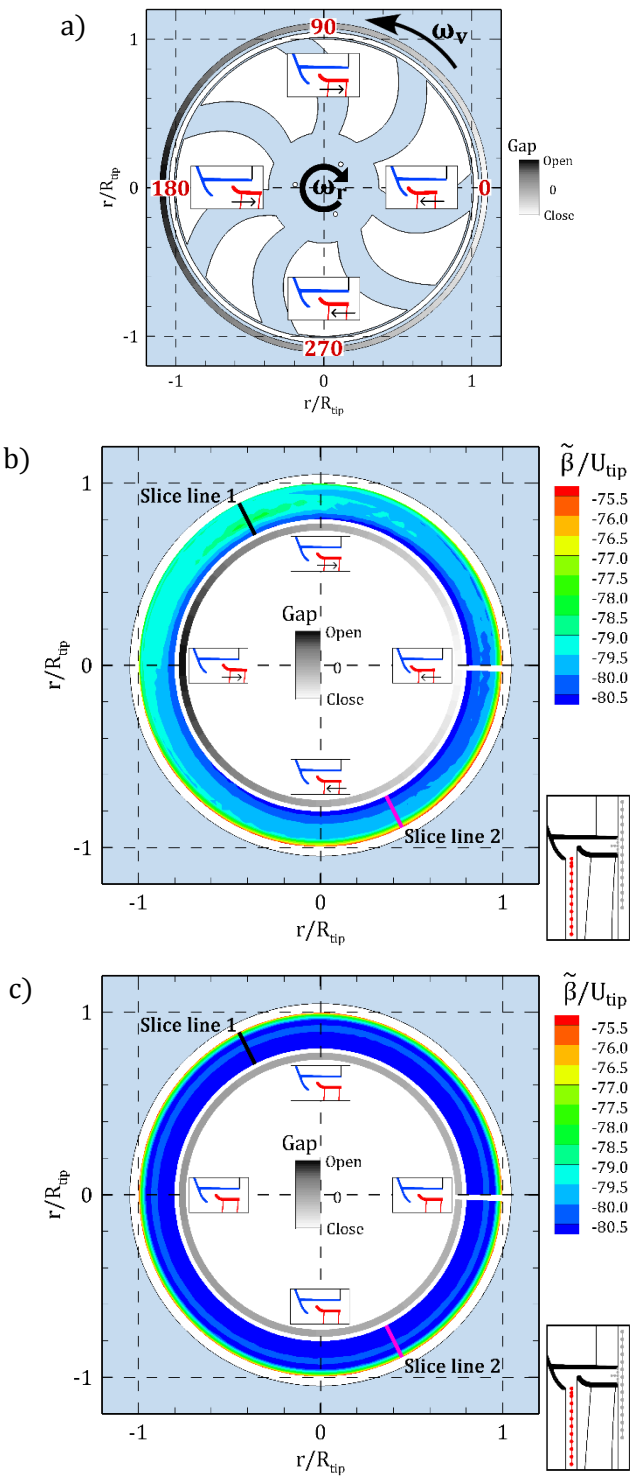

Fig. 5.25. Double phase average (Vibro periodicity) of LDV radial traverse measurements upstream of the fan. a) Direction of rotation of the rotor (ω_r) and whirling motion (ω_v), plus four schematic positions and a circular black and white contour strip illustrating the gap opening. b) β angle (Flutter). c) β angle (No-Flutter).

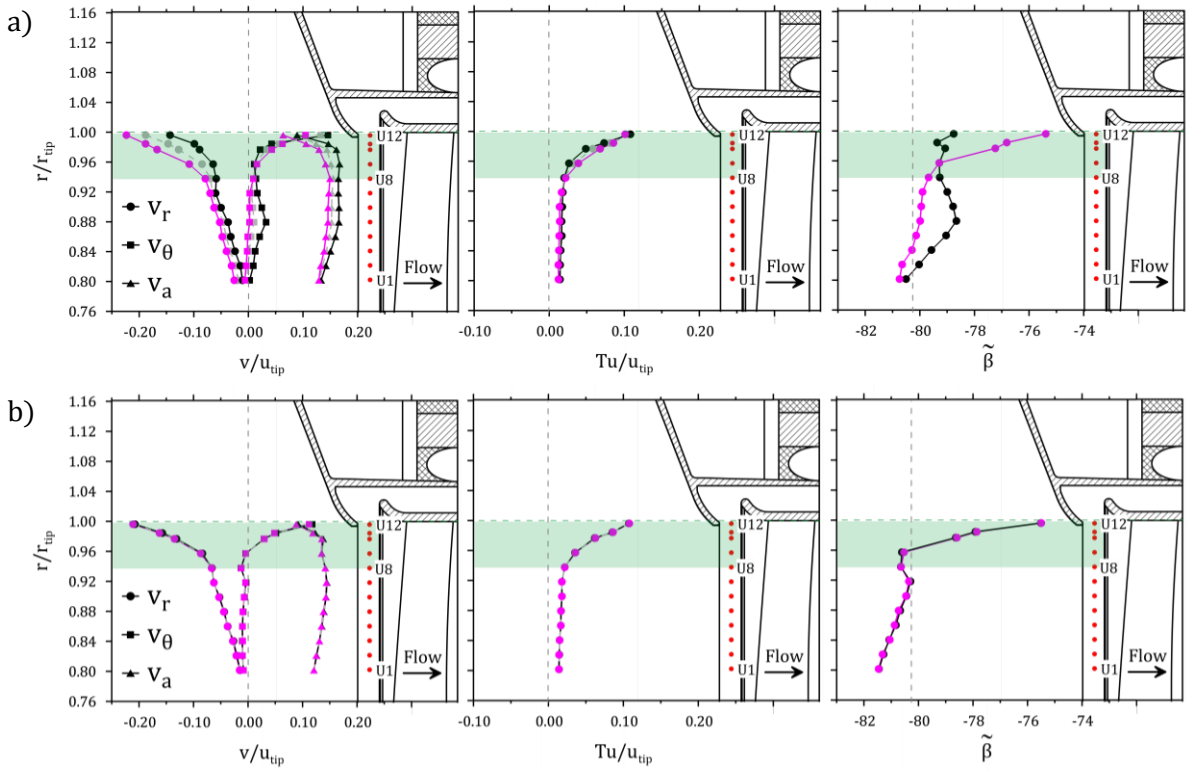

Fig. 5.26. The radial traverse of three velocity components at slice lines 1 (black line) and 2 (magenta line) compared to the mean velocity profile (dashed gray line). a) Flutter case. b) No-Flutter case.

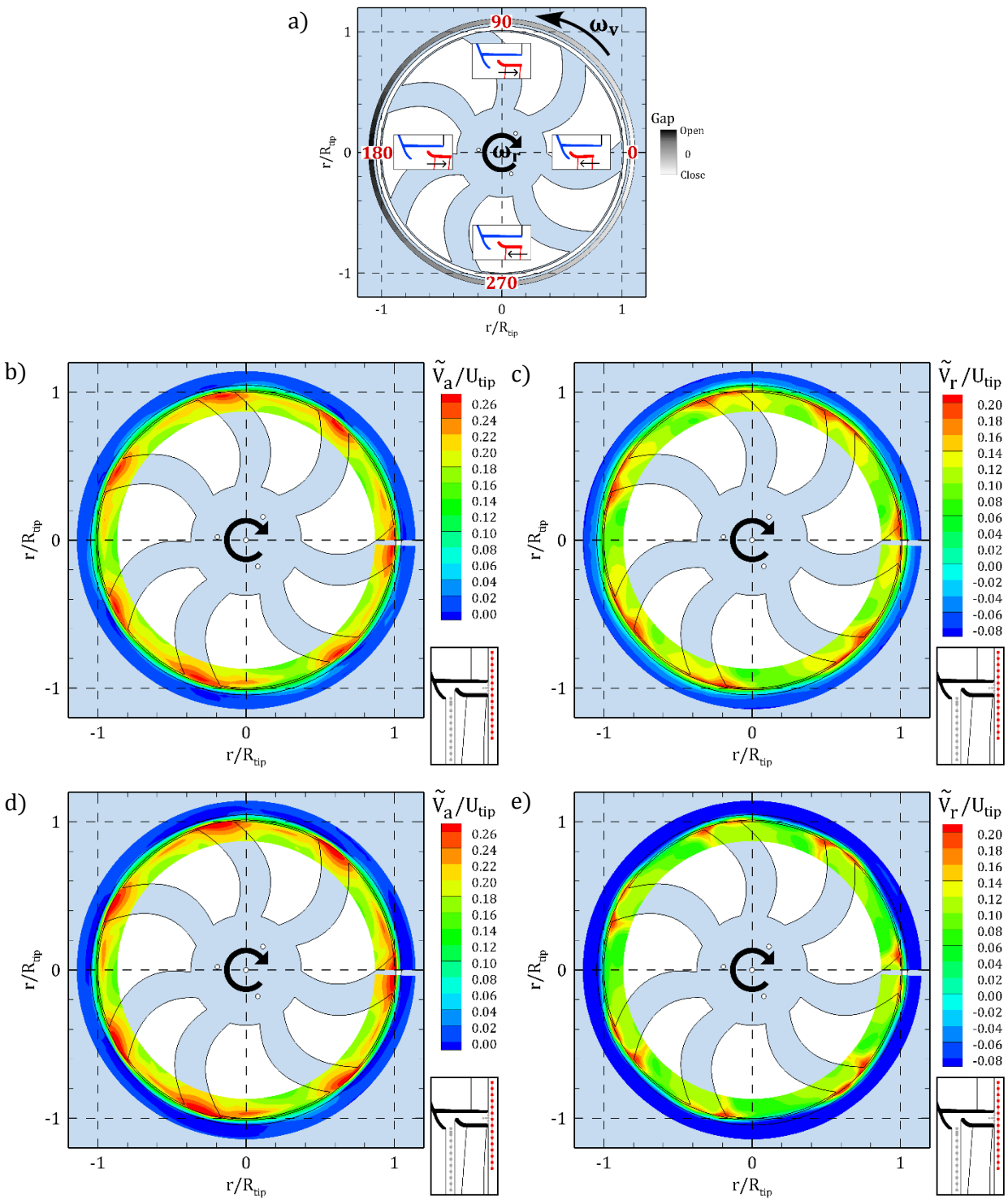

Fig. 5.27. Double phase average (Tacho periodicity) of LDV radial traverse measurements downstream of the fan. a) Direction of rotation of the rotor (ω_r) and whirling motion (ω_v), plus four schematic positions and a circular black and white contour strip illustrating the gap opening. b) Axial velocity (Flutter). c) Radial velocity (Flutter). d) Axial velocity (No-Flutter). e) Radial velocity (No-Flutter).

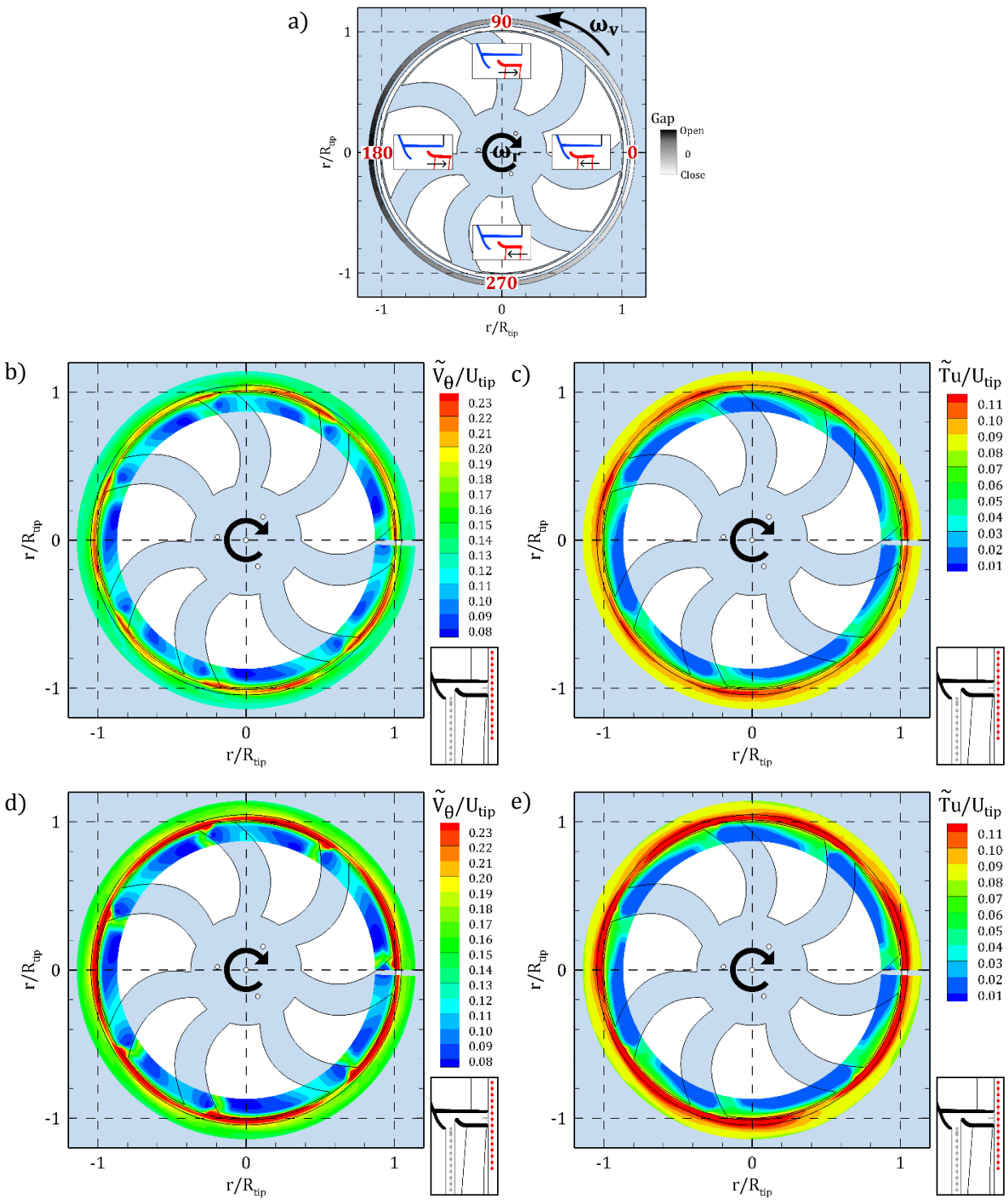

Fig. 5.28. Double phase average (Tacho periodicity) of LDV radial traverse measurements downstream of the fan. a) Direction of rotation of the rotor (ω_r) and whirling motion (ω_v), plus four schematic positions and a circular black and white contour strip illustrating the gap opening. b) Tangential velocity (Flutter). c) Turbulence intensity (Flutter). d) Tangential velocity (No-Flutter). e) Turbulence intensity (No-Flutter).

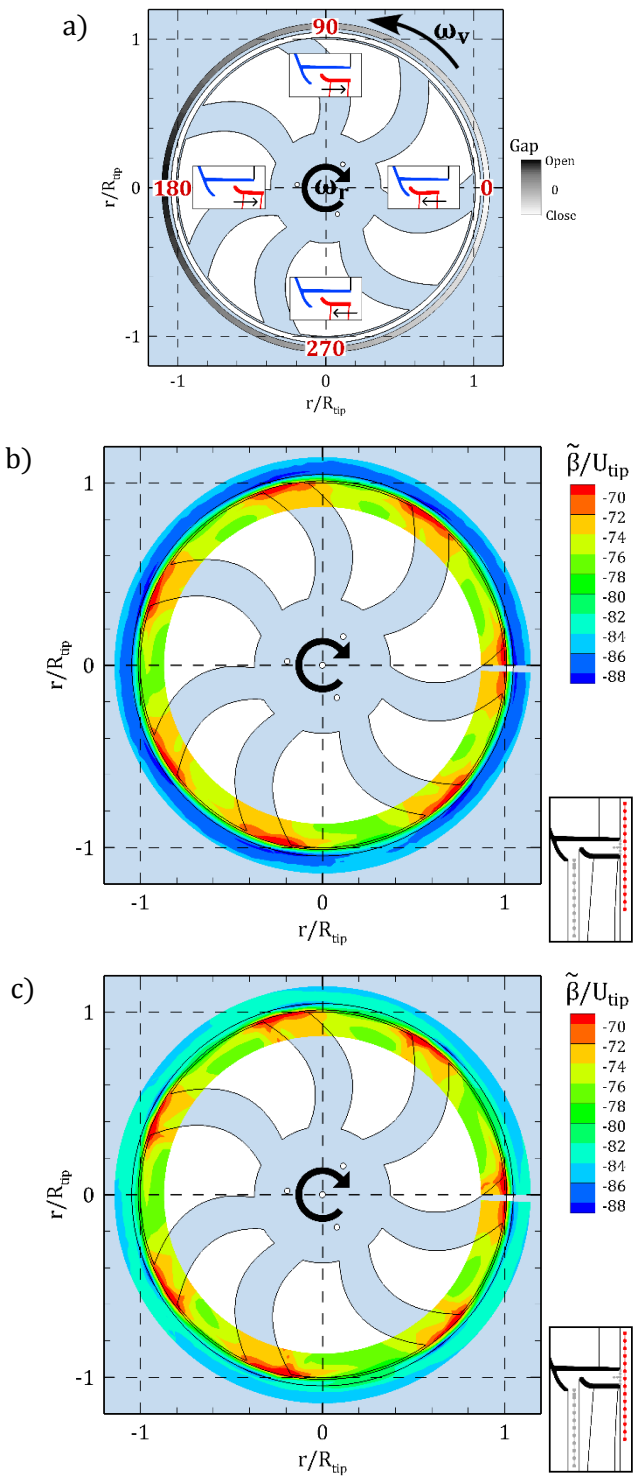

Fig. 5.29. Double phase average (Tacho periodicity) of LDV radial traverse measurements downstream of the fan. a) Direction of rotation of the rotor (ω_r) and whirling motion (ω_v), plus four schematic positions and a circular black and white contour strip illustrating the gap opening. b) β angle (Flutter). c) β angle (No-Flutter).

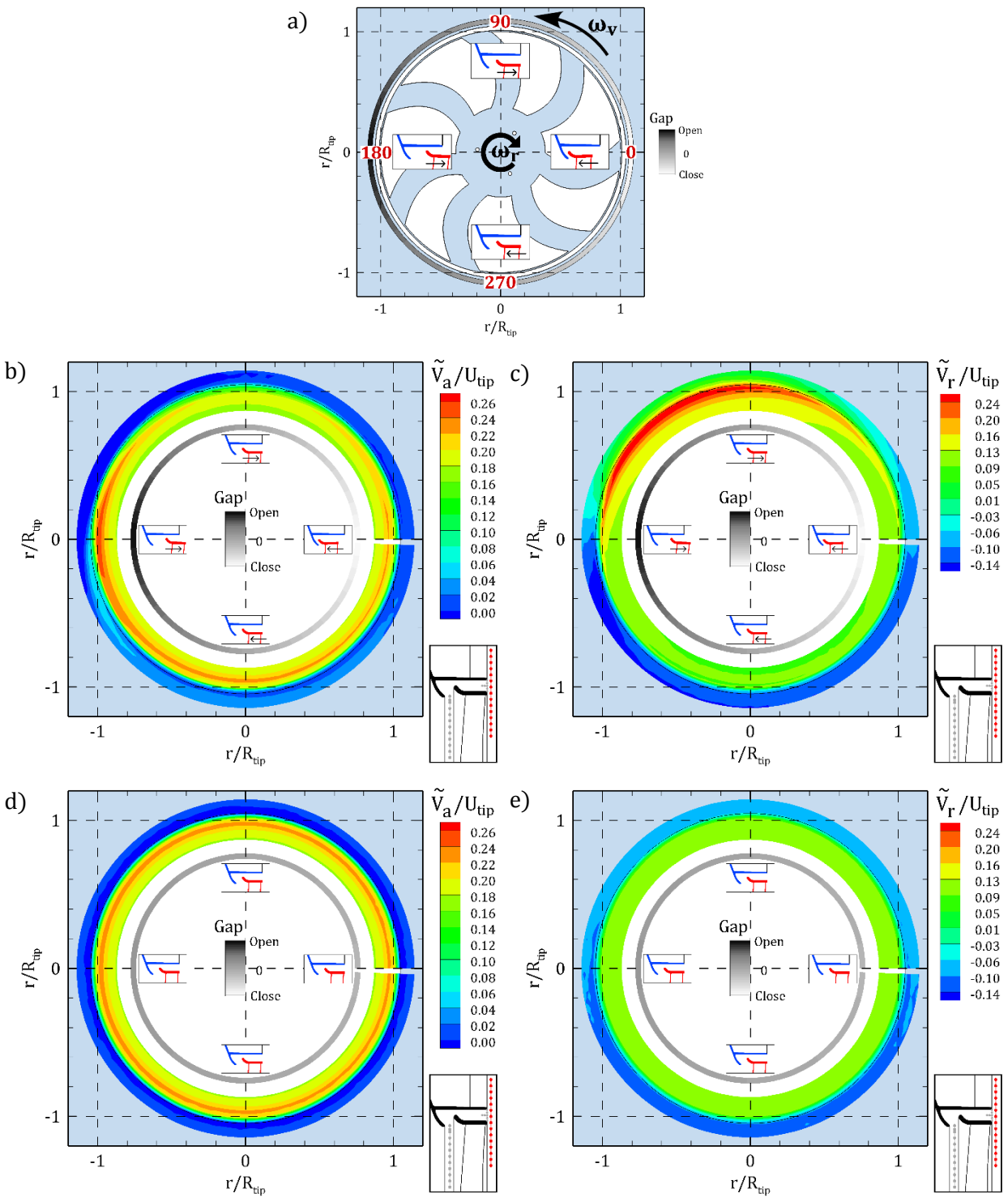

Fig. 5.30. Double phase average (Vibro periodicity) of LDV radial traverse measurements downstream of the fan. a) Direction of rotation of the rotor (ω_r) and whirling motion (ω_v), plus four schematic positions and a circular black and white contour strip illustrating the gap opening. b) Axial velocity (Flutter). c) Radial velocity (Flutter). d) Axial velocity (No-Flutter). e) Radial velocity (No-Flutter).

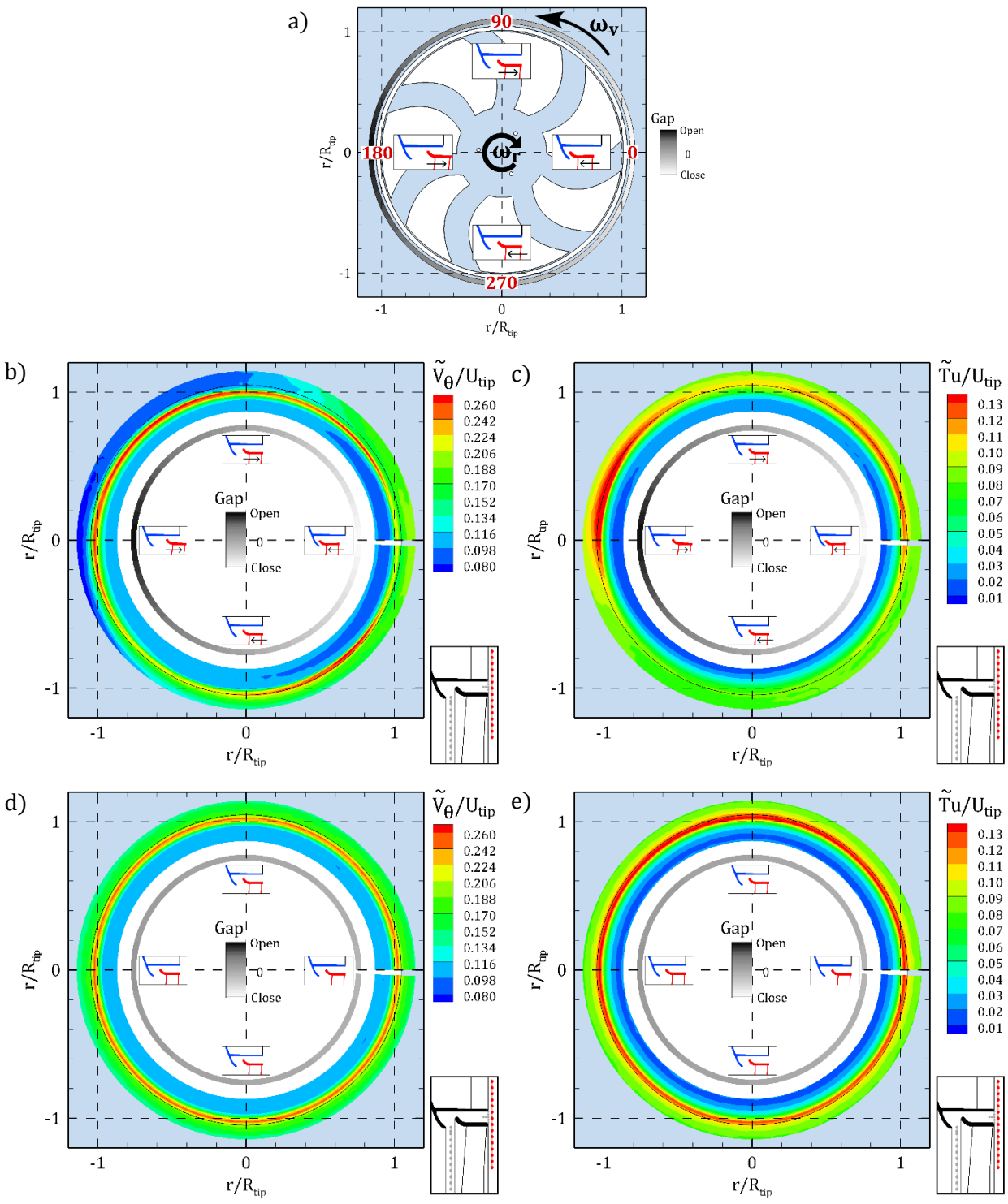

Fig. 5.31. Double phase average (Vibro periodicity) of LDV radial traverse measurements downstream of the fan. a) Direction of rotation of the rotor (ω_r) and whirling motion (ω_v), plus four schematic positions and a circular black and white contour strip illustrating the gap opening. b) Tangential velocity (Flutter). c) Turbulence intensity (Flutter). d) Tangential velocity (No-Flutter). e) Turbulence intensity (No-Flutter).

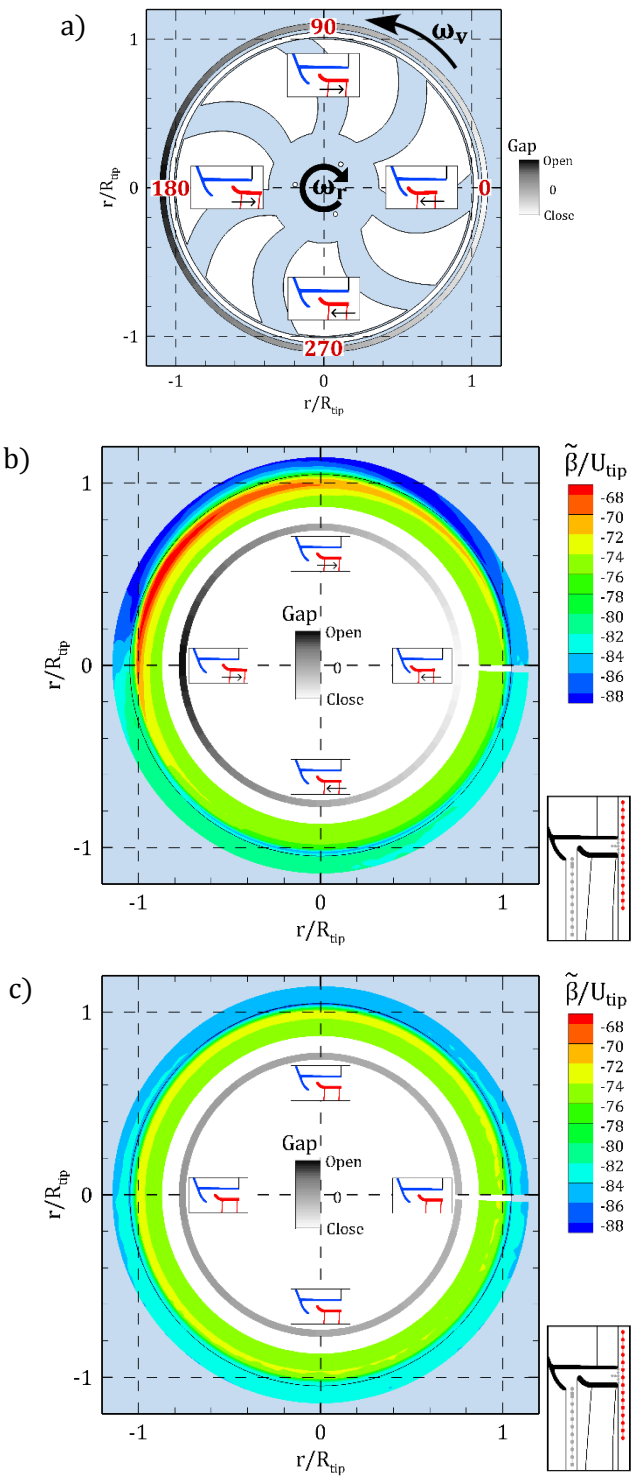

Fig. 5.32. Double phase average (Vibro periodicity) of LDV radial traverse measurements downstream of the fan. a) Direction of rotation of the rotor (ω_r) and whirling motion (ω_v), plus four schematic positions and a circular black and white contour strip illustrating the gap opening. b) β angle (Flutter). c) β angle (No-Flutter).

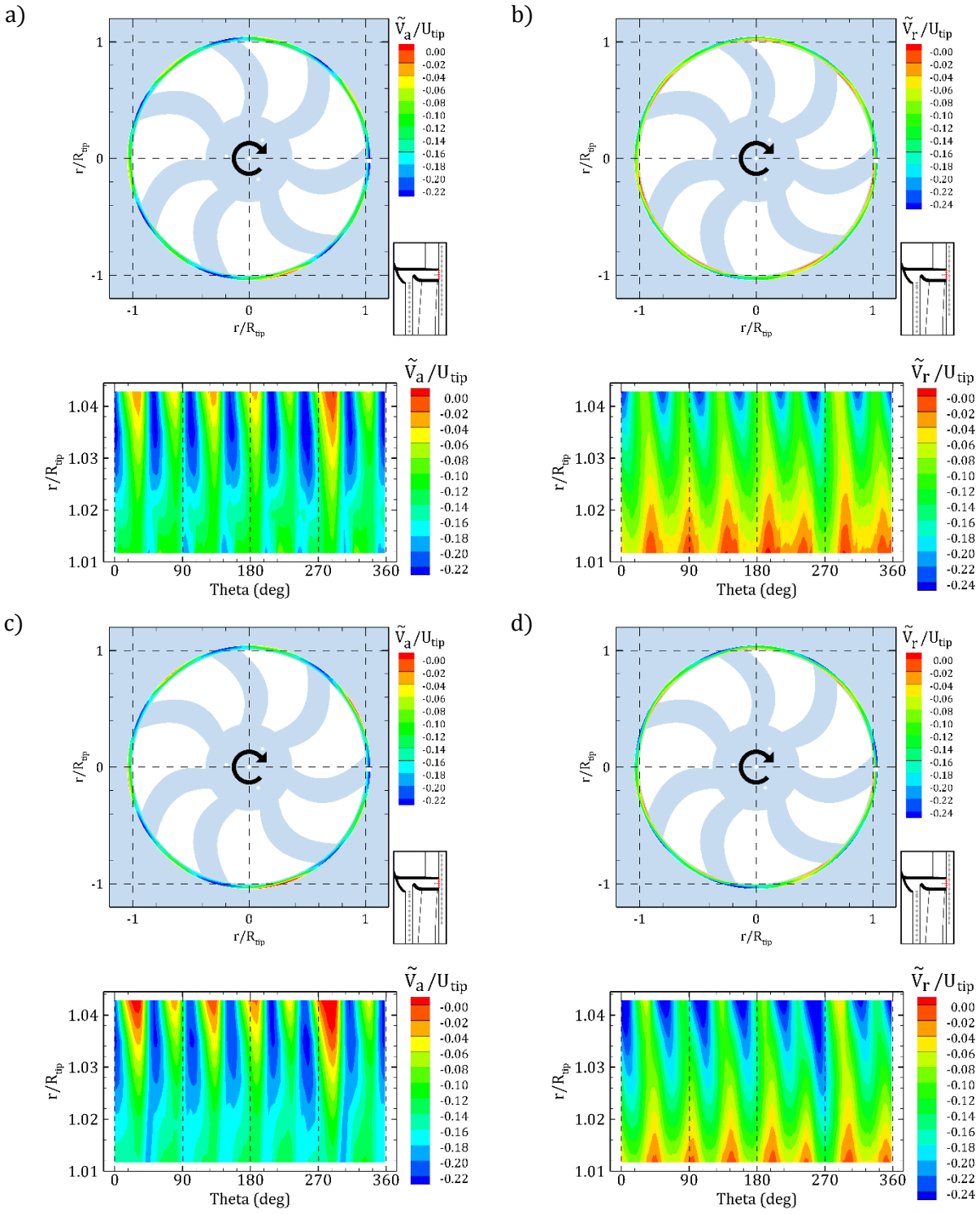

Fig. 5.33. Double phase average (Tacho periodicity) of LDV radial traverse measurements at gap entrance. a) Axial velocity (Flutter). b) Radial velocity (Flutter). c) Axial velocity (No-Flutter). e) Radial velocity (No-Flutter).

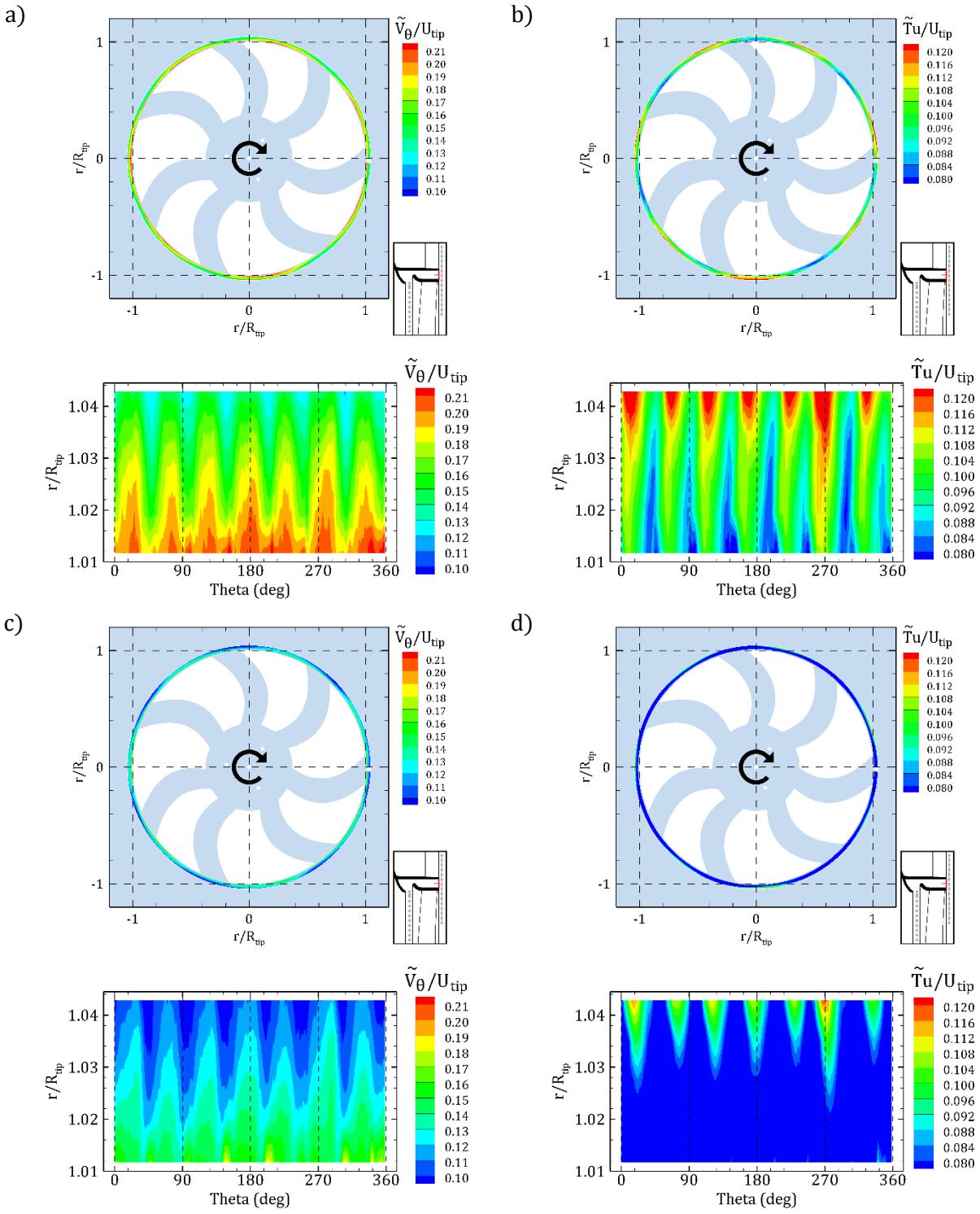

Fig. 5.34. Double phase average (Tacho periodicity) of LDV radial traverse measurements at gap entrance. a) Tangential velocity (Flutter). b) Turbulence intensity (Flutter). c) Tangential velocity (No-Flutter). e) Turbulence intensity (No-Flutter).

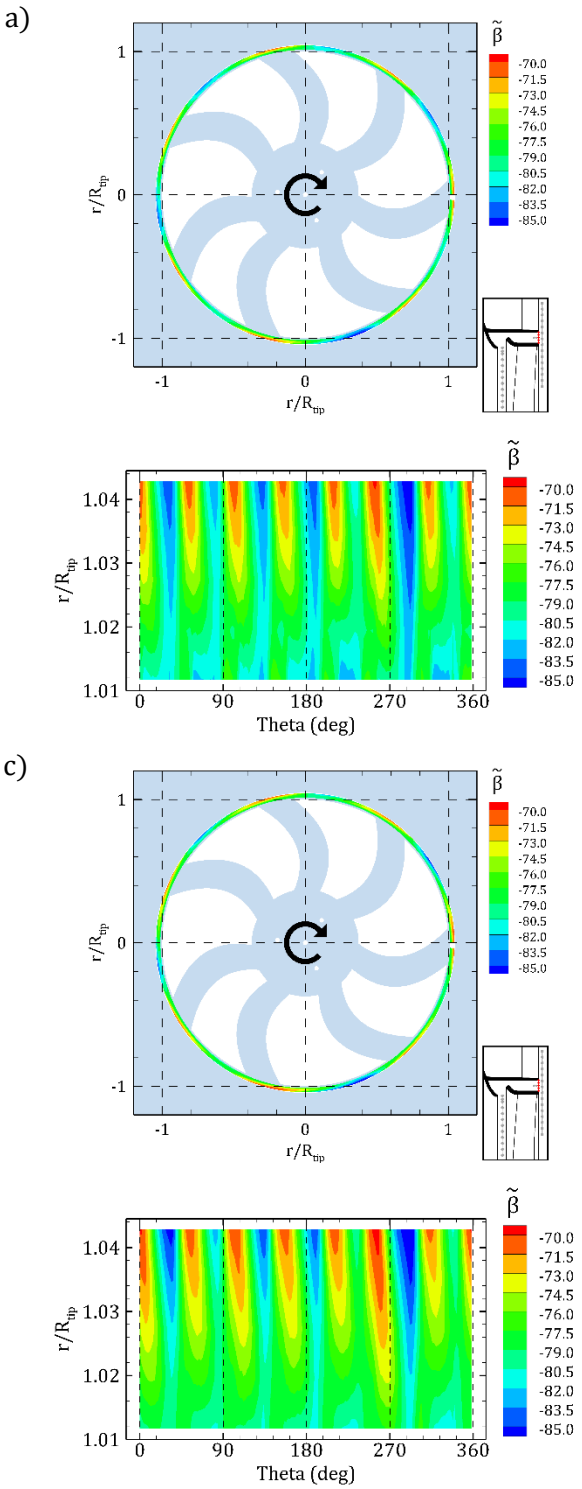

Fig. 5.35. Double phase average (Tacho periodicity) of LDV radial traverse measurements at gap entrance. a) β angle (Flutter). b) β angle (No-Flutter).

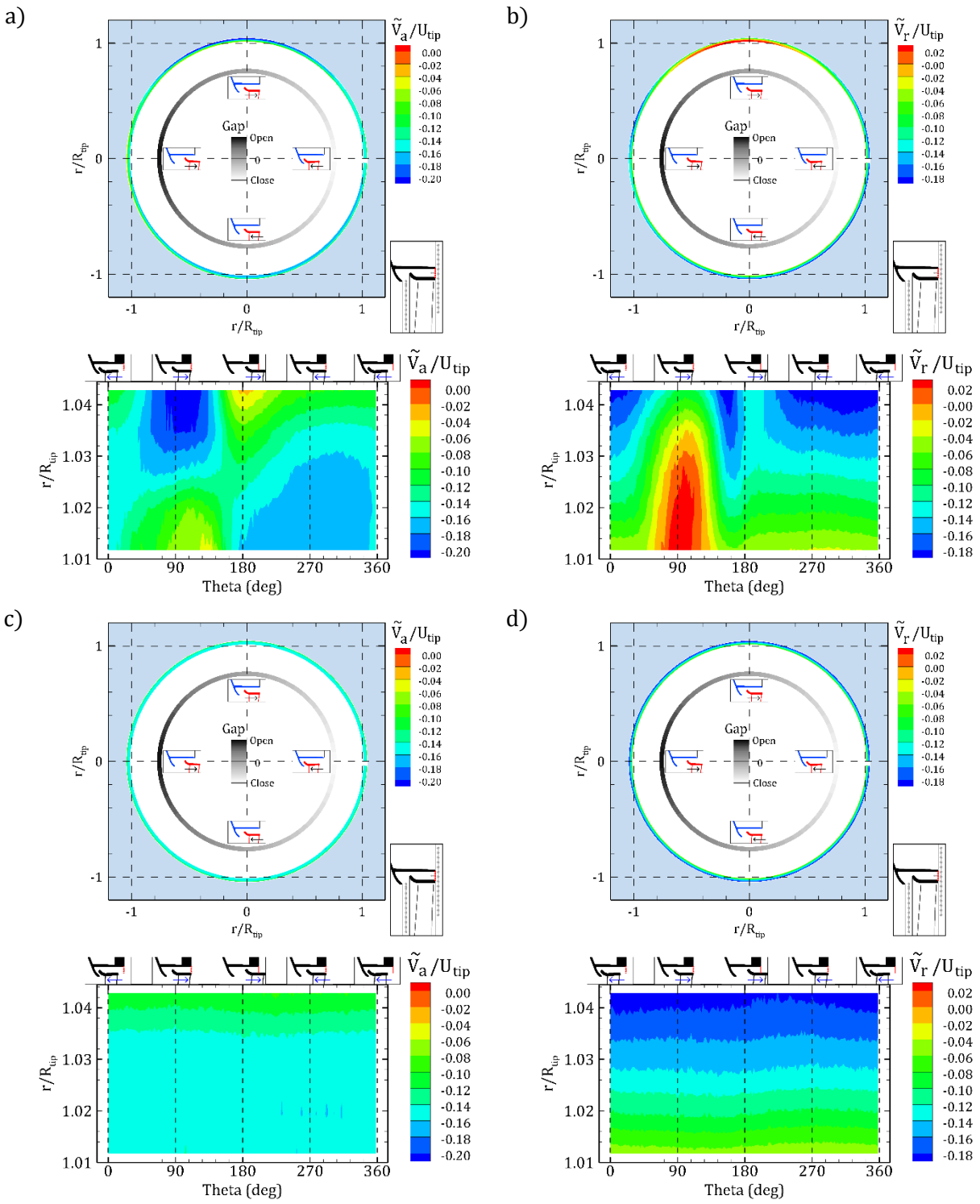

Fig. 5.36. Double phase average (Vibro periodicity) of LDV radial traverse measurements at gap entrance. a) Axial velocity (Flutter). b) Radial velocity (Flutter). c) Axial velocity (No-Flutter). e) Radial velocity (No-Flutter).

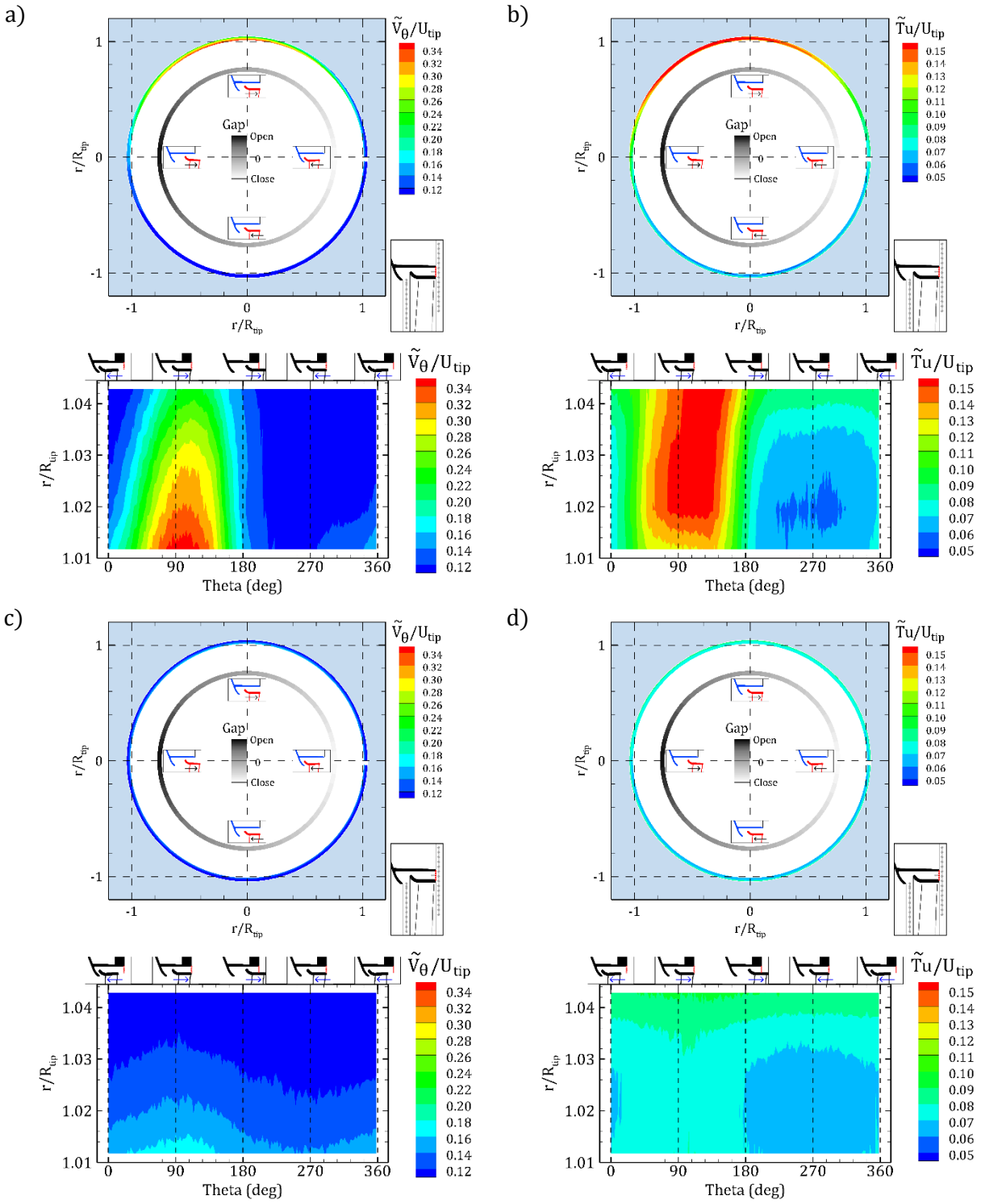

Fig. 5.37. Double phase average (Vibro periodicity) of LDV radial traverse measurements at gap entrance. a) Tangential velocity (Flutter). b) Turbulence intensity (Flutter). c) Tangential velocity (No-Flutter). e) Turbulence intensity (No-Flutter).

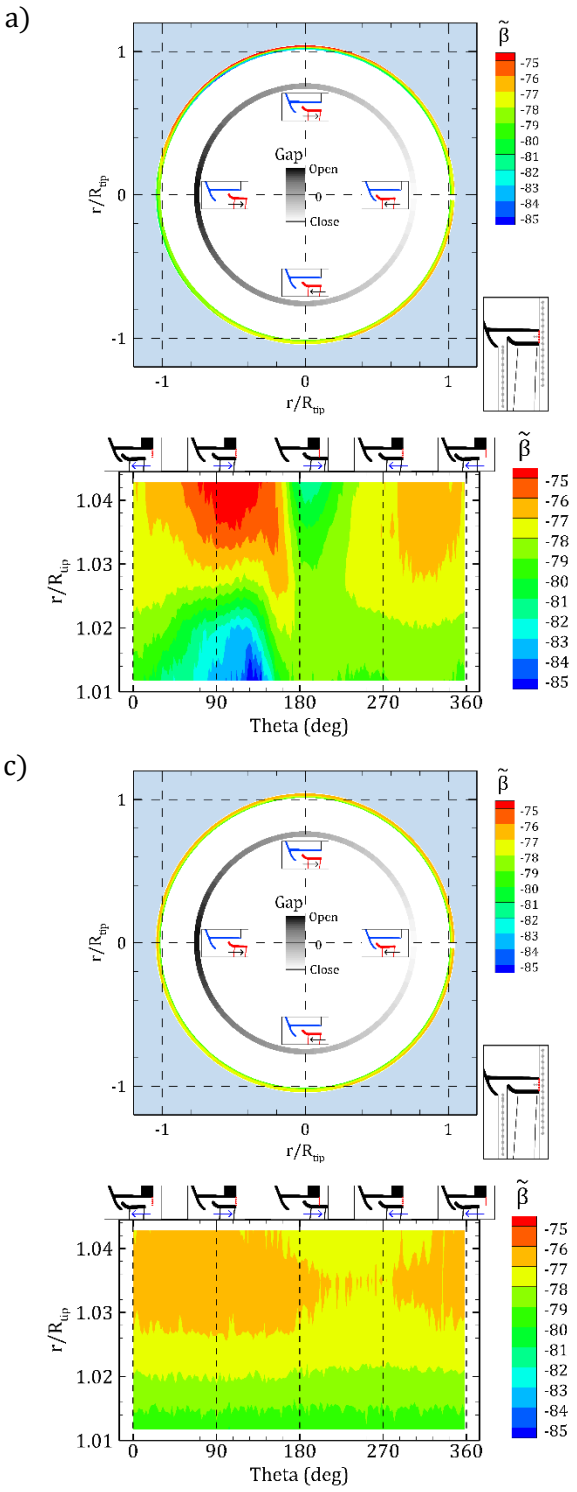

Fig. 5.38. Double phase average (Vibro periodicity) of LDV radial traverse measurements at gap entrance. a) β angle (Flutter). b) β angle (No-Flutter).

6. CONCLUSIONS

Throughout this thesis, an experimental study of the high-amplitude and low-frequency vibration of a low-speed fan provided with a rotating shroud is reported. This vibration, which takes place at a frequency $f_v \cong 7.3$ Hz when the fan approaches the design speed of $f_r = 42.5$ Hz, has been identified as the first backward whirling mode of the rotor that, consistenly, counterrotates at the same frequency f_v. It may be classified as an aeroelastic problem.

In order to measure and characterize this vibration, various mechanical and aerodynamic measurements have been performed. To this aim, a new test stand has been designed which is suitable for simultaneous mechanic and aerodynamic measurements on fans.

Mechanical investigations have been taken by means of both accelerometers and optical vibrometers. The latter has allowed a preliminary measure of the axial position of the ring at a very low rotational speed, confirming the visual observation that the ring is axially nonplanar due to the presence of bumps whose origin is the molding process employed for manufacturing the fan. As a result, peaks in the power spectral density of the ring axial displacement signal are expected at the f_r harmonics could be due to a residual static unbalance but such peaks surely receive an important contribution from to the periodic passage of the ring bumps in front of the vibrometer probe.

The dynamical behavior of the fan assembly has been preliminarily characterized by means of FEM and experimental modal analysis, which have provided consistent results and have shown that the modal frequencies of rotor and casing are much larger than f_v. Then, the Campbell diagram of the fan has been obtained by means of both FEM and experimental; the analysis of modal shapes and frequencies proved that the observed low-frequency vibration is related to the first backward mode of the system, consisting of a precession motion superposed to the revolution about the rotational axis. In addition, all the other important modes, e.g., first and second backward and forward ones, have been analyzed. The assumed backward direction of rotation of the low-frequency whirling mode has been experimentally confirmed by measuring the phase difference between the signal from two vibrometers located at almost 90 degrees angular positions.

Then, the low-frequency aeroelastic behavior of the fan has been investigated. In order to study the axial oscillation of the rotor, vibrometric measurements have been performed on the rotor ring at different operating points along the characteristic curves of the fan. Then, a map of vibration amplitude has been plotted together with the characteristic curves of the fan, showing the dependency of the vibration amplitude on the operating condition (flow rate, head, and rotational

speed). Based on the visual observation of the vibration, three typical behaviors have been considered: High amplitude vibration (Flutter), no perceived vibration (No-Flutter), and intermittent vibration. It has been found that, at the design point, the high-amplitude oscillation onsets when f_r increases and approaches the design rotational speed; the same happens at the design rotational speed operation approaching the design point from the both high and low head.

The analysis of the PSD plots related to two extreme cases, Flutter and No-Flutter, has shown that although those have different heights, a low-frequency peak is always present, thus suggesting that the vibration is caused by resonance. In the former case, it has been observed that f_v decreases when f_r increases; such an observation has been confirmed by the Campbell diagram obtained by wavelet analysis of a vibrometer signal acquired during a low-acceleration rotational speed ramp. Furthermore, it has been found that, in the Flutter case, peaks at 2nd, 3rd, and 4th harmonics of f_v are present, opposite to the No-Flutter case. In the Flutter case only, side peaks shifted of $\pm f_v$ multiples are present besides the ones at the f_r harmonics, a feature typical of frequency modulation. . By comparing the two signals of the vibrometer at the rotor ring and accelerometer at the motor which have been measured simultaneously it has been discovered that in the Flutter case the amplitude of the vibration at the rotor ring is more than 10 times higher than at the motor.

The confirmation that the excitation is aeroelastic arrived by observing that positioning a thin bar downstream of the fan close to the gap but without any contact immediately suppresses the large-amplitude vibration and removing the bar the vibration rapidly re-onsets. This indicates that the excitation is not purely mechanical, since the bar may act on the system only by changing the flow field, specifically, both recirculating and leakage flows. Furthermore, it has been observed that increasing the roughness of the external surface of the rotor ring has the same effect as positioning the bar. This indicates that the leakage flow is involved in the vibration, suggesting that the feedback loop is as follows: the vibration yields a rotating variation of the gap size, which in turn yields a fluctuation in the leakage flow, which impacts the blades, eventually resulting in a fluctuating aerodynamic load that causes the vibration.

Theoretical models for structural dynamics and aerodynamic forces have been developed. Such models confirm that a counterrotating flow pattern may yield a rotating aerodynamic force pattern at frequencies observed in the vibrometer signal PSD and that fluctuations in the rotational speed may yield the apparent frequency modulation effect due to ring non-planarity combined with the vibration.

A complete series of aerodynamic measurements have been carried out, employing complementary techniques (PIV and LDA), to supply general information on the flow as well as deepen the unsteady flow involved in the flutter phenomenon.

The PIV measurements have shown there is no relevant difference in the time mean flow between Flutter and No-Flutter cases; the obstruction disk mounted downstream of the rotor forces the fan outflow to become centrifugal at a very short distance, but a centripetal flow close to the mounting panel is present, which may be considered a recirculating one. Such a recirculating flow merges with the rotor outflow and results in the backflow entering the gap between the rotating ring and the stationary shroud (the leakage flow). By analyzing the instantaneous PIV snapshots, it has been found that at the interface between the rotor outflow and the recirculating flow, large-scale eddies are present, an observation confirmed by the performed POD analysis.

The mean flow field has also been measured in radial traverses close to the gap region by means of an LDA system, confirming that the leakage flow enters from the gap downstream of the fan and mixes with the rotor inflow upstream of the fan when it leaves the gap. This affects all of the three velocity components upstream of the fan at radial positions close to the gap outlet; in this radial position, the flow has a tangential velocity component and it is more centripetal than the lower radii inflow due to the leakage flow leaving the gap outlet.

A new double phase ensemble average technique has been developed to distinguish the effects of two periodic parts (rotation and vibration periodicity, detected by tachometer and vibrometer signals) of the flow; to the author's knowledge, such a technique has never been employed. Using this novel technique, periodic parts of velocity profiles of the flow field upstream and downstream of the fan have been studied.

Analyzing the ensemble average flow based on Tacho-periodicity has shown the expected effect of the periodic blade passage present in velocity profiles; comparing No-Flutter and Flutter cases shows that apart from minor differences there is no dissimilarity between the two time-mean flow fields. Analyzing the ensemble average flow based on Vibro-periodicity has shown the effect of the precession motion of the rotor. In the Flutter case, a periodicity related to the precession motion of the rotor is present in all of the velocity components, while in the No-Flutter case, velocity components are axisymmetric without any periodicity. The Vibro-periodicity ensemble average shows that the flutter also affects the relative flow angle at the rotor inlet, and consequently the angle of attack at the blade tips, which finally causes the aeroelastic phenomenon: unsteady flow excites vibration, and vibration generates unsteady flow; this change in the flow field is periodic and links to

the gap outlet area size and precession motion; another interesting finding is that the maxima and minima in the velocity field are located at angular positions different from the ones at which the gap outlet area is maximum and minimum, but a certain delay exists. This phase delay of all of the relevant quantities needs a deeper future study as it plays a crucial role in creating the negative feedback that allows aeroelastic vibrations to onset and self-sustain.

A few important limitations inherent to the aerodynamic studies need to be considered. First, problems due to optical access and reflections during the PIV and LDA measurements. Second, in this study, a non-time-resolved PIV system has been used, resulting in a slow acquisition for collecting a sufficiently large data set for the double phase ensemble average technique to be applicable. Third, the instantaneous blade force should be known in order to study all of the physical quantities involved in the phenomenon; to this aim, the instantaneous pressure on the blades should be measured, but this requires a special setup including pressure transducers flush mounted on the blade and data transmission from the rotor.

Summarizing, this research answered many issues about the observed flutter but it also raised many questions in need of further investigation. More research is needed to deepen the aerodynamic analysis: for instance joint vibrometric, anemometric, and instantaneous surface pressure measurements. Several attempts have been done using the Hot-Film measurements to study the instantaneous flow inside the gap, with the aim of identifying vortical structures inside the gap but non-conclusive, partially contradictory results were obtained; this difficulty in analyzing the leakage flow development inside the gap could be circumvented by means by CFD analysis.

7. REFERENCES

[1] Longhouse, R. E. (1978). Control of tip-vortex noise of axial flow fans by rotating shrouds. Journal of sound and vibration, 58(2), 201-214.

[2] Canepa, E., Cattanei, A., Jafelice, F., Zecchin, F. M., & Parodi, D. (2018). Effect of rotor deformation and blade loading on the leakage noise in low-speed axial fans. Journal of Sound and Vibration, 433, 99-123.

[3] Canepa, E., Cattanei, A., Zecchin, F. M., & Parodi, D. (2019). Large-scale unsteady flow structures in the leakage flow of a low-speed axial fan with rotating shroud. Experimental Thermal and Fluid Science, 102, 1-19.

[4] Canepa, E., Cattanei, A., & Mazzocut Zecchin, F. (2019). Leakage noise and related flow pattern in a low-speed axial fan with rotating shroud. International Journal of Turbomachinery, Propulsion and Power, 4(3), 17.

[5] Zhu, T., Lallier-Daniels, D., Sanjosé, M., Moreau, S., & Carolus, T. (2018). Rotating coherent flow structures as a source for narrowband tip clearance noise from axial fans. Journal of Sound and Vibration, 417, 198-215.

[6] Magne, S., Moreau, S., & Berry, A. (2015). Subharmonic tonal noise from backflow vortices radiated by a low-speed ring fan in uniform inlet flow. The Journal of the Acoustical Society of America, 137(1), 228-237.

[7] Pardowitz, B., Tapken, U., & Enghardt, L. (2012). Time-resolved rotating instability waves in an annular cascade. In 18th AIAA/CEAS Aeroacoustics Conference (33rd AIAA Aeroacoustics Conference) (p. 2132).

[8] Pardowitz, B., Tapken, U., Neuhaus, L., & Enghardt, L. (2015). Experiments on an axial fan stage: time-resolved analysis of rotating instability modes. Journal of Engineering for Gas Turbines and Power, 137(6).

[9] Moreau, S., & Sanjose, M. (2016). Sub-harmonic broadband humps and tip noise in low-speed ring fans. The Journal of the Acoustical Society of America, 139(1), 118-127.

[10] Magne, S., Moreau, S., & Berry, A. (2015). Subharmonic tonal noise from backflow vortices radiated by a low-speed ring fan in uniform inlet flow. The Journal of the Acoustical Society of America, 137(1), 228-237.

[11] Na, G. D., Kameier, F., Springer, N., & Mauß, M. (2016, June). Numerical Simulations of unsteady aerodynamic effects in the blade tip region of cooling fans. In Turbo Expo: Power for Land, Sea, and Air (Vol. 49682, p. V001T09A015). American Society of Mechanical Engineers.

[12] Dowell, E. H., Scanlan, R. H., Sisto, F., Curtiss Jr, H. C., & Saunders, H. (2015). Aeroelasticity in Turbomachines. A modern course in aeroelasticity, 409-438.

[13] Marshall, J. G., & Imregun, M. (1996). A review of aeroelasticity methods with emphasis on turbomachinery applications. Journal of fluids and structures, 10(3), 237-267.

[14] (2007). ISO 5801:2007 Industrial Fans—Performance Testing Using Standardized Airways. International Organization for Standardization, Geneva, Switzerland.

[15] DANTEC DYNAMICS. (2022). Measurement Principles of PIV.

https://www.dantecdynamics.com/solutions-applications/solutions/fluid-mechanics/particle-image-velocimetry-piv/measurement-principles-of-piv/

[16] DANTEC DYNAMICS. (2022). Measurement Principles of LDA.

https://www.dantecdynamics.com/solutions-applications/solutions/fluid-mechanics/laser-doppler-anemometry-lda/measurement-principles-of-lda/

[17] Hussain, A. K. M. F., & Reynolds, W. C. (1970). The mechanics of an organized wave in turbulent shear flow. Journal of Fluid Mechanics, 41(2), 241-258.

[18] Kelly, S. G. (2006). Advanced vibration analysis. CRC Press.

[19] Mace, B. R., & Manconi, E. (2012, September). Mode veering in weakly coupled systems. In Proceedings of the ISMA conference.

[20] Carassale, L., Cattanei, A., Zecchin, F. M., & Moradi, M. (2020). Leakage flow flutter in a low-speed axial-flow fan with shrouded blades. Journal of Sound and Vibration, 475, 115275.

[21] Cattanei, A., Zecchin, F. M., Di Pasquali, A., & Lazari, A. (2021). Effect of the uneven blade spacing on the noise annoyance of axial-flow fans and side channel blowers. Applied Acoustics, 177, 107924.

[22] Grant, I. (1997). Particle image velocimetry: a review. Proceedings of the Institution of Mechanical Engineers, Part C: Journal of Mechanical Engineering Science, 211(1), 55-76.

[23] Prasad, A. K., Adrian, R. J., Landreth, C. C., & Offutt, P. W. (1992). Effect of resolution on the speed and accuracy of particle image velocimetry interrogation. Experiments in Fluids, 13(2), 105-116.

[24] Lengani, D., Simoni, D., Ubaldi, M., & Zunino, P. (2014). POD analysis of the unsteady behavior of a laminar separation bubble. Experimental Thermal and Fluid Science, 58, 70-79.